Core-Shell Functionalised Carbon Nanoparticles
Synthesis, Electrochemistry, and Fluorescence

Lawrence, Katherine

Award date:
2013

Awarding institution:
University of Bath

CORE-SHELL FUNCTIONALISED CARBON NANOPARTICLES: SYNTHESIS, ELECTROCHEMISTRY, AND FLUORESCENCE

Katherine Lawrence

A thesis submitted for the degree of Doctor of Philosophy

University of Bath

Department of Chemistry

May 2013

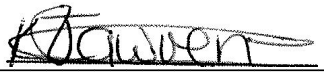

Katherine Lawrence

Table of Contents

Acknowledgements

I gratefully acknowledge Professor Frank Marken for being an inspirational supervisor who believed in me and enabled me to get to where I am today. I also thank my co-supervisor, Professor Tony James, who provided me with some unforgettable experiences throughout my PhD. Thanks are also extended to Dr. Steve Bull who convinced me to stay at Bath University and to do my PhD.

I have supervised a number of undergraduate students throughout my PhD, some of whom directly contributed towards my research progress. Therefore, I would like to thank Charlotte Baker, Peter Haffenden, Emma Lampard, and Xiaoyu (Helen) Jin.

During my PhD, I was able to undertake a research visit at Dalian University of Technology. I acknowledge Professor Jianzhang Zhao for accommodating me as part of his group during this time. I also thank a number of colleagues that I was fortunate enough to collaborate with; namely Dr. Stephen Flower, Dr. Sofia Pascu, Dr. John Mitchels, and Haobo Ge at the University of Bath; Professor Yi-Tao Long of East China University of Science and Technology; Dr. Nick Evans and Dr Mónica Felipe-Sotelo from Loughborough University; Dr Geoffrey Nelson and Professor John Foord at the University of Oxford; Dr. Stan Botchway at Rutherford Appleton Laboratory; and Dr. John Watkins currently at Princeton University.

Finally I would like to thank all members of both the Marken and James groups (past and present) for making my postgraduate experience a fun and rewarding time. Specifically, I would like to thank Dr. Steve Flower and Dr. Sara Dale for being extremely motivational, for sharing some of their wealth of knowledge with me, and for making me smile on a daily basis!

Finally, I acknowledge the EPSRC for a DTA scholarship, which funded my postgraduate research.

"*Nothing great was ever achieved without enthusiasm.*"

– Ralph Waldo Emerson, 19th Century

Abstract

Carbon nanoparticles constitute a class of important materials that have uses in many different fields. This thesis focuses on the synthesis and surface modification of different carbon nanoparticles and each novel nanomaterial is demonstrated to have a specific sensing application.

Carbon blacks play a significant role in the research that is presented herein. Emperor 2000, a commercial bulk-produced carbon black available from Cabot Corporation, is the starting material for many of the investigations. The surface of Emperor 2000 is shown to be susceptible to physisorption, through π-π stacking. These interactions are exploited to append pyrene-based compounds onto the surface of the carbon nanoparticles. This methodology results in carbon nanoparticles with surface boronic acid functionality that is demonstrated to be affective in the electrochemical detection of catecholic caffeic acid.

Emperor 2000 carbon nanoparticles are commercially produced with phenylsulphonic acid functional groups on the surface. This functionality is subjected to synthetic methods to obtain carbon nanoparticles with extremely hydrohphobic character, which are demonstrated as important substrates for probing lipophilic redox systems and lipid character under different experimental conditions.

Fluorescent carbon nanodots (C-dots) are another important form of carbon nanoparticle. Herein, the facile synthesis of C-dots that possess intrinsic pyridine functionality is described. These nanodots exhibit two-photon fluorescence that is exhibited both in solution and in HeLa cells. The nanodots are demonstrated to have the potential to be developed into nanomedicines and biocompatible scaffolds for new drug delivery mechanisms.

These straightforward synthesis, modification, and application methods demonstrate the effectiveness and the versatility of carbon nanoparticles. This class of nanomaterial is generally outclassed by modern and more fashionable carbon nanotubes and graphene-based systems. However, carbon nanoparticles are more cost effective and readily available carbon-based nanomaterials that can be used for a wide range of applications.

List of Abbreviations

AFM	atomic force microscopy
BE	binding energy
C-dots	carbon nanodots
CLSM	confocal laser scanning microscope
CNP	carbon nanoparticle
CNT	carbon nanotube
CoQ_{10}	coenzyme Q_{10}
CV	cyclic voltammogram/cyclic voltammetry
DDTC	diethyldithiocarbamate
DMPC	1,2-dimyristoyl-sn-glycero-3-phosphocholine
DMPC-Q_{10}	1,2-dimyristoyl-sn-glycero-3-phosphocholine-coenzyme Q_{10} composite
DOA	dioctylamine
DSC	differential scanning calorimetry
EMEM	Eagle's modified essential medium
FLIM	fluorescence lifetime imaging microscopy
FTIR	fourier-transfor infrared
FWHH	full width half height
GFP	green fluorescent protein
HTC	hydrothermal conversion
ICT	internal charge transfer
ITO	tin-doped indium oxide

LOD	limit of detection
MnTPP	5,10,15,20-tetraphenyl-21H,23H-porphinato manganese(III) chloride
MWNT	multi-walled carbon nanotubes
NIR	near infrared
[O]	oxidised species concentration
OHP	outer Helmholtz plane
P1	weakly bound caffeic acid
P2	strongly bound caffeic acid
P4VP	poly-(4-vinylpyridine)
P4VP C-dots	P4VP polymer aggregates containing carbonised P4VP C-dots
PAH	polycyclic aromatic hydrocarbon
PBS	phosphate buffer solution
PDDAC	poly-(diallyldimethylammonium chloride)
PEG	poly(ethylene-glycol)
PVA	polyvinyl alcohol
PZC	point of zero charge
QD	quantum dot
QY	quantum yield
[R]	reduced species concentration
(S_0)	molecular ground state
(S_1)	first singlet excited state
(S_2)	second singlet excited state
SCE	saturated calomel electrode

SEM	scanning electron microscopy
SWNT	single-walled carbon nanotube
(T_1)	first triplet excited state
T_1	4-borono-1-(pyren-2-ylmethyl)pyridin-1-ium chloride
T_2	4-borono-1-(2-(pyren-2-yl)ethyl)pyridin-1-ium chloride
T_3	4-borono-1-(3-(pyren-2-yl)propyl)pyridin-1-ium chloride
TCSPC	time-correlated single photon counting
TEM	transmission electron microscopy
TICT	twisted interanl charge transfer
T_m	gel-fluid transition point
TMOS	tetramethoxysilane
XPS	X-ray photoelectron spectroscopy
λ_{em}	emission wavelength
λ_{ex}	excitation wavelength

Chapter 1

Carbon Nanoparticles: Formation and Application in Electrochemical and Fluorescent Analysis

Contents

1.1 Introduction to Carbon Nanoparticles

Nanoparticle research was pioneered by Michael Faraday in 1857 when he investigated thin films of gold, resulting in the discovery of colloidal gold.[1] Since 1857, nanoparticles have received substantial attention, which can be attributed to the fact that they have extremely large surface-area-to-volume ratios that result in differing properties of nanoparticles compared to bulk samples of the same/similar material.[2, 3] The large surface area of nanoparticles provides a great number of active sites in which target molecules can bind and interact;[4] therefore, the surface is considered a very important component of a nanoscale material.[3]

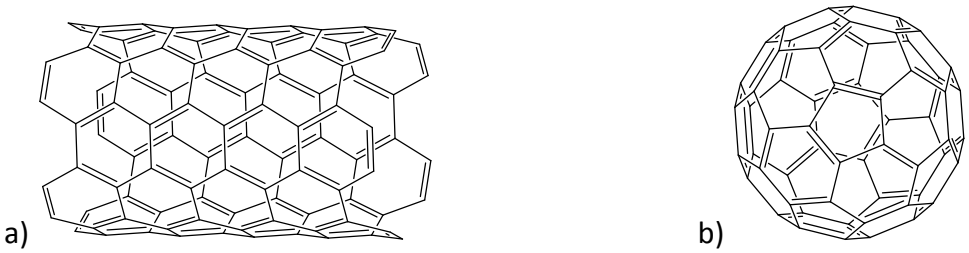

Figure 1.1 - Nanoparticle examples a) a carbon nanotube b) a C_{60} nanocage.

A diverse array of nanoscale particles has been produced, which can be fabricated from a range of materials, such as platinum, gold, carbon etc., and form an assortment of shapes including spherical nanoparticles, nanotubes, and nanocages, see Figure 1.1.[5] Nanoparticles have received significant attention as they exhibit many unique functions and characteristics that are attributed to their nanoscale dimensions, typically 1-100 nm diameters.[4, 6, 7]

One of the first methods of nanoparticle synthesis to be reported was published in 1976 by Birrenbach and Speise. This report demonstrated that a water and hexane-based reverse micellar system was used to investigate the use of nanoparticles as drug carriers.[8] This led to a large amount of research into nanomaterials; however, more recently surface immobilised arrays of nanoparticles have received more attention.[9, 10] When the arrays were immobilised onto surfaces, it enabled the nanoparticulates to be developed into sensors. This was possible because the outer surface of the nanoparticles is the first component of the particulate to interact with the environment.

This means that, although nanoparticles are often referred to by the core material (i.e., carbon), the surface properties of any given nanoparticle are closely, and sometimes implicitly, linked to their application (Figure 1.2).[3] By means of surface modification, nanoparticles can be functionalised so that they exhibit certain properties; therefore, there is the potential for a vast number of substrates to be detected using nanoparticle-based methodologies.

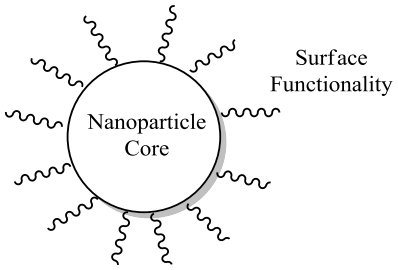

Figure 1.2 - Schematic diagram of a generic nanoparticle.

Carbon nanomaterials receive a huge amount of research interest. With the discovery of carbon nanotubes (CNTs) by Iijima in 1991[11] and graphene by Novoselov and Geim in 2004,[12] nanocarbons represent an ever expanding research area. In contrast to newer, more fashionable nanocarbons, carbon nanoparticles (CNPs) have been around for a number of decades. The earliest known use for CNPs was as a pigment for prehistoric wall art,[13] since then CNPs have established a wider range of scientific and technological applications, and became an extremely important material in the rubber and tyre industries as fillers to elongate the lifetime of polymers.[14-18]

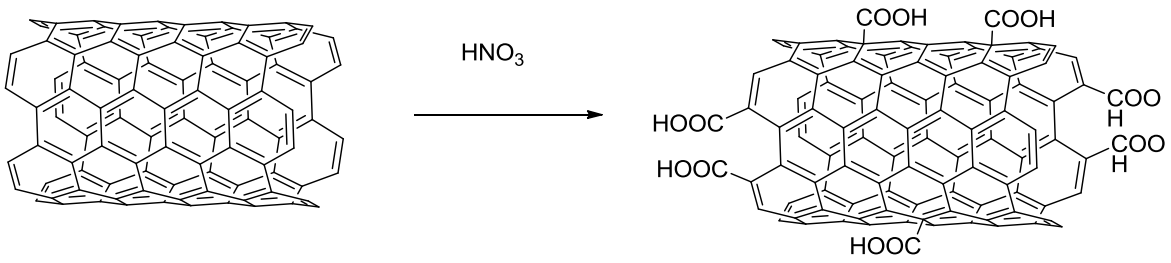

Figure 1.3 - Scheme representing the covalent functionalisation of single-walled carbon nanotubes (SWNTs) by nitric acid oxidation.

CNTs are cylindrical tubes of sp^2 hybridised carbon that have received a large amount of attention with regards to nanotechnology, especially for the purposes of sensing and drug delivery applications.[19-22] Generally, CNTs can be divided into two discrete classes of nanomaterial. Single-walled carbon nanotubes (SWNTs) consist of a layer of graphene rolled along a vector to form a cylindrical tube with a diameter of approximately 1 nm.[23] Multi-walled carbon nanotubes (MWNTs) are formed from more than one graphene sheet being rolled into concentric tubes that have much larger diameters, ranging from 10 to 100 nm.[24] CNTs are associated with a number of toxicity and health issues, mainly because of their hydrophobic nature.[20] Many functionalisation strategies have been used to modify the surface of CNTs to alter the hydrophobicity and to increase biocompatibility. A common route for the modification of CNTs is to use diazonium chemistry to covalently attach molecules to the side walls.[19] This can lead to the appendage of peptides, proteins, and other moieties for targeted drug delivery or optimised sensing applications.

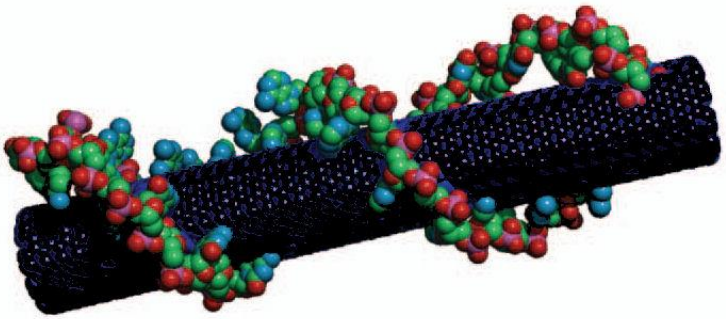

Figure 1.4 - SWNT with a single strand of DNA modifying the surface through π-π stacking. Reproduced from reference.[25]

The most common modification of CNTs documented in the literature is oxidation at CNT defects and tube ends, see Figure 1.3. This involves the formation of carboxyl groups from oxidising agents, quite often nitric acid, which results in CNTs that are of a much more hydrophilic nature.[26, 27] Other covalent functionalisation techniques that have been applied include the application of cycloaddition reactions to the CNT side walls,[28, 29] the addition of hydrophilic polymers such as poly(ethylene-glycol) (PEG),[30, 31] and conjugation of biological molecules. Non-covalent modifications have also been applied to CNTs by the physisorption of compounds through the π-π

interactions that occur between the side walls of the nanotubes and aromatic compounds with available delocalised electrons, see Figure 1.4.[25, 32-34]

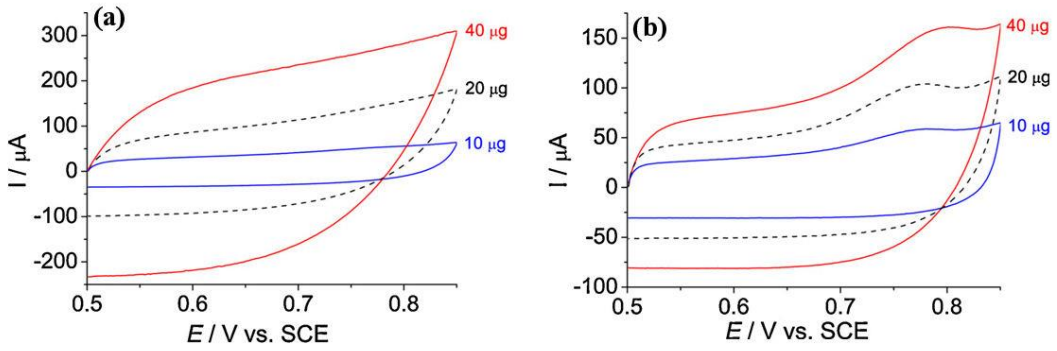

Figure 1.5 - Cyclic voltammograms (scan rate 200 mV s^{-1}) for 50 µM nicotine in 0.1 M phosphate buffer (pH 7.4) at a glassy carbon electrode modified with (a) MWNTs and (b) CNPs. Reproduced from reference.[35]

CNTs are widely employed for the direct modification of electrodes, whereas the much less expensive alternative, carbon nanoparticles have received very little attention in comparison. A study by Lo and co-workers in 2012 compared the activity of optimised CNP-modified electrodes with optimised MWNT-modified electrodes for the detection of nicotine.[35] The capacitive current was considerably higher in the CNT-modified system compared to the CNP equivalent; however, in both cases the non-Faradaic current increased as a function of deposition amount consistent with increasing active surface areas. Perhaps surprisingly, the Faradaic oxidation signal for nicotine was more clearly resolved on the CNP-modified electrode as the large capacitive current on the CNT-modified electrode resulted in the oxidation peak being obscured, see Figure 1.5. Using both CNPs and CNTs resulted in nanostructured electrodes that gave much improved limit of detection (LOD) compared to the standard working electrode; however, optimised CNP-modified electrodes could achieve a LOD of 2.0 ± 0.3 µM nicotine, whereas the optimised CNT-modified equivalent could only detect 5.0 ± 0.3 µM nicotine.[35]

CNPs offer many of the advantages of other nanocarbons including extremely high surface area, conductivity and a multitude of reactive surface and adsorption sites.[36, 37] Also, CNPs are generally much more economically viable than other

nanocarbons as they are relatively inexpensive and are produced commercially in bulk quantities. The term CNPs incorporates a variety of materials such as carbon blacks, carbon dots (C-dots), and core-shell carbon composites. In this introductory chapter, I will discuss the importance of the less-hyped CNPs and summarise recent research that is being performed on these types of materials. This thesis will then demonstrate other applications of modified CNPs, many of the new carbon-based materials can be considered as less expensive and less complex alternatives to modified CNTs.

1.2 Formation of Carbon Nanoparticles

The formation of solid carbon materials in the nanometre size order has been studied for many years and remains an important area of research in a number of fields. Strict size control is preferred but this remains a challenge. There are currently two main techniques used to synthesise carbon nanoparticles, each have a large number of variables, which can lead to nanomaterials with very different properties. These methods are discussed in more detail in the following sections.

1.2.1 Synthesis through Combustion Methods

For many years, the formation of CNPs has been achieved by using either the pyrolysis (pre-mixture of fuel and air) or incomplete (oxygen diffusing into a gaseous fuel) combustion of hydrocarbons. Polymer precursors are popular for pyrolysis methodologies; this is because the fuel is required to be thermally stable and able to form useful carbon residues following high-temperature processing.[38] The carbonisation process can occur by using a number of different techniques, premixed flame methods are most common, in which the oxidiser is mixed with the hydrocarbon fuel in advance ensuring that all reactants are readily available.[39, 40] Laminar diffusion flames burn slower as the rate of combustion is limited by the rate at which the oxidiser diffuses into the fuel supply.[41, 42] Turbulent flames operate by mixing the oxidiser and the fuel for prolonged times until ignition occurs,[43, 44] also many other flame-based methods have been utilised.[45-47]

The incomplete combustion of hydrocarbons leads to the formation of condensed carbonaceous particles in the nanometre diameter range, these combustion-generated materials tend to exhibit the transport and surface related phenomena associated with nanoparticles in addition to maintaining molecular features such as chemical reactivity.[48] These CNPs, often called carbon blacks, occur through condensed-phase material formation. The combustion of hydrocarbons to form carbonaceous nanomaterials follows an entropically favourable mechanism that is attributed to gas production. The most common intermediate in hydrocarbon pyrolysis is acetylene, although the formation of acetylene from saturated hydrocarbons is endothermic, the process is associated with a large release of hydrogen gas, which significantly increases the entropy of the process. Berthelot suggested that acetylene was a necessary intermediate for solid carbon formation,[49] as did Porter who explained that simultaneous polymerisation and hydrogenation of acetylene was essential to CNP formation.[50] The formation of benzene is considered to be the next step in the mechanism; this is an exothermic process and a decrease in enthalpy is observed due to bond formation; however, this is an entropically disfavoured process but the Gibbs free energy is slightly reduced overall. Polycyclic aromatic hydrocarbons (PAHs) form over time because of entropically favourable conversions from benzene and eventually, solid carbon particles are formed as further dehydrogenation occurs.[51, 52]

1.2.2 Hydrothermal Conversion Methods

The hydrothermal method of processing materials originally described the way in which water changed the Earth to form rocks and minerals at high temperatures and pressures. More recently, hydrothermal processing was defined as any chemical reaction in the presence of a solvent (usually aqueous solvents, as non-aqueous processing is often termed solvothermal) at elevated temperatures and pressures, within a closed system.[53] Hydrothermal carbonisation (HTC) utilises hydrothermal conditions as a technique to synthesise carbonaceous materials from inexpensive and widely available precursors such as carbohydrates,[54-56] polymers,[57, 58] and biomass,[59, 60] to name a few.[61] The HTC process has advanced since it was pioneered for the synthesis of solid state oxides[62] and sulfides,[63] and is now utilised for the synthesis of a wide range of new solid materials with control over their shape, size, and functionality.[64]

HTC has many other advantages over conventional processing methods; the experiments are simple and cost effective, there is better control over nucleation, greater dispersion and rates of reaction, as well as being more environmentally friendly as the process is carried out in a closed vessel.[38, 53, 59] The HTC process usually takes place at temperatures between 160 and 200 ^{o}C.[65] During the course of the experiments, the starting material undergoes dehydration, condensation, polymerisation, and aromatisation to yield colloidal carbon nanoparticles.[38] One of the major advantages of HTC methods rather than combustion methods is that the surface of the nanoparticles tends to have a much more diverse surface functionality. That is to say, that the surface can be modelled on the precursor material.[56]

1.3 Characterisation of Carbon Nanoparticles

Early characterisation studies of carbon black films was performed within the group of Fletcher by using optical imaging at solid liquid interfaces.[66] During these investigations carbon black particles were deposited onto cellulose-coated glass slides from a water suspension. This enabled the extinction coefficient of carbon black to be obtained as 1.6 x 10^{6} m^{-1}; with this information, absorbance imaging was used to determine both absorbance and film thickness at liquid-liquid emulsion drop surfaces, see Figure 1.6. This technique proved to be a relatively straight forward method to characterise carbon films on both solid and liquid interfaces, which clearly demonstrated the tendency of commercially available Emperor 2000 carbon nanoparticles to form aggregates.[66]

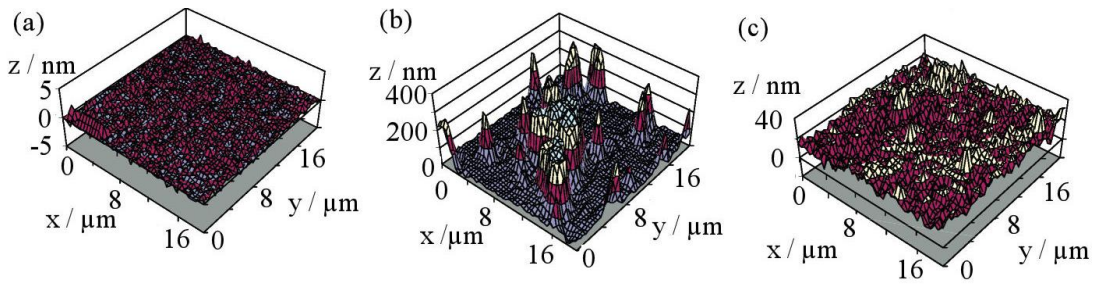

Figure 1.6 - Light path length (z-value) images derived from absorbance imaging of (a) clean cellulose-coated glass surface (b) deposited film of Emperor 2000 CNPs before washing and (c) a film of Emperor 2000 CNPs on cellulose-coated glass after washing with SDS solution. Reproduced from reference.[66]

Many other surface analysis techniques are used to characterise a range of novel carbon nanoparticles. One very common way to elucidate the molecular properties of nanomaterials is to use X-ray photoelectron spectroscopy (XPS). XPS is a quantitative characterisation technique that involves the irradiation of the material of interest with an X-ray beam. XPS can be used to study the energy distribution of electrons that are emitted from X-ray-irradiated species.[67] Unlike other techniques, XPS can be used to investigate all electrons in a species; therefore, the core electrons can be studied in addition to the more easily accessible valence electrons. Following X-ray irradiation, electrons are emitted and the relative binding energies can be obtained, which then leads to information regarding the chemical environment of each atom present in the sample.[67]

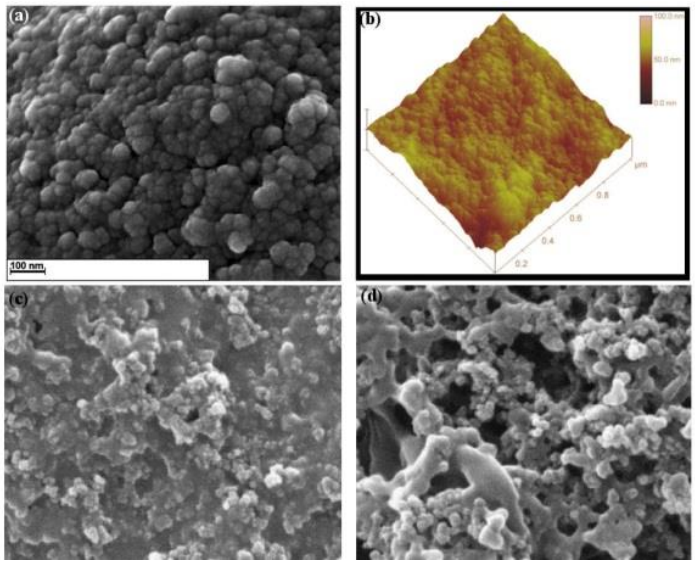

Figure 1.7 - (a) SEM image and (b) AFM image of TMOS/CNP/Laccase modified electrode (reproduced from reference).[68] SEM images of (c) CNPs/PVA and (d) Hb/CNPs/PVA on glass slides (reproduced from reference).[69]

Microscopy is often used to identify the characteristics of nanomaterials. Scanning electron microscopy (SEM) and atomic force microscopy (AFM) can be used to obtain visual information regarding the surface morphology of nanoparticles.[68-71] For example, Szot and co-workers from the Opallo group utilised these two techniques in a complimentary basis. SEM indicated that carbon nanoparticles form globular structures on the surface of a tetramethoxysilane (TMOS)/CNP/laccase electrode, and AFM was

able to demonstrate that the CNPs were evenly distributed throughout the film, see Figure 1.7(a) and (b).[68] Yu and a team from Wuhan University have shown how different film growth conditions can lead to different morphologies and porosities. In one study, they showed that polyvinyl alcohol (PVA)-CNP films resulted in compacted nanostructured films on glass, whereas when haemoglobin was introduced into the matrix, the films formed a three-dimensional porous film, Figure 1.7(c) and (d).[69] In addition to these imaging techniques, transmission electron microscopy (TEM) can be used to study the inner structure and contours of nanoscale materials. This technique allows for nanoparticle size distribution information to be obtained.[60, 71-73] A further optical imaging microscopy that can be used is Brewster angle microscopy (BAM); this technique is based on the Brewster angle, which is the angle at which *p*-polarised light does not reflect off of a specific surface.[74] Any changes in the surface morphology or composition will, therefore, result in reflection at the Brewster angle. BAM can provide lateral information regarding the structure of monolayers, and has demonstrated an excellent ability to detect phase transitions.[75]

1.4 Commercially Available Carbon Black

One of the main commercial uses for carbon black is as an additive to polymeric materials, with great emphasis on the tyre industry. The stabilising effects of carbon nanoparticles on rubber lifetimes arise for a number of different reasons. The surface groups of the nanomaterials are known to interact with polar rubber materials, which result in reinforcement of the polymer.[76] These surface groups are typically carboxylic acids, phenol, quinone and lactone groups, which attach to the graphitic edge planes of carbon nanoparticles.[50] Pěna investigated the behaviour of carbon blacks in more detail and discovered that the efficiency of the nanoparticles on prolonging the lifetime of the rubbers was increased with increasing concentration and decreasing particle size.[77] During this research, it was realised that carbon black pigments were effective as single- and triplet-state quenchers of carbonyl chromophores present in low density polyethylene.[77] Further to this, the adsorption of antioxidants and specific light stabilisers onto the surface of the carbon black pigments were investigated by using flow microcalorimetry. This showed that the adsorption activity is related to the number of active functional groups on the surface of the carbon black material. It was

also clear that carbon nanoparticles with highly oxidised surfaces showed a greater adsorption affinity for the stabilisers. This resulted in the realisation that the surface functionality of the carbon black greatly affected the stabilisation properties of the additives.[78-81]

Although a large number of carbon nanomaterials are actively utilised in industrial applications and in academic research, carbon nanoparticles, especially carbon blacks, constitute some of those most commonly used. This can largely be attributed to their advantageous mesoporous structure combined with inexpensive manufacturing costs. Therefore, there are a number of commercially available carbon black nanoparticles, which have a diverse array of surface functionalities. One of the most frequently exploited carbon blacks is Vulcan XC-72R (Vulcan).[82, 83] This carbon black material is particularly popular for the development of electroactive catalysts because it exhibits beneficial characteristics, namely high surface area and good electrical conductivity. Vulcan is provided on a large scale by Cabot Corporation. It has interesting surface chemistry as the surface is essentially furnished with quinone moieties.[83] This surface functionality renders Vulcan an important precursor material to undergo a vast number of surface modifications. The major surface chemistry associated with Vulcan is oxidation; a large number of studies have demonstrated how different oxidation conditions result in Vulcan nanoparticles with differing functional groups at the surface, such as, carboxyl groups, lactones, anhydrides, phenols, and additional quinone groups.[83-87] For these reasons, Vulcan is considered the most utilised carbon black.

Vulcan carbon blacks have been important in the development of platinum-supported electrocatalysts. A common preparation for such catalysts is through the incipient wetness impreganation method.[88] This type of electrocatalyst can be used for a number of important technological applications, for example it is most often found in fuel cells.[87, 89] The electrocatalytic activity of such carbon-based catalysts can be tuned by adjusting the surface functionalities and subsequently the catalyst morphology.[90] The electron transfer in Pt/Vulcan electrodes occurs through the oxygen atoms that are located at the surface of the support; therefore, the metal/support interaction is important, and this can be altered by surface modifications on the Vulcan carbon material, which will result in more efficient functional groups and chemical linkages at the Pt/C surface as well as increasing the surface area.[90, 91] Hence, the

electrocatalytic activity for such carbonaceous materials can be adjusted by changing the morphology through the surface functionality.

The morphological characteristics of carbon black nanomaterials are largely discussed in terms of individual nanoparticles, agglomerates, and primary particles. Individual nanoparticles tend to be on the size order of 1 to 50 nm, aggregates are rigid and discrete colloidal entities that consist of a group of individual particles, and primary particles are non-discrete components that are made of disordered clusters of individual particles and aggregates to form spherical shapes with a large size distribution.[92] The most commonly used technique for studying the morphology of such nanomaterials is SEM, see Figure 1.7.

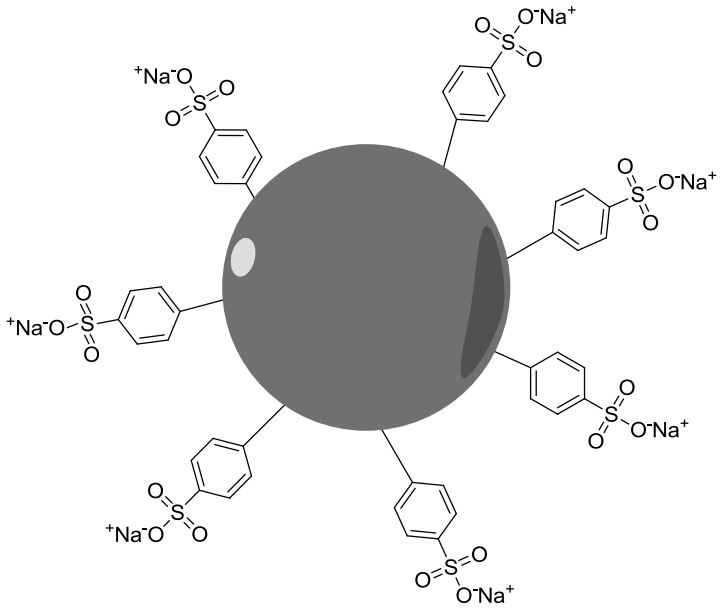

Figure 1.8 - Schematic representation of an Emperor 2000 carbon nanoparticle.

The focus of this thesis is another carbon black that is commercially available from Cabot Corporation; Emperor 2000 carbon nanoparticles. These nanoparticles are a form of carbon black that contain predominantly phenylsulfonate groups on the surface, as shown in the schematic illustration in Figure 1.8. These carbon nanoparticles are produced through a method that is based on diazonium chemistry.[93, 94] Emperor 2000 nanoparticles provide an excellent starting material for covalent attachment of molecules, physisorption through π-π stacking mechanisms, and hydrothermal wrapping

techniques to deliver functionalised core-shell materials. These methods will be discussed in more detail in the relevant results and discussion section of this thesis.

1.4.1 Covalent Surface Modification Strategy

Industrially manufactured Emperor 2000 carbon nanoparticles with surface phenylsulfonate (also known as tosyl) groups have been used for a number of electrochemical investigations, and in 2008 Rassaei formed stable films by using this material in different ways. Drop-cast methods involving solvent evaporation onto glassy carbon electrodes was used[95] as well as layer-by-layer deposition.[37] However, both of these methods required a binder. To further the capabilities of this electrochemically active material, the introduction and modification of functional groups was explored to improve the chemical selectivity and charge density at the active surface.[96, 97] Watkins and colleagues in the Marken group utilised the Emperor 2000 carbon nanoparticles as the starting material and developed a method to convert the negative sulfonate functionality into positive amine groups. This was achieved by converting the sulfonate groups into reactive sulfonyl chloride species by using thionyl chloride, before reaction with a diamine to form a sulfonamide linker and terminal amine units, see Figure 1.9.[97]

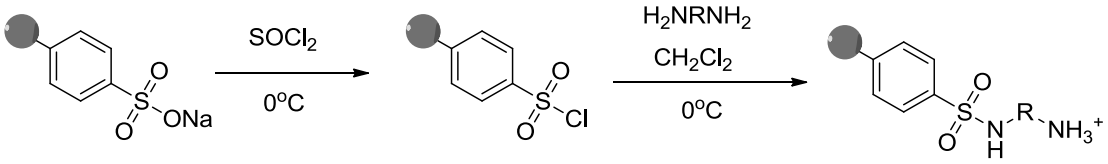

Figure 1.9 - Method used by Watkins et al. to convert the surface charge from negative to positive. Reproduced from reference.[97]

This work enabled new Emperor 2000-based nanocomposite materials to be formed through the mixing of the starting material and the product as the complementary surface charges assembled into an ionic film. Also, this surface modification method resulted in nanoparticles with available amine functionality that could be used for a number of further functionalisations, such as, the covalent attachment of redox active

moieties[98] or subjecting the particles to amide coupling conditions to append other interesting molecules.[99]

1.4.2 Surface Modification by Hydrothermal Wrapping

Hydrothermal methodologies can be used to convert a variety of precursor materials into carbonaceous nanomaterials, as discussed in section 1.2.2. An important factor in the design of a HTC method is the choice of precursor material as this will have a strong influence on the resulting surface functionality of the carbonised nanomaterial. Starting materials that contain amine groups have been shown to result in nanomaterials with positively charged surface features.[100-102] Chitosan has been subjected to the HTC method and was demonstrated to agree with previous literature reports by forming highly positively charged materials; however, like many materials formed in this way, it was revealed to be completely electrochemically insulating, which could be attributed to a layer of poorly carbonised material that acts as a barrier to electron transfer, see Figure 1.10.[65] This methodology was then applied to chitosan in combination with Emperor 2000 carbon nanoparticles, known to be highly conducting, and a method for producing core-shell carbon was reported that resulted in an electrically conducting nanomaterial.[65]

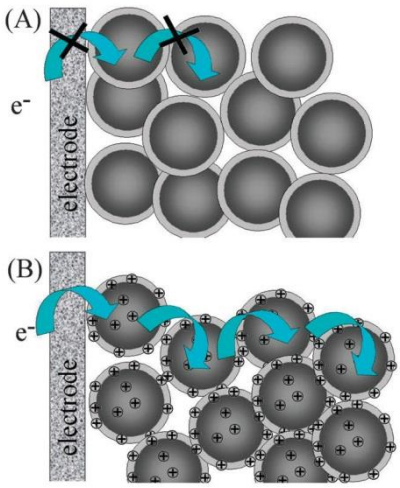

Figure 1.10 - Schematic drawing of core-shell carbon nanoparticles with (A) blocking shells (B) electrically open shells. Reproduced from reference.[103]

Further studies have shown that control of shell thickness and shell properties are possible and these prove to be crucial factors for accessing desired advanced functional characteristics. In the case of chitosan-Emperor 2000 core-shell carbon-hydrothermal nanoparticulates, the product was strongly pH responsive over all accessible aqueous pH values.[103] The composite exhibited high capacitance and improved conductivity in acidic conditions compared to poor conductivity and insignificant capacitance in alkaline media.[103]

1.5 Electrochemistry of Carbon Nanoparticles and Nanocomposites

Carbon nanoparticles in electrochemistry can be adhered to a number of different working electrodes including glassy carbon, graphite, tin-doped indium oxide (ITO) etc. by using drop-cast methodologies. Nanoparticles are commonly prepared as suspensions in ethanol,[65, 103] water,[97, 104] and other solvents.[69, 72] This allows a drop to be placed directly onto the working electrode and evaporated to form either a continuous film or a layer of discrete nanoparticles, depending on the concentration of the solution and the drying process. If the chemical composition of the carbon nanoparticles and the deposition solvent allow, then this can form an insoluble film that allows for electrochemical analysis and characterisation.

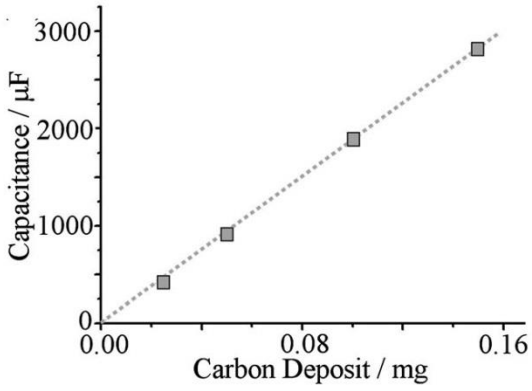

Figure 1.11 - Plot of the capacitance (from cyclic voltammetry data - scan rate 50 mV s^{-1}, 0.1 M phosphate buffer pH 2) *versus* the amount of carbon deposit. Reproduced from reference.[103]

The deposition volume results in different film thicknesses and active surface areas. If the deposited carbon nanoparticles have good conductivity, then there should be an increase in the capacitive current proportional to the deposition volume, as demonstrated by Xia and collaborators.[103] This study reported a completely electrochemically active core-shell film with a specific capacitance of 18 F g^{-1} and linear dependence was observed with increasing amounts of carbon added, see Figure 1.11.[103] In contrast, an earlier study by Xia looked at the same material with a thicker shell composition.[65] This resulted in an electrochemically inactive material and as a result it was only the ITO capacitance that was observed, as shown in Figure 1.12. This can be explained by poor conductivity of the carbon-based nanoparticles, which resulted in no change in capacitance as a function of deposition amount.[65] It is important to note, that the capacitance of sp^2 carbon is also dependent upon the electron occupancy.

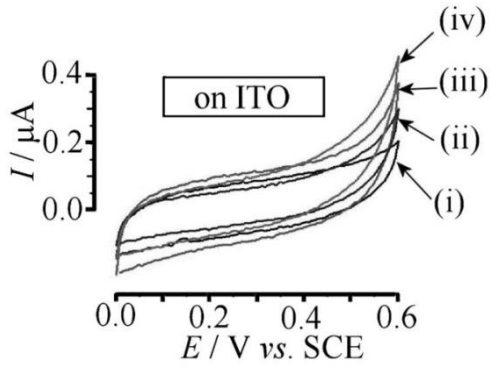

Figure 1.12 - Cyclic voltammograms (scan rate 100 mV s^{-1}) for (i) 10 µg (ii) 25 µg (iii) 50 µg (iv) 100 µg of carbon deposit on ITO in 0.1 M phosphate buffer pH 2. Reproduced from reference.[65]

Covalent immobilisation onto the carbon nanoparticles enables a range of interesting materials to be developed and studied with improved surface area; this allows these materials to be investigated in greater detail and further the understanding of the carbonaceous materials. Anthraquinone is one such redox active species that has been exploited in this way through covalent attachment to Emperor 2000 carbon nanoparticles.[98] Anthraquinone functionality has been important for investigating processes such as pH sensing,[105, 106] oxygen reduction,[107, 108] thiol reactions,[109] and as a redox mediator.[110] In the covalently bound form, anthraquinones provide a reversible redox system that is robust over a large pH

range.[106] The anthraquinone moiety has been successfully bound to Emperor 2000 carbon nanoparticles through ethylene diamine-modified carbon nanoparticles[97] reacting with bromomethyl-anthraquinone.[98] The nanoscale of the carbon material leads to increased bulk density of anthraquinones in the pores of the nanoparticle aggregates; this contributes to unique buffer capacity effects being witnessed. That is to say, at pH values corresponding to the maximum buffer capacity (i.e., pH 2, 7, and 12 in the case of phosphate buffer) an increased peak current is observed in addition to a lower peak-to-peak separation.

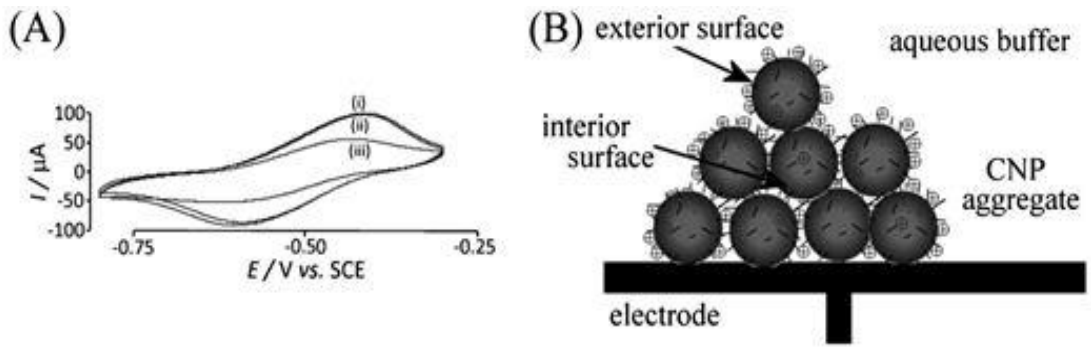

Figure 1.13 - (A) CVs (scan rate 20 mV s^{-1}) for anthraquinone-modified carbon nanoparticles (10 mL of 2 mg mL^{-1} onto 3 mm glassy carbon working electrode) immersed in 0.1 M phosphate buffer pH 7 with (i) no pre-treatment (ii) pre-treatment by immersion into 1 mM NBu_4Cl (iii) pre-treatment by immersion into 1 mM $KBPh_4$ (B) Schematic representation of anthraquinone-modified carbon nanoparticle aggregates when deposited onto the electrode surface where the pore interior and exterior surfaces show reactivity differences. Reproduced from reference.[98]

The peak shape is also affected by the pore-reactivity, which is influenced by the surface charge of the modified carbon nanoparticles. The secondary amine linker is protonated over a large pH window that introduces a net positive charge onto the particulate surface. When the modified electrode is immersed into a solution of negatively charged BPh_4^- solution prior to electrochemical investigation, the current values for both the anodic and cathodic peaks are reduced to half of the initial current, as shown in Figure 1.13. This equates to the anthraquinone moieties that are embedded within the pores of the film, which are becoming inactive because of physisorbed anions. This demonstrates the ability of modified Emperor 2000 carbon nanoparticles to act as high-density carriers for redox active species.[98]

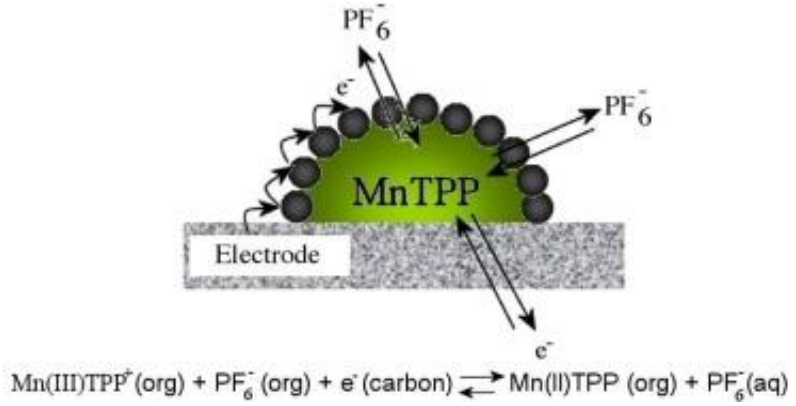

Figure 1.14 - Schematic representation of the interaction of a CNP stabilised microdroplet with an ITO electrode surface based on 5,10,15,20-tetraphenyl-21H,23H-porphinato manganese(III) chloride (MnTPP) undergoing a one electron reduction at surface-bound CNP, upon reduction PF_6^- is transferred from the organic phase to the surrounding aqueous phase. Reproduced from reference.[111]

Carbon nanoparticles have been shown to successfully catalyse simultaneous electron transfer and ion transfer processes at triple phase boundary junctions.[111] CNPs have been used for a number of decades to stabilise liquid|liquid interfaces with high binding constants and strong stabilising effects.[112-114] Unlike conventional surfactants, CNPs act as nanoparticle surfactants that create triple-phase boundary zones with space between the individual particles where interesting chemical and electrochemical reactions can occur at the initial liquid|liquid interface.[111] In 2007, MacDonald and co-workers created microdroplets of a two-phase mixture that contained a redox active species, these resulting microdroplets were stabilised by using CNPs, and then immobilised on ITO electrode surfaces, see Figure 1.14. The modified electrodes showed good electrochemical responses and the CNPs were thought to act in two ways: to stabilise the liquid|liquid interface and to provide interfacial electron channels. This provided a novel way to probe ion-transfer reactions in organic oils at ITO electrodes, and for the development of ion-transfer sensors.[111]

1.6 Electrochemical Applications of Functionalised Carbon Nanomaterials

Functionalised carbon nanoparticles can have a number of applications as electrochemical probes. Modifying electrodes with specifically functionalised CNPs can

result in highly sensitive redox sensors for a number of targets. One such application is for the detection of pollutants in the environment.[115, 116] Of recent interest is the analysis of personal care product and pharmaceutical ingredients to ensure the prevention of concentrations building to harmful levels.[117, 118] Vidal and collaborators used Emperor 2000 CNPs to create modified electrodes for the detection of two common ingredients in personal care products[104]; triclosan – a common ingredient in consumer disinfectants,[119] deodorants and medical creams, and benzophenone-3 – a UV filter present in many sunscreens and cosmetics, Figure 1.15.[120] Both compounds are found in common household products and can have a detrimental effect on the environment; this can occur through transfer in the wastewater system. Both triclosan and benzophenone-3 pose as low toxicity compounds; however, under certain conditions photodegradation can occur to produce derivatives, which impact the environment.[121, 122]

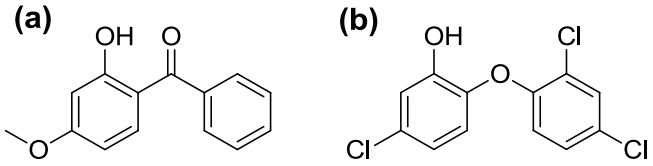

Figure 1.15 - Chemical structure of (a) benzophenone-3 and (b) triclosan

In the experiments by Vidal and co-workers, the CNPs acted for two purposes, the first was to extract the desired analyte from the sample and the second was to allow for voltammetric investigation. The analytes readily adsorbed to the anionic surface of the CNPs and the modified CNPs were easily dispersed in water allowing for simple deposition of a large surface area sample onto a working electrode providing a probe effective in binding polyaromatic phenols. This methodology enabled both target molecules to be analysed with a LOD in the micro-molar concentration region.[104]

Emperor 2000 CNPs have been the focus of a number of bioelectrocatalytic studies. Both Jensen[72] and Szot[68] have used Emperor 2000 carbon nanoparticles to create modified electrode surfaces to probe the direct electron transfer communication between the electrode and *Cerrena* laccase enzymes for the bioelectrocatalytic reduction of O_2 to water. Direct electron transfer can be advantageous with respect to mediated enzymatic

electrodes as the complexity is reduced, also toxicity and stability issues can be avoided.[123, 124] However, many direct mechanism have problems associated with low amounts of the enzyme being accessible because of poor orientation, which is required for direct electron transfer to occur.[72] One approach to overcome these drawbacks is to introduce a high surface area electrode material such as carbon nanoparticles; this not only provides an increased surface concentration of the active enzyme but can also stabilise the enzymes.[125]

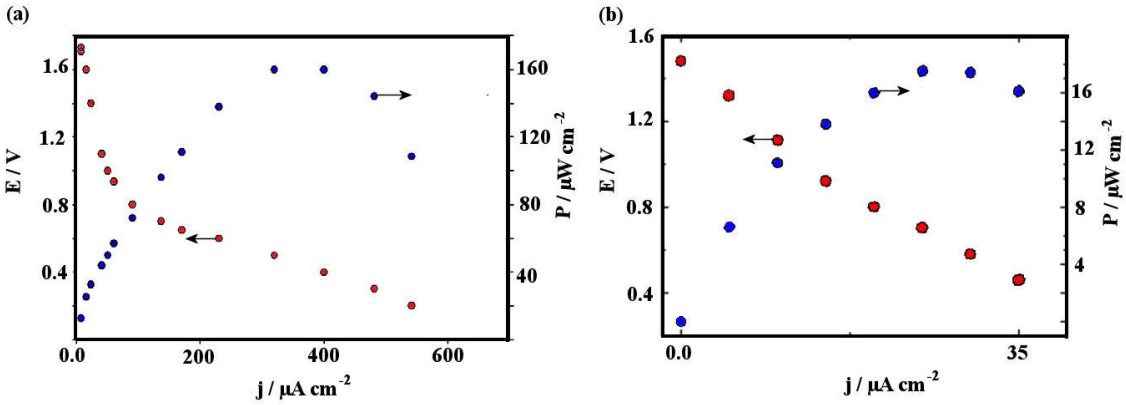

Figure 1.16 - Current-voltage (red) and current-power (blue) dependence for Zn/O_2 biofuel cell based on (a) *Cerrena maxima*-CNP (b) *Cerrena unicolor*-CNP biocathodes. Reproduced from references.[68, 72].

Szot and co-workers prepared films containing Emperor 2000 CNPs and laccase from *Cerrena unicolor* in a sol-gel matrix on ITO electrodes. To achieve successful enzyme orientation for electron transfer to occur between the CNPs and the enzyme active site, the laccase was mixed with a solution of CNPs in water to allow the enzymes to adsorb onto the carbonaceous surface.[68] In contrast, Jensen and team produced a biocomposite through entrapment of CNPs within a *Cerrena maxima* laccase-polymer matrix.[72] The sulfonate modification of the carbon nanoparticles results in preferable orientation of the enzyme compared with the immobilisation of the enzyme on hydrophobic unmodified carbon black. This could be attributed to a more favourable electron transfer being possible between the Emperor 2000 nanoparticles with a hydrophilic nature and the hydrophilic enzyme surface.[72] Both Szot and Jensen successfully tested the electrode as a biocathode in a zinc-dioxygen biofuel cell, which provided large voltages from the combination of the low potential Zn/Zn^{2+} anode and

the high potential bioelectrocatalytic dioxygen reduction at the cathode.[126, 127] Szot reported a maximum power density of 17.6 μW cm^{-2} at 0.7 V for *Cerrena unicolor*-CNP bioelectrodes,[68] whereas Jensen achieved a maximum power density of 160 μW cm^{-2} at 0.5 V for *Cerrena maxima*-CNP bioelectrodes, see Figure 1.16.[72] This research demonstrated promise for the development of simple and cost-effective CNP-based biocathodes for biofuel cells.

1.7 Fluorescence of Carbon Nanoparticles

Fluorescent carbon nanoparticles are often referred to as carbon nanodots, or C-dots. One of the characteristic properties of carbon nanodots is that they have intrinsic luminescent properties[128] and a diameter generally not exceeding 10 nm.[60, 129] These fluorescent C-dots were first identified as a class of nanomaterial in 2004[130] and since then a number of methods for the production of such materials have been reported. These include electrochemical,[131] laser ablation,[132] combustion,[71] microwave,[133] and most commonly hydrothermal techniques,[60, 129, 134] as described in section 1.2.2. Because of the range of simple, rapid, and cost-effective methods to produce C-dots, they provide an excellent alternative to other carbon nanomaterials. In addition to this, C-dots make promising alternatives to quantum dots (QDs) because of the luminescent properties that they possess and their relatively benign impact on the environment.[128, 135] QDs are fluorescent semi-conductor nanomaterials commonly utilised in bioimaging; however, they are metal-based materials, rendering them inherently toxic and of environmental concern.[136, 137]

In addition to using specific chemical compounds for the formation of fluorescent carbon nanoparticles, some groups have looked at taking waste products, such as fruit peel, to subject to hydrothermal methods in order to produce useful carbon nanomaterials in an economical and green way.[60] In a study by Lu *et al*., pomelo peel was used to synthesise water-soluble carbon nanoparticles by a simple hydrothermal method.[60] One of the major drawbacks of these carbon nanodots compared to quantum dots is that the quantum yield tends to be much lower, unless surface passivation is performed involving the covalent attachment of organic moieties.[71, 132, 138] However, the carbon nanodots resulting from pomelo peel produced a

quantum yield of approximately 6.9 %, which shows a great improvement on most c-dots that have a quantum yield of less than 1 %.[60, 139, 140] Lu and co-workers went on to show that the C-dots they produced could act as fluorescent probes for label-free detection of Hg^{2+}. The fluorescence of the C-dots was quenched by Hg^{2+} as it was able to facilitate electron transfer and promote electron/hole recombination.[60, 141, 142] The pomelo peel-based C-dots showed improved sensitivity compared to previous carbon nanomaterial-based Hg^{2+} detection,[142] achieving a limit of detection of 0.23 nM.[60] Ray and team also developed carbon nanoparticle synthetic routes to achieve increased quantum yield; however, this time a soot-based method was used.[71] The carbon soot was refluxed with nitric acid until a water-soluble supernatant was obtained. This technique has previously been used by other groups but the obtained water-soluble nanoparticles had extremely low quantum yields, less than 0.1 %.[143] Ray and co-workers demonstrated that if only the smallest nanoparticles, ~12.5 nm diameter, were separated by centrifugation, a marked improvement in the quantum yield could be achieved, that is, an increase from less than 0.1 % to approximately 3 %.[71] These unmodified carbon nanoparticles were incubated with cells and displayed certain interactions with cells, while retaining their fluorescence; however, surface modification was required for the nanoparticles to enter cells and some cell death was observed.[71]

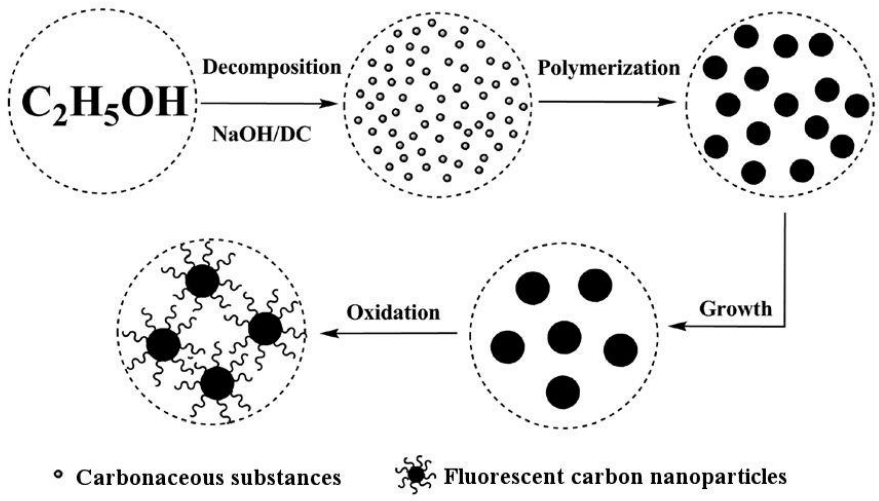

Figure 1.17 - Schematic growth model for fluorescent carbon nanoparticles. Reproduced from reference.[73]

In 2011, Li and co-workers demonstrated a very simple technique to form fluorescent carbon nanodots through the electrochemical treatment of ethanol.[73] A current was passed between two electrodes and ethanol within a double-layer that was thought to decompose into carbonaceous substances, which can polymerise and grow, before undergoing surface oxidation to form fluorescent C-dots, Figure 1.17.[73] These carbon nanodots exhibited a quantum yield of approximately 4 %, showing potential to be used as fluorescent probes for sensing applications.[73]

Carbon black nanoparticles have also been used for fluorescent sensing applications. For example, Panchompoo and collaborators modified the surface of Monarch 430 carbon black with fluorescein by using a simple physisorption process.[144] These fluorescein-modified nanoparticles were effectively used as a fluorescent probe for the detection of Pd(II) in water.[144] Palladium is very important in synthetic organic chemistry as it is used to catalyse a variety of reactions, perhaps most importantly is the use of Pd(II) in coupling chemistry, for which Heck, Negishi, and Suzuki became Nobel laureates in 2010.[145-149] Residual palladium from synthetic applications is often found to leach into waste water systems resulting in palladium being found in the environment; this can be detrimental to the health of both humans and animals.[150-152] The probes developed by Panchompoo and co-workers were effective as the fluorescence intensity of the modified carbon nanoparticles was quenched with increasing Pd(II) concentration, with a LOD of 1.07 µM, much below the recommended oral concentration of less than 5 ppm (approximately 47 µM).[144, 149]

1.8 Summary and Outlook

Nanoscience and nanotechnology has been a huge area of growth over the last decade. Carbon nanoparticles are extremely important materials and have been shown to equal and exceed the quality of carbon nanotubes. Many of the notorious carbon nanomaterials, including graphene and carbon nanotubes, are very expensive, difficult to work with, and pose serious health risks. Carbon nanoparticles are a much cheaper alternative. They can be produced in a number of different ways, most commonly by using hydrothermal or combustion techniques. It is then possible to functionalise the CNPs in a variety of ways with many routes being comparable to methods used on

carbon nanotubes. CNPs have produced a number of effective electrochemical and fluorescent probes for the sensitive detection of many different species.

This thesis will focus on the synthesis and functionalisation of different carbon nanoparticles as well as the characterisation and application of the modified CNPs for specific sensing applications. The methodologies used herein will include the covalent attachment and physisorption of compounds onto Emperor 2000 carbon black, hydrothermal treatment of a polymer to yield novel C-dot materials, and a combination of carbon black with hydrothermal methods to create a polymer-wrapped core-shell nanocomposite. Each of these new carbon-based nanomaterials is demonstrated to be useful in the development of electrochemical or fluorescent sensing applications.

1.9 References

1. Faraday, M., *The Bakerian Lecture: Experimental Relations of Gold (and Other Metals) to Light,* Philosoph. Trans. R. Soc. London, 1857, **147**, 145-181.
2. Alivisatos, A.P., *Semiconductor Clusters, Nanocrystals, and Quantum Dots,* Science, 1996. **271**, 933-937.
3. Christian, P., F. Von der Kammer, M. Baalousha, and T. Hofmann, *Nanoparticles: Structure, Properties, Preparation and Behaviour in Environmental Media,* Ecotoxicology, 2008, **17**, 326-343.
4. Lahiff, E., C. Lynam, N. Gilmartin, R. O'Kennedy, and D. Diamond, *The Increasing Importance of Carbon Nanotubes and Nanostructured Conducting Polymers in Biosensors,* Anal. Bioanal. Chem., 2010, **398**, 1575-1589.
5. de Dios, A.S. and M.E. Diaz-Garcia, *Multifunctional Nanoparticles: Analytical Prospects,* Anal. Chim. Acta, 2010, **666**, 1-22.
6. Lalena, J.N. and D.A. Cleary, *Principles of Inorganic Materials Design*, Second ed., 2010, New Jersey, Wiley.
7. Medina, C., M.J. Santos-Martinez, A. Radomski, O.I. Corrigan, and M.W. Radomski, *Nanoparticles: Pharmacological and Toxicological Significance,* Br. J. Pharmacol., 2007, **150**, 552-558.
8. Birrenbach, G. and P.P. Speiser, *Polymerized Micelles and Their Use as Adjuvants in Immunology,* J. Pharm. Sci., 1976, **65**, 1763-1766.
9. Pileni, M.P., *Optical Properties of Nanosized Particles Dispersed in Colloidal Solutions or Arranged in 2D or 3D Superlattices,* New J. Chem., 1998, **22**, 693-702.
10. Fendler, J.H. and F.C. Meldrum, *The Colloid-Chemical Approach to Nanostructured Materials,* Adv. Mater., 1995, **7**, 607-632.
11. Iijima, S., *Helical Microtubules of Graphitic Carbon,* Nature, 1991. **354**, 56-58.
12. Novoselov, K.S., A.K. Geim, S.V. Morozov, D. Jiang, Y. Zhang, S.V. Dubonos, I.V. Grigorieva, and A.A. Firsov, *Electric Field Effect in Atomically Thin Carbon Films,* Science, 2004, **306**, 666-669.
13. Ospitali, F., D.C. Smith, and M. Lorblanchet, *Preliminary Investigations by Raman Microscopy of Prehistoric Pigments in the Wall-Painted Cave at Roucadour, Quercy, France,* J. Raman Spectrosc., 2006, **37**, 1063-1071.
14. Sarkar, S.N. and R.A. Komoroski, *NMR Imaging of Morphology, Defects, and Composition of Tire Composites and Model Elastomer Blends,* Macromolecules, 1992, **25**, 1420-1426.
15. Veith, A.G. and V.E. Chirico, *Quantitative Study of the Carbon-Black Reinforcement System for Tire Tread Compounds,* Rubber Chem. Technol., 1979, **52**, 748-763.
16. Stewart, E.J., *Reinforcement Effects on Treadwear of Silane Modified Silicas vs Carbon-Black in Various Blends in SBR Passenger Tire Tread Compounds,* J. Elastomers Plast., 1977, **9**, 439-449.
17. Okel, T.A. and W.H. Waddell, *Silica Properties Rubber Performance Correlation - Carbon Black-Filled Rubber Compounds,* Rubber Chem. Technol., 1994, **67**, 217-236.
18. Janzen, J. and G. Kraus, *Correlating Structure and Function - Carbon-Black Properties and Tire Wear,* Chem. Tech., 1976, **6**, 338-342.

19. Zhang, Q.D., B. Piro, V. Noel, S. Reisberg, and M.C. Pham, *Functionalization of Single-Walled Carbon Nanotubes for Direct and selective Electrochemical Detection of DNA,* Analyst, 2011, **136**, 1023-1028.
20. Liu, Z., S. Tabakman, K. Welsher, and H. Dai, *Carbon Nanotubes in Biology and Medicine: In vitro and in vivo Detection, Imaging and Drug Delivery,* Nano Research, 2009, **2**, 85-120.
21. Singh, R., D. Pantarotto, D. McCarthy, O. Chaloin, J. Hoebeke, C.D. Partidos, J.P. Briand, M. Prato, A. Bianco, and K. Kostarelos, *Binding and Condensation of Plasmid DNA onto Functionalized Carbon Nanotubes: Toward the Construction of Nanotube-Based Gene Delivery Vectors,* J. Am. Chem. Soc., 2005, **127** 4388-4396.
22. Pantarotto, D., R. Singh, D. McCarthy, M. Erhardt, J.P. Briand, M. Prato, K. Kostarelos, and A. Bianco, *Functionalized Carbon Nanotubes for Plasmid DNA Gene Delivery,* Angew. Chem. Int. Ed., 2004, **43**, 5242-5246.
23. Iijima, S. and T. Ichihashi, *Single-Shell Carbon Nanotubes of 1-nm Diameter,* Nature, 1993, **363**, 603-605.
24. Liu, Y., D.C. Wu, W.D. Zhang, X. Jiang, C.B. He, T.S. Chung, S.H. Goh, and K.W. Leong, *Polyethylenimine-Grafted Multiwalled Carbon Nanotubes for Secure Noncovalent Immobilization and Efficient Delivery of DNA,* Angew. Chem. Int. Ed., 2005, **44**, 4782-4785.
25. Kam, N.W.S., M. O'Connell, J.A. Wisdom, and H.J. Dai, *Carbon Nanotubes as Multifunctional Biological Transporters and Near-Infrared Agents for Selective Cancer Cell Destruction,* Proc. Natl. Acad. Sci. USA, 2005, **102**, 11600-11605.
26. Zhang, J., H.L. Zou, Q. Qing, Y.L. Yang, Q.W. Li, Z.F. Liu, X.Y. Guo, and Z.L. Du, *Effect of Chemical Oxidation on the Structure of Single-Walled Carbon Nanotubes,* J. Phys. Chem. B, 2003, **107**, 3712-3718.
27. Datsyuk, V., M. Kalyva, K. Papagelis, J. Parthenios, D. Tasis, A. Siokou, I. Kallitsis, and C. Galiotis, *Chemical Oxidation of Multiwalled Carbon Nanotubes,* Carbon, 2008, **46**, 833-840.
28. Ojima, I., *Guided Molecular Missiles for Tumor-Targeting Chemotherapy-Case Studies using the Second-Generation Taxolds as Warheads,* Acc. Chem. Res., 2008, **41**, 108-119.
29. Lee, K.M., L.C. Li, and L.M. Dai, *Asymmetric End-Functionalization of Multi-Walled Carbon Nanotubes,* J. Am. Chem. Soc., 2005, **127**, 4122-4123.
30. Martin, C.R. and P. Kohli, *The Emerging Field of Nanotube Biotechnology,* Nat. Rev. Drug Discovery, 2003, **2**, 29-37.
31. Star, A., J.C.P. Gabriel, K. Bradley, and G. Gruner, *Electronic Detection of Specific Protein Binding using Nanotube FET Devices,* Nano Lett., 2003, **3**, 459-463.
32. Chen, J., H.Y. Liu, W.A. Weimer, M.D. Halls, D.H. Waldeck, and G.C. Walker, *Noncovalent Engineering of Carbon Nanotube Surfaces by Rigid, Functional Conjugated Polymers,* J. Am. Chem. Soc., 2002, **124**, 9034-9035.
33. Chen, R.J., Y.G. Zhang, D.W. Wang, and H.J. Dai, *Noncovalent Sidewall Functionalization of Single-Walled Carbon Nanotubes for Protein Immobilization,* J. Am. Chem. Soc., 2001, **123**, 3838-3839.
34. Wu, P., X. Chen, N. Hu, U.C. Tam, O. Blixt, A. Zettl, and C.R. Bertozzi, *Biocompatible Carbon Nanotubes Generated by Functionalization with Glycodendrimers,* Angew. Chem. Int. Ed., 2008. **47**, 5022-5025.

35. Lo, T.W.B., L. Aldous, and R.G. Compton, *The Use of Nano-Carbon as an Alternative to Multi-Walled Carbon Nanotubes in Modified Electrodes for Adsorptive Stripping Voltammetry*, Sens. Actuators, B, 2012, **162**, 361-368.
36. Macdonald, S.M., K. Szot, J. Niedziolka, F. Marken, and M. Opallo, *Introducing Hydrophilic Carbon Nanoparticles into Hydrophilic Sol-Gel Film Electrodes*, J. Solid State Electrochem., 2008, **12**, 287-293.
37. Rassaei, L., M.J. Bonne, M. Sillanpaa, and F. Marken, *Binding Site Control in a Layer-by-Layer Deposited Chitosan-Carbon Nanoparticle Film Electrode*, New J. Chem., 2008, **32**, 1253-1258.
38. Lu, A.-H., G.-P. Hao, Q. Sun, X.-Q. Zhang, and W.-C. Li, *Chemical Synthesis of Carbon Materials With Intriguing Nanostructure and Morphology,* Macromol. Chem. Phys., 2012, **213**, 1107-1131.
39. Oktem, B., M.P. Tolocka, B. Zhao, H. Wang, and M.V. Johnston, *Chemical Species Associated with the Early Stage of Soot Growth in a Laminar Premixed Ethylene-Oxygen-Argon Flame,* Combust. Flame, 2005, **142**, 364-373.
40. Sgro, L.A., G. Basile, A.C. Barone, A. D'Anna, P. Minutolo, A. Borghese, and A. D'Alessio, *Detection of Combustion Formed Nanoparticles,* Chemosphere, 2003, **51**, 1079-1090.
41. Dobbins, R.A., R.A. Fletcher, and H.C. Chang, *The Evolution of Soot Precursor Particles in a Diffusion Flame,* Combust. Flame, 1998, **115**, 285-298.
42. Dobbins, R.A., G.J. Govatzidakis, W. Lu, A.F. Schwartzman, and R.A. Fletcher, *Carbonization Rate of Soot Precursor Particles,* Combust. Sci. Technol., 1996, **121**, 103-121.
43. Hu, B. and U.O. Koylu, *Size and Morphology of Soot Particulates Sampled from a Turbulent Nonpremixed Acetylene Flame*, Aerosol Sci. Technol., 2004, **38**, 1009-1018.
44. Hu, B., B. Yang, and U.O. Koylu, *Soot Measurements at the Axis of an Ethylene/Air Nonpremixed Turbulent Jet Flame*. Combust. Flame, 2003, **134**, 93-106.
45. Ma, J.L., T.H. Fletcher, and B.W. Webb, *Thermophoretic Sampling of Coal-Derived Soot Particles During Devolatilization*, Energy Fuels, 1995, **9**, 802-808.
46. Blevins, L.G., R.A. Fletcher, B.A. Benner, E.B. Steel, and G.W. Mulholland, *The Existence of Young Soot in the Exhaust of Inverse Diffusion Flames*, Proc. Combus. Inst., 2002, **29**, 2325-2333.
47. Merchan-Merchan, W., A.V. Saveliev, and L.A. Kennedy, *Carbon Nanostructures in Opposed-Flow Methane Oxy-Flames,* Combust. Sci. Technol., 2003, **175**, 2217-2236.
48. D'Anna, A., *Combustion-Formed Nanoparticles,* Proc. Combust. Inst., 2009, **32**, 593-613.
49. Berthelot, M., *Action de la Chaleur sur Quelques Carbures D'hydrogène,* C. R. Hebd. Séances Acad. Sci., 1866, **62**, 947 - 949.
50. Donnet, J.-B., *Carbon Black: Science and Technology*. Second ed., 1993, Marcel Dekker Inc., New York.
51. Wang, H. and M. Frenklach, *A Detailed Kinetic Modeling Study of Aromatics Formation in Laminar Premixed Acetylene and Ethylene Flames,* Combust. Flame, 1997, **110**, 173-221.
52. Wang, H., *Formation of Nascent Soot and Other Condensed-Phase Materials in Flames,* Proc. Combust. Inst., 2011. **33**, 41-67.
53. Yoshimura, M. and K. Byrappa, *Hydrothermal Processing of Materials: Past, Present and Future,* J. Mater. Sci., 2008, **43**, 2085-2103.

54. Wang, Q., H. Li, L.Q. Chen, and X.J. Huang, *Novel Spherical Microporous Carbon as Anode Material for Li-Ion Batteries*, Solid State Ionics, 2002, **152**, 43-50.
55. Sakaki, T., M. Shibata, T. Miki, H. Hirosue, and N. Hayashi, *Reaction Model of Cellulose Decomposition in Near-Critical Water and Fermentation of Products*, Bioresour. Technol., 1996, **58**, 197-202.
56. Sun, X.M. and Y.D. Li, *Colloidal Carbon Spheres and their Core/Shell Structures with Noble-Metal Nanoparticles*, Angew. Chem. Int. Ed., 2004, **43**, 597-601.
57. Chang-Chien, C.-Y., C.-H. Hsu, T.-Y. Lee, C.-W. Liu, S.-H. Wu, H.-P. Lin, C.-Y. Tang, and C.-Y. Lin, *Synthesis of Carbon and Silica Hollow Spheres with Mesoporous Shells using Polyethylene Oxide/Phenol Formaldehyde Polymer Blend*, Eur. J. Inorg. Chem., 2007, **24**, 3798-3804.
58. Klinkamnarong, J., E. Swatsitang, and S. Maensiri, *Nanocrystalline Hydroxyapatite Powders by a Chitosan-Polymer Complex Solution Route: Synthesis and Characterization*, Solid State Sci., 2009, **11**, 1023-1027.
59. Hu, B., K. Wang, L. Wu, S.-H. Yu, M. Antonietti, and M.-M. Titirici, *Engineering Carbon Materials from the Hydrothermal Carbonization Process of Biomass*, Adv. Mater., 2010, **22**, 813-828.
60. Lu, W., X. Qin, S. Liu, G. Chang, Y. Zhang, Y. Luo, A.M. Asiri, A.O. Al-Youbi, and X. Sun, *Economical, Green Synthesis of Fluorescent Carbon Nanoparticles and Their Use as Probes for Sensitive and Selective Detection of Mercury(II) Ions*, Anal. Chem., 2012, **84**, 5351-5357.
61. Titirici, M.-M. and M. Antonietti, *Chemistry and Materials Options of Sustainable Carbon Materials Made by Hydrothermal Carbonization*, Chem. Soc. Rev., 2010, **39**, 103-116.
62. Rabenau, A., *The Role of Hydrothermal Synthesis in Preparative Chemistry*, Angew. Chem. Int. Ed., 1985, **24**, 1026-1040.
63. Corbett, J.D., *Polyatomic Zintl Anions of the Posttransition Elements*, Chem. Rev., 1985, **85**, 383-397.
64. Walton, R.I., *Subcritical Solvothermal Synthesis of Condensed Inorganic Materials*, Chem. Soc. Rev., 2002, **31**, 230-238.
65. Xia, F., M. Pan, S. Mu, M.D. Jones, D. Wolverson, and F. Marken, *Chitosan-Based Hydrothermal Nanocarbon: Core-Shell Characteristics and Composite Electrodes*, Electroanalysis, 2012, **24**, 1703-1708.
66. Binks, B.P., Z.G. Cui, and P.D.I. Fletcher, *Optical Microscope Absorbance Imaging of Carbon Black Nanoparticle Films at Solid and Liquid Surfaces*, Langmuir, 2006, **22**, 1664-1670.
67. Hollander, J.M. and W.L. Jolly, *X-ray Photoelectron Spectroscopy*, Acc. Chem. Res., 1970, **3**, 193-200.
68. Szot, K., W. Nogala, J. Niedziolka-Joensson, M. Joensson-Niedziolka, F. Marken, J. Rogalski, C.N. Kirchner, G. Wittstock, and M. Opallo, *Hydrophilic Carbon Nanoparticle-Laccase Thin Film Electrode for Mediatorless Dioxygen Reduction SECM Activity Mapping and Application in Zinc-Dioxygen Battery*, Electrochim. Acta, 2009, **54**, 4620-4625.
69. Yu, J.-J., F.-Q. Zhao, and B.-Z. Zeng, *Characterization and Electrochemical Study of Hemoglobin-Carbon Nanoparticles-Polyvinyl Alcohol Nanoporous Hybrid Film*, J. Solid State Electrochem., 2008, **12**, 1167-1172.

70. Ibrahim, N.B., Lawrence, K., James, T.D., Xia, F., Pan, M., Mu, S., Mitchels, J.M., Marken, F., *Surface Dopylated Carbon Nanoparticles Sense Gas-Induced pH Changes*, Sens. Actuators, B, 2011, **161**, 184-190.
71. Ray, S.C., A. Saha, N.R. Jana, and R. Sarkar, *Fluorescent Carbon Nanoparticles: Synthesis, Characterization, and Bioimaging Application*, J. Phys. Chem. C, 2009, **113**, 18546-18551.
72. Jensen, U.B., M. Vagin, O. Koroleva, D.S. Sutherland, F. Besenbacher, and E.E. Ferapontova, *Activation of Laccase Bioelectrocatalysis of O_2 Reduction to H2O by Carbon Nanoparticles*, J. Electroanal. Chem., 2012, **667**, 11-18.
73. Li, H., H. Ming, Y. Liu, H. Yu, X. He, H. Huang, K. Pan, Z. Kang, and S.-T. Lee, *Fluorescent Carbon Nanoparticles: Electrochemical Synthesis and their pH Sensitive Photoluminescence Properties*, New J. Chem., 2011, **35**, 2666-2670.
74. Webster, J. and S. Langridge, *Applications of Index Matching in Reflectometry, SANS and Brewster Angle Microscopy*, Curr. Opin. Colloid Interface Sci., 1999, **4**, 186-189.
75. Overbeck, G.A., D. Honig, and D. Mobius, *Visualization of 1st-Order and 2nd-Order Phase-Transitions in Eicosanol Monolayers using Brewster-Angle Microscopy*, Langmuir, 1993, **9**, 555-560.
76. Bandyopadhyay, S., P.P. De, D.K. Tripathy, and S.K. De, *Effect of Chemical Interaction Between Surface Oxidized Carbon Black and Carboxylated Nitrile Rubber on Dynamic Properties*, J. Appl. Polym. Sci., 1995, **58**, 719-727.
77. Allen, N.S., J.M. Pena, M. Edge, and C.M. Liauw, *Behaviour of Carbon Black Pigments as Excited State Quenchers in LDPE*, Polym. Degrad. Stab., 2000, **67**, 563-566.
78. Pena, J.M., N.S. Allen, C.L. Liauw, M. Edge, and B. Valance, *Factors Influencing the Adsorption of Stabilizers onto Carbon Black: Flow Microcalorimetry Studies*, J. Vinyl Addit. Technol., 2000, **6**, 62-68.
79. Pena, J.M., N.S. Allen, M. Edge, C.M. Liauw, F. Santamaria, O. Noiset, and B. Valange, *Factors Affecting the Adsorption of Stabilisers on to Carbon Black (Flow Micro-Calorimetry and FTIR Studies) - Part I - Primary Phenolic Antioxidants*, J. Mater. Sci., 2001, **36**, 2885-2898.
80. Pena, J.M., N.S. Allen, M. Edge, C.M. Liauw, and B. Valange, *Factors Affecting the Adsorption of Fatty Acids, Alcohols and Aromatic Compounds on to Carbon Black Pigments (Flow Micro-Calorimetry Studies)*, Dyes Pigm., 2001, **49**, 29-49.
81. Pena, J.M., N.S. Allen, M. Edge, C.M. Liauw, and B. Valange, *Factors Affecting the Adsorption of Stabilisers on to Carbon Black (Flow Micro-Calorimetry Studies) - 4. Secondary Antioxidants*, Polym. Degrad. Stab., 2001, **72**, 31-45.
82. Maiyalagan, T., C. Mahendiran, K. Chaitanya, R. Tyagi, and F.N. Khan, *Electro-Catalytic Performance of Pt-Supported Poly (O-Phenylenediamine) Microrods for Methanol Oxidation Reaction*, Res. Chem. Intermed., 2012, **38**, 383-391.
83. Figueiredo, J.L., M.F.R. Pereira, M.M.A. Freitas, and J.J.M. Orfao, *Modification of the Surface Chemistry of Activated Carbons*, Carbon, 1999. **37**, 1379-1389.
84. Aksoylu, A.E., M. Madalena, A. Freitas, M.F.R. Pereira, and J.L. Figueiredo, *The Effects of Different Activated Carbon Supports and Support Modifications on the Properties of Pt/AC Catalysts*, Carbon, 2001, **39**, 175-185.

85. Samant, P.V., F. Goncalves, M.M.A. Freitas, M.F.R. Pereira, and J.L. Figueiredo, *Surface Activation of a Polymer Based Carbon,* Carbon, 2004, **42**, 1321-1325.
86. Feng, R., M. Li, and J. Liu, *Synthesis of Core-Shell Au@Pt Nanoparticles Supported on Vulcan XC-72 Carbon and their Electrocatalytic Activities for Methanol Oxidation,* Colloids Surf., A, 2012, **406**, 6-12.
87. Pietron, J.J., *Dual-Pathway Kinetics Assessment of Sulfur Poisoning of the Hydrogen Oxidation Reaction at High Surface-Area Platinum/Vulcan Carbon Electrodes,* J. Electrochem. Soc., 2009, **156**, B1322-B1328.
88. Calvillo, L., M. Gangeri, S. Perathoner, G. Centi, R. Moliner, and M.J. Lazaro, *Effect of the Support Properties on the Preparation and Performance of Platinum Catalysts Supported on Carbon Nanofibers,* J. Power Sources, 2009, **192**, 144-150.
89. Barsukov, I.V., C.S. Johnson, J.E. Doninger, and V.Z. Barsukov, eds. *New Carbon Based Materials for Electrochemical Energy Storage Systems: Batteries, Supercapacitors and Fuel Cells*, 2006, Springer, Berlin.
90. Antolini, E., *Carbon Supports for Low-Temperature Fuel Cell Catalysts,* Appl. Catal., B, 2009, **88**, 1-24.
91. Yu, X. and S. Ye, *Recent Advances in Activity and Durability Enhancement of Pt/C Catalytic Cathode in PEMFC - Part I. Physico-Chemical and Electronic Interaction Between Pt and Carbon Support, and Activity Enhancement of Pt/C Catalyst,* J. Power Sources, 2007, **172**, 133-144.
92. Sanders, I.J. and T.L. Peeten, *Carbon Black: Production, Properties & Uses*, 2011, London, Nova Science Publishers Inc.
93. Belmont, J.A., R.M. Amici, and C.P. Galloway, *Manufacture and use of Diazonium Salt-Modified Carbon Black*, 1996, Cabot Corporation, USA, 119.
94. Belmont, J.A., *Manufacture of Carbon Products Containing an Attached Organic Group Formed by Reaction with Diazonium Salts, and the Carbon Products Obtained*, 1996, Cabot Corporation, USA, 27.
95. Rassaei, L., M. Sillanpaa, and F. Marken, *Modified Carbon Nanoparticle-Chitosan Film Electrodes: Physisorption Versus Chemisorption,* Electrochim. Acta, 2008, **53**, 5732-5738.
96. Abiman, P., G.G. Wildgoose, A. Crossley, and R.G. Compton, *Removal of Palladium Ions from Aqueous Systems by Chemically Modified Cysteine Carbon Powder,* J. Mater. Chem., 2008, **18**, 3948-3953.
97. Watkins, J.D., R. Lawrence, J.E. Taylor, S.D. Bull, G.W. Nelson, J.S. Foord, D. Wolverson, L. Rassaei, N.D.M. Evans, S.A. Gascon, and F. Marken, *Carbon Nanoparticle Surface Functionalisation: Converting Negatively Charged Sulfonate to Positively Charged Sulfonamide,* Phys. Chem. Chem. Phys., 2010, **12**, 4872-4878.
98. Watkins, J.D., K. Lawrence, J.E. Taylor, T.D. James, S.D. Bull, and F. Marken, *Carbon Nanoparticle Surface Electrochemistry: High-Density Covalent Immobilisation and Pore-Reactivity of 9,10-Anthraquinone,* Electroanalysis, 2011, **23**, 1320-1324.
99. Bin Ibrahim, N., K. Lawrence, T.D. James, F. Xia, M. Pan, S. Mu, J.M. Mitchels, and F. Marken, *Surface-Dopylated Carbon Nanoparticles Sense Gas-Induced pH Changes*, Sens. Actuators B, 2012, **161**, 184-190.
100. White, R.J., N. Yoshizawa, M. Antonietti, and M.-M. Titirici, *A Sustainable Synthesis of Nitrogen-Doped Carbon Aerogels,* Green Chem., 2011, **13**, 2428-2432.

101. White, R.J., M. Antonietti, and M.-M. Titirici, *Naturally Inspired Nitrogen Doped Porous Carbon,* J. Mater. Chem., 2009, **19**, 8645-8650.
102. Zhao, L., L.-Z. Fan, M.-Q. Zhou, H. Guan, S. Qiao, M. Antonietti, and M.-M. Titirici, *Nitrogen-Containing Hydrothermal Carbons with Superior Performance in Supercapacitors,* Adv. Mater., 2010, **22**, 5202-5206.
103. Xia, F., M. Pan, S. Mu, Y. Xiong, K.J. Edler, I. Idini, M.D. Jones, S.C. Tsang, and F. Marken, *Hydrothermal Core-Shell Carbon Nanoparticle Films: Thinning the Shell Leads to Dramatic pH Response,* Phys. Chem. Chem. Phys., 2012, **14**, 15860-15865.
104. Vidal, L., A. Chisvert, A. Canals, E. Psillakis, A. Lapkin, F. Acosta, K.J. Edler, J.A. Holdaway, and F. Marken, *Chemically Surface-Modified Carbon Nanoparticle Carrier for Phenolic Pollutants: Extraction and Electrochemical Determination of Benzophenone-3 and Triclosan,* Anal. Chim. Acta, 2008, **616**, 28-35.
105. Wildgoose, G.G., M. Pandurangappa, N.S. Lawrence, L. Jiang, T.G.J. Jones, and R.G. Compton, *Anthraquinone-Derivatised Carbon Powder: Reagentless Voltammetric pH Electrodes,* Talanta, 2003, **60**, 887-893.
106. Lafitte, V.G.H., W. Wang, A.S. Yashina, and N.S. Lawrence, *Anthraquinone-Ferrocene Film Electrodes: Utility in pH and Oxygen Sensing,* Electrochem. Commun., 2008, **10**, 1831-1834.
107. Maia, G., F.C. Maschion, S.T. Tanimoto, K. Vaik, U. Maeeorg, and K. Tammeveski, *Attachment of Anthraquinone Derivatives to Glassy Carbon and the Electrocatalytic Behavior of the Modified Electrodes Toward Oxygen Reduction,* J. Solid State Electrochem., 2007, **11**, 1411-1420.
108. Seinberg, J.-M., M. Kullapere, U. Maeeorg, F.C. Maschion, G. Maia, D.J. Schiffrin, and K. Tammeveski, *Spontaneous Modification of Glassy Carbon Surface with Anthraquinone from the Solutions of its Diazonium Derivative: An Oxygen Reduction Study,* J. Electroanal. Chem., 2008, **624**, 151-160.
109. Briggs, M.K., E. Desavis, P.A. Mazzer, R.B. Sunoj, S.A. Hatcher, C.M. Hadad, and P.G. Hatcher, *A New Approach to Evaluating the Extent of Michael Adduct Formation to PAH Quinones: Tetramethylammonium Hydroxide (TMAH) Thermochemolysis with GC/MS,* Chem. Res. Toxicol., 2003, **16,** 1484-1492.
110. Vuorema, A., P. John, M. Keskitalo, M.F. Mahon, M.A. Kulandainathan, and F. Marken, *Anthraquinone Catalysis in the Glucose-Driven Reduction of Indigo to Leuco-Indigo,* Phys. Chem. Chem. Phys., 2009, **11**, 1816-1824.
111. MacDonald, S.M., P.D.I. Fletcher, Z.-G. Cui, M. Opallo, J. Chen, and F. Marken, *Carbon Nanoparticle Stabilised Liquid|Liquid Micro-Interfaces for Electrochemically Driven Ion-Transfer Processes,* Electrochim. Acta, 2007, **53**, 1175-1181.
112. Binks, B.P. and C.P. Whitby, *Nanoparticle Silica-Stabilised Oil-in-Water Emulsions: Improving Emulsion Stability,* Colloids Surf., A, 2005, **253**, 105-115.
113. Aveyard, R., B.P. Binks, and J.H. Clint, *Emulsions Stabilised Solely by Colloidal Particles,* Adv. Colloid Interface Sci., 2003, **100**, 503-546.
114. Glaser, N., D.J. Adams, A. Boeker, and G. Krausch, *Janus Particles at Liquid-Liquid Interfaces,* Langmuir, 2006, **22**, 5227-5229.
115. Eljarrat, E. and D. Barcelo, *Priority Lists for Persistent Organic Pollutants and Emerging Contaminants Based on their Relative Toxic Potency in Environmental Samples,* Trac-Trend Anal. Chem., 2003, **22**, 655-665.

116. Eljarrat, E. and D. Barcelo, *Toxicity Potency Assessment of Persistent Organic Pollutants in Sediments and Sludges, Handbook of Environmental Chemistry*, D. Barcelo: Editor, 2004.
117. Daughton, C.G. and T.A. Ternes, *Pharmaceuticals and Personal Care Products in the Environment: Agents of Subtle Change?* Environ. Health Perspect., 1999, **107**, 907-938.
118. Lindsey, M.E., M. Meyer, and E.M. Thurman, *Analysis of Trace Levels of Sulfonamide and Tetracycline Antimicrobials, in Groundwater and Surface Water using Solid-Phase Extraction and Liquid Chromatography/Mass Spectrometry,* Anal. Chem., 2001, **73**, 4640-4646.
119. Okumura, T. and Y. Nishikawa, *Gas Chromatography Mass Spectrometry Determination of Triclosans in Water, Sediment and Fish Samples via Methylation with Diazomethane,* Anal. Chim. Acta, 1996, **325**, 175-184.
120. Peck, A.M., *Analytical Methods for the Determination of Persistent Ingredients of Personal Care Products in Environmental Matrices,* Anal. Bioanal. Chem., 2006, **386**, 907-939.
121. Sanchez-Prado, L., M. Llompart, M. Lores, M. Fernandez-Alvarez, C. Garcia-Jares, and R. Cela, *Further Research on the Photo-SPME of Triclosan,* Anal. Bioanal. Chem., 2006, **384**, 1548-1557.
122. Latch, D.E., J.L. Packer, W.A. Arnold, and K. McNeill, *Photochemical Conversion of Triclosan to 2,8-Dichlorodibenzo-p-Dioxin in Aqueous Solution,* J. Photochem. Photobiol., A, 2003, **158**, 63-66.
123. Kavanagh, P., P. Jenkins, and D. Leech, *Electroreduction of O_2 at a Mediated Melanocarpus Albomyces Laccase Cathode in a Physiological Buffer,* Electrochem. Commun., 2008, **10**, 970-972.
124. Soukharev, V., N. Mano, and A. Heller, *A Four-Electron O_2-Electroreduction Biocatalyst Superior to Platinum and a Biofuel Cell Operating at 0.88 V,* J. Am. Chem. Soc., 2004, **126**, 8368-8369.
125. Szot, K., J.D. Watkins, S.D. Bull, F. Marken, and M. Opallo, *Three Dimensional Film Electrode Prepared from Oppositely Charged Carbon Nanoparticles as Efficient Enzyme Host*, Electrochem. Commun., 2010, **12**, 737-739.
126. Heller, A., *Potentially Implantable Miniature Batteries,* Anal. Bioanal. Chem., 2006, **385**, 469-473.
127. Smolander, M., H. Boer, M. Valkiainen, R. Roozeman, M. Bergelin, J.-E. Eriksson, X.-C. Zhang, A. Koivula, and L. Viikari, *Development of a Printable Laccase-Based Biocathode for Fuel Cell Applications*, Enzyme Microb. Technol., 2008, **43**, 93-102.
128. Yang, Y., J. Cui, M. Zheng, C. Hu, S. Tan, Y. Xiao, Q. Yang, and Y. Liu, *One-Step Synthesis of Amino-Functionalized Fluorescent Carbon Nanoparticles by Hydrothermal Carbonization of Chitosan,* Chem. Commun., 2012, **48**, 380-382.
129. Bourlinos, A.B., A. Stassinopoulos, D. Anglos, R. Zboril, V. Georgakilas, and E.P. Giannelis, *Photoluminescent Carbogenic Dots,* Chem. Mater., 2008, **20**, 4539-4541.
130. Xu, X.Y., R. Ray, Y.L. Gu, H.J. Ploehn, L. Gearheart, K. Raker, and W.A. Scrivens, *Electrophoretic Analysis and Purification of Fluorescent Single-Walled Carbon Nanotube Fragments,* J. Am. Chem. Soc., 2004, **126**, 12736-12737.
131. Zheng, L., Y. Chi, Y. Dong, J. Lin, and B. Wang, *Electrochemiluminescence of Water-Soluble Carbon Nanocrystals Released Electrochemically from Graphite,* J. Am. Chem. Soc., 2009, **131**, 4564-4565.

132. Sun, Y.P., B. Zhou, Y. Lin, W. Wang, K.A.S. Fernando, P. Pathak, M.J. Meziani, B.A. Harruff, X. Wang, H.F. Wang, P.J.G. Luo, H. Yang, M.E. Kose, B.L. Chen, L.M. Veca, and S.Y. Xie, *Quantum-Sized Carbon Dots for Bright and Colorful Photoluminescence,* J. Am. Chem. Soc., 2006, **128**, 7756-7757.
133. Zhu, H., X. Wang, Y. Li, Z. Wang, F. Yang, and X. Yang, *Microwave Synthesis of Fluorescent Carbon Nanoparticles with Electrochemiluminescence Properties,* Chem. Commun., 2009, **34**, 5118-5120.
134. Hsu, P.-C. and H.-T. Chang, *Synthesis of High-Quality Carbon Nanodots from Hydrophilic Compounds: Role of Functional Groups,* Chem. Commun., 2012, **48**, 3984-3986.
135. Yang, S.-T., X. Wang, H. Wang, F. Lu, P.G. Luo, L. Cao, M.J. Meziani, J.-H. Liu, Y. Liu, M. Chen, Y. Huang, and Y.-P. Sun, *Carbon Dots as Nontoxic and High-Performance Fluorescence Imaging Agents,* J. Phys. Chem. C, 2009, **113**, 18110-18114.
136. Ming, H., Z. Ma, Y. Liu, K. Pan, H. Yu, F. Wang, and Z. Kang, *Large Scale Electrochemical Synthesis of High Quality Carbon Nanodots and their Photocatalytic Property*, Dalton Trans. (Cambridge, England: 2003), 2012, **41**, 9526-9531.
137. Li, H., X. He, Z. Kang, H. Huang, Y. Liu, J. Liu, S. Lian, C.H.A. Tsang, X. Yang, and S.-T. Lee, *Water-Soluble Fluorescent Carbon Quantum Dots and Photocatalyst Design,* Angew. Chem. Int. Ed., 2010, **49**, 4430-4434.
138. Zhao, Q.-L., Z.-L. Zhang, B.-H. Huang, J. Peng, M. Zhang, and D.-W. Pang, *Facile Preparation of Low Cytotoxicity Fluorescent Carbon Nanocrystals by Electrooxidation of Graphite,* Chem. Commun., 2008, **41**, 5116-5118.
139. Liu, H., T. Ye, and C. Mao, *Fluorescent Carbon Nanoparticles Derived from Candle Soot,* Angew. Chem. Int. Ed., 2007, **46**, 6473-6475.
140. Liu, R., D. Wu, S. Liu, K. Koynov, W. Knoll, and Q. Li, *An Aqueous Route to Multicolor Photoluminescent Carbon Dots Using Silica Spheres as Carriers,* Angew. Chem. Int. Ed., 2009, **48**, 4598-4601.
141. Xia, Y.-S. and C.-Q. Zhu, *Use of Surface-Modified CdTe Quantum Dots as Fluorescent Probes in Sensing Mercury (II),* Talanta, 2008, **75**, 215-221.
142. Zhou, L., Y. Lin, Z. Huang, J. Ren, and X. Qu, *Carbon Nanodots as Fluorescence Probes for Rapid, Sensitive, and Label-Free Detection of Hg2+ and Biothiols in Complex Matrices,* Chem. Commun., 2012, **48**, 1147-1149.
143. Stober, W., A. Fink, and E. Bohn, *Controlled Growth of Monodisperse Silica Spheres in Micron Size Range,* J. Colloid Interface Sci., 1968, **26**, 62-69.
144. Panchompoo, J., L. Aldous, M. Baker, M.I. Wallace, and R.G. Compton, *One-Step Synthesis of Fluorescein Modified Nano-Carbon for Pd(II) Detection via Fluorescence Quenching,* Analyst, 2012, **137**, 2054-2062.
145. Yu, S.Y., H.-W. Rhee, and J.-I. Hong, *Fluorescent Sensing System for Palladium(II) Based on the Heck Reaction,* Tetrahedron Lett., 2011, **52**, 1512-1514.
146. Miyaura, N. and A. Suzuki, *Palladium-Catalyzed Cross-Coupling Reactions of Organoboron Compounds,* Chem. Rev., 1995, **95**, 2457-2483.
147. Phan, N.T.S., M. Van Der Sluys, and C.W. Jones, *On the Nature of the Active Species in Palladium Catalyzed Mizoroki-Heck and Suzuki-Miyaura Couplings - Homogeneous or Heterogeneous Catalysis, a Critical Review,* Adv. Synth. Catal., 2006, **348**, 609-679.

148. Hatanaka, Y. and T. Hiyama, *Cross-Coupling of Organosilanes with Organic Halides Mediated by Palladium Catalyst and Tris(Diethylamino)Sulfonium Difluorotrimethylsilicate,* J. Org. Chem., 1988, **53**, 918-920.
149. Garrett, C.E. and K. Prasad, *The Art of Meeting Palladium Specifications in Active Pharmaceutical Ingredients Produced by Pd-Catalyzed Reactions,* Adv. Synth. Catal., 2004, **346**, 889-900.
150. Liu, T.Z., S.D. Lee, and R.S. Bhatnagar, *Toxicity of Palladium*, Toxicol. Lett., 1979, **4**, 469-473.
151. Li, H., J. Fan, J. Du, K. Guo, S. Sun, X. Liu, and X. Peng, *A Fluorescent and Colorimetric Probe Specific for Palladium Detection,* Chem. Commun., 2010, **46**, 1079-1083.
152. Li, H., J. Fan, F. Song, H. Zhu, J. Du, S. Sun, and X. Peng, *Fluorescent Probes for Pd2+ Detection by Allylidene-Hydrazone Ligands with Excellent Selectivity and Large Fluorescence Enhancement,* Chem. Eur. J., 2010, **16**, 12349-12356.

Chapter 2

Electrochemical Theory

Contents

2.1 Introduction to Electrochemistry

Electrochemistry is a diverse field that can broadly be described as the study of chemical reactions associated with electricity. This includes the study of chemical changes that are either instigated by electricity or result in the production of electricity. Electrochemistry encompasses many aspects of science and is the study of charge transfer (i.e., electron transfer) that occurs between electrodes and reactant molecules, both at an interface and the space in between. Generally, charge transfer can occur in two directions, that is, a redox species can either gain an electron from the electrode to form the reduced species [e.g., Equation (2.1)],, or it can donate an electron to the electrode surface to form the oxidised species [e.g., Equation (2.2)].[1]

$$Fe^{3+}{}_{(aq)} + e^{-} \rightarrow Fe^{2+}{}_{(aq)} \quad (2.1)$$

$$Fe^{2+}{}_{(aq)} \rightarrow Fe^{3+}{}_{(aq)} + e^{-} \quad (2.2)$$

By applying a potential to an electrochemical system, data regarding the mechanism as well as kinetic information can be obtained. There are also other parameters that could potentially control the rate of charge transfer including the nature of the working electrode surface and the reactivity of the reactant, that is, how easily it can be oxidised or reduced. The oxidative/reductive processes are displayed as the observed current, otherwise known as a Faradaic current, the magnitude of which is given by Equation (2.3) where i = current, n = the number of electrons, A = electrode area, F = Faraday constant, and j = flux (the amount of material undergoing electrochemical reaction per unit area within a unit time).[1]

$$i = nAFj \quad (2.3)$$

There are a number of possible electrode setups that can be used within an electrochemical cell; however, the most common is a three-electrode arrangement, which will be focused on in this report with emphasis on using a potentiostatic sweeping-voltage analysis technique. In this three-electrode arrangement, the electrochemical cell contains a reference electrode, counter electrode, and a working electrode, see Figure 2.1a. A potentiostat is used as a feedback amplifier that controls the potential of the working electrode.

In electrochemical experiments, the reaction of interest occurs at the surface of the working electrode and the interfacial potential between this surface and the solution is measured. A reference electrode is used to provide an arbitrary zero point because it is not possible to determine the absolute value of the interfacial potential. A good reference electrode is non-polarisable and the potential remains constant when a small current is passed. Therefore, the reference electrode holds a fixed interfacial potential difference under normal conditions and the measured potential difference is derived from the difference between this known reference value and the potential at the working electrode. The reference electrode is present to provide a stable and fixed potential, to make certain that this is the case, a counter electrode is added to the cell. The use of such a system allows the potential difference at the electrode | electrolyte interface to be measured and controlled by a potentiostat.

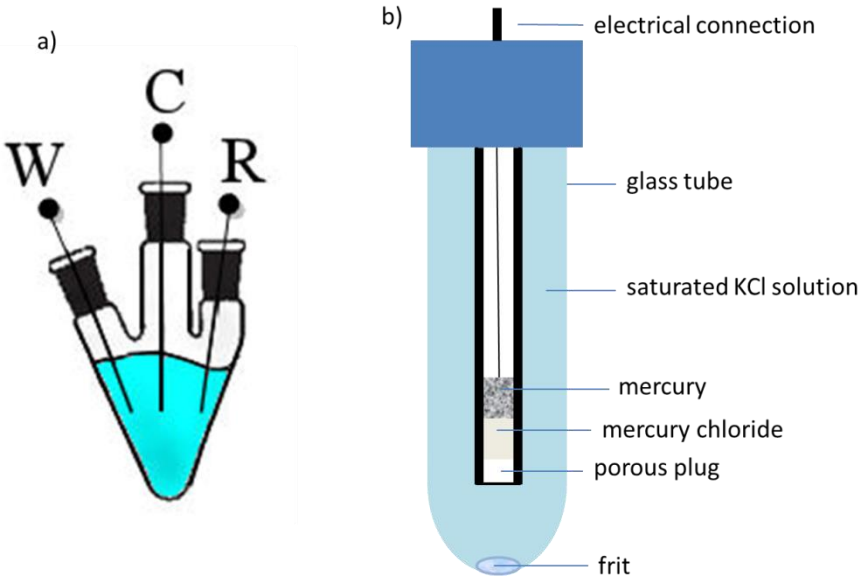

Figure 2.1. a) A typical three-electrode cell set-up, and b) a schematic representation of a saturated calomel electrode

The saturated calomel electrode (SCE) is a common reference electrode, and was used for all experiments detailed in this thesis. The potential of the SCE, the same as all electrodes, is determined by the Nernst equation (see Chapter 2.5.1 for more details). The Nernstian expression for the SCE electrode is shown in Equation (2.4), where E is the applied potential, E^0 is the standard redox potential, K_{sp} is the activity constant of the solubility product, and a_{Cl^-} is the activity of the chloride ions. From Equation (2.4), it can be seen that the potential is dependent on the activity (or concentration) of the chloride ions. Within the SCE electrode, the aqueous KCl solution is saturated and so the concentration is high and the activity is determined by the solubility of the KCl. The potential of the electrode remains relatively constant, with an electrode potential of 0.24 V versus the standard hydrogen electrode at 25 ^{o}C; therefore, the SCE is a suitable reference electrode.

$$E = E^0_{Hg_2^{2+}/Hg} + \frac{RT}{2F} lnK_{sp} - lna^2_{Cl^-} \quad (2.4)$$

The counter electrode is made of an inert material, such as platinum, and should have a large surface area to ensure facile electron transfer, that is, so that it is not a rate limiting factor. An electrochemical experiment is generally focused on the reaction taking place at the working electrode. A current flows between the working electrode and the counter electrode to ensure that any potential drop at the reference/surface interface is constant and not affected by large applied potentials. [1]

There is a diverse range of electrochemical applications including sensing,[2, 3] synthetic production of inorganic chemicals,[4] and energy conversion in the form of solar cells[5, 6] or fuel cells.[7, 8] Electrochemical sensing is an extremely active research area with a number of different focuses, for example the detection of low-level analytes such as glucose in complex bodily fluids,[9] or the detection of pharmaceuticals in waste effluent and the analysis of obscure analytes and heavy metals.[5] This thesis focuses on using new materials for effective sensing applications.

2.2 Solution-Phase Electrochemistry

In general, an electrochemical process occurs across the interface of two phases: the electrolyte and the electrode. The electrolyte is defined as the phase through which the movement of ions occurs and this therefore, acts as the charge carrier. The electrolyte can be fused salts or ionic liquids, but most commonly liquid solutions are used and this is commonly referred to as solution-phase electrochemistry.

Within any electrochemical experiment, the working electrode is the site at which electronic movement, otherwise known as charge transfer, takes place during a redox process. In a solution phase experiment, the reactant species must move from the bulk electrolyte solution to the electrode surface and consequently the redox product must then move from the interface and return to the bulk. (Figure 2.2)

There are five processes which are considered to be important during an electrochemical reaction, as indicated in Figure 2.2, any of which can behave as the rate determining step. The mass transfer to transport the reactive material, that is, processes (ii) and (iv), can be one of three mechanisms; diffusion, convection, or migration (vide infra).

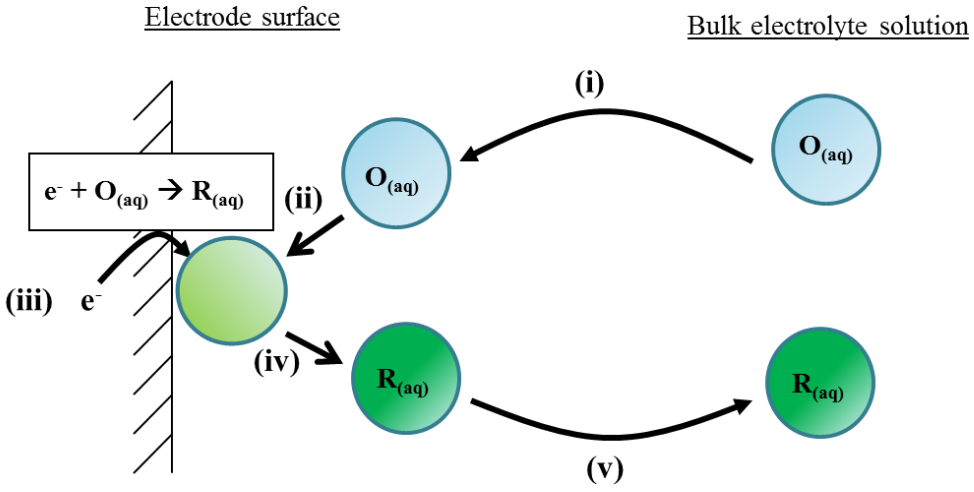

Figure 2.2. The processes that occur in a reductive electrochemical experiment at the electrolyte | electrode interface; (i) movement of the active species to the electrode surface, (ii) adsorption onto the surface of the electrode, (iii) electron transfer, (iv) desorption, and (v) movement of the reduced species back to the bulk solution.

2.3 Mass-Transfer

Mass transfer is defined as the movement of material from one location in the electrolyte solution to another. It can occur for one of two reasons; (i) a difference between the electrical or chemical potential at either of the two locations, or (ii) from movement of an element across a concentration gradient in solution. The three mechanisms of mass-transfer are diffusion, convection, and migration, and are discussed in the following sections.

2.3.1 Diffusion

Diffusion is the transfer of a species across a concentration gradient; in terms of electrochemistry this can be considered a gradient of chemical potential.[10] Diffusion occurs in order to maximise the entropy of the system and create more disorder. It is the simple movement of a species from an area of high concentration to an area of low concentration, following the concentration gradient. The rate of diffusion depends upon the specific concentration gradient at any given point.[11] Fick describes the laws of diffusion mathematically, Fick's first law of diffusion, see Equation (2.5), represents the diffusional flux, that is, the number of moles diffusing per unit area per second. When this was combined with studying the concentration change within a certain area, Fick developed his second law, see Equation (2.6), where j is the flux, D is the diffusion coefficient, [O] is the concentration of the species, and x is the distance from the electrode surface.[12]

$$j_{ox} = -D_{ox} \frac{\partial [O]}{\partial x} \tag{2.5}$$

$$\frac{\partial [ox]}{\partial t} = D_{ox} \frac{\partial^2 [O]}{\partial x^2} \tag{2.6}$$

In an electrochemical experiment, the amount of oxidised or reduced material changes with the applied potential and the scan rate, this results in a concentration gradient by

which diffusion can occur. Fick's second law is of more importance in electrochemistry than the first, as electrochemical experiments tend to focus on changes in concentration as a function of time.

2.3.2 Convection

Convection that is caused by a density gradient (natural convection) and forced convection are two types of mass transport that occur when forces act upon the solution.[10] Any solution can possess thermal gradients or differences in density within the solution, these forces result in natural convection and can also be induced within an electrochemical reaction; such forces are generally considered undesirable. Forced convection can be induced by applying forces to the system, which can be achieved in a number of ways, for example by stirring the electrolyte solution or having gas bubble through the liquid. If these forces are applied unintentionally, the results can be detrimental; however, by purposefully enforcing and controlling these convection techniques, natural convection implications can be overcome.[13]

2.3.3 Migration

The transportation of charged ions to and from the electrode surface according to an electrical potential gradient is known as migration. These migrational movements are initiated and controlled by the electrostatic forces applied to an electrochemical system, that is, those due to the potential drop at the electrode surface | electrolyte solution interface. In order to minimise the effect of this mass transport route in an electrochemical experiment, the electrolyte solution employed is generally of a concentration in the order of 0.1 M, i.e., of reasonably high concentration.

2.4 The Electrode Surface | Electrolyte Interface and the Electrical Double Layer

In an electrochemical system there are forces and interactions that occur between the solid electrode surface and the electrolyte solution. These processes can be modelled in order to understand the mechanisms occurring at the solid | liquid interface. When an electrode is placed into electrolyte solution, an interfacial region is produced, which is known as the double layer. In an electrochemical system where an electrical circuit is utilized to measure current at an electrode this double layer can be considered a capacitor where the electronic surface charge is caused by an excess of ions near to the electrode surface. In order for the working electrode to obtain the correct potential, the double layer capacitor must be charged. This means that a capacitive charge flows within the electrical circuit, which is independent of the oxidation or reduction of any species in the system (Faradaic species). This capacitive current provides information regarding the electrical double layer and the active area of the electrode surface.[14]

In 1853 Helmholtz was the first to identify interactions occurring at the interface of a solid electrode and a liquid electrolyte, suggesting the presence of a double layer.[15] Helmholtz later, in 1879 proposed a simple model to explain the concept of an electrical double layer at the surface of a metal in contact with an electrolyte.[16] The double layer was postulated to arise from the presence of excess charge density (positive or negative) at the electrode surface, which would be neutralized by equal and opposite charge density found in the electrolyte solution. The ions within the solution approach the electrode until they reach the minimum distance possible from the surface of the electrode; this is known as the outer Helmholtz plane (OHP). Therefore, the Helmholtz model states that the excess charge density at the electrode surface is balanced completely by a compact layer of counter-ions that form the OHP. This double layer theory resembles that of a capacitor as the two charged layers are separated by a certain distance, therefore the potential drop in the electrical double layer would be linear, see Figure 2.3(a).[15]

In the early 20th century, Gouy and Chapman found that the counter balancing charge density was not exclusively located in the OHP due to thermal motion dispersing excess ions into the solution. The thermal motion, otherwise known as Brownian motion – the random motion of particles suspended within a fluid, showed that the counter ions were

not simply immobilised at the electrode surface, but spread throughout the solution as a diffuse layer. This meant that in the theorised diffuse double layer, the potential drop is highest closer to the electrode surface; however, the potential drop would fall as it moved further into the diffuse layer, that is, away from the electrode due to the Boltzmann distribution Figure 2.3(b).[17, 18]

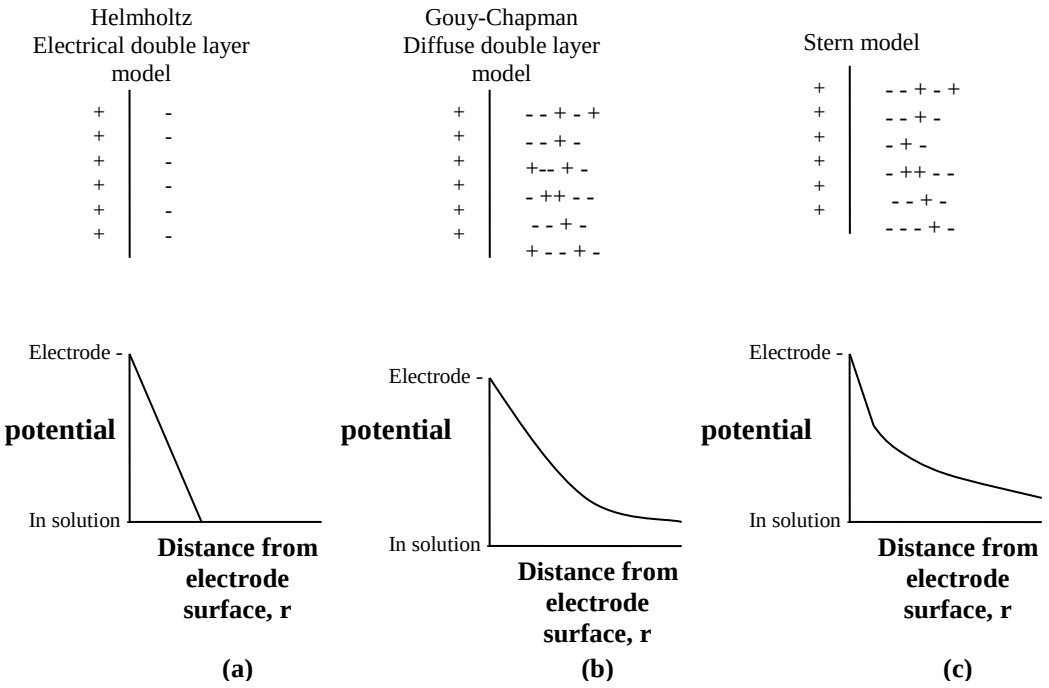

Figure 2.3. Schematic representations of (a) Helmholtz, (b) Gouy-Chapman and (c) Stern models

The two aforementioned theories were combined in 1924 when Stern accepted the electrical double layer theory; however, he theorised that this could not fully neutralise the surface of the electrode. Stern also recognised the importance of Brownian motion to form a diffuse double layer and stated that it was this that counter-balanced the remaining charge density Figure 2.3(c).[19] More recent studies accept the Stern model; however, they have highlighted that polar solvents such as water, which have a dipole moment, interact with the electrode surface and the level of the interaction is dependent upon the dielectric constant of the solvent, Figure 2.4.[20] Also represented in Figure 2.4 are the inner and outer

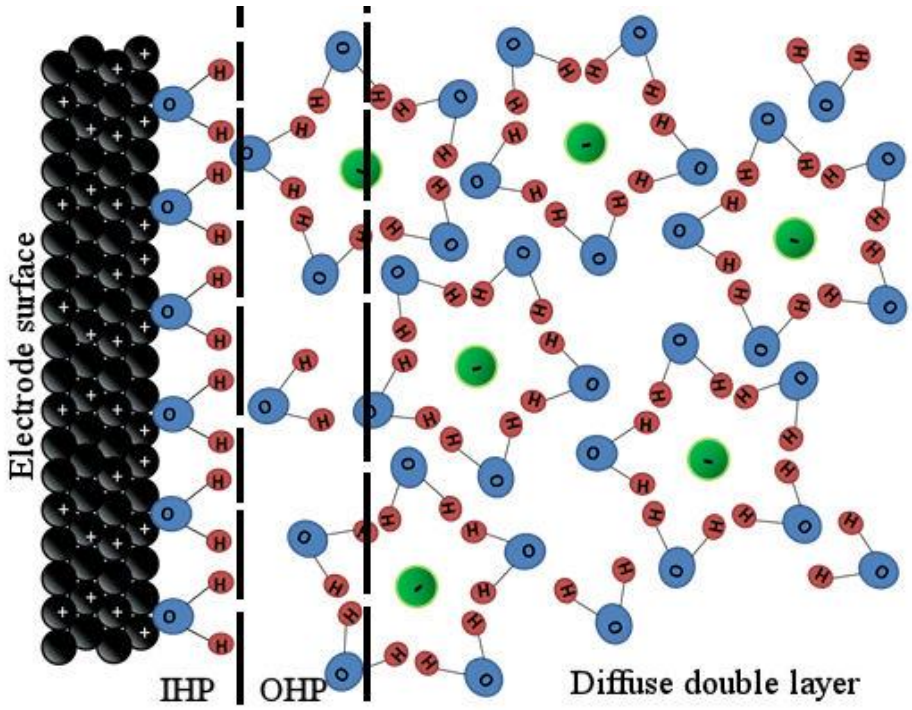

Figure 2.4. Schematic of an electrical double layer illustrating how water molecules align due to the δ^- charge on the oxygen atoms and hydrated ions in the diffuse double layer that compensate for any remaining charge

2.5 Electrochemical Thermodynamics

Throughout chemistry, thermodynamics is used to describe the changes in energy and entropy during a reaction, typically at equilibrium. This is no different in electrochemistry, and since electrochemical reactions involve passing a current to alter the Gibbs free energy, the reaction can usually be brought to, or very near to, the reaction equilibrium.

An electrochemical reaction involves the transfer of electrons between the electrode and electrolyte. When the reaction reaches equilibrium there will be a net electrical charge both on the electrode and in the electrolyte phase. If the equilibrium lies towards the oxidative products then the electrode will have a net negative charge and the electrolyte an equal and opposite charge (in the case of a reductive product there will be a net positive charge at the electrode). In this situation an electrode potential is established, that is, there is a difference in electrical potential between the electrode surface and the electrolyte.

The development of an electrode potential at the electrode | electrolyte interface can also be discussed in terms of energy levels. The electrode has a number of electronic conduction bands in which electrons are able to "hop" in order to bind the free cations. The energy levels produced through bond formations form a continuous band of energy levels which fill with electrons up to the Fermi level, that is, the energy level at which the probability of an electron occupying it is a half. The ions dispersed within the electrolyte have discrete energy levels which correspond to unfilled molecular orbitals of the oxidised species. For the reaction stated in Equation (2.7), $Fe(CN)_6^{4-}$ is formed upon the transfer of an electron from the electrode into unfilled molecular orbital of $Fe(CN)_6^{3-}$.

$$Fe(CN)_6^{3-}(aq) + e^- \rightleftarrows Fe(CN)_6^{4-}(aq) \tag{2.7}$$

By applying a more negative potential difference to a system, the number of electrons is increased, which subsequently raises the Fermi level of the electrode. This creates a driving force for an electron to transfer from the electrode into an empty orbital of the redox species. Whereas, if a more positive potential difference is applied to a system, electrons are effectively removed from the electrode, thus reducing the Fermi level to an energy level below that of the electron in the redox species. Therefore, an electron can spontaneously transfer to the electrode from the redox molecule. Electrochemical methods usually involve the "sweeping" of the potential and therefore can sweep the potential from a process being not-spontaneous to spontaneous. The potential at which the process becomes spontaneous is the standard redox potential and sweeping the potential past this point will result in an electrochemical signal.

$$\Delta G = \Delta G^o + RTlnK_{rxn} \tag{2.8}$$

$$\Delta G = -nFE \tag{2.9}$$

Any reaction is spontaneous when the change in Gibbs free energy is zero. According to Equations (2.8) and (2.9), where ΔG is the change in Gibbs free energy, ΔG^o is the standard Gibbs free energy, R is the universal gas constant (8.314 J K^{-1} mol^{-1}), K_{rxn} is the equilibrium constant, i.e., [products]/[reactants], n = the number of electrons transferred, F = the Faraday constant, and E = the applied potential, any reaction can theoretically become spontaneous using electrochemistry if a high enough potential is applied, i.e., $\Delta G < 0$.

2.5.1 The Nernst Equation

The Nernst equation relates the applied potential difference to the concentration of oxidised and reduced species in solution. This can be achieved by substituting Equation (2.9) into Equation (2.8) and rearranging to give Equation (2.10), where E^o is the standard redox potential, [O] and [R] are the concentration of oxidised and reduced species, respectively.

$$E = E^o + \frac{RT}{nF} ln \frac{[O]}{[R]} \tag{2.10}$$

The Nernst equation can be used to relate electrochemical properties with thermodynamic information. It can also be seen that small changes in potential can lead to large changes in the concentration of oxidation or reduction products.

The potential difference is not a measurable quantity as the quantification of the chemical potential difference across a single interface is not possible. The working, reference, and counter electrodes all contribute to the interfacial potential difference. By using Ohms Law the electrode potential, E, can be described in terms of potential differences to further explain the Nernst equation [Equation (2.11)]. To do this, a steady-state potential difference is introduced in the form of a reference electrode.

$$E = (\Delta\phi^{WE} - \Delta\phi^{RE}) + iR_{sol} \tag{2.11}$$

In Equation (2.11) the potential is calculated from the potential difference of the working electrode ($\Delta\phi^{WE} = \phi^{metal(WE)} - \phi^{electrolyte}$) measured in during an electrochemical experiment as well as the potential difference at the reference electrode ($\Delta\phi^{RE}$) and the applied current (i), which are both constants. R_{sol} is the resistance of the solution. Collectively iR_{sol} are known as the potential drop, which should be as small as possible.

Combination of the Nernst equation and Ohms law demonstrate that the concentrations of oxidised or reduced species in a system can be changed by controlling the interfacial potential difference at the working electrode.

2.6 Electron Transfer Kinetics

Transfer kinetics is important in electrochemistry as an electrode process is limited by how many electrons can transfer at the electrode surface and how fast. In a kinetically controlled system the electrochemical response is dominated by the rate determining step. This can be any of the five processes introduced in Section 2.2; mass transfer to the electrode surface, adsorption to the surface, electron transfer, desorption from the surface back into solution, and finally mass transfer back into the bulk. Two common situations are: (i) a mass transport limited system where the current is limited by slow transport of the molecules or (ii) an electron-transfer limited system, where the transport of molecules is fast but the reaction process is slow. The rate of transfer of a charged species across the electrochemical interface is related to the potential difference between the electrode and the electrolyte.

The rate of an electrochemical reaction can be determined by considering the activation barrier that charge transfer must overcome. The current density is often useful for describing this, that is, the electrical current per unit area of the electrode surface, which can be related to the reaction rate by using Equation (2.12):

$$i = nFv \tag{2.12}$$

where i is the current density, n is the number of electrons transferred, F is Faraday's constant, and v is the reaction rate at the surface of the electrode. In an electrochemical system i can be measured and controlled, and is the difference between the forward and reverse current densities on the electrode, that is, the net current density when the system is not at equilibrium. This can be expressed as the difference between anodic partial current density and the cathodic partial current density, Equation (2.13):

$$i = i_{\text{ox}} - i_{\text{red}} \tag{2.13}$$

Considering a reversible redox reaction;

$$O + ne^- \underset{k_{ox}}{\overset{k_{red}}{\rightleftharpoons}} R^{n-} \tag{2.14}$$

the rate of reduction and oxidation are described by Equations (2.15) and (2.16), respectively.

$$v_{red} = k_{red} C_{ox} = -\frac{i_{red}}{nF} \tag{2.15}$$

$$v_{ox} = k_{ox} C_{red} = \frac{i_{ox}}{nF} \tag{2.16}$$

where k is the rate constant and C is the concentration at the electrode surface. At equilibrium $i_{\text{red}} = i_{\text{ox}} = i_{\text{o}}$.

The activation energy and the rate constant are related by the Arrehnius Equation (2.17):

$$k_{(ox\ \text{OR}\ red)} = A\exp^{\frac{-E_{A\ (ox\ \text{OR}\ red)}}{RT}} \tag{2.17}$$

in which E_A is the activation energy and A is a constant.

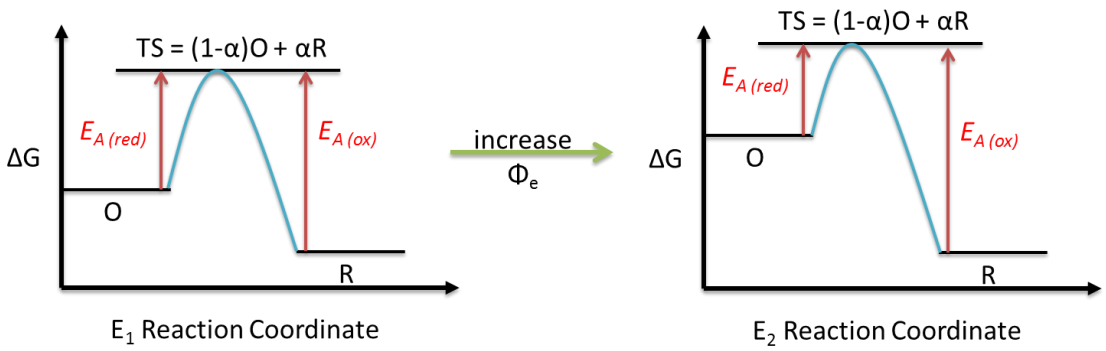

Figure 2.5. The effect of potential on the activation energy for an electrochemical reduction reaction.

By increasing the potential at the electrode (ϕ_e), the energy level of the reactant is increased (by 1 unit). This is because the electron comes from the electrode at which the potential was increased. The energy of the transition state is therefore also increased [but not to the same extent as the electrode, i.e., (1 – α) unit], and the product energy remains unchanged. This results in the reductive E_A being reduced and the oxidative E_A being increased, see Figure 2.5. From this it can clearly be seen that the rate constant is dependent upon the potential, and when related back to the current density, see Equation (2.13), it can be seen that the equilibrium current densities, i_0, are equal and can be denoted as Equations (2.18) and (2.19) for the oxidative and reductive process, respectively.

$$i_{red} = i_0 \exp^{\frac{(1-\propto)nF(E-E^O)}{RT}} \tag{2.18}$$

$$i_{ox} = i_0 \exp^{\frac{-\propto nF(E-E^O)}{RT}} \tag{2.19}$$

In order to overcome the barrier to activation so as to exceed the E_A, an overpotential must be applied ($\eta = E - E^O$). By combining this and substituting Equations (2.18) and (2.19) into the aforementioned Equation (2.13), it allows an expression to be obtained that describes the steady-state voltammetry when the electron transfer process is the rate-limiting step, Equation (2.20). This is commonly known as the Butler-Volmer equation.

$$i = i_o(exp^{\frac{(1-\propto)nF\eta}{RT}} - exp^{\frac{-\propto nF\eta}{RT}}) \quad (2.20)$$

$$i_o = nFk^o C_R^{(\propto)} C_O^{(1-\propto)} \quad (2.21)$$

The Butler-Volmer equation provides a relationship between the current density, *i*, and the charge-transfer overpotential, η, in terms of the exchange current density, i_0, and the transfer coefficient, α. From this equation, it can be determined that for large deviations from the equilibrium potential, that is, large η values, the partial currents approach the net current. Therefore, for large positive η values, i_{ox} tends towards *i*, and i_{red} tends towards *I* for large negative η values.

2.7 Cyclic Voltammetry

Cyclic Voltammetry is one of the most important electrochemical techniques. Cylic voltammetry experiments are performed in a stationary solution, and therefore rely implicitly upon the diffusion of material to the electrode surface. The experiment applies a potential, E_1, to the working electrode, this is a potential at which redox processes do not occur. The potential is then increased to a point at which electron transfer occurs rapidly, E_2 and finally reversed back to E_1. This can be displayed graphically as a function of time (Figure 2.6). The applied potential is a function of the speed at which the potential is ramped (scan rate) and time.

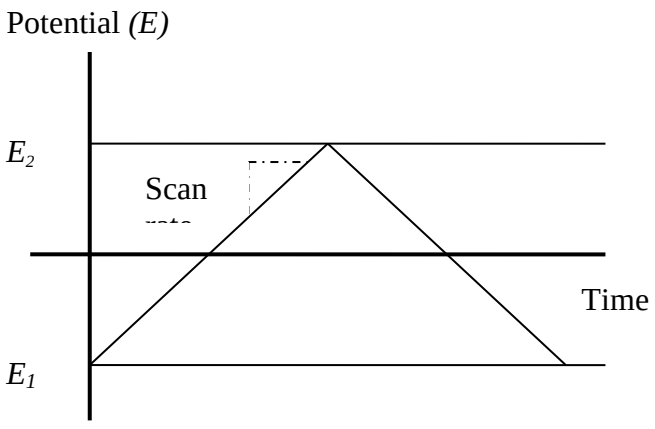

Figure 2.6. A graph to show potential as a function of time during a cyclic voltammetry experiment

A cyclic voltammogram (CV) displays a lot of information by its shape alone. As the potential is ramped it reaches a point at which oxidation occurs at the electrode surface, initiating an increase in current (a peak emerges). As the potential is further increased, the current increases exponentially until it reaches a maxima, known as the peak current, i_p. This first part of the peak is dependent upon the electrochemical rate constant for the oxidative process. Once the peak maximum is achieved, there is no longer an excess of material at the surface and the peak current is dependent upon diffusion of material from the bulk to the electrode surface. The reverse is true for the reduction of the material and therefore shows a similar shape for reversible redox processes.

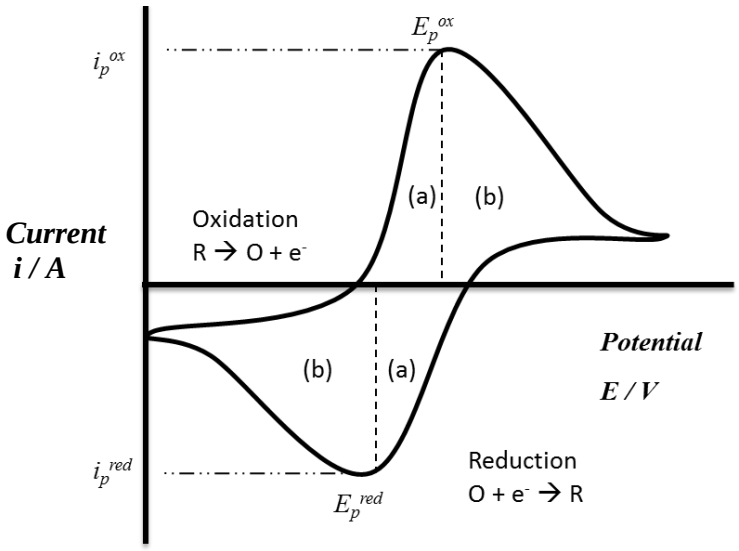

Figure 2.7. Cyclic voltammogram for an electrochemically reversible system where (a) is the section of the peak that is representative of Butler-Volmer kinetics and (b) describes diffusion-control

A reversible electrochemical system occurs when diffusion is slow relative to the electron transfer process; therefore, it displays Nernstian behaviour, that is, the process obeys the Nernst Equation (2.10). This results in a specific peak separation (E_p^{ox}-E_P^{red}), and for a one-electron transfer a peak separation of ~57 mV is observed (Figure 2.7).[1]

$$| E_p^{ox} - E_p^{red} | = 2.218 \frac{RT}{nF} \qquad (2.22)$$

The Nernst Equation is also based on Equation (2.22), which originates from the historical analysis of CV traces, where E_p^{ox}-E_P^{red} is the peak separation, R is the gas constant (8.314 J K^{-1} mol^{-1}), T is the temperature, n is the number of electrons transferred, and F is the Faraday constant (96485 C mol^{-1}).

2.8 Solid Phase Electrochemistry

In sensor development, the key recognition site needs to be located as close to the transducer as possible. For an electrochemical sensor, this is achieved by immobilisation of the redox species on the electrode itself. These electrodes are commonly referred to as chemically modified electrodes. The chemical behaviour of the electrode surface can be altered by modification using chemical reagents, and these modified electrodes can be prepared in many ways. The major difference for immobilised systems is that the redox species is not usually replenished from the bulk solution and therefore no diffusion control is observed.

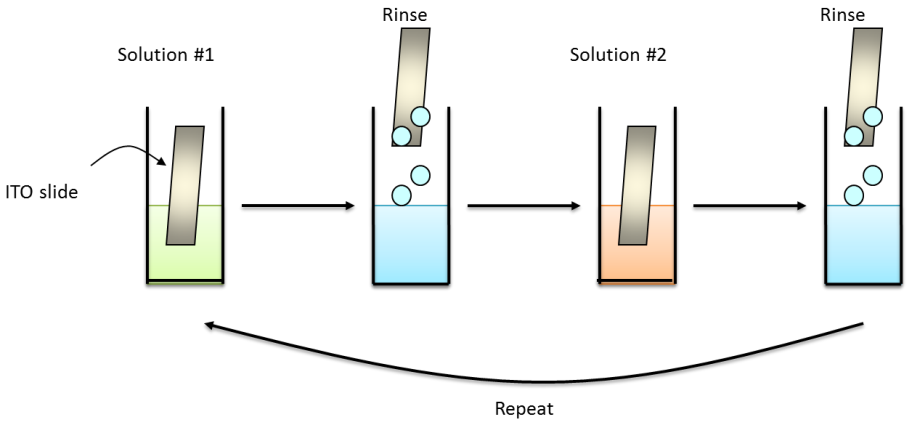

Figure 2.8. Schematic of layer-by-layer deposition

The electrode substrate employed is usually a metallic, carbon, or semiconductor electrode, which is often used directly as the electrode in the unmodified form. Monolayer formation at the electrode surface is one option for the modification of an electrode. This can be achieved by adsorption – when a substance spontaneously

adsorbs onto the interface from the bulk solution. A recent example of this is the chemisorption of sodium diethyldithiocarbamate (DDTC) to a copper electrode for use in corrosion inhibition.[21] Monolayers can also be obtained by covalent attachment – linking from groups already present at the surface to desirable components such as recognition moieties. In 2010, Leroux and co-workers developed an efficient synthesis for covalently attaching an ethynyl aryl monolayer to a carbon electrode surface which then coupled with ferrocenyl reagents to show redox activity, this highlighted a successful surface modification, for example see Figure 2.9(a).[22]

A common technique for electrode modification is to form a conducting film over the electrode surface. This can be achieved in a number of ways. One simple way is to use a layer-by-layer dip-coating method, for example by taking a tin-doped indium oxide (ITO), coated glass slide with negatively charged surface particles and dipping it into a solution containing a positively charged species. The layers can be built up by repeated dipping with a complimentary solution, for example a positively charged polymer such as poly-(diallyldimethylammonium chloride), PDDAC with negatively charged Emperor 2000 carbon nanoparticles (Figure 2.8).[23] After the dip coating is complete the organic residues can be eliminated by heating in a furnace at high temperature.[23-27] This technique also results in an electrode such as that illustrated in Figure 2.9(a).

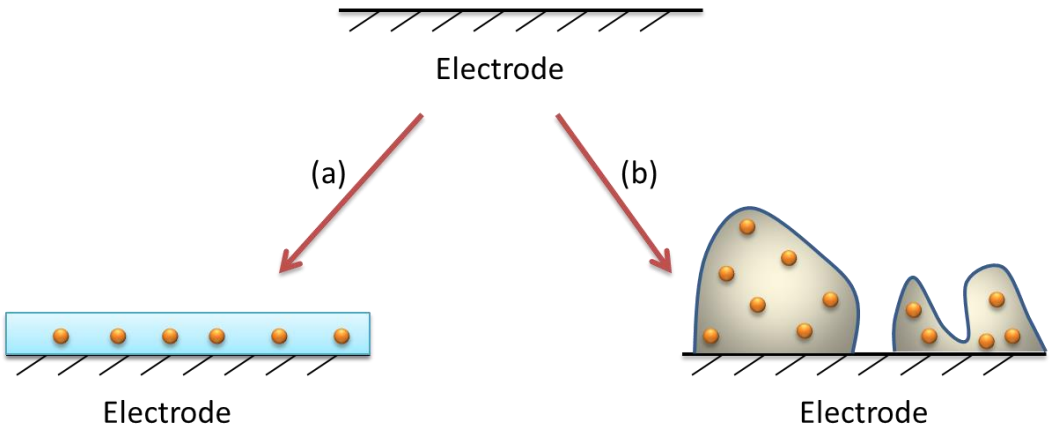

Figure 2.9. Examples of a continuous film (a) and a porous modified electrode with particulate formation on the surface (b)

Nanoparticle functionalisation followed by deposition onto an electrode is another widely researched area of modified electrode development. Following synthetic techniques to functionalise the surface of the nanoparticles, a solvent can be added so that a solution or suspension of the nanoparticles can be formed. A droplet of this can then be deposited onto the electrode surface and all solution can be evaporated to leave a film of solid nanoparticles on the surface of the electrode, see Figure 2.9(b).[28, 29]

2.8.1 Immobilised Redox Systems

Redox systems adsorbed onto the surface of the electrode are no longer diffusion controlled processes. The redox moiety itself is now held at the surface of the electrode and as there is no diffusion process; therefore, the shape of a typical cyclic voltammogram changes, Figure 2.10.

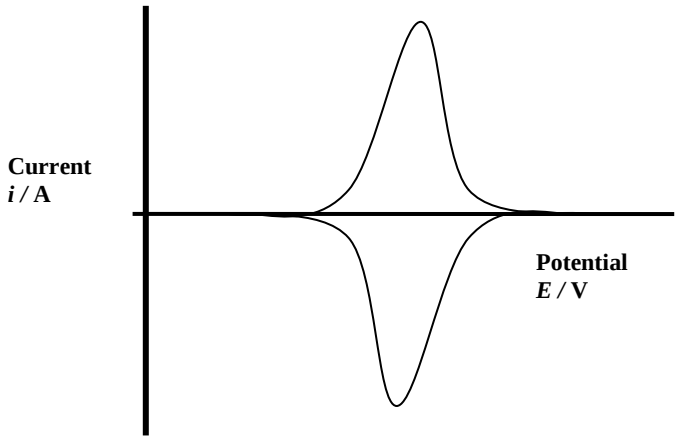

Figure 2.10. Theoretical cyclic voltammogram for a reversible system immobilised on an electrode surface

As mentioned previously, successful electrochemical sensor systems are based on the immobilisation of the redox system onto the electrode itself. This enables the sensor to function with minimum human intervention. This is because no further reagents need to be added to the system for detection to occur. This methodology has received a great level of interest and recent literature publications demonstrate its versatility.[24, 30-32]

Dong and collaborators developed an electrochemical sensor for small molecules such as adenosine by creating a sensing interface immobilised on a gold electrode surface. To achieve this, the gold electrode was immersed into a gold nanoparticle solution to form a film of gold nanoparticles. This was later reacted with a ferrocene labelled probe solution to obtain the active sensor. A key feature of this development was that the sensor could be regenerated after detection was complete by thermally removing the labelled probe layer followed by the reaction of a fresh portion of probe solution to the gold nanoparticle surface. [33]

In 2011, Li and co-workers successfully fabricated a sensor for the detection of a cancer biomarker. To achieve this they immobilised an antibody onto graphene sheets via an amidation reaction. The functionalised graphene sheets were then deposited and evaporated onto the surface of a glassy carbon electrode which can then accept further materials. The immobilisation of further specifically functionalised materials enables development of specific sensing devices. This base electrode has potential to allow many interesting materials to be further immobilised onto the surface thus a multipurpose sensor can be achieved from this basic methodology.[34]

2.9 Summary

This chapter demonstrates the theory behind the electrochemical methods used in this thesis. Herein, carbon nanomaterials are developed for the development of sensors, and the electrochemical methods discussed in this introductory chapter are used to monitor this development. Electrochemical sensing materials are established, and most of the methods utilised in this thesis involve surface-immobilised cyclic voltammetry experiments.

2.10 References

1. Fisher, A.C., *Electrode Dynamics*, Oxford Chemistry Primers. 1996, Oxford: Oxford University Press.
2. Wu, Z.S., M.M. Guo, S.B. Zhang, C.R. Chen, J.H. Jiang, G.L. Shen, and R.Q. Yu, *Reusable Electrochemical Sensing Platform for Highly Sensitive Detection of Small Molecules Based on Structure-Switching Signaling Aptamers*, Anal. Chem., 2007, **79**, 2933-2939.
3. Meadows, D., *Recent Developments with Biosensing Technology and Applications in the Pharmaceutical Industry,* Adv. Drug Delivery Rev., 1996. **21**, 179-189.
4. Pletcher, D. and F. Walsh, *Industrial Electrochemistry*, Second ed., 1990, Cambridge, Springer.
5. Toivola, M., J. Halme, K. Miettunen, K. Aitola, and P.D. Lund, *Nanostructured Dye Solar Cells on Flexible Substrates-Review,* Int. J. Energ. Res., 2009, **33**, 1145-1160.
6. Kim, B., J.K. Koh, J. Kim, W.S. Chi, J.H. Kim, and E. Kim, *Room Temperature Solid-State Synthesis of a Conductive Polymer for Applications in Stable I-2-Free Dye-Sensitized Solar Cells*, ChemSusChem, 2012, **5**, 2173-2180.
7. Wang, H., *Formation of Nascent Soot and Other Condensed-Phase Materials in Flames,* Proc. Combust. Inst., 2011, **33**, 41-67.
8. Wei, J., P. Liang, K. Zuo, X. Cao, and X. Huang, *Carbonization and Activation of Inexpensive Semicoke-Packed Electrodes to Enhance Power Generation of Microbial Fuel Cells*, ChemSusChem, 2012, **5**, 1065-1070.
9. Dawson, K., M. Baudequin, and A. O'Riordan, *Single on-Chip Gold Nanowires for Electrochemical Biosensing of Glucose,* Analyst, 2011, **136**, 4507-4513.
10. Bard, A.J. and L.R. Faulkner, *Electrochemical Methods*, first ed., 1980, New York, John Wiley & Sons.
11. Compton, R.G. and C.E. Banks, *Understanding Voltammetry*, 2007, Singapore: World Scientific Publishing.
12. Fick, A., *On Liquid Diffusion,* Philos. Mag, 1855 (2009 online), **10**, 30-39.
13. Crow, D.R., *Principles and Applications of Electrochemistry*, fourth ed., 1994, Glasgow: Chapman & Hall.
14. Stojek, Z., *The Electrical Double Layer and Its Structure*, in *Electroanalytical Methods*, F. Scholz, 2010, Springer, Heidelberg.
15. Helmholtz, H., *Ueber Einige Gesetze der Vertheilung Elektrischer Ströme in Körperlichen Leitern mit Anwendung auf die Thierisch- Elektrischen Versuche*, Ann. Phys. Und. Chem (Leipzig), 1853, **89**, 211-234.
16. Helmholtz, H., *Studien Über Electrische Grenzschichten*, Ann. d. Physik, 1879, **7**, 337-382.
17. Gouy, L.G., *Sur la Constitution de la Charge Électrique à la Surface d'un* Électrolyte, J. Phys. Théorique et Appliquée, 1910, **9**, 457-468.
18. Chapman, D.L., Lond. Edinb. Dublin Philos. Mag., 1913, **25**.
19. Stern, O.Z., *Zur Theorie der Elektrolytischen Doppelschicht,* Z. Elktrochem. Angew. P., 1924, **30**, 508-516.
20. Parsons, R., *The Electrical Double Layer: Recent Experimental and Theoretical Developments,* Chem. Rev., 1990, **90**, 813-826.
21. Liao, Q.Q., Z.W. Yue, D. Yang, Z.H. Wang, Z.H. Li, H.H. Ge, and Y.J. Li, *Inhibition of Copper Corrosion in Sodium Chloride Solution by the Self-*

Assembled Monolayer of Sodium Diethyldithiocarbamate, Corros. Sci., 2011, **53**, 1999-2005.
22. Leroux, Y.R., H. Fei, J.M. Noel, C. Roux, and P. Hapiot, *Efficient Covalent Modification of a Carbon Surface: Use of a Silyl Protecting Group To Form an Active Monolayer,* J. Am. Chem. Soc., 2010, **132**, 14039-14041.
23. Amiri, M., S. Shahrokhian, and F. Marken, *Ultrathin Carbon Nanoparticle Composite Film Electrodes: Distinguishing Dopamine and Ascorbate,* Electroanalysis, 2007, **19**, 1032-1038.
24. Cummings, C.Y., A.H. Roweth, A.K.Z. Ching, A.T.A. Jenkins, J.M. Mitchels, S. Shariki, S.Y. Liew, W. Thielemans, D.A. Walsh, and F. Marken, *Facile Cation Electro-Insertion into Layer-By-Layer Assembled Iron Phytate Films,* Electrochem. Commun., 2010, **12**, 1722-1726.
25. Rassaei, L., M.J. Bonne, M. Sillanpaa, and F. Marken, *Binding Site Control in a Layer-By-Layer Deposited Chitosan-Carbon Nanoparticle Film Electrode,* New J. Chem., 2008, **32**, 1253-1258.
26. Rassaei, L., M. Sillanpaa, E.V. Milsom, X.H. Zhang, and F. Marken, *Layer-By-Layer Assembly of Ru^{3+} and Si8O208- into Electrochemically Active Silicate Films,* J. Solid State Electrochem., 2008, **12**, 747-755.
27. Shrestha, S., C.M.Y. Yeung, F. Marken, C.E. Mills, and S.C. Tsang, *Layer-by-Layer Deposition of Praseodymium Oxide on Tin-Doped Indium Oxide (ITO) Surface,* Sens. Actuators, B, 2007, **123**, 400-406.
28. Vidal, L., A. Chisvert, A. Canals, E. Psillakis, A. Lapkin, F. Acosta, K.J. Edler, J.A. Holdaway, and F. Marken, *Chemically Surface-Modified Carbon Nanoparticle Carrier for Phenolic Pollutants: Extraction and Electrochemical Determination of Benzophenone-3 and Triclosan,* Anal. Chim. Acta, 2008, **616**, 28-35.
29. Watkins, J.D., R. Lawrence, J.E. Taylor, S.D. Bull, G.W. Nelson, J.S. Foord, D. Wolverson, L. Rassaei, N.D.M. Evans, S.A. Gascon, and F. Marken, *Carbon Nanoparticle Surface Functionalisation: Converting Negatively Charged Sulfonate to Positively Charged Sulfonamide,* Phys. Chem. Chem. Phys., 2010, **12**, 4872-4878.
30. Das, M. and P. Goswami, *Direct Electrochemistry of Alcohol Oxidase using Multiwalled Carbon Nanotube as Electroactive Matrix for Biosensor Application,* Bioelectrochemistry, 2013, **89**, 19-25.
31. Kochius, S., A.O. Magnusson, F. Hollmann, J. Schrader, and D. Holtmann, *Immobilized Redox Mediators for Electrochemical NAD(P)(+) Regeneration,* Appl. Microbiol. Biotechnol., 2012, **93**, 2251-2264.
32. Scheller, F.W., U. Wollenberger, C. Lei, W. Jin, B. Ge, C. Lehmann, F. Lisdat, and V. Fridman, *Bioelectrocatalysis by Redox Enzymes at Modified Electrodes,* J. Biotechnol., 2002. **82**, 411-24.
33. Wang, J., F. Wang, and S. Dong, *Methylene Blue as an Indicator for Sensitive Electrochemical Detection of Adenosine Based on Aptamer Switch,* J. Electroanal. Chem., 2009, **626**, 1-5.
34. Li, H., Q. Wei, J. He, T. Li, Y. Zhao, Y. Cai, B. Du, Z. Qian, and M. Yang, *Electrochemical Immunosensors for Cancer Biomarker with Signal Amplification Based on Ferrocene Functionalized Iron Oxide Nanoparticles,* Biosens. Bioelectron., 2011, **26**, 3590-3595.

Chapter 3

Fluorescence: A Spectroscopic Tool and Imaging Technique

Contents

3.1 Luminescence

Luminescence is the general term for the emission of light from a substrate when an electronic transition occurs from an electronically excited state to the ground electronic state. Luminescence can be divided into two categories dependent upon the nature of the excited state. When an incident photon is of sufficient energy to promote an electron from a molecular ground state (S_0) into a level of higher energy, it can then decay back to S_0 by a number of pathways resulting in either fluorescence or phosphorescence.

Fluorescence occurs when an electron in a singlet excited state (S_1) decays to the ground state (S_0) by emission of photons. This process results in the rapid emission of a photon as it is a spin allowed process i.e., the electron in the excited state is of opposite spin to that in the ground state. The emission rates are also rapid; this results in short lifetimes of the singlet states, typically around 10 ns.[1] This means that light can be used to transfer information in real-time regarding events that are taking place on the molecular level;[2-4] Ambrose and co-workers demonstrated in 1999 that single fluorescent molecules could be observed under controlled conditions.[5] The emitted light travels through space, meaning that it can be used as an extremely useful remote optical tool for analysing dynamic systems such as living organisms.[2]

Phosphorescence is the luminescence resulting from the decay of an electron from a triplet excited state (T_1) to the ground state (S_0). Instead of fast decay back to the S_0 state (i.e., fluorescence), an electron can undergo a non-radiative decay process to enter the T_1 state, which is of lower energy than S_1 but higher than S_0. This is a forbidden emission as the electron in the T_1 excited orbital is in the same spin state as the electron in the ground state. As this is a forbidden transition, the lifetime of triplet states are longer and some last as long as several seconds. Therefore, phosphorescence tends to be less favoured with regards to optical sensing compared with fluorescence techniques.

A Jablonski diagram is used to illustrate the processes that occur for the absorption and emission of light, Figure 3.1. Jablonski diagrams detail molecular processes that can occur to the excited states as well as highlighting the routes of decay, which do not result in the emission of light, these processes are in competition with fluorescence.[6]

The singlet ground, first and second states (S_0, S_1 and S_2 respectively) are the electronic energy levels at which fluorophores can exist in a number of vibrational levels. Initially

light is absorbed and the fluorophore is usually excited to a higher vibrational energy level within an excited orbital i.e., S_1 or S_2. The excitation is a vertical transition as the timescale (~10^{-15} s) is too short for the position of the nuclei to change, this is known as the Franck-Condon principle.[7-9] Molecules then relax from the excited Franck-Condon vibrational state to the lowest vibrational level of the excited orbital *via* internal conversion and vibrational energy losses through collisions with solvent molecules. This is an iso-energetic equilibration process that generally occurs within 10^{-12} s and any remaining energy is given off as light. The photon expelled from the equilibrated excited state (or locally excited state) will be at a specific emission wavelength that is related to both the initial and final electronic and vibrational energy levels that the electron has occupied. This is dictated by Kasha's rule[10] and the result of this is that generally an emission spectrum will look the same regardless of the excitation wavelength absorbed.

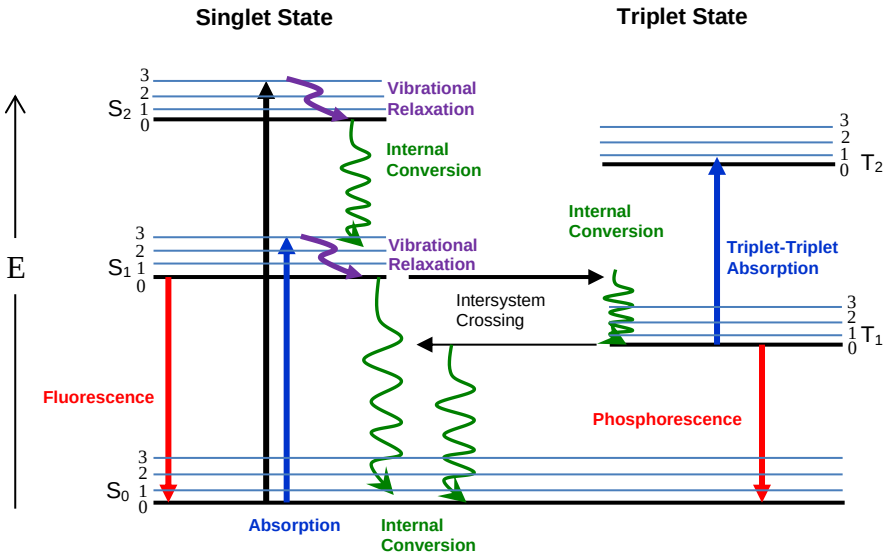

Figure 3.1 A typical Jablonski diagram showing the possible excitation and emission processes that can take place.

For completeness it is important to mention that molecules in the first excited singlet state can also undergo a process called intersystem crossing. The molecules can spin convert and move from S_1 to T_1 (first excited triplet state), from here they can relax to emit a photon *via* phosphorescence. The process of intersystem crossing is made easier

when heavy atoms are present and so phosphorescence is more common for molecules containing atoms such as bromine or iodine.

3.2 Characteristics of Fluorescence Spectra

One of the most common characteristics is for the emission spectrum to be a mirror image of the absorbance spectrum. This is due to the combination of the Franck-Condon principle and Kasha's rule as often the same transitions are involved in the absorption and emission processes, Figure 3.2.[7-9, 11] For fluorescent molecules in solution, the fluorescence emission tends to be observed at a higher wavelength than the excitation, i.e., the emission is of a lower energy than that of the absorbed light. This was first seen in 1852 by Stokes and this phenomenon was labelled the "Stokes shift".[12] The reduction in energy for the emission relates to the equilibration of the excited electron to the lowest vibrational energy level of the orbital.

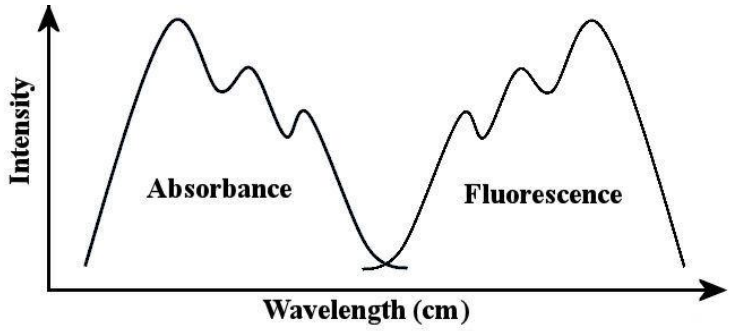

Figure 3.2 Theoretic absorption and fluorescence emission spectra to highlight the general symmetric nature when following both the Franck-Condon principle and Kasha's rule

Fluorescence spectroscopy is very sensitive to the surrounding environment and because of this, the Stokes shift can be influenced by other factors including temperature and pH.[13, 14] The fluorophore can interact with the local environment *via* a number of mechanisms, for example the pKa of the fluorophore can lead to different species being produced dependent on the pH of the system and thus the lowest excited state energy can differ at different pH values. Also, some fluorophores are able to form an internal charge transfer (ICT) state[15] or a twisted internal charge transfer (TICT) state[16], upon excitation these molecules are able to form species with increased charge separation. Depending on the nature of the solvent present, it can be

this ICT state (in polar solvents) or the locally excited state (in non-polar solvents) that has the lowest excited state energy.[1] However, the solvent and its polarity has an even more influential role on the Stokes shift due to direct interactions between the fluorophore and surrounding solvent molecules.[17, 18]

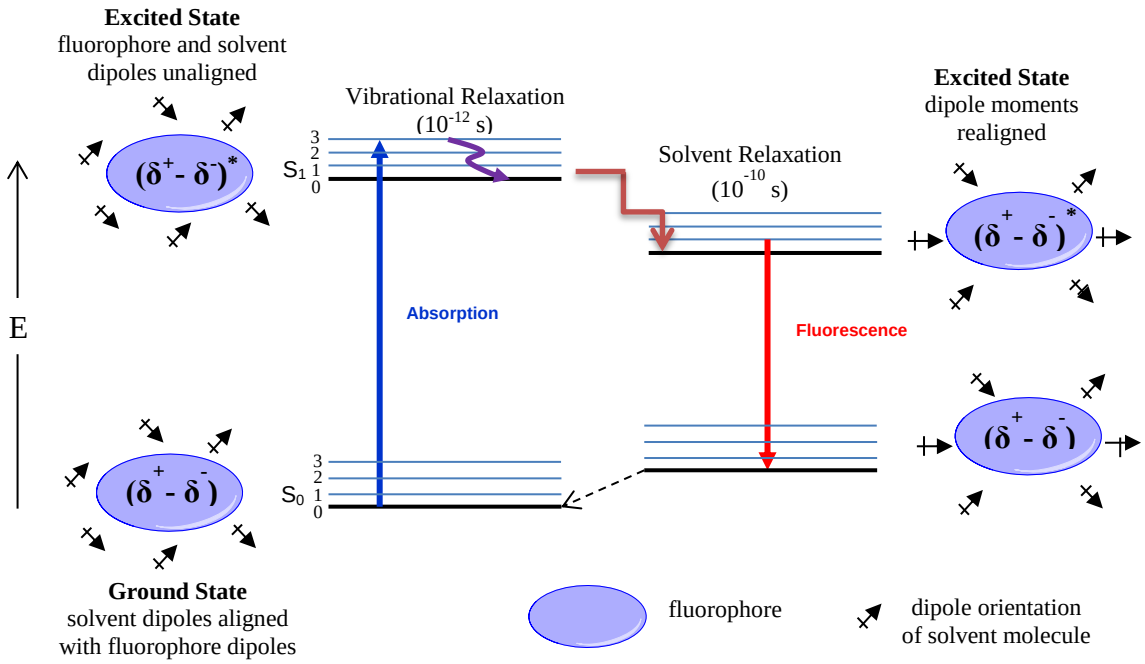

Figure 3.3 The reorganisation of solvent molecules around the excited fluorophore allows dipole-dipole interactions to reduce the energy of the excite S_1 state. The solvent relaxation; therefore, results in a bathochromic shift of the emission band.

After a fluorophore has been excited to a higher vibrational energy level of S_1, the excess vibrational energy is lost through collisions with solvent molecules as the electrons relax to the lowest vibrational energy level (as discussed in section 3.1). These solvent molecules can also influence the energy level of the excited state (i.e., S_1). The solvent molecules surrounding a fluorophore have a dipole moment that can interact with the dipole moment of the fluorophore itself. This dipole-dipole interaction results in an ordered array of solvent molecules surrounding the fluorophore. The energy difference between S_0 and S_1 results in a difference in the molecular dipole moment, often the excited fluorophore has a much greater dipole moment in the excited state, thus upon excitation, the surrounding solvent molecules must rearrange themselves in order to maintain a dipole-dipole interaction, Figure 3.3.[1] This process, known as

solvent relaxation, is more dramatic when the solvent is more polar as more re-orientation is required, which results in further collisions occurring between the electrons and solvent molecules.[1, 18] Therefore, this results in further energy being lost and hence the energy of the excited state (S_1) is lowered and effectively stabilized by increased solvent polarity. The energy gap between S_1 and S_0 is now lower, thus the wavelength is longer and the Stokes shift is increased. The increase in wavelength is known as a bathochromic shift and represents a smaller energy gap between the ground and excited states.[19, 20] It is important to note that for solvents at room temperature, the typical relaxation time is 10 to 100 ps, which is too great to have an impact on the excitation energy; however, it is much lower than the lifetime of the S_1 excited state (~ 10 ns).[1] Therefore, it is an increase in Stokes shift that is observed rather than a bathochromic shift of both the absorbance and emission spectra with the same Stokes shift.

3.3 Fluorescent Sensing

Sensors are very important analytical tools that produce a measurable signal in response to the presence of certain analytes or a change in the physical or chemical surroundings.[21, 22] The first component of any sensor is a target recognition site; the target can be any optical property, a small organic molecule, proteins, DNA or even cells.[23, 24] The second section of a sensor is signal transduction, this is important for converting the recognition event into a detectable signal; such as fluorescence or electrochemical signals, Figure 3.4. These two components enable information to be received and transformed into a compatible form, so that it can be interpreted with our understanding and knowledge.

Fluorescent sensors do not to cause significant disturbance to the system in which they are being observed because as they are able to report a significant amount of information from very low concentrations (typically µ-molar).[1] Fluorescence is; therefore, an invaluable sensing tool that can be used for the fundamental study of molecular interactions and the surrounding chemical environment. Initial fluorescent sensing focused on using structurally simple fluorophores; however, more recent

research has become more focused on the development of specific sensors for the recognition of particular moieties.[25, 26]

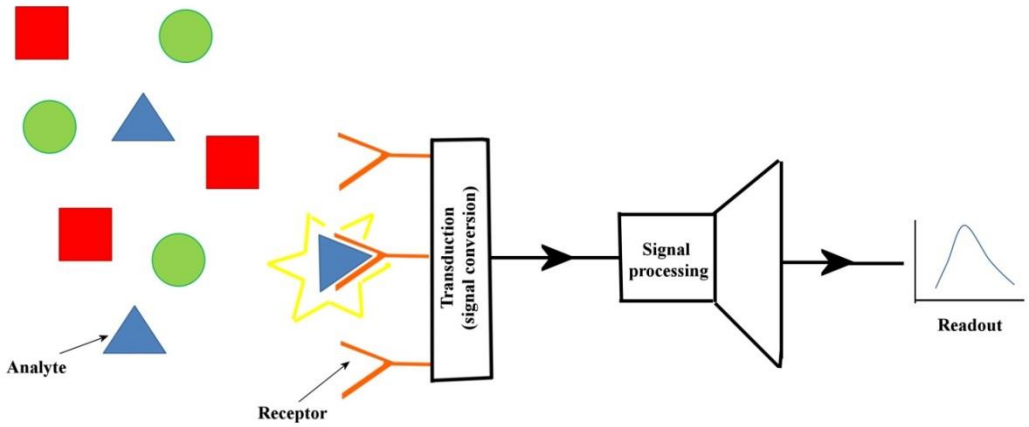

Figure 3.4 A schematic representation of a generic sensor

3.3.1 Measurable Characteristics from Fluorescence Spectroscopy

There are a number of properties that a fluorophore possesses, which can be measured and are important in sensing. The most common and easy to measure parameter is the fluorescence intensity, which is obtained when the fluorophore is initially excited at a specific excitation wavelength, $\lambda_{ex.}$ Following excitation, the fluorophore displays an emission with a certain intensity distribution. The intensity is dependent upon molar extinction coefficient, ε, the excitation wavelength, λ_{ex}, as well as the number of photons that are emitted compared to the number of photons absorbed, this ratio is known as the quantum yield, Φ_f.[27] The direct measurement of Φ_f is not often possible as it requires the absolute measurement of the photons emitted, which involves specialist equipment in order to maintain a complete photon balance.[28] As an alternative, relative Φ_f measurements are routinely obtained following a method introduced by Parker and Rees, whereby the fluorescence of the unknown is compared to a fluorescence standard that contains a fluorophore with a known Φ_f.[29] The Φ_f is then calculated by Equation 3.1, where Φ = quantum yield, D = integrated area of the fluorescence emission peak, A = absorbance at the excitation wavelength, I = flux at the

excitation wavelength and η = refractive index ($_R$ and $_S$ refer to the reference and the sample, respectively).

$$\Phi_S = \Phi_R . \left(\frac{D_S}{D_R}\right) . \left(\frac{A_R}{A_S}\right) . \left(\frac{I_R}{I_S}\right) . \left(\frac{\eta_S}{\eta_R}\right)^2 \quad (3.1)$$

An additional parameter that can be measured using fluorescence techniques is the lifetime of fluorescence. The fluorescence lifetime, τ, is the average length of time that the fluorophore remains in the excited state and is characteristic for any given fluorophore in a specific environment.[27] This additional information is extremely useful for distinguishing the fluorescence of the fluorophore from other fluorescent components, such as the auto-fluorescence when looking at tissue and at substrates in the cell medium.[30]

$$\frac{dN(t)}{dt} = -(\Gamma + k)N(t) \quad (3.2)$$

The rate of decay of excited fluorophores can be described by Equation 3.2 where N(t) = the number of excited molecules at time, *t*, Γ = the radiative decay rate constant that is characteristic for the fluorophore as it represents the rate of emission, *k* = the rate constant for the sum of all non-radiative decay mechanisms that relate to the interaction of the fluorophore with its local environment.[31, 32] Because emission is a random event and each individual excited fluorophore has the same probability of emitting a photon at any time, there is an exponential decay in the population of the excited state, which is given by Equation (3.3):

$$N(t) = N_0 e^{-1/\tau} \quad (3.3)$$

After excitation, a population of fluorophore molecules enter the excited state and; therefore, Equation 3.4 is achieved, i.e., an exponential decay. From this it is possible to see that the fluorescence lifetime is the time that it takes for the excited molecules to decay to 36.8 % ($1/e$ = 0.368) of the original fluorescence intensity (i.e., the time the excited state reaches 36.8 % of its original population). Therefore, the fluorescence lifetime can be described as the average length of time in which a fluorophore remains in its excited state.[31-33]

$$\frac{N(t)}{N_0} = e^{-1/\tau} \tag{3.4}$$

Fluorescence lifetime imaging microscopy (FLIM) was initially used to obtain information from specific locations within different mediums and this proved a breakthrough technique for visualizing and measuring certain substances within cells and tissue.[34-36] In following research, FLIM was successfully coupled to confocal laser scanning microscopes (CLSMs) in order to obtain three-dimensionally resolved fluorescence lifetime information from across entire cells as well as throughout cell media containing multiple cells.[37, 38] It is the ability of a CLSM to scan the z-axis through solution, normal to the electrode that provides it with a much greater advantage over a standard fluorimeter.[39] This extra dimension of analysis allows for the profiling of multilayer structures without damaging the substrate and prevents blurring that results in standard fluorescence measurements due to the collection of light from above and below the focal plane.[40, 41]

In 1990, a further breakthrough in fluorescence imaging was achieved with the introduction of two-photon laser scanning microscopes that enabled multi-photon excitation of fluorophores.[42] This provided multi-wavelength capabilities and produced fluorescence images with greater contrast, Figure 3.5 shows a lifetime image of a mouse intestine recorded using two-photon excitation and processed with the fluorescence intensity as the brightness and the colour representing the fluorescence lifetime.[30]

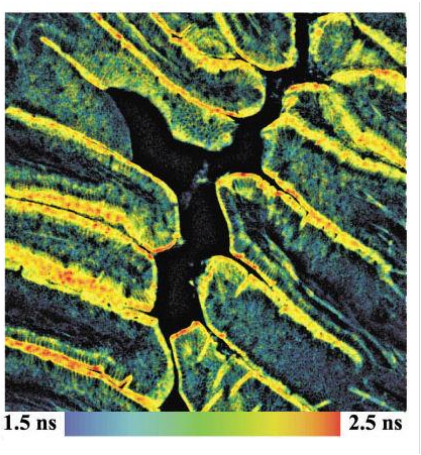

Figure 3.5 A two-photon lifetime image of a mouse intestine sample stained with Alexa Fluor 350, Alexa Fluor 568 and Sytox Green, reproduced from [30]

Multiphoton excitation is achieved by using longer excitation wavelengths for two or even three photon absorption to achieve the same energy level as one-photon absorption, Figure 3.6.[1, 43, 44] Because of the lower energy excitation, multiphoton microscopy is less damaging to samples than single photon experiments and makes it a favourable addition or alternative to study delicate materials such cells and other biological samples.[45]

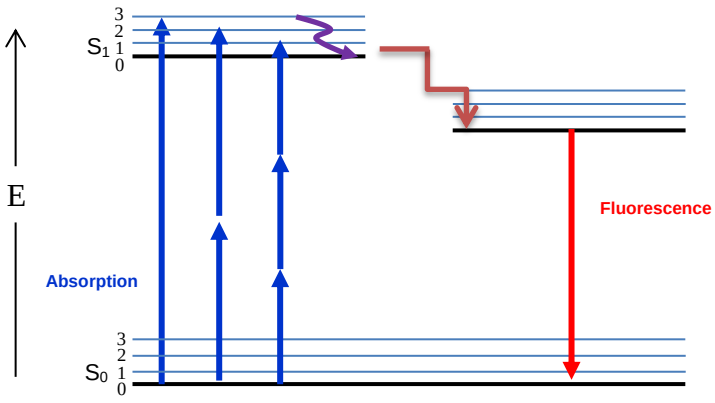

Figure 3.6 Jablonski diagram to show that one-, two- or three-photon excitation results in the same fluorescence emission and lifetime

In multiphoton excitation experiments, the photon absorption occurs simultaneously; therefore, high intensity illumination is required, this is achieved using titanium-sapphire lasers.[1, 46] The selection rules for single, two and three-photon excitation are different, which results in the excited fluorophores entering different excited vibrational levels; however, the emission occurs from the same relaxed excited state irrespective of the absorption process. This results in fluorescence lifetimes and emission spectra that are the same independent of it being obtained *via* one-, two- or three-photon excitation.[1]

3.4 Summary

In this thesis carbon nanoparticles with intrinsic fluorescent properties are synthesized and investigated. Using the discussed fluorescent techniques, the fluorescent properties and potential applications of the novel carbon nanomaterial are explored.

3.5 References

1. Lakowicz, J.R., *Principles of Fluorescence Spectroscopy*, third ed., 2006, Springer, New York, 1-26 and 607-621.
2. Bissell, R.A., A.P. De Silva, H.Q.N. Gunaratne, P.L.M. Lynch, G.E.M. Maguire, and K. Sandanayake, *Molecular Fluorescent Signaling with Fluor Spacer Receptor Systems - Approaches to Sensing and Switching Devices via Supramolecular Photophysics*, Chem. Soc. Rev., 1992, **21**, 187-195.
3. Heupel, W.-M. and D. Drenckhahn, *Extending the Knowledge in Histochemistry and Cell Biology*, Histochem. Cell Biol., 2010, **133**, 1-40.
4. Bohmer, M. and J. Enderlein, *Fluorescence Spectroscopy of Single Molecules Under Ambient Conditions: Methodology and Technology*, ChemPhysChem, 2003, **4**, 792-808.
5. Ambrose, W.P., P.M. Goodwin, J.H. Jett, A. Van Orden, J.H. Werner, and R.A. Keller, *Single Molecule Fluorescence Spectroscopy at Ambient Temperature*, Chem. Rev., 1999, **99**, 2929-2956.
6. Chen, R.F. and J.R. Knutson, *Mechanism of Fluorescence Concentration Quenching of Carboxyfluorescein in Liposomes - Energy-Transfer to Nonfluorescent Dimers*, Anal. Biochem., 1988, **172**, 61-77.
7. Franck, J. and E.G. Dymond, *Elementary Processes of Photochemical Reactions*, Trans. Faraday Soc., 1926, **21**, 536-542.
8. Condon, E.U., *Nuclear Motions Associated with Electron Transitions in Diatomic Molecules*, Physical Review, 1928, **32**, 858-872.
9. Condon, E., *A Theory of Intensity Distribution in Band Systems*, Physical Review, 1926, **28**, 1182-1201.
10. Kasha, M., *Characterization of Electronic Transitions in Complex Molecules*, Discuss. Faraday Soc., 1950, **9**, 14-19.
11. Birks, J.B., *Birks Photophysics of Aromatic Molecules*, 1970, John Wiley & Sons, New York.
12. Stokes, G.G., *On the Change of Refrangibility of Light*, Philos. Trans. R. Soc. London, 1852, **142**, 463-562.
13. Yi, L.-l., L.-p. Shang, Z.-f. Li, and H. Deng, *Effect of Temperature and pH on the Fluorescence Characteristic of Oily Waste Water*, Spectrosc. Spect. Anal., 2011, **31**, 1571-1573.
14. Park, K.K., J.W. Park, and A.D. Hamilton, *Solvent and pH Effects on the Fluorescence of 7-(Dimethylamino)-2-fluorenesulfonate*, J. Fluoresc., 2007, **17**, 361-369.
15. Lippert, E., W. Lüder, F. Moll, W. Nägele, H. Boos, H. Prigge, and I. Seibold-Blankenstein, *Umwandlung von Elektronenanregungsenergie*, Angew. Chem., 1961, **73**, 695-706.
16. Zhao, G.-J. and K.-L. Han, *pH-Controlled Twisted Intramolecular Charge Transfer (TICT) Excited State via Changing the Charge Transfer Direction*, Phys. Chem. Chem. Phys., 2010, **12**, 8914-8918.
17. Fdez. Galvan, I., M. Elena Martin, A. Munoz-Losa, M. Luz Sanchez, and M.A. Aguilar, *Solvent Effects on the Structure and Spectroscopy of the Emitting States of 1-Phenylpyrrole*, J. Chem. Theory Comput., 2011, **7**, 1850-1857.
18. Demeter, A., T. Berces, L. Biczok, V. Wintgens, P. Valat, and J. Kossanyi, *Comprehensive Model of the Photophysics of N-phenylnaphthalimides: The Role of Solvent and Rotational Relaxation*, J. Phys. Chem., 1996, **100**, 2001-2011.

19. Haidekker, M.A., T.P. Brady, D. Lichlyter, and E.A. Theodorakis, *Effects of Solvent Polarity and Solvent Viscosity on the Fluorescent Properties of Molecular Rotors and Related Probes,* Bioorg. Chem., 2005, **33**, 415-425.
20. Liu, L., Y. Sun, S. Wei, X. Hu, Y. Zhao, and J. Fan, *Solvent Effect on the Absorption and Fluorescence of Ergone: Determination of Ground and Excited State Dipole Moments*, Spectrochim. Acta, A, 2012, **86**, 120-123.
21. Iqbal, S.S., M.W. Mayo, J.G. Bruno, B.V. Bronk, C.A. Batt, and J.P. Chambers, *A Review of Molecular Recognition Technologies for Detection of Biological Threat Agents*, Biosens. Bioelectron., 2000, **15**, 549-578.
22. Tsien, R.Y., *Fluorescent and Photochemical Probes of Dynamic Biochemical Signals Inside Living Cells,* Fluorescent Chemosensors for Ion and Molecule Recognition, 1993, **538**, 130-146.
23. Lvov, Y., K. Ariga, I. Ichinose, and T. Kunitake, *Assembly of Multicomponent Protein Films by Means of Electrostatic Layer-by-Layer Adsorption,* J. Am. Chem. Soc., 1995, **117**, 6117-6123.
24. Lvov, Y., G. Decher, and G. Sukhorukov, *Assembly of Thin-Films by Means of Successive Deposition of Alternate Layers of DNA and Poly(allylamine),* Macromolecules, 1993, **26**, 5396-5399.
25. Liu, Y.-W., C.-H. Chen, and A.-T. Wu, *A Turn-On and Reversible Fluorescence Sensor for Al^{3+} Ion*, Analyst, 2012, **137**, 5201-5203.
26. Ke, I.-S., M. Myahkostupov, F.N. Castellano, and F.P. Gabbai, *Stibonium Ions for the Fluorescence Turn-On Sensing of F^- in Drinking Water at Parts per Million Concentrations*, J. Am. Chem. Soc., 2012, **134**, 15309-15311.
27. Rurack, K. and M. Spieles, *Fluorescence Quantum Yields of a Series of Red and Near-Infrared Dyes Emitting at 600-1000 nm*, Anal. Chem., 2011, **83**, 1232-1342.
28. Rurack, K., *Fluorescence Quantum Yields: Methods of Determination and Standards*, in *Standardization and Quality Assurance in Fluorescence Measurements I*, U. Resch-Genger, Editor. 2008, Springer, Berlin, Heidelberg, 101-145.
29. Parker, C.A. and W.T. Rees, *Correction of Fluorescence Spectra and Measurement of Fluorescence Quantum Efficiency*, Analyst, 1960, **85**, 587-600.
30. Becker, W., A. Bergmann, M.A. Hink, K. Konig, K. Benndorf, and C. Biskup, *Fluorescence Lifetime Imaging by Time-Correlated Single-Photon Counting,* Microsc. Res. Tech., 2004, **63**, 58-66.
31. Lakowicz, J.R., *Fluorescence Lifetime Imaging,* Anal. Biochem., 1992, **202**, 316-330.
32. Kuwana, E. and E.M. Sevick-Muraca, *Fluorescence Lifetime Spectroscopy in Multiply Scattering Media with Dyes Exhibiting Multiexponential Decay Kinetics*, Biophys. J., 2002, **83**, 1165-1176.
33. Spencer, R.D., *Fluorescence Lifetimes: Theory, Instrumentation, and Application of Nanosecond Fluorometry*, 1970, University of Illinois at Urbana-Champaign.
34. Dix, J.A. and A.S. Verkman, *Mapping of Fluorescence Anisotropy in Living Cells by Ratio Imaging - Application to Cytoplasmic Viscosity*, Biophys. J., 1990, **57**, 231-240.
35. Dix, J.A. and A.S. Verkman, *Pyrene Eximer Mapping in Cultured Fibroblasts by Ratio Imaging and Time-Resolved Microscopy,* Biochemistry, 1990, **29**, 1949-1953.

36. Keating, S.M. and T.G. Wensel, *Nanosecond Fluorescence Microscopy - Emission Kinetics of Fura-2 in Single Cells,* Biophys. J., 1991, **59**, 186-202.
37. Buurman, E.P., R. Sanders, A. Draaijer, H.C. Gerritsen, J.J.F. Vanveen, P.M. Houpt, and Y.K. Levine, *Fluorescence Lifetime Imaging Using a Confocal Laser Scanning Microscope,* Scanning, 1992, **14**, 155-159.
38. Morgan, C.G., A.C. Mitchell, and J.G. Murray, *Prospects for Confocal Imaging Based on Nanosecond Fluorescence Decay Time,* J. Microsc.-Oxford, 1992, **165**, 49-60.
39. Bowyer, W.J., J. Xie, and R.C. Engstrom, *Fluorescence Imaging of the Heterogeneous Reduction of Oxygen,* Anal. Chem., 1996, **68**, 2005-2009.
40. Sheppard, C.J.R. and D.M. Shotton, *Microscopy Handbooks: Confocal Laser Scanning Microscopy,* Microscopy Handbooks, 1997, first ed., Garland Science, USA.
41. Cannan, S., I.D. Macklam, and P.R. Unwin, *Three-Dimensional Imaging of Proton Gradients at Microelectrode Surfaces Using Confocal Laser Scanning Microscopy,* Electrochem. Commun., 2002, **4**, 886-892.
42. Denk, W., J.H. Strickler, and W.W. Webb, *2-Photon Laser Scanning Fluorescence Microscopy,* Science, 1990, **248**, 73-76.
43. Friedrich, D.M. and W.M. McClain, *2-Photon Molecular Electronic Spectroscopy,* Annu. Rev. Phys. Chem., 1980, **31**, 559-577.
44. Wirth, M.J., A. Koskelo, and M.J. Sanders, *Molecular Symmetry and 2-Photon Spectroscopy,* Appl. Spectrosc., 1981, **35**, 14-21.
45. Diaspro, A., *Introduction to Two-Photon Microscopy,* Microsc. Res. Tech., 1999, **47**, 163-164.
46. Hu, Z., G.D. Pantos, N. Kuganathan, R.L. Arrowsmith, R.M.J. Jacobs, G. Kociok-Koehn, J. O'Byrne, K. Jurkschat, P. Burgos, R.M. Tyrrell, S.W. Botchway, J.K.M. Sanders, and S.I. Pascu, *Interactions Between Amino Acid-Tagged Naphthalenediimide and Single Walled Carbon Nanotubes for the Design and Construction of New Bioimaging Probes,* Adv. Funct. Mater., 2012, **22**, 503-518.

Chapter 4

Fluxional Characteristics and Pore Effects of Pyrene Boronic Acids Anchored onto Carbon Nanoparticle Supports

Contents

Thanks to Masters Student Peter Haffenden who carried out his final year project as part of this study.

This work has been accepted for publication in New Journal of Chemistry;

DOI: 10.1039/C3NJ00017F.

4.1 Abstract

Pyrene-modified boronic acids self-assemble onto graphitic and carbonaceous surfaces. By the same mechanism, pyrene moieties are shown to self-assemble around commercially available negatively charged phenylsulfonic acid-modified carbon nanoparticles of approximately 9-18 nm in diameter (Emperor 2000, Cabot Corporation, for further information see Chapter 1). Previous work has developed a synthetic route to append pyrene groups onto different boronic acid scaffolds. These boronic acid-based compounds are then physisorbed onto the surface of carbon nanoparticles through the pyrene functionality. The boronic acid-modified carbon nanoparticles that are produced are insoluble in water and can readily be deposited onto graphite electrodes for use in electroanalytical applications. The binding of the terminal boronic acid groups are demonstrated to bind to caffeic acid, which is a common catechol, otherwise referred to as an ortho-quinol. An electrochemical investigation was performed to understand the mechanism, which is based on ligand fluxionality.

The non-covalently modified electrodes based on nanoparticle aggregates are sensitive to caffeic acid and exhibit Langmuirian binding constants approaching 10^6 mol^{-1} dm^3. The molecular structure of the pyrene-appended boronic acid affects the ability of the boronic acid moiety to bind to the caffeic acid. More importantly, the fluxional transformation of the strongly bound caffeic (with a high oxidation potential) into the weakly bound (with a lower oxidation potential) form is affected by the change in the length of the carbon linker that is present between the boronic acid and the pyrene moieties. The resulting design principles for improved scaffold structures for boronic acid receptors are discussed.

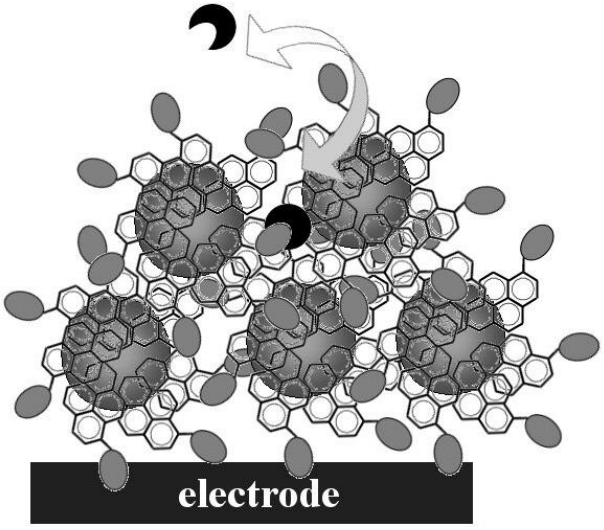

4.2 Introduction

Carbon nanoparticles (CNPs) such as those derived from carbon blacks[1] provide a versatile platform for the development of electroanalytical tools[2] with high active surface areas and a high degree of functionalisation.[3] In contrast to the more structurally pure forms of nanocarbons, such as carbon nanotubes (CNTs)[4] or graphene,[5] carbon nanoparticles are used widely in industry, available at low cost, and have an approved safety record, as discussed in the Introduction section of this thesis.

In recent studies, CNPs have been the focus of a large number of investigations[6] including the transformation of commercial CNP surface functionality from sulfonate to sulfonamide,[7] interactions between CNPs and redox enzymes,[8] the use of CNPs to modify liquid-liquid interfaces,[9] CNPs as a support for electrochemically active proteins,[10] as CNP building blocks for layer-by-layer electrostatically assembled films,[11] and CNPs as a gas sensor component.[12] This chapter demonstrates that negatively charged CNPs (Emperor 2000, Cabot Corp.) can be functionalised non-covalently with previously reported pyrene-appended pyridinium boronic acids (see Figure 4.1).[13]

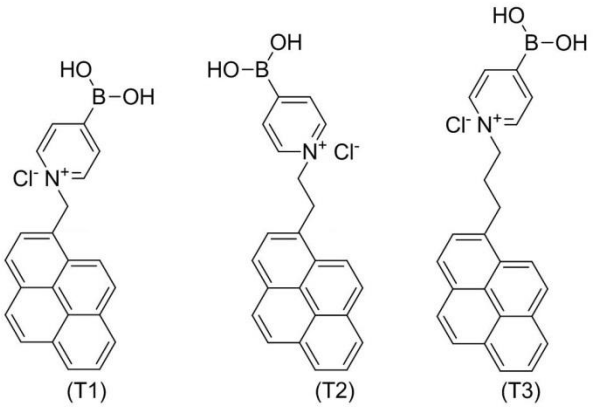

Figure 4.1. The molecular structures of 4-borono-1-(pyren-2-ylmethyl)pyridin-1-ium chloride (T1), 4-borono-1-(2-(pyren-2-yl)ethyl)pyridin-1-ium chloride (T2), and 4-borono-1-(3-(pyren-2-yl)propyl)pyridin-1-ium chloride (T3).[13]

Boronic acids have extensive chemistry and are commonly used synthetically for Suzuki cross-coupling reactions, which are of high importance especially in the pharmaceutical industry.[14-18] Boronic acids also have an extremely important role as versatile chemo-

receptors for a number of substrates such as saccharides[19] including glucose[20] as well as α-hydroxy-carboxylates[21] and ortho-quinols such as alizarin red S.[22] There are extensive literature reviews that detail the recent developments in this field that further highlight the importance of optimising boronic acids for specific functions.[23, 24] Within the Marken group, a number of electroanalytical studies have been performed that incorporate different boronic acids into droplet deposits,[25] nano-cellulose, and dendrimer assemblies.[26] These studies demonstrate that the combination of boronic acids with electrochemical techniques can result in extremely useful, rapid, and accurate analytical testing methodologies. Also, a dodecyl-modified boronic acid has been shown to create monolayer deposits on basal plane pyrolytic graphite electrode surfaces, which provided a strong basis for this study.[27] Herein a pyrene-appended pyridinium boronic acid receptor is deposited onto different carbonaceous materials. The pyrenes are shown to self-assemble onto the surface of (A) graphite and (B) carbon nanoparticles to create different carbon materials that are furnished with a surface layer of boronic acids (see Figure 4.2).

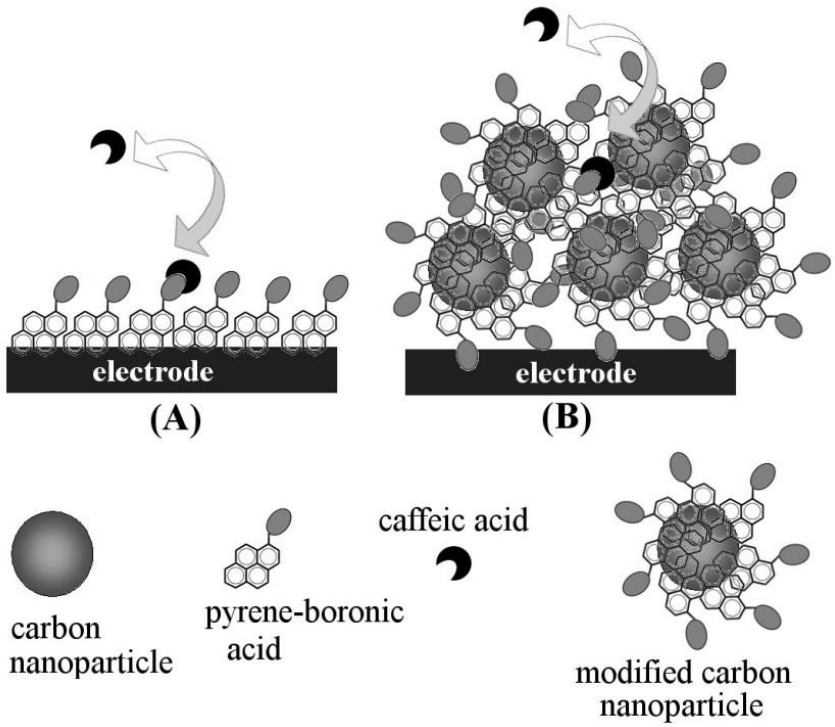

Figure 4.2. Schematic drawing of (A) a pyrene-appended boronic acid modified graphite electrode and (B) pyrene-appended boronic acid modified carbon nanoparticle film immobilised onto a graphite electrode.

Terminal pyrene-linker units have previously been employed for the functionalisation of hydrophobic or graphitic surfaces such those in graphene[28] and in CNT substrates.[29] These assembly processes, which result in the formation of layered pyrene moieties are predominantly driven by dispersion forces that arise between the substrate and the pyrene group. The self-assembly is also promoted by the low solubility of pyrene derivatives in aqueous media. Herein negatively charged phenylsulfonamide furnished carbon nanoparticles are combined with positively charged pyrene-appended pyridinium boronic acids (see Figure 4.1) in order to exploit additional electrostatic interactions. Three different boronic acids with a mono-, di-, and tri-methylene bridge (T1, T2, and T3, respectively) are employed and compared. The minor variations in the molecular structure of the boronic acid (T1–T3) are demonstrated to have a considerable effect on the ability of the formed pyrene-assemblies to bind through the boron atom to ortho-quinols such as caffeic acid.

4.3 Experimental

4.3.1 Reagents

Ortho-phosphoric acid, dichloromethane, and acetonitrile were purchased from Fisher Scientific. Emperor 2000 sulfonate derivatised carbon nanoparticles (approximately 9-18 nm diameters) were obtained from Cabot Corporation. All other chemical reagents including caffeic acid and sodium hydroxide were obtained from Aldrich and used without purification. Demineralised and filtered water was obtained from a Thermo Scientific water purification system (Barnstead Nanopure) with a resistivity approximately 18.2 MOhm cm. The resistance (R) of a material is proportional to the length (l) and inversely proportional to the surface area (A), and the resistivity (ρ) is the constant of proportionality, see Equation 4.1. The value of the resistivity quantifies the extent at which a specific material opposes the flow of an electrical current. Therefore, it is more facile for a current to flow through a material with a lower the resistivity.

$$R = {\rho l}/{A} \tag{4.1}$$

4.3.2 Instrumentation

For all voltammetric studies a microAutolab III potentiostat system (EcoChemie, Netherlands) was used with a Pt wire counter electrode and a KCl-saturated calomel (SCE) reference electrode (Radiometer). The working electrode was a 4.9 mm diameter basal plane pyrolytic graphite (Le Carbone UK Ltd., Pyrocarbon) disc electrode mounted into a Teflon casing. All experiments were performed at room temperature, that is, 22 ± 2 ^{o}C. Scanning electron microscopy (SEM) images were obtained using a JEOL JSM6301F microscope. Fluorescence measurements were recorded by using a fluoroSENS fluorimeter (Gilden Photonics, UK) with fluoroSENS system software version 1.88.7.

4.3.3 Modification of Carbon Nanoparticles and Basal Plane Pyrolytic Graphite

Three pyrene-based compounds were used in this study that has previously been synthesised within the James group, see Figure 4.1.[13] The carbon linker between the pyrene moiety and the pyridinium boronic acid moiety in each compound differed and ranged from one to three carbons in length (Figure 4.1). Acetonitrile was used to dissolve the functionalised boronic acids and form 1 mM solutions of T1, T2, and T3.

The basal plane pyrolytic graphite electrode surfaces were prepared by polishing with carborundum paper (grade 1000) and rinsing with distilled water before dipping the electrode into a 1 mM pyrene solution (T1, T2, or T3 pyrene in acetonitrile) for ten minutes. The electrode was then removed and allowed to dry in air before rinsing with distilled water.

The pyrene boronic acid exhibited an emission peak at approximately 380 nm after excitation at 338 nm; see Figure 4.3(A), which shows the results for T1. To modify the Emperor 2000 CNPs with pyrene boronic acid, Emperor 2000 CNPs were added to 10 mL of 0.1 mM pyrene solution. After stirring the solution for ten minutes, it was allowed to stand for 20 minutes so that the carbon nanoparticles could settle-out. This process was followed by using fluorescence spectroscopy. Emperor 2000 CNPs were added portion-wise to the fluorescent solution containing the modified pyrene boronic acid, and after each addition the mixture was left to stand. This was to allow the CNPs to settle out of solution

and leave the supernatant containing any pyrene boronic acid that had not physisorbed onto the surface of the particles; the supernatant was used directly for fluorescent measurements.

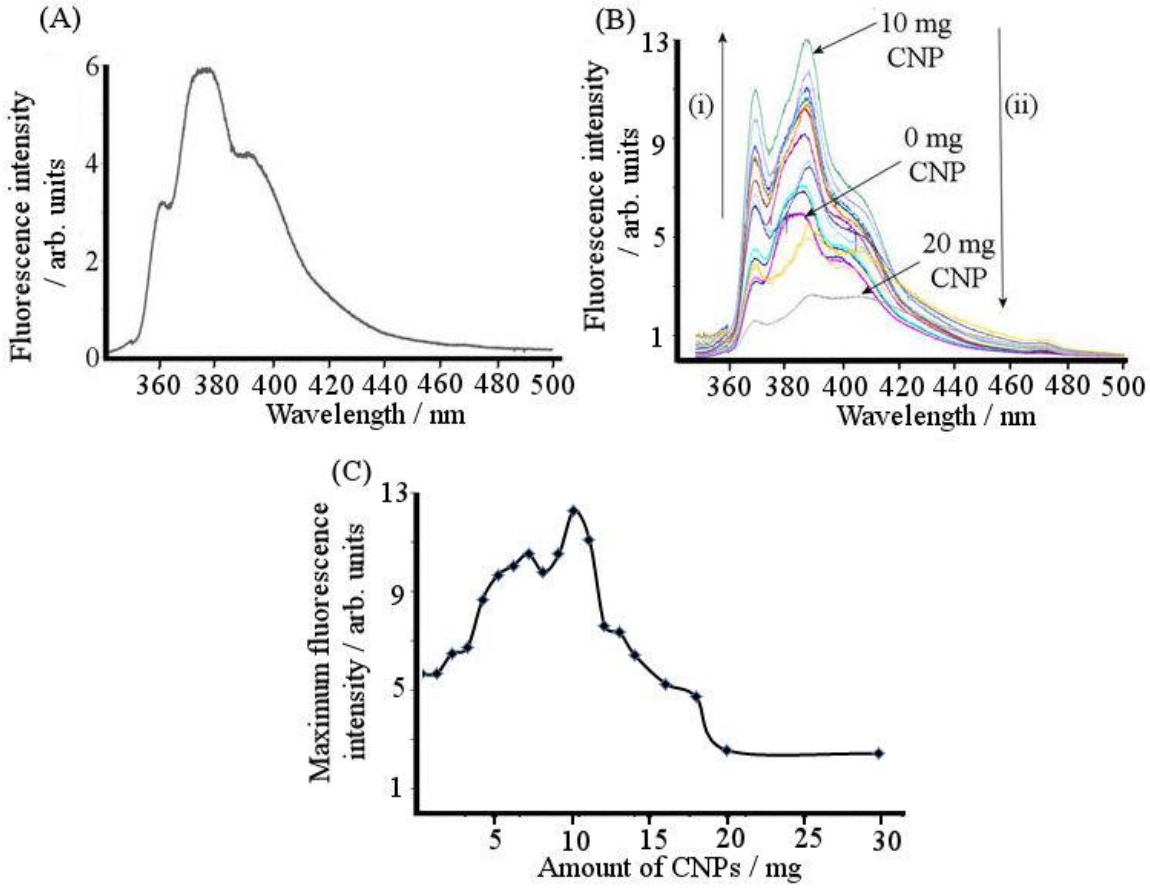

Figure 4.3. Fluorescent spectra for 0.1 mM T1-pyrene boronic acid after excitation at 338 nm with (A) no CNPs and (B) increasing wt % of carbon nanoparticles from 0 to 66.7 wt %; (i) represents the increase in intensity between 0 and 33.3 wt % and (ii) represents the decrease in fluorescent intensity between 33.3 wt % and 66.7 wt % CNPs added. (C) A plot of the maximum fluorescence intensity as the number of CNPs added increased.

Interestingly, the fluorescence intensity began to increase with increasing amounts of CNPs, see Figure 4.3(B) and (C). This could be associated with the pyrene fluorophore being present in the excimer form at higher concentrations, which would appear red-shifted relative to the monomer.[30-33] As the pyrene boronic acid moieties bind adsorb onto the CNPs, they are being removed from the solution and the effective concentration in the solution is decreased. Therefore, the initial increase in fluorescence intensity with decreasing concentration was likely due to the pyrene favouring the mono-form over the excimer. After 10 mg (33.3 wt %) of Emperor 2000 had been added to the solution, a

maximum fluorescence was reached; Figure 4.3B(i) and (C). Upon subsequent additions of CNPs, the fluorescence decreased because of the mono-pyrene moieties being strongly adsorbed onto the surface of the CNPs; Figure 4.3B(ii). After 20 mg of CNPs were added to the solution, the supernatant exhibited very poor fluorescence response and further additions made negligible difference. Therefore, 20 mg CNPs (i.e., 66.7 wt %) were used to bind the pyrene boronic acid compounds in a 0.1 mM solution.

The supernatant acetonitrile was decanted and rinsed before the solid was placed into an oven at 80 ^{o}C overnight to remove all of the remaining solvent and to dry the modified nanoparticles. The boronic acid modified nanoparticles were dispersed in fresh acetonitrile (3 mg mL^{-1}) by ultrasonication for 30 minutes. Typically 5 µL of the resulting solution was drop cast onto a polished graphite electrode and allowed to dry in air, resulting in a 15 µg deposit of modified CNPs as a film on the electrode surface. SEM images of the bare and modified graphite surfaces are shown in Figure 4.4. When an image of a blank graphite surface was compared to an image of the same surface after 5 µL of modified CNPs have been deposited, it was clearly observed that an uneven film of nanoparticle aggregates has formed.

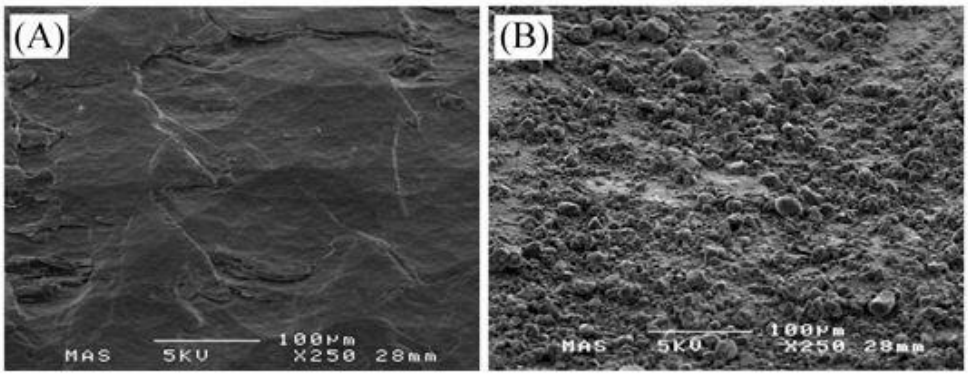

Figure 4.4. SEM images for (A) a bare graphite electrode and (B) a 15 µg pyrene-boronic acid-CNP modified graphite electrode.

4.4 Results and Discussion

4.4.1 Caffeic Acid Redox Activity: Free and Bound

Caffeic acid is an anti-oxidant[34] that contains a redox active ortho-quinol species, which undergoes a 2 H^+ / 2 e^- oxidation to form the corresponding ortho-quinone (see Equation 4.2).[35] The ortho-quinol unit is a 1,2-diol that is able to bind to boronic acid functional groups through boronic ester formation.[36]

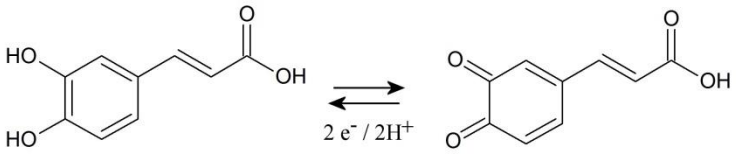

(4.2)

A cyclic voltammogram (CV) for the oxidation of 0.17 mM caffeic acid in pH 7 buffered phosphate solution is shown in Figure 4.5A(iv) and CVs obtained under the same conditions but in the presence of T1 (i), T2 (ii), or T3 (iii) that is bound non-covalently to a graphite electrode are shown for comparison. At the bare graphite electrode, the chemically reversible oxidation of caffeic acid (process P1 in Figure 4.5) was observed at 0.15 V versus a SCE (consistent with previous literature reports).[37] Assuming semi-infinite diffusion to a flat electrode, the Randles-Sevcik equation (see Equation 4.3) could be used to estimate the diffusion controlled peak current for a two-electron oxidation.[38]

$$I_{p,\text{diffusion}} = 0.446nFAc\sqrt{\frac{nF\nu D}{RT}} \tag{4.3}$$

In this equation the number of electrons transferred per molecule is n = 2, F denotes the Faraday constant (96485 C mol^{-1}) , A = 19 × 10^{-6} m^2 is the electrode area, c = 0.17 mol m^{-3}

where c is the concentration, *v* denotes the scan rate, *R* is the universal gas constant, and $D = 0.5 \times 10^{-9}$ m^2s^{-1} where *D* is the approximate diffusion coefficient for caffeic acid at pH 7.[39] The peak current was calculated as 12.4 μA, which was in excellent agreement with the observed peak current in Figure 4.5A(iv), thus confirming semi-infinite diffusion conditions.

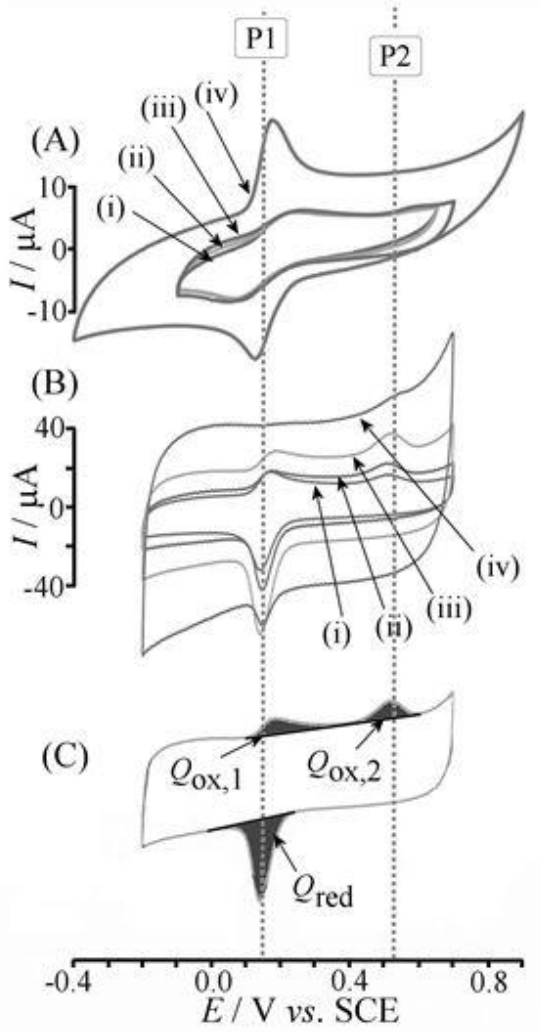

Figure 4.5. (A) Cyclic voltammograms (scan rate 50 mVs^{-1}) for 0.17 mM caffeic acid using (i) T1-modified graphite (ii) T2-modified graphite (iii) T3-modified graphite (iv) bare graphite electrode immersed in 0.1 M phosphate buffer solution at pH 7 (B) Cyclic voltammograms (50 mVs^{-1}) for 0.01 mM caffeic acid in 0.1 M phosphate buffer solution at pH 7 using graphite electrodes with (i) 3 μg T1-modified CNPs (ii) 15 μg T1-modified CNPs (iii) 30 μg T1-modified CNPs (iv) 60 μg T1-modified CNPs immobilised. (C) Data from Biii with peak integration indicated.

At the surface of the pyrene-modified graphite electrode, the capacitive current was reduced (by approximately 50%) because of pyrene functionalisation of the surface resulting in a partial surface-blocking effect. Furthermore, the Faradaic peaks for the

oxidation and reduction of caffeic acid were also much lower and the peak shape had significantly broadened (i.e., the electrode was partially blocked). Clearly the process was now under kinetic rather than semi-infinite diffusion control. At the same mid-point potential as the solution caffeic acid in solution is a process associated with a weak binding mechanism. The likely interaction of caffeic acid with the boronic acid appeared to be required as part of the electron transfer process. That is, random electron transfer to the caffeic acid species in solution was suppressed; however, orbital-controlled electron transfer to the boronic acid-bound caffeic acid was active (vide infra). Therefore P1 is thought to be due to weakly bound caffeic acid as well as the solution phase redox process, which is evidenced by bridging between the signals for P1 and P2 (vide infra).

When comparing the effect of the three different boronic acids (T1, T2, and T3, Figure 4.1), a minor additional oxidation peak was observed at approximately 0.6 V versus a. SCE when T3 was bound to the graphitic surface. This process (P2), although weak, was attributed to the caffeic acid that was strongly bound to the boronic acid (Equation 4.4).

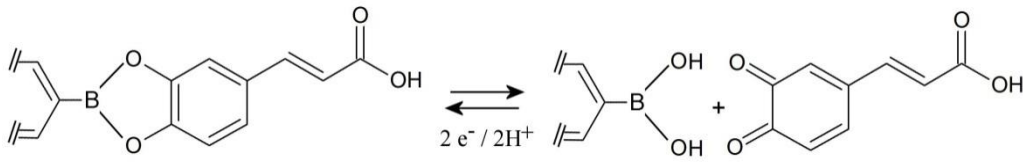

(4.4)

The amount of pyrene-boronic acid on the electrode surface was expected to be relatively high because of the evaporation method applied during adsorption. Integration of the charge under the oxidation/reduction peak for the bound caffeic acid suggests a charge of approximately 20 μC, which would be consistent with 0.1 nmol binding sites or a 6 Å × 6 Å area per binding site. However, the simple binding model suggested in Equation 4.4 may not be appropriate if a second caffeic acid molecule was able to bind to the boronic acid receptor. The carboxylate functional group can also bind in addition to, or instead of the ortho-quinone (vide infra).

When the boronic acid-modified CNPs were employed instead of the bare graphite electrode, additional capacitive background currents and additional Faradaic currents were

observed. Figure 4.5(B) shows the effect of changing the amount of CNPs for the T1-modified material immersed in 10 μM caffeic acid. At this low concentration, the voltammetric responses were dominated by adsorbed caffeic acid and contributions from caffeic acid diffusing to the electrode could be completely ignored. Both processes P1 and P2 were detected most clearly for a 15 μg CNP deposit. Both of the oxidation responses exhibited a similar charge under the voltammetric peak [see $Q_{ox,1}$ and $Q_{ox,2}$ in Figure 4.5(C)] with the reduction peak in P1 exhibiting twice the charge, that is, $Q_{red} = Q_{ox,1} + Q_{ox,2}$. It could be inferred that two types of adsorbed caffeic acid were present under these conditions, with P1 linked to weaker binding (in addition to caffeic acid free in the solution) and P2 linked to stronger (and likely covalent) adsorption, see Figure 4.6. When linked to the ortho-quinol, the boronic acid offered a second weaker binding site, which is proposed here as the reason for process P1 to remain active (vide infra). Therefore, there was no loss of caffeic acid as inferred by Equation 4.4 and even after oxidation the caffeic acid appeared to remain weakly bound. When there was too much of the carbon nanoparticle material deposited onto the electrode, the Faradaic currents appears weaker [see Figure 4.5B(iv)], which was likely to be attributed to inaccessible regions within CNP aggregates. Therefore, in the following experiments a 15 μg carbon nanoparticle deposit was used in order to optimise the voltammetric responses.

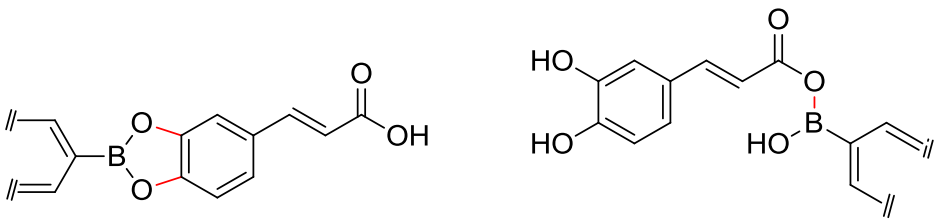

Strong bidentate binding, P2 Weak monodentate binding, P1

Figure 4.6. The two binding modes that give rise to redox processes P1 and P2.

4.4.2 Caffeic Acid Redox Activity: Fluxionality

The voltammetric data obtained for boronic acids T1, T2, and T3 as a function of scan rate are displayed in Figure 4.7. In all three cases, the modified nanoparticle electrode exhibited a clear reversible signal for the weakly bound caffeic acid (P1) with a midpoint potential of

0.16 V versus a SCE. An oxidation peak for the strongly bound caffeic acid (P2) was also observed at approximately 0.55 V versus a SCE. Interestingly, at slower scan rates the strongly bound caffeic acid was no longer detected but at higher scan rates (>0.05 Vs^{-1}) the peak became significant. This scan rate effect was linked to a configurational change (referred to as fluxionality), in which a strongly bound bi-dentate caffeic acid (see Equation 4.4) was transformed within the time scale of the voltammetric scan into a weakly bound caffeic acid (i.e., it became mono-dentate), as shown in Equation 4.5.

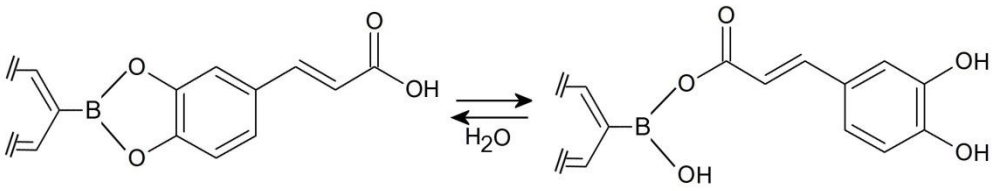

(4.5)

This process could have involved two neighbouring boronic acids on the electrode surface, for example, through a bridging transition state. The rate constant for this isomerisation could be estimated from the transition scan rate by using Equation 4.6. An additional consideration here is the release of protons during oxidation which in porous carbon aggregates could aid the configurational change.

$$v_{trans} \text{ as } k_{iso} = \frac{v_{trans}F}{RT} = \frac{0.05 \times 96487}{8.31 \times 293} = 2 \text{ s}^{-1} \quad (4.6)$$

When the peak responses for P2 were compared, only T1 and T3 showed significant signals, which suggested that the strong complex formed with T2 was either (i) energetically unfavourable or (ii) the configurational change was too rapid to be observed at this scan rate. A poor response was observed for T2, as shown in Figure 4.7(B), and therefore, only the strongly bound form for T2 was observed; the purely energetic causes were ruled out. This could be attributed to the fluxional change between the two binding modes occurring on a timescale that is too fast to be observed. Because of the structural similarities between T1, T2, and T3, the binding constant for all three cases

was assumed to be similar. The binding is assumed to be strong but with a kinetic "Achilles heel" (i.e., a fast k_{iso}), in particular for T2.

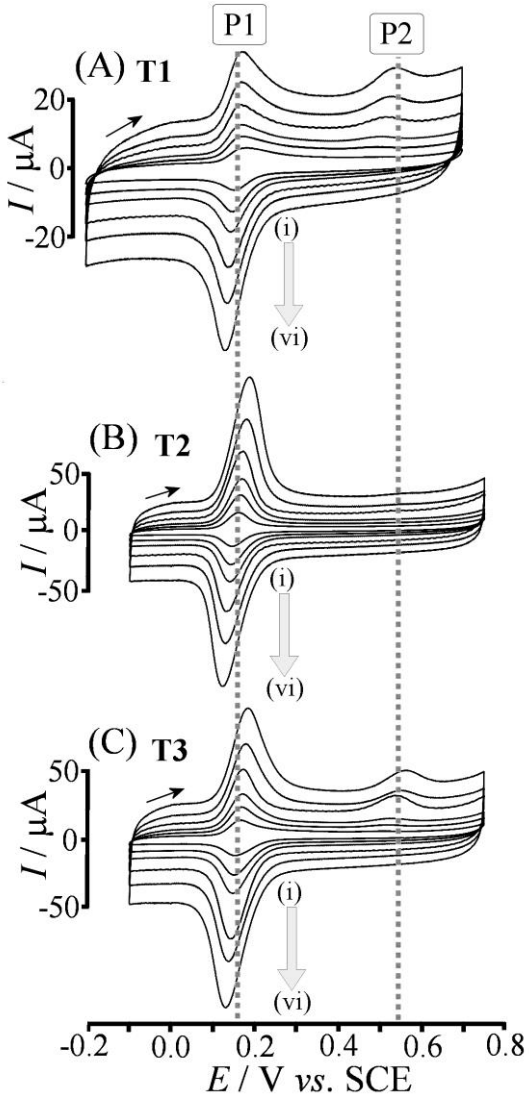

Figure 4.7. Cyclic voltammograms for 0.01 mM caffeic acid at (i) 10, (ii) 20, (iii) 30, (iv) 50, (v) 70, and (vi) 100 mVs^{-1} with 15 µg of (A) T1-modified CNPs (B) T2-modified CNPs (C) T3-modified CNPs immobilized on a graphite electrode and immersed in 0.1 M phosphate buffer at pH 7.

4.4.3 Caffeic Acid Redox Activity: Concentration Effects

The effect of caffeic acid concentration on the voltammetric responses was also investigated (see Figure 4.8). The reversible current signal (P1) increased with increasing concentrations of caffeic acid, which was indicative of a weak interaction as well as minor

contributions from either double-layer trapping or the physical trapping of caffeic acid within carbon nanoparticle aggregate pores (in this concentration range physical trapping can be assumed insignificant because of the small pore volume).

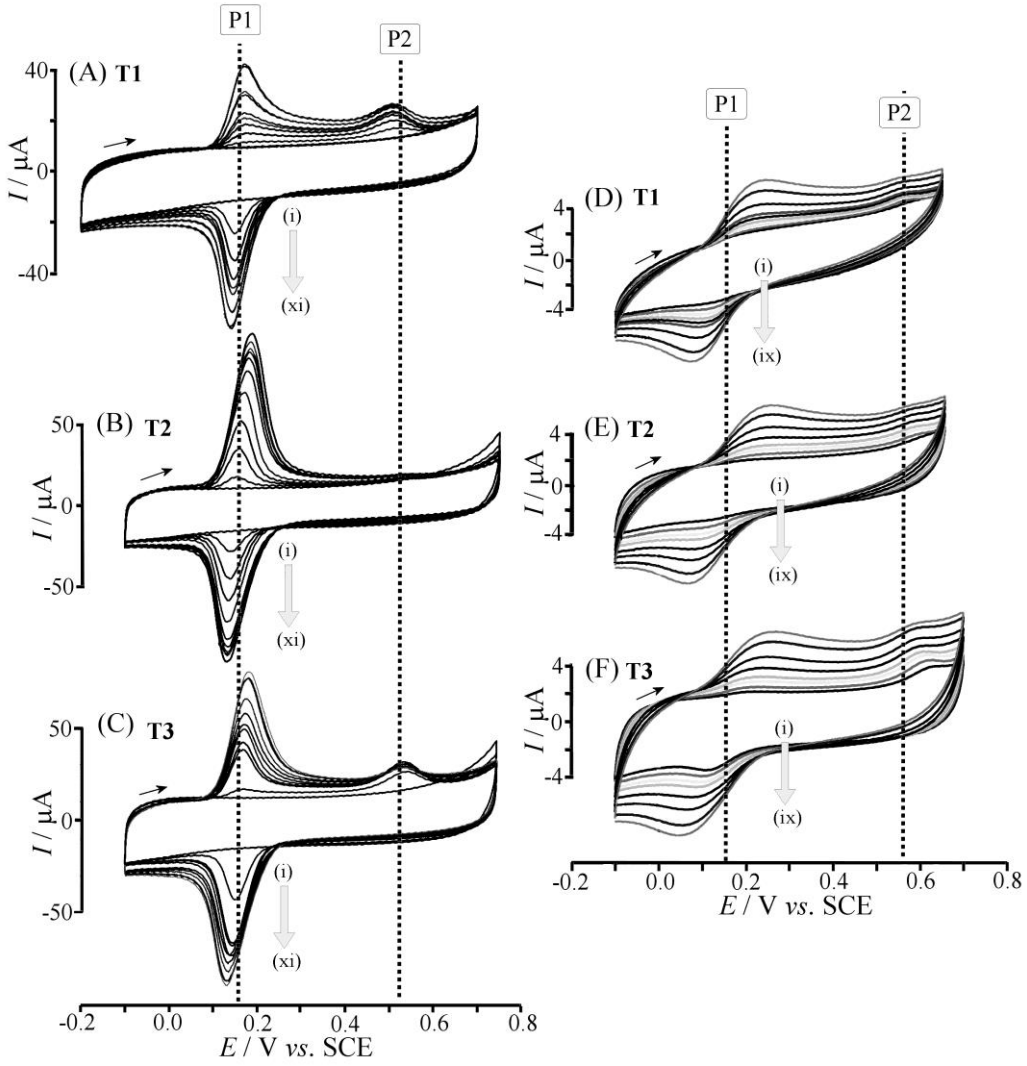

Figure 4.8. (A-C) Cyclic voltammograms (50 mV s^{-1}) with increasing caffeic acid concentration from (i) 0.0, (ii) 2.5, (iii) 5.0, (iv) 7.5 (v) 10.0, (vi)12.5, (vii) 15.0, (viii) 17.5, (ix) 20.0, (x) 22.5, to (xi) 25 μM with (A) T1-modified, (B) T2-modified, and (C) T3-modified CNPs (15 μg) deposited onto a graphite electrode. (D-F) Cyclic voltammograms (50 mV s^{-1}) with increasing caffeic acid concentration from (i) 0.5, (ii) 1.0, (iii) 1.5, (iv) 2.0 (v) 2.5, (vi) 3.0, (vii) 5.0, (viii) 8.0, to (ix) 10.0 μM with (D) T1-modified, (E) T2-modified, and (F) T3-modified graphite electrode immersed in 0.1 M phosphate buffer solution at pH 7.

Conversely, the bound caffeic acid peak (P2) for T1 and T3 increased to a maximum, which represented the point at which all of the available boronic acid moieties were

occupied. The current bridge between P1 and P2 provided further evidence of the isomerisation demonstrated in Equation 4.5.

Very similar features were observed for both the modified nanoparticle electrode [Figure 4.8(A) to (C)] and the modified graphite electrode [see Figure 4.8(D) to (F)]. However, the features of the nanoparticle aggregate peak were strongly enhanced and in particular, process P2 was more readily identified in the presence of CNPs. According to the data in Figure 4.8, the three different boronic acids do not behave in the same manner and T2 showed enhanced fluxionality and only T1 and T3 displayed prominent P2 peaks. In the case of T3, this peak emerged at low concentration (at approximately 1 μM caffeic acid), which was indicative of a Langmuirian binding constant of approximately 10^6 mol^{-1} dm^3. However, further quantitative analysis of the voltammetric data was hindered by the rapid transformation between the strongly bound and weakly bound ortho-quinols.

The analytically useful voltammetric response, P2, was observed more prominently for the pyrene-appended boronic acid T3. However, it was strongly affected by the fluxional behaviour of the boronic acid complex. A longer poly-methylene linker between pyrene and boronic acid demonstrated to be beneficial, with T3 providing the largest response for P2. However, in future this type of fluxionality could be suppressed, for example by external co-ligands or by internal N-donor atoms to intra-molecularly "lock" the boronic acid complex after it has bound to the ortho-quinol.[40]

4.5 Conclusions

The work in this chapter has shown that carbon nanoparticles provide excellent substrate materials for the self-assembly of pyrene-appended pyridinium boronic acid receptor molecules. In contrast to the poor performance of a simple graphite electrode surface (at which the predominantly suppressed solution phase electron transfer process was observed), carbon nanoparticle substrates provide optimised peak responses with high sensitivity to caffeic acid, that is, in the micro-molar range. A wide range of different pyrene-appended receptor systems could be bound to carbon nanoparticles using this methodology to provide versatile new sensor platforms.

Future studies regarding these materials could lead to improved designs of the pyrene-appended boronic acid receptors on nanoparticle electrodes. For example, N-donor functionality can be introduced to slow down the fluxional processes [31] and "lock-in" the bound ortho-quinol to provide clearer detection of P2 processes (avoiding the transformation to the weakly bound ortho-quinol seen that is observed in the process represented by P1). This investigation has clearly demonstrated the need to consider kinetic/dynamic factors in future boronic acid chemoreceptor redox sensor development.

4.6 References

1. Sanders, I.J. and T.L. Peeten, *Carbon Black: Production, Properties & Uses*, 2011, London: Nova Science Publishers Inc.
2. Lo, T.W.B., L. Aldous, and R.G. Compton, *The Use of Nano-Carbon as an Alternative to Multi-Walled Carbon Nanotubes in Modified Electrodes for Adsorptive Stripping Voltammetry*, Sens. Actuators, B, 2012, **162**, 361-368.
3. Watkins, J.D., K. Lawrence, J.E. Taylor, T.D. James, S.D. Bull, and F. Marken, *Carbon Nanoparticle Surface Electrochemistry: High-Density Covalent Immobilisation and Pore-Reactivity of 9,10-Anthraquinone,* Electroanalysis, 2011, **23**, 1320-1324.
4. Wildgoose, G.G., C.E. Banks, H.C. Leventis, and R.G. Compton, *Chemically Modified Carbon Nanotubes for Use in Electroanalysis,* Microchim. Acta, 2006, **152**, 187-214.
5. Pumera, M., *Graphene-Based Nanomaterials and their Electrochemistry*, Chem. Soc. Rev., 2010, **39**, 4146-4157.
6. Lawrence, K., J.D. Watkins, T.D. James, J.E. Taylor, S.D. Bull, G.W. Nelson, J.S. Foord, Y.-T. Long, and F. Marken, *Dioctylamine-Sulfonamide-Modified Carbon Nanoparticles as High Surface Area Substrates for Coenzyme Q10-Lipid Electrochemistry,* Electroanalysis, 2012, **24**, 1003-1010.
7. Watkins, J.D., R. Lawrence, J.E. Taylor, S.D. Bull, G.W. Nelson, J.S. Foord, D. Wolverson, L. Rassaei, N.D.M. Evans, S.A. Gascon, and F. Marken, *Carbon Nanoparticle Surface Functionalisation: Converting Negatively Charged Sulfonate to Positively Charged Sulfonamide*, Phys. Chem. Chem. Phys., 2010, **12**, 4872-4878.
8. Szot, K., J.D. Watkins, S.D. Bull, F. Marken, and M. Opallo, *Three Dimensional Film Electrode Prepared from Oppositely Charged Carbon Nanoparticles as Efficient Enzyme Host,* Electrochem. Commun., 2010, **12**, 737-739.
9. MacDonald, S.M., P.D.I. Fletcher, Z.-G. Cui, M. Opallo, J. Chen, and F. Marken, *Carbon Nanoparticle Stabilised Liquid|Liquid Micro-Interfaces for Electrochemically Driven Ion-Transfer Processes,* Electrochim. Acta, 2007, **53**, 1175-1171.
10. Szot, K., W. Nogala, J. Niedziolka-Joensson, M. Joensson-Niedziolka, F. Marken, J. Rogalski, C.N. Kirchner, G. Wittstock, and M. Opallo, *Hydrophilic Carbon Nanoparticle-Laccase Thin Film Electrode for Mediatorless Dioxygen Reduction SECM Activity Mapping and Application in Zinc-Dioxygen Battery,* Electrochim. Acta, 2009, **54**, 4620-4625.
11. Shariki, S., O.T.L. Cox, D.A. Tickell, M.P.P. Morais, J.M.H. van den Elsen, T.D. James, S.E.C. Dale, S. Bending, and F. Marken, *Coil-by-Coil Assembly of Poly Acrylamide-co-3-(methacryl-amido)-phenylboronic Acid with Polydiallyldimethyl-ammonium to Give Alizarin Red S Responsive Films,* J. Mater. Chem., 2012, **22**, 18999-19006.
12. Ibrahim, N.B., Lawrence, K., James, T.D., Xia, F., Pan, M., Mu, S., Mitchels, J.M., Marken, F.,, *Surface Dopylated Carbon Nanoparticles Sense Gas-Induced pH Changes,* Sens. Actuators, B, 2011, **161**, 184-190.
13. Nishimura, T., S.-Y. Xu, Y.-B. Jiang, J.S. Fossey, K. Sakurai, S.D. Bull, and T.D. James, *A Simple Visual Sensor with the Potential for Determining the Concentration of Fluoride in Water at Environmentally Significant Levels,* Chem. Commun., 2012, **49**, 478-80.

14. Phan, N.T.S., M. Van Der Sluys, and C.W. Jones, *On the Nature of the Active Species in Palladium Catalyzed Mizoroki-Heck and Suzuki-Miyaura Couplings - Homogeneous or Heterogeneous Catalysis, a Critical Review,* Adv. Synth. Catal., 2006, **348**, 609-679.
15. Miyaura, N., K. Yamada, and A. Suzuki, *New Stereospecific Cross-Coupling by the Palladium-Catalyzed Reaction of 1-Alkenylboranes with 1-Alkenyl or 1-Alkynyl Halides,* Tetrahedron Lett., 1979, **20**, 3437-3440.
16. Miyaura, N. and A. Suzuki, *Stereoselective Synthesis of Arylated (E)-Alkenes by the Reaction of Alk-1-enylboranes with Aryl Halides in the Presence of Palladium Catalyst,* Chem. Commun., 1979, **19**, 866-867.
17. Miyaura, N. and A. Suzuki, *Palladium-Catalyzed Cross-Coupling Reactions of Organoboron Compounds,* Chem. Rev., 1995, **95**, 2457-2483.
18. Astruc, D., *The 2010 Chemistry Nobel Prize to RF Heck, E. Negishi, and A. Suzuki for Palladium-Catalyzed Cross-Coupling Reactions,* Anal. Bioanal. Chem., 2011, **399**, 1811-1814.
19. James, T.D., M.D. Phillips, and S. Shinkai, *Boronic Acids in Saccharide Recognition,* 2006, Royal Society of Chemistry, Cambridge.
20. James, T.D., *Saccharide-Selective Boronic Acid Based Photoinduced Electron Transfer (PET) Fluorescent Sensors*, in *Creative Chemical Sensor Systems*, T. Schrader, Editor, 2007, 107-152.
21. Katif, N., R.A. Harries, A.M. Kelly, J.S. Fossey, T.D. James, and F. Marken, *Boronic Acid-Facilitated Alpha-Hydroxy-Carboxylate Anion Transfer at Liquid/Liquid Electrode Systems: the EICrev Mechanism*, J. Solid State Electrochem., 2009, **13**, 1475-1482.
22. Kubo, Y., A. Kobayashi, T. Ishida, Y. Misawa, and T.D. James, *Detection of Anions using a Fluorescent Alizarin-Phenylboronic Acid Ensemble,* Chem. Commun., 2005, **22**, 2846-2848.
23. Fossey, J.S., F. D'Hooge, J.M.H. van den Elsen, M.P.P. Morais, S.I. Pascu, S.D. Bull, F. Marken, A.T.A. Jenkins, Y.-B. Jiang, and T.D. James, *The Development of Boronic Acids as Sensors and Separation Tools,* Chem. Rec., 2012, **12**, 464-478.
24. Bull, S.D., M.G. Davidson, J.M.H. van den Elsen, J.S. Fossey, A.T.A. Jenkins, Y.-B. Jiang, Y. Kubo, F. Marken, K. Sakurai, J. Zhao, and T.D. James, *Exploiting the Reversible Covalent Bonding of Boronic Acids: Recognition, Sensing, and Assembly,* Acc. Chem. Res., 2012, **46**, 312-326.
25. Collins, A.M., J.D. Watkins, N. Katif, Y.-J. Huang, Y.-B. Jiang, T.D. James, S.D. Bull, and F. Marken, *Liquid Vertical Bar Liquid Electrochemical Bicarbonate and Carbonate Capture Facilitated by Boronic Acids,* Chem. Commun., 2011, **47**, 12002-12004.
26. Bonne, M.J., E. Galbraith, T.D. James, M.J. Wasbrough, K.J. Edler, A.T.A. Jenkins, M. Helton, A. McKee, W. Thielemans, E. Psillakis, and F. Marken, *Boronic Acid Dendrimer Receptor Modified Nanofibrillar Cellulose Membranes,* J. Mater. Chem., 2010, **20**, 588-594.
27. Huang, Y.-J., Y.-B. Jiang, J.S. Fossey, T.D. James, and F. Marken, *Assembly of N-Hexadecyl-pyridinium-4-boronic Acid Hexafluorophosphate Monolayer Films with Catechol Sensing Selectivity,* J. Mater. Chem., 2010, **20**, 8305-8310.
28. Mann, J.A., J. Rodriguez-Lopez, H.D. Abruna, and W.R. Dichtel, *Multivalent Binding Motifs for the Noncovalent Functionalization of Graphene,* J. Am. Chem. Soc., 2011, **133**, 17614-17617.

29. Zloczewska, A., M. Joensson-Niedziolka, J. Rogalski, and M. Opallo, *Vertically Aligned Carbon Nanotube Film Electrodes for Bioelectrocatalytic Dioxygen Reduction,* Electrochim. Acta, 2011, **56**, 3947-3953.
30. Ito, F., T. Kakiuchi, T. Sakano, and T. Nagamura, *Fluorescence Properties of Pyrene Derivative Aggregates Formed in Polymer Matrix Depending on Concentration*, Phys. Chem. Chem. Phys., 2010, **12**, 10923-10927.
31. Jadhav, S.A., S.R. Pujari, and S.R. Patil, *Photophysics of Exciplex Emission of Crystalline Biphenyl Doped by Pyrene,* Indian J. Pure Ap. Phys., 2000, **38**, 43-47.
32. Lekha, P.K. and E. Prasad, *Tunable Emission of Static Excimer in a Pyrene-Modified Polyamidoamine Dendrimer Aggregate through Positive Solvatochromism,* Chem.-Eur. J., 2011, **17**, 8609-8617.
33. Matsui, K. and N. Usuki, *Excimer Fluorescence of Pyrene in Sol-Gel Silica,* Bull. Chem. Soc. Jpn., 1990, **63**, 3516-3520.
34. Di Carlo, G., A. Curulli, R.G. Toro, C. Bianchini, T. De Caro, G. Padeletti, D. Zane, and G.M. Ingo, *Green Synthesis of Gold-Chitosan Nanocomposites for Caffeic Acid Sensing,* Langmuir, 2012, **28**, 5471-5479.
35. Hotta, H., M. Ueda, S. Nagano, Y. Tsujino, J. Koyama, and T. Osakai, *Mechanistic Study of the Oxidation of Caffeic Acid by Digital Simulation of Cyclic Voltammograms,* Anal. Biochem., 2002, **303**, 66-72.
36. Pizer, R. and L. Babcock, *Mechanism of Complexation of Boron Acids with Catechol and Substituted Catechols,* Inorg. Chem., 1977, **16**, 1677-1681.
37. Hapiot, P., A. Neudeck, J. Pinson, H. Fulcrand, P. Neta, and C. Rolando, *Oxidation of Caffeic Acid and Related Hydroxycinnamic Acids,* J. Electroanal. Chem., 1996, **405**, 169-176.
38. Scholtz, F., *Electroanalytical Methods*, 2002, Springer, Berlin, 64.
39. Giacomelli, C., K. Ckless, D. Galato, F.S. Miranda, and A. Spinelli, *Electrochemistry of Caffeic Acid Aqueous Solutions with pH 2.0 to 8.5,* J. Braz. Chem. Soc., 2002, **13**, 332-338.
40. Nishiyabu, R., Y. Kubo, T.D. James, and J.S. Fossey, *Boronic Acid Building Blocks: Tools for Sensing and Separation,* Chem. Commun., 2011, **47**, 1106-1123.

Chapter 5

Dioctylamine Functionalised Carbon Nanoparticles as Substrates for Electrochemical Analysis in Lipids

Contents

Thanks to Geoffrey Nelson and John Foord for help with XPS.

This work has been published in Electroanalysis; DOI: 10.1002/elan.201200121

K. Lawrence, J. D. Watkins, T. D. James, J. E. Taylor, S. D. Bull, G. W. Nelson, J. S. Foord, Y. T. Long and F. Marken, Electroanalysis, ***2012**, 24,* 1003-1010.

5.1 Abstract

Sulfonic acid modified carbon nanoparticles (CNPs) that have a diameter in the range of approximately 9-18 nm are functionalised to produce CNPs that are furnished with dioctylaminesulfonamide moieties on the surface. These modified CNPs are characterised and employed as high surface area substrates to study coenzyme Q_{10} and 1,2-dimyristoyl-*sn*-glycero-3-phosphocholine-Q_{10} (DMPC-Q_{10}) redox processes. The modified CNPs provide a highly hydrophobic carbon substrate with a specific capacitance of approximately 25 F g^{-1} when no redox system has been added to the system. When coenzyme Q_{10} or DMPC-Q_{10} are immobilised onto the CNPs, the capacitance is lowered and therefore, results in well-defined voltammetric responses. Coenzyme Q_{10} is reduced and oxidised back in a pH-dependent process that displays a switch in mechanism at approximately pH 7. The DMPC-Q_{10} deposit shows very similar characteristics to those of pure coenzyme Q_{10}, but with improved reproducibility and greater sensitivity. Both redox systems, coenzyme Q_{10} and DMPC-Q_{10}, are found to be sensitive to Na^+ concentration in the electrolyte and the mechanistic implications of this are discussed in this chapter.

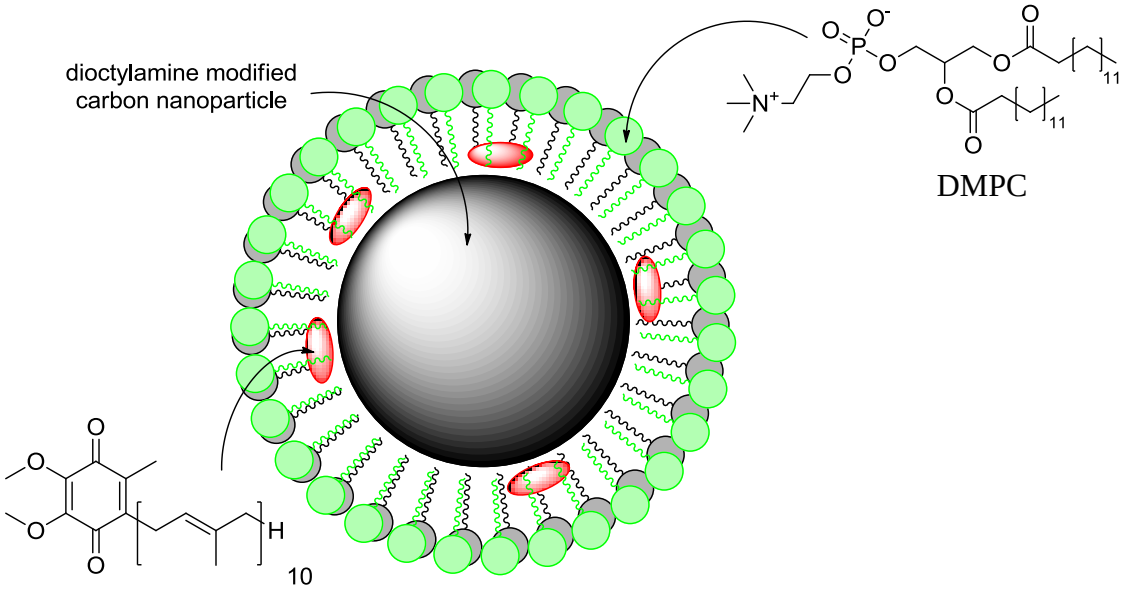

5.2 Introduction

Carbon supports are ubiquitous in electrochemistry and are often important in technical processes such as those in fuel cells and energy storage[1] or in sensors.[2] Many new types of carbon materials and nanocarbons have been developed[3] and surface functionalisation methods through diazonium chemistry,[4] electrochemical functionalisation,[5] plasma reactions,[6] or silanisation procedures[7] have been exploited for improved selectivity and reactivity. CNPs with sulfonic acid functionalisation are in large scale industrial use (e.g. as colorants; Emperor 2000, Cabot Corporation) and these particles have recently been exploited in electroanalysis[8] and for further surface functionalisation.[9] It has been demonstrated that it is possible to combine negatively charged sulfonate-modified particles (Emperor 2000) with positively charged sulfonamide-modified CNPs to give novel nanostructured carbon film materials for applications in bio-electrochemical processes.[10] The amine functionalisation route allowed redox systems such as anthraquinone to be covalently linked[11] and protein coupling chemistry to be applied to produce dopamine-functionalised CNPs.[12] Herein CNPs are hydrophobised by introducing dioctylamine-sulfonamide surface functionality.

Lipophilic redox systems are of great importance, in particular for biological membrane processes. Coenzyme Q_{10} is an essential redox mediator in the mitochondrial electron transfer chain.[13] The reduced form of coenzyme Q_{10}, ubiquinol 10, is a free radical scavenger that can prevent oxidative damage to cell membranes and minimize oxidative stress by forming ubiquinone 10, the oxidised form of coenzyme Q_{10}.[14] Although coenzyme Q_{10} is ubiquitous in the human body, the ratio of ubiquinol to ubiquinone can be used as a redox marker for certain diseases, which can be found in the blood circulation.[15] For example, low ubiquinol/ubiquinone ratios have been linked to people with liver disease,[16] neurodegenerative disease,[17-19] and coronary artery diseases.[20] The total amount of coenzyme Q_{10} varies from person to person and one report stated that children and young adults typically have low levels of coenzyme Q_{10} in their blood compared to adults, whereas this amount decreases again in the elderly.[21] Therefore, the ratio is a better indicator for disease, rather than the absolute value.

The electrochemistry of coenzyme Q_{10} immobilised on glassy carbon,[22] gold,[23] and mercury electrodes has been extensively studied.[24-26] Over a pH range of 2 to 12 the reduction of coenzyme Q_{10} involves a two-electron two-proton conversion to ubiquinol (see Equation 5.1).[27] Therefore, the corresponding standard potential is pH as well as environment (lipid) dependent.

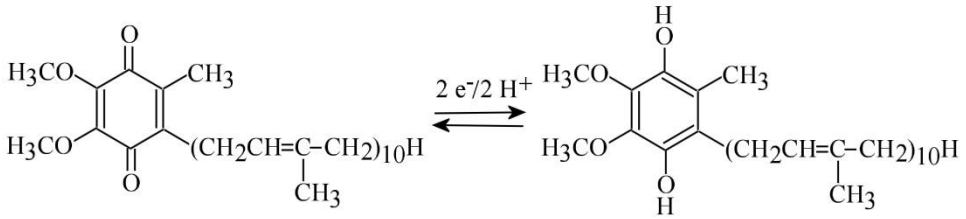

(5.1)

Gordillo and Schiffrin[27] carefully analysed the redox processes of coenzyme Q_{10} adsorbed onto mercury and compared the findings with redox processes for coenzyme Q_{10} in a dioleyl phosphatidyl choline lipid film on mercury. During this study, four pH zones were identified, which displayed distinct mechanistic features. For pH values greater than 14, a reduction process occurred through a reversible two-electron pathway without protonation. For pH values between 14 and 12 irreversibility of electron transfer was observed, which was linked to the ubiquinol dianion protonation step. At a pH value of approximately 9.2 an increased level of irreversibility in electron transfer was observed, which Gordillo and Schiffrin proposed to be associated with a second proton transfer step forming the neutral product, as indicated in Equation 5.1. Under acidic pH conditions a bifurcation in mechanism was evident, this was demonstrated by the presence of two pairs of voltammetric peaks; therefore, additional disproportionation pathways were proposed. In addition to the mechanistic changes, very wide peak-to-peak separations were observed at pH values less than 7.[27]

The complexity of the overall reaction mechanism for coenzyme Q_{10} reduction is associated with acid-base equilibria for the semi-ubiquinol (pK_1 = 5.5 to 7) and for the ubiquinol (pK_1 = 12 and pK_2 13.6).[27] In previous studies coenzyme Q_{10} was investigated at planar electrodes and, for example when studied using mercury

electrodes, coenzyme Q_{10} was proposed to be fully embedded into the lipid film on the electrode, which occurred through surface adsorption.

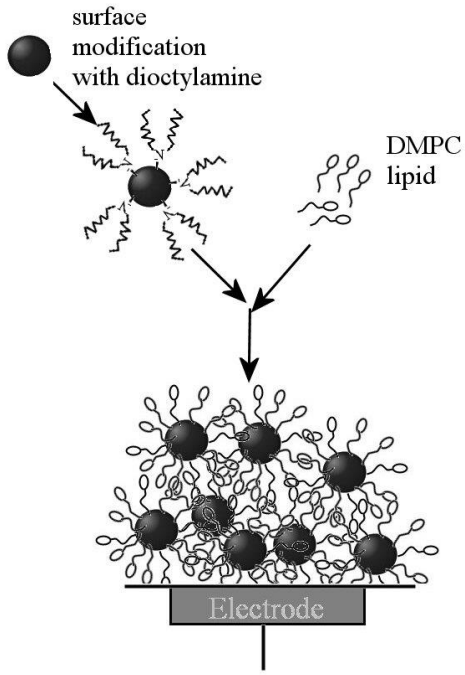

Figure 5.1 - Schematic drawing of hydrophobic CNPs, prepared via dioctylamine (DOA) surface functionalisation, assembled with lipid into a modified electrode with electroactive nanocomposite film.

In this study, coenzyme Q_{10} redox processes were investigated on a substrate of dioctylamine-sulfonamide functionalised CNPs. Under these conditions, that is, a highly curved lipid film, the coenzyme Q_{10} molecules (which have a molecular length of approximately 5 nm) were likely to be in a highly disordered arrangement. Because of the high intrinsic surface area (see Figure 5.1), the use of hydrophobic particles resulted in the enhancement of voltammetric signals and the coverage-dependent processes were able to be resolved. The ability of the hydrophobic CNPs to support a lipid film for the study of prototype membrane redox processes was explored (see Figure 5.1). Coenzyme Q_{10} and DMPC were co-deposited to form a composite film, and the Q_{10}-DMPC membrane redox processes were compared with the processes observed for pure coenzyme Q_{10} on bare CNP substrate. In these experiments DMPC lipid could have been present by adsorbing onto the hydrophobic CNPs or as a disordered gel-phase that was approaching gel-fluid transition point, T_m = 23.8 ^oC.[28, 29] Compared to

traditional lipid film voltammetry experiments pioneered by Tien,[30] the molecular film structure formed in these experiments was more disordered. However, the methodology developed in this study could be of wider use for the investigation of lipid film electroanalysis, transitions, and reactivity.

5.3 Experimental Section

5.3.1 Reagents

Emperor 2000 sulfonate-derivatised CNPs used as the starting material were obtained from Cabot Corporation. Other reagents were used without further purification: ortho-phosphoric acid (Fisher Scientific), dichloromethane (Fisher Scientific, reagent grade), acetonitrile (Fisher Scientific, HPLC grade), potassium carbonate (Aldrich 99+%, ACS reagent), sodium hydroxide (Aldrich, Sigma ultra, 98%). Demineralised and filtered water was taken from a Thermo Scientific water purification system (Barnstead Nanopure) with approximately 18.2 MΩ cm resistivity.

5.3.2 Instrumentation

For all voltammetric studies a microAutolab III potentiostat system (EcoChemie, Netherlands) was used with a Pt wire counter electrode and a KCl-saturated Calomel (SCE) reference electrode (Radiometer, Copenhagen). A 3 mm diameter glassy carbon electrode (BAS Inc.) served as the working electrode. X-ray photoelectron spectroscopy (XPS) was conducted by using a home-built system containing a hemispherical analyser (VSW Ltd.), and the samples were excited by using a monochromatic Al Kα X-ray source at 1486.6 eV. Spectra were background corrected using a Shirley background scan and peak fitting was conducted using the XPSPEAK (version 4.1) software package. Peak areas were normalised using the atomic sensitivity factors.[31] The adventitious C1s photoelectron peak (285.0 eV) was used to calibrate the XPS peak positions The temperature was $22 \pm 2\ ^{o}C$.

5.3.3 Procedure for Surface Modification of Carbon Nanoparticles

(A) Emperor 2000 CNPs (1 g) were added to dry dichloromethane (50 mL) in a 250 mL round bottom flask, before being placed in an ultrasonic bath for 30 minutes. The flask was then placed in an ice bath and cooled to 0 ºC while being degassed with N_2, before thionyl chloride (10 mL) was added drop-wise, see Scheme 1. The resulting suspension was stirred for 2-3 hours until the flask reached room temperature. The excess solvent was removed by distillation to obtain a dry black powder.

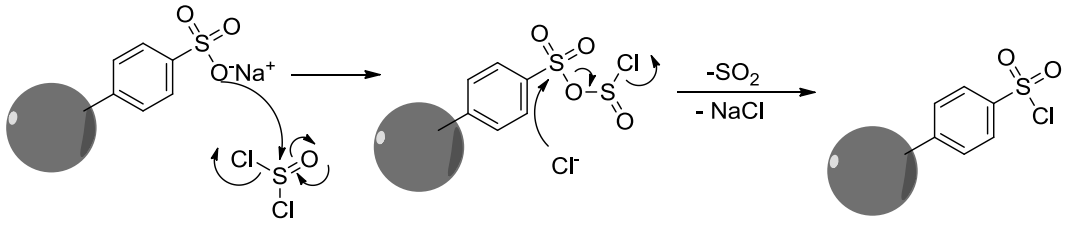

Scheme 1. The reaction of the Emperor 2000 carbon nanoparticles with thionyl chloride.

(B) Dioctylamine (DOA, 10 mL) was added to a clean 250 mL round bottom flask containing dry dichloromethane (30 mL) and cooled to 0 ºC by using an ice bath. The chlorinated nanoparticles from (A) were added portion-wise over a 1 hour period under continued stirring, see Scheme 2. Once all of the chlorinated nanoparticles from (A) were added the reaction was stirred for a further 2-3 hours while allowing it to reach room temperature. Excess dichloromethane were removed by distillation to obtain a thick, black oil. After washing with ethanol, 1 M HCl (5 mL) was added with distilled water (100 mL) to yield a black solid. The product was collected by Büchner filtration and carefully washed with 1 M HCl and water before drying in an 80 ºC oven.

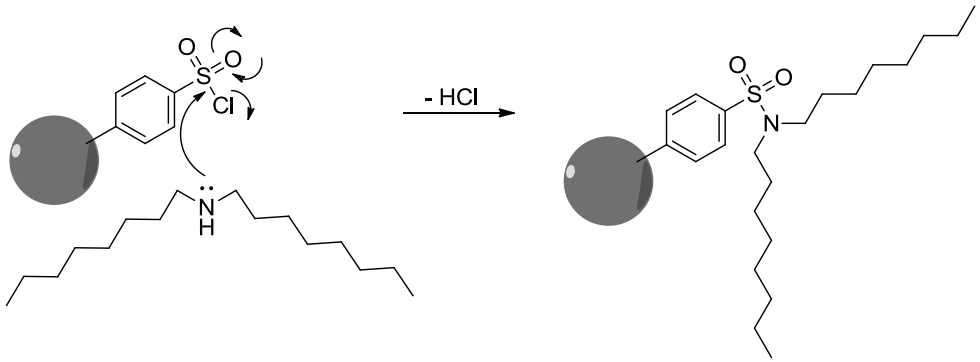

Scheme 2. Reaction between dioctylamine and the chlorinated carbon nanoparticles.

5.3.4 XPS Surface Characterisation

Powder samples of dioctylamine-sulfonamide functionalised CNPs were analysed by XPS to identify any surface compositional changes, with respect to the Emperor 2000 starting material. In a survey scan [see Figure 5.2(A)] prominent signals for carbon and oxygen were identified in addition to weaker signals for sulfur and nitrogen.

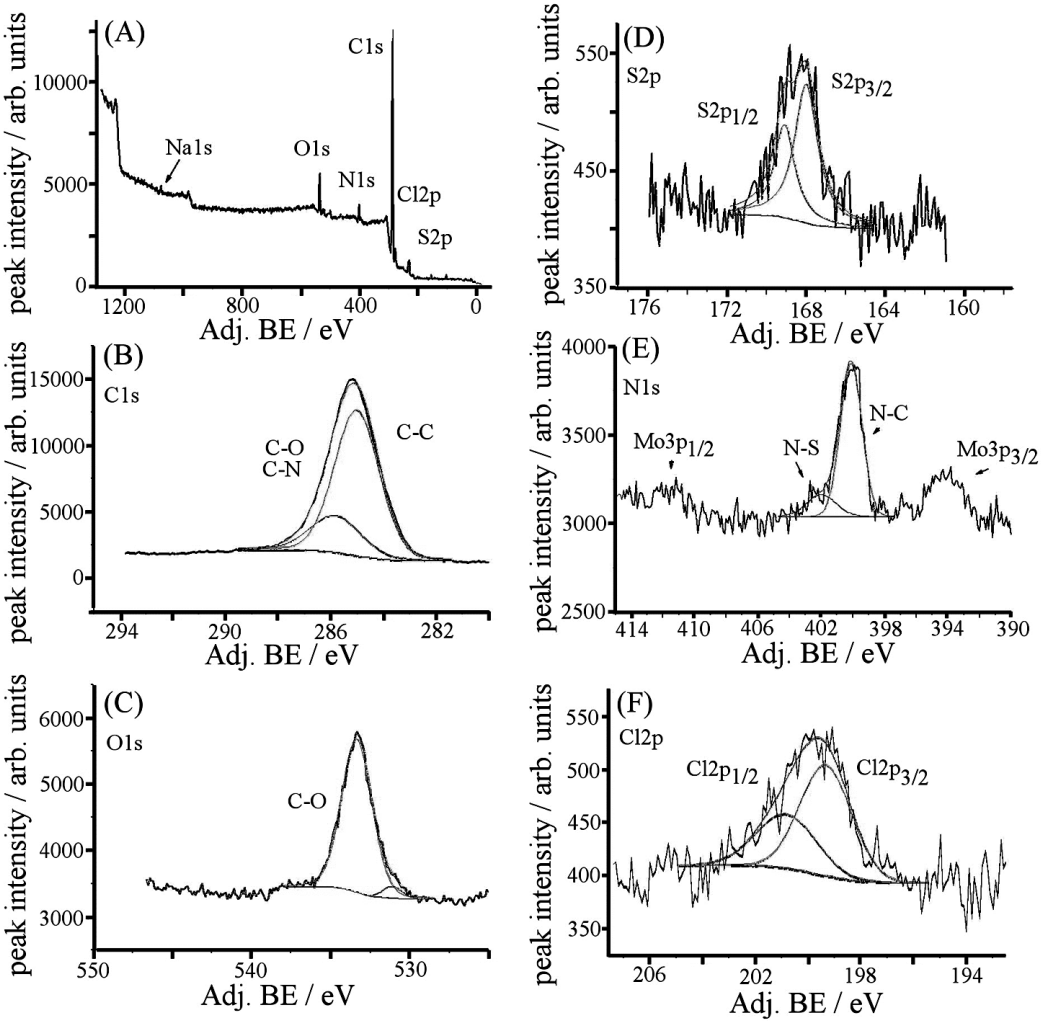

Figure 5.2 - XPS data for dioctylamine-sulfonamide functionalised CNP powder (NaOH washed): (A) survey scan, (B) carbon C1s data, (C) oxygen O1s data, (D) sulfur S2p data, (E) nitrogen N1s data (Mo from sample holder), and (F) chlorine Cl2p data. Binding energies were adjusted to C1s = 285.0 eV.

Two samples were investigated, which were washed with either aqueous 0.1 M NaOH or 0.1 M HCl. The obtained surface compositional data were very similar both samples contained low level chlorine. The presence of chlorine in the alkaline-washed sample is

likely to be caused by residual from the thionyl chloride reaction. There was no evidence for protonated amine functionalities, that is, no enhancement of the chlorine/chloride signals was observed. Low level sodium [see Figure 5.2(A)] was observed after washing with NaOH, which could be attributed to ionic interactions with remaining carboxylate functional groups.

The most interesting graph, the N1s spectra [Figure 5.2(E)], is well-resolved with a prominent N-C peak and a shoulder at higher binding energy (BE), which could be assigned to N-S bonding. The width and intensity of the peaks assigned to N-C and N-S suggest that there was a wide range of N1s chemical environments in this sample. The estimated ratio of S:N of approximately 0.25 suggests the presence of additional DOA moieties that could be attached to the carboxylate groups. The C1s spectra [Figure 5.2(B)] also show interesting features. It is clear that a wide variety of C1s chemical environments were present in the sample. It is likely that the peaks represent, from lowest to highest binding energy: C-C (285 eV), C-O, C-S/C-N, and C=O. The O1s spectra indicate the presence of other O1s chemical environments in addition to the C-O environment. The additional peaks can be attributed to C=O and O=S. The estimated errors for the peak positions were calculated to be approximately ± 0.25 eV.

$$\frac{Peak\ Area}{Atomic\ Sensitivity\ Factor\ x\ Transmission\ Function} = Normalized\ Peak\ Area \qquad (5.2)$$

The XPS elemental ratios can be calculated by using Equation 5.2. This allowed the direct comparison of these ratios, as shown in Table 5.1. The XPS peak area ratios were corrected by using the atomic sensitivity factors.[21]

Table 5.1. Summary of most important elemental ratios from XPS data for dioctylamine-sulfonamide functionalised CNPs washed with 0.1 M HCl (Sample 1) or 0.1 M NaOH (Sample 2). Calculated errors are approximately 10-15%.

	Wash	**O1s/C1s**	**S2p/C1s**	**N1s/C1s**	**S2p/O1s**	**S2p/N1s**	**Cl2p/C1s**
Sample 1	HCl	0.065	0.007	0.02	0.11	0.30	0.004
Sample 2	NaOH	0.074	0.006	0.03	0.08	0.19	0.004

The XPS data confirms that the dioctylamine-sulfonamide surface functional groups were present. They also demonstrate that the effect of pre-treatment with aqueous HCl or NaOH is insignificant, which is consistent for this type of functionality.

5.3.5 Electrode Preparation

The working electrodes were prepared by depositing 5 μL of a sonicated toluene solution (containing 3 mg mL^{-1} dioctylamine-functionalised CNPs, for DMPC-Q_{10} studies this solution also contained 3.4 mg mL^{-1} DMPC in toluene) onto a 3 mm diameter glassy carbon electrode. After evaporation of the toluene, the deposited film consisted of 15 μg hydrophobic CNPs, 1 nmol coenzyme Q_{10}, and 25 nmol DMPC lipid. The ratio of components was varied as required throughout the study, as detailed.

5.4 Results and Discussion

5.4.1 Voltammetric Characterisation of Hydrophobic CNPs

The presence of DOA that was predominantly bound as sulfonamide to the CNP surface caused deposits on the electrode surfaces to be strongly adhered and water-insoluble (hydrophobic) in contrast to the more hydrophilic sulfonate-furnished CNP starting material (Emperor 2000). The deposits at glassy carbon electrode surfaces were formed readily by depositing through solvent evaporation from a toluene suspension, this allowed the deposited films to be studied by using cyclic voltammetry (CV). Figure 5.3(A) shows typical voltammetric responses obtained for (i) 15 μg hydrophobic CNPs, (ii) 1 nmol coenzyme Q_{10}, and (iii) a combination of both coenzyme Q_{10} and 15 μg particles deposited onto a 3 mm glassy carbon electrode, which was immersed into aqueous 0.5 M phosphate buffer solution (PBS) at pH 7.

$$C = \frac{I_{capacitance}}{scan\,rate} = \frac{4\times10^{-6}A}{0.01} = 400\ \mu F \qquad (5.3)$$

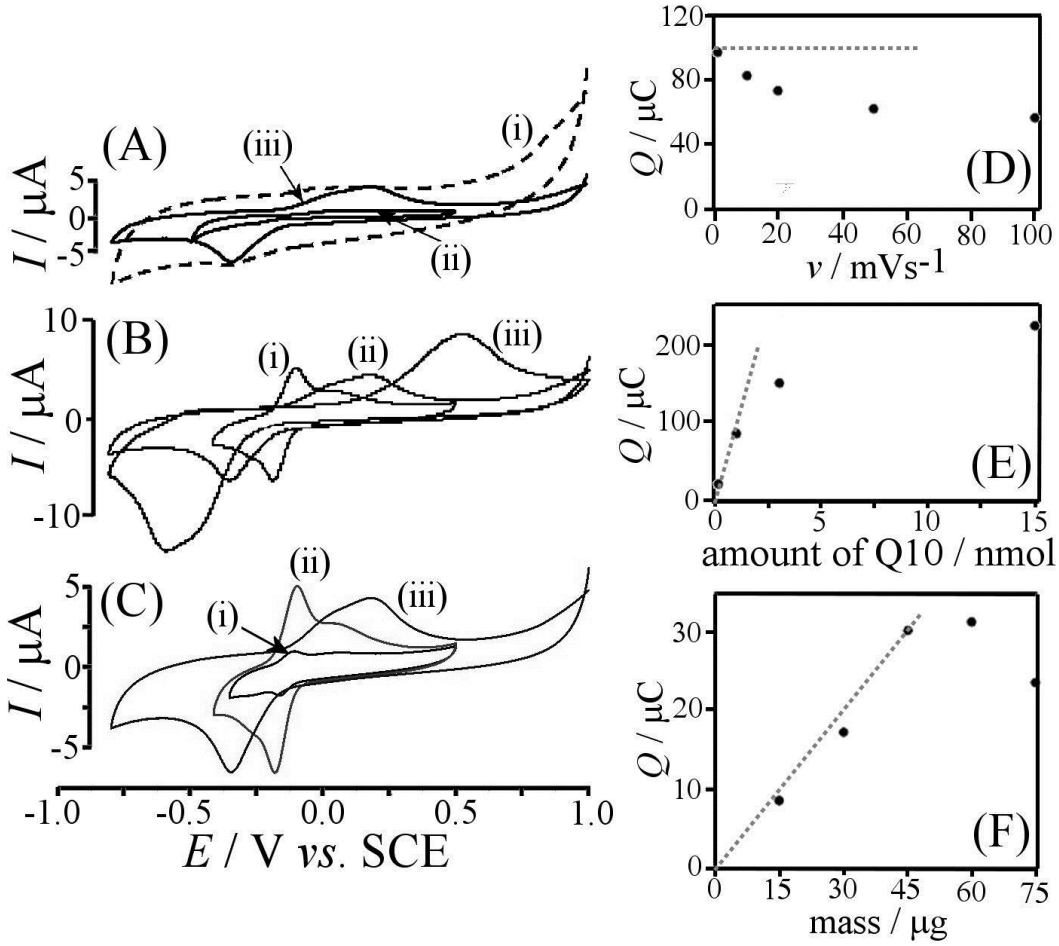

Figure 5.3 - (A) CVs (scan rate 10 mVs^{-1}) for (i) 15 µg hydrophobic CNPs, (ii) 3 nmol Q_{10}, and (iii) 3 nmol Q_{10} with 15 µg hydrophobic CNPs; deposited onto a glassy carbon electrode and immersed in 0.5 M PBS at pH 7. (B) CVs for (i) 1 nmol, (ii) 3 nmol, and (iii) 15 nmol Q_{10} with 15 µg hydrophobic CNPs deposited onto a glassy carbon electrode. (C) CVs for (i) 0.1 nmol, (ii) 1 nmol, and (iii) 3 nmol Q_{10} with 15 µg hydrophobic CNPs deposited onto a glassy carbon electrode. (D) Plot of anodic peak charge against scan rate. (E) Plot of the anodic peak charge against coverage of Q_{10} in nmol, at a constant 15 µg carbon loading. (F) Plot of the anodic peak charge for 0.1 nmol Q_{10} versus hydrophobic CNP mass. The dashed line is indicating the one-electron transfer mechanism.

The hydrophobic CNPs affected the capacitive background current of the electrode by approximately 25 F g^{-1} (400 µF for 15 µg CNPs), calculated by using Equation 5.3. However, the modified CNPs did not contribute to the electrochemical current response. Coenzyme Q_{10} immobilised onto bare glassy carbon electrodes displayed a reduction and back-oxidation peak response centred at E_{mid} (= ½ $E_{p,ox}$ + ½ $E_{p,red}$) = -0.15 V versus a SCE, as expected for the overall two-electron two-proton reduction (see Equation 5.1).[26] However, when immobilised onto the hydrophobic CNPs, a considerably enhanced current response was observed for coenzyme Q_{10} [Figure 5.3A(iii)] with a charge under the reduction peak of approximately 80 µC, corresponding to almost one

electron per coenzyme Q_{10} molecule that was immobilised at the electrode surface. The reason for this deviation from the anticipated two-electron characteristics could be because of the solid state nature of the coenzyme Q_{10} deposit or some trapping of coenzyme Q_{10} within the carbon aggregates, thus making it inaccessible to the electrolyte.

The capacitive background current was affected by the presence of coenzyme Q_{10}, this was likely because of the hydrophobic nature of coenzyme Q_{10} [compare Figure 5.3A(i) and (iii)]. Experiments conducted with different amounts of coenzyme Q_{10} co-deposited with hydrophobic CNPs onto glassy carbon electrodes demonstrated a considerable change in the peak-to-peak separation. Figure 5.3(B) and (C) show data for 0.1, 1, 3, and 15 nmol coenzyme $Q_{10,}$ the voltammetric responses all centred around E_{mid} = -0.15 V versus a SCE. However, the peak-to-peak separation changes from approximately 55 mV for 0.1 nmol coverage to approximately 1 V for 15 nmol coverage, and two distinct pairs of peaks were observed at lower coverage. The charge under the peak (cathodic or anodic) converged to approximately that expected for a one-electron reduction. Additional experiments conducted with a fixed ratio of coenzyme Q_{10} to hydrophobic CNPs [see Figure 5.3(F)] revealed a similar trend with convergence to a charge of approximately one electron per coenzyme Q_{10} molecule at the electrode surface (dashed line). With more than 50 μg hydrophobic CNPs immobilised, the voltammetric peaks became poorly resolved from the background capacitive response. It is possible that under these conditions and at pH 7 the first one electron reduction was fast with the second electron transfer kinetically slow because of a coupled protonation; therefore, resulting in poorly resolved voltammograms. Schiffrin suggested the importance of disproportionation processes that lead to such bifurcation and appearance of a second pair of peaks.[27] A further interpretation of this phenomenon could be the involvement of Na^+ cations which can lead to additional redox peaks for solid state redox conversions.[32, 33]

The effects of pH on the voltammetric responses for coenzyme Q_{10} reduction were investigated. Figure 5.4(A) shows typical voltammetric responses for 1 nmol coenzyme Q_{10} immobilised with 15 μg hydrophobic CNPs at (i) pH 12, (ii) pH 7, and (iii) pH 2. Both a systematic shift in midpoint potential and a pH-dependent change in peak-to-peak separation were observed. This shift in midpoint potential is consistent with a

Nernstian shift of approximately 60 mV per pH unit for a two-electron two-proton process, as previously observed and described by Schiffrin and co-workers.[27] Only at highly alkaline pH, that is, pH values greater than 12, do changes in the mechanism occur from two-electron two-proton to two-electron one-proton and finally to a two-electron process.[27] A significant deviation was observed at pH 7, which was caused by the presence of two distinct pairs of peaks that resulted in a distortion of the data [see Figure 5.4A(ii)]. Overall, the shift in midpoint potential and the change in peak-to-peak separation are consistent with previous literature reports.

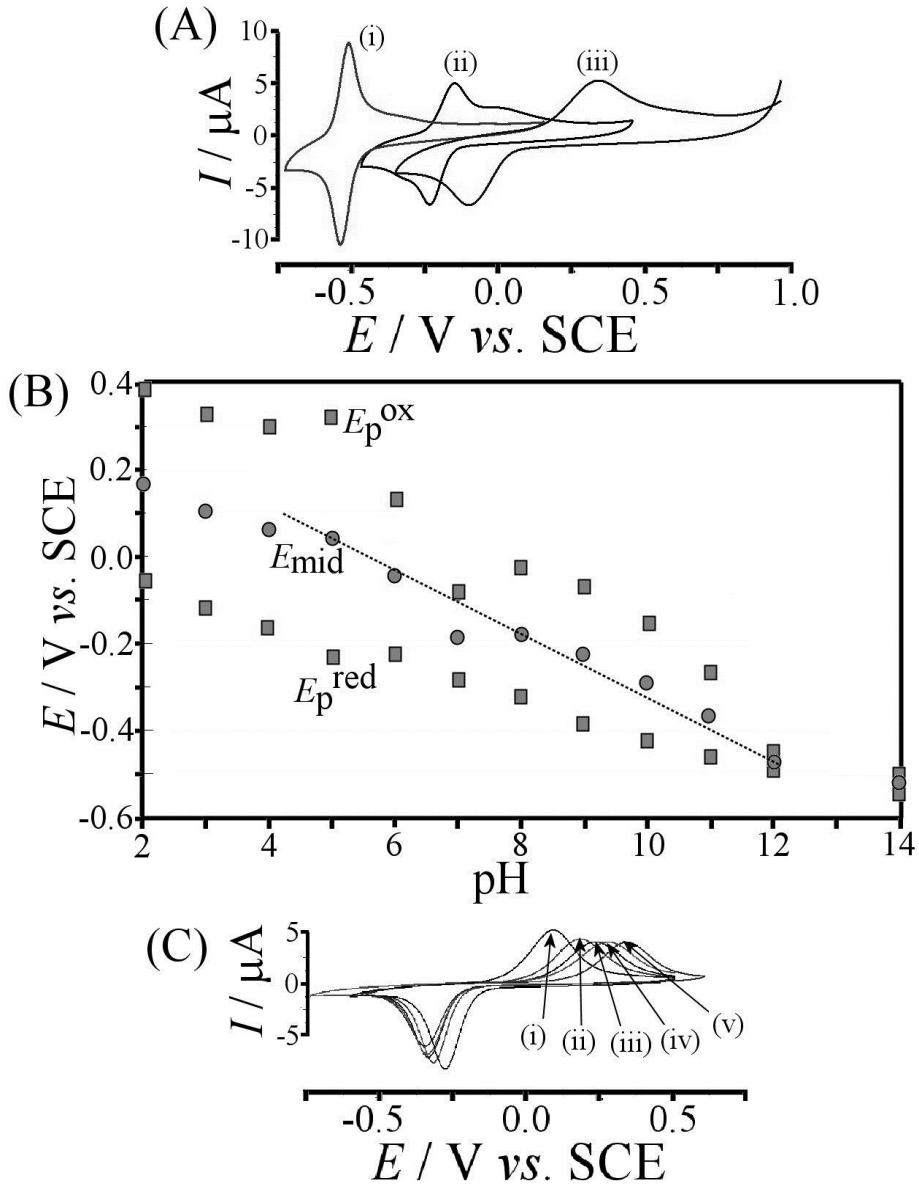

Figure 5.4 - (A) CVs (scan rate 10 mVs^{-1}) for the reduction and back-oxidation of 1 nmol Q_{10} in 15 μg CNP immobilised at a glassy carbon electrode and immersed in aqueous 0.5 M PBS at pH (i) 12, (ii) 7, and (iii) 2. (B) Plot of peak potentials $E_{p,ox}$ and $E_{p,red}$ and the midpoint potential E_{mid} (= ½ $E_{p,ox}$ + ½ $E_{p,red}$) versus pH. (C) CVs (scan rate 10 mVs^{-1}) for the reduction and back-oxidation of 1 nmol Q_{10} on 15 μg CNP immobilised at a glassy carbon electrode and immersed in aqueous 0.5 M PBS at pH 7 with (i) 0, (ii) 0.5, (iii) 1.0, (iv) 2.0, and (v) 5.0 M NaCl added.

Recent literature has suggested the importance of cation effects in addition to the effect of pH on the voltammetric responses for coenzyme Q_{10} reduction. The binding of Ca^{2+} to coenzyme Q_{10} derivatives has been proposed in a previous investigation.[34] Figure 5.4(C) shows a set of voltammograms recorded for the reduction of 1 nmol coenzyme Q_{10} as a function of Na^+ concentration. The cathodic peak was only weakly affected, whereas the anodic peak was shifted significantly as the concentration of NaCl was increased. This result implies an involvement of Na^+ in the mechanism at pH 7. The ubiquinol could be interacting with Na^+ in the aqueous phase that resulted in a decrease in the rate of electron transfer (vide infra).

5.4.2 Voltammetric Characterisation of CNPs with DMPC Lipid

The hydrophobic dioctylamine furnished CNPs have been demonstrated to be useful as carriers for hydrophobic redox systems such as coenzyme Q_{10}, but also as a nanostructured substrate for lipid films. Herein, it is demonstrated that DMPC, a neutral lipid, could be used in conjunction with coenzyme Q_{10}. 25 nmol DMPC per 15 μg was selected to give approximately a mono-layer coverage of the modified CNPs (based on an estimate of 2000 DMPC molecules per nanoparticle assuming an approximate diameter of 10 nm). Figure 5.5(A) shows typical CVs that were obtained with 0.1 nmol coenzyme Q_{10}. The capacitive background current observed in these experiments (approximately 8 μF) was considerably lower compared with that of 15 μg hydrophobic CNPs without lipid (approximately 400 μF, vide supra). The capacitance was reduced for the lipid-coated nanoparticle electrode surface. As DMPC was added to the surface of the electrode it was likely blocking some of the active surface sites, leading to a decrease in the active surface area. This decrease in capacitance is expected because the capacitance (C) is proportional to the active area of the electrode (A), see Equation 5.4 (where ε_r is the dielectric constant, ε_0 is the permittivity constant, and d is the distance between the electroactive surface and the electrolyte).

$$C = \varepsilon_r \varepsilon_0 \frac{A}{d} \tag{5.4}$$

For coenzyme Q_{10} co-deposited with DMPC, well-defined reduction and back-oxidation peak responses were observed [see Figure 5.5(A)]. The charge under the peak was approximately 4 μC and independent of the scan rate, whereas a charge of approximately 20 μC is expected for a two-electron process. The less than complete electrolysis could be attributed to coenzyme Q_{10} being concealed within CNP aggregates (coenzyme Q_{10} diffusion is likely to be extremely slow below the gel-fluid transition point).[28]

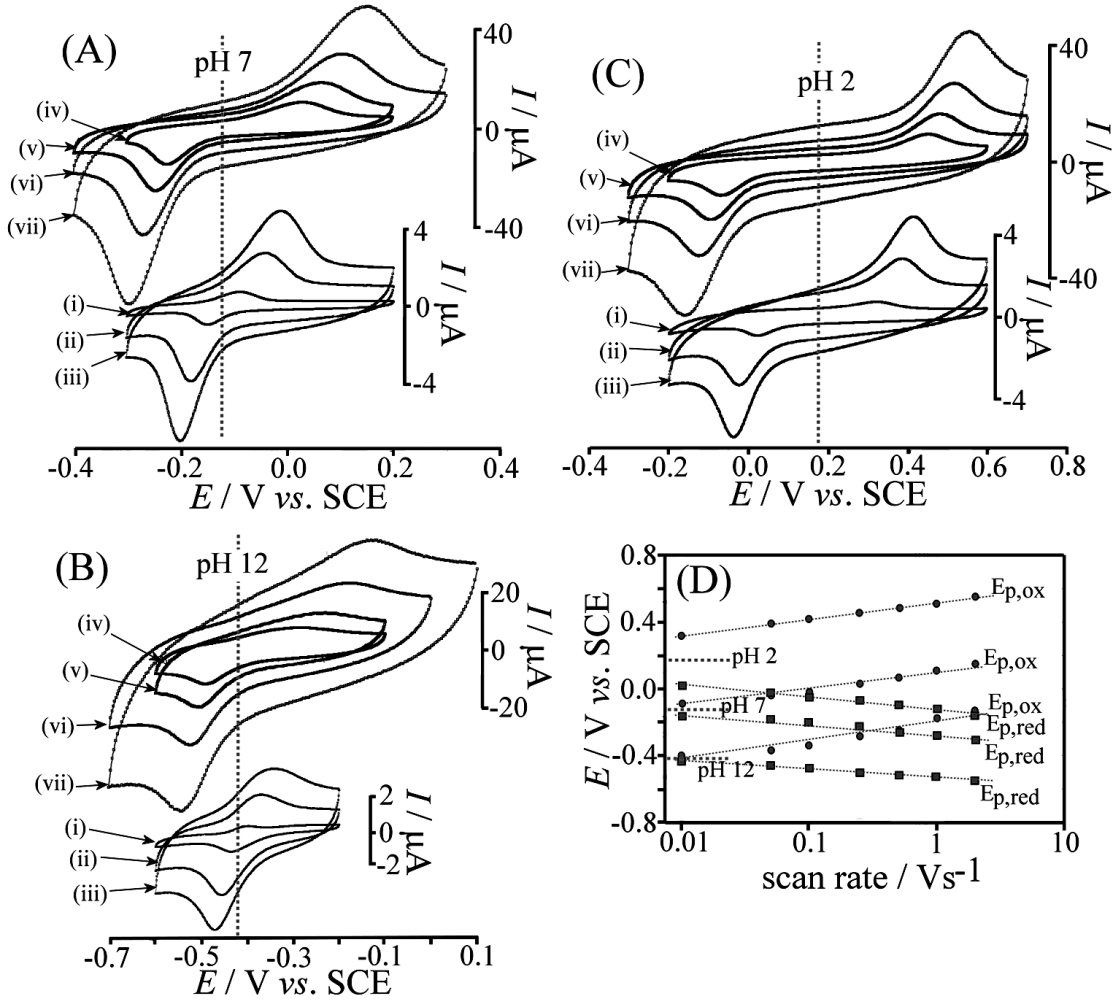

Figure 5.5 - (A) CVs (scan rate (i) 0.01, (ii) 0.05, (iii) 0.1, (iv) 0.25, (v) 0.5, (vi) 1.0, and (vii) 2.0 Vs^{-1}) for the reduction and back-oxidation of 0.1 nmol Q_{10} in 25 nmol DMPC/15 μg CNP immobilised at a glassy carbon electrode and immersed in aqueous 0.5 M PBS at pH 7. (B) As above at pH 12. (C) As above at pH 2. (D) Plot of the peak potentials for oxidation and reduction as a function of scan rate.

The peak positions of the coenzyme Q_{10} reduction and back-oxidation were shifted almost linearly with the logarithm of the scan rate [see Figure 5.5(D)], this is consistent

with the expected electron transfer kinetic effects of this system. When the DMPC-Q_{10} films were investigated as a function of electrolyte solution pH, a characteristic shift in midpoint potential and a widening of the peak-to-peak separation in more acidic media were observed, consistent with the data obtained in the absence of lipid. A summary of the pH effects on the voltammetric currents are shown in Figure 5.6(A) and (B). A shift of approximately 60 mV per pH unit in the E_{mid} value is consistent with that expected for a two-electron two-proton reduction and is in agreement with literature reports studying coenzyme Q_{10}.[27] The E_{mid} plot in Figure 5.6(B), in the presence of DMPC, is almost identical to that in Figure 5.4(B), without DMPC; however, in the absence of DMPC a more complex voltammetric behaviour is observed.

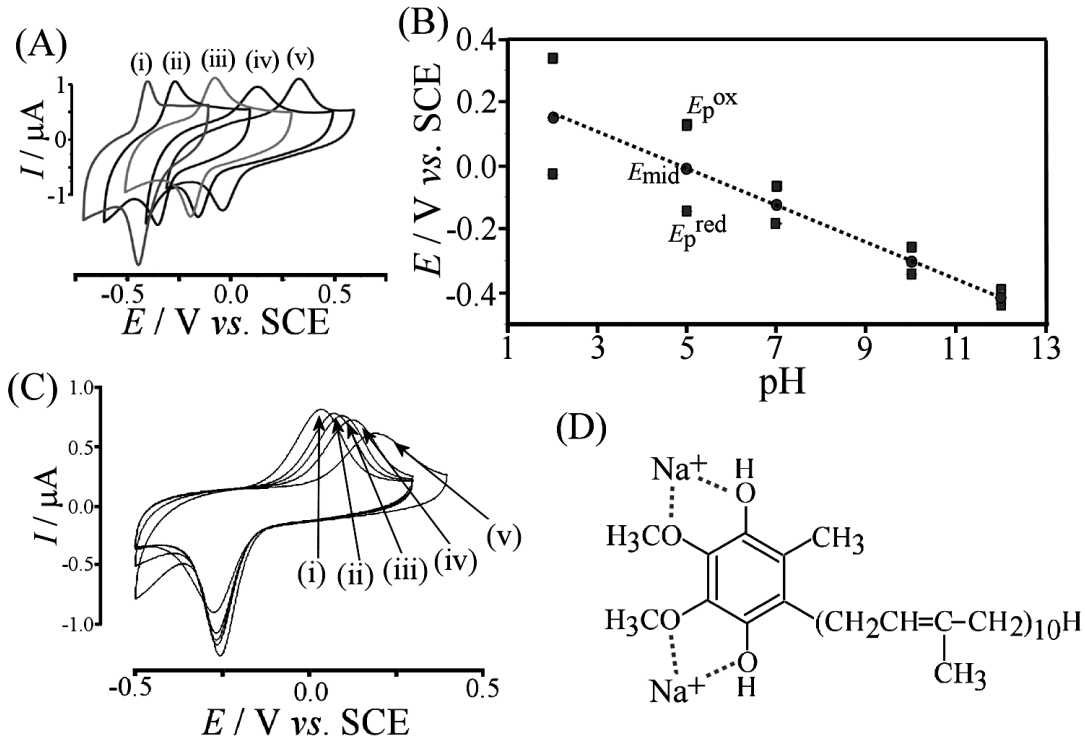

Figure 5.6 - (A) CVs (scan rate 10 mVs^{-1}) for the reduction and back-oxidation of 0.1 nmol Q_{10} in 25 nmol DMPC/15 μg CNP immobilised at a glassy carbon electrode and immersed in aqueous 0.5 M PBS at pH (i) 12, (ii) 10, (iii) 7, (iv) 5, and (v) 2. (B) Plot of peak potentials $E_{p,ox}$ and $E_{p,red}$ and the midpoint potential E_{mid} (= ½ $E_{p,ox}$ + ½ $E_{p,red}$) versus pH. (C) CVs (scan rate 10 mVs^{-1}) for the reduction and back-oxidation of 0.1 nmol Q_{10} in 25 nmol DMPC/15 μg hydrophobic CNPs immobilised at a glassy carbon electrode and immersed in aqueous 0.5 M PBS at pH 7 with (i) 0, (ii) 0.5, (iii) 1.0, (iv) 2.0, and (v) 5.0 M NaCl added. (D) Suggested interaction of coenzyme Q_{10} with Na^+.

Finally, the effect of added electrolyte, here NaCl, was investigated. The CVs in Figure 5.6(C) demonstrate that the cation concentration affected the anodic peak response and the shift observed was comparable to that observed for the coenzyme Q_{10} responses in

the absence of DMPC [see Figure 5.4(C)]; however, the magnitude of the shift was much lower in the presence of DMPC. A similar mechanism must be in operation in both cases and the interaction of the coenzyme Q_{10} headgroup with Na^+, as demonstrated in Figure 5.6(D), provides a reasonable interpretation.

5.5 Conclusions

The dioctylamine-sulfonamide functionalised CNP substrate has been investigated for the direct immobilisation of coenzyme Q_{10} and for coenzyme Q_{10} immobilised within a DMPC lipid film. Enhanced voltammetric responses were observed, and in particular for the lipid film, high sensitivity with low levels of coenzyme Q_{10} was achieved, which could be attributed to the suppression of the capacitive background current. The interaction of the reduced form of the coenzyme Q_{10} redox system with Na^+ has been observed for both pure coenzyme Q_{10} and DMPC-Q_{10} systems that have been immobilised on modified-nanoparticle substrates. This cation interaction is proposed to be associated with a change in the rate of electron transfer.

The new hydrophobic dioctylamine-sulfonamide-modified CNP substrate is versatile and can be used to study both hydrophobic redox systems and lipid films. In future, this could be beneficial for a wider range of lipid electroanalysis problems, for example in the study of drug – lipid interactions or for the analysis for biological lipid mixtures and cell membranes.

5.6 References

1. Barsukov, I.V., C.S. Johnson, J.E. Doninger, and V.Z. Barsukov, *New Carbon Based Materials for Electrochemical Energy Storage Systems: Batteries, Supercapacitors and Fuel Cells*, 2006, Springer, Berlin.
2. Scida, K., P.W. Stege, G. Haby, G.A. Messina, and C.D. Garcia, *Recent Applications of Carbon-Based Nanomaterials in Analytical Chemistry: Critical Review,* Anal. Chim. Acta, 2011, **691**, 6-17.
3. Akasaka, T., F. Wudl, and N. S., eds. *Chemistry of Nanocarbons*, 2010, Wiley-Blackwell, New York.
4. Barriere, F. and A.J. Downard, *Covalent Modification of Graphitic Carbon Substrates by Non-Electrochemical Methods,* J. Solid State Electrochem., 2008, **12**, 1231-1244.
5. Pinson, J. and F. Podvorica, *Attachment of Organic Layers to Conductive or Semiconductive Surfaces by Reduction of Diazonium Salts,* Chem. Soc. Rev., 2005, **34**, 429-439.
6. Denisenko, A., A. Romanyuk, L.A. Kibler, and E. Kohn, *Surface Structure and Electrochemical Characteristics of Boron-Doped Diamond Exposed to rf N-2-Plasma,* J. Electroanal. Chem., 2011, **657**, 164-171.
7. Hou, S.F., M.L. Kasner, S.J. Su, K. Patel, and R. Cuellari, *Highly Sensitive and Selective Dopamine Biosensor Fabricated with Silanized Graphene,* J. Phys. Chem. C, 2010, **114**, 14915-14921.
8. Vidal, L., A. Chisvert, A. Canals, E. Psillakis, A. Lapkin, F. Acosta, K.J. Edler, J.A. Holdaway, and F. Marken, *Chemically Surface-Modified Carbon Nanoparticle Carrier for Phenolic Pollutants: Extraction and Electrochemical Determination of Benzophenone-3 and Triclosan,* Anal. Chim. Acta, 2008, **616**, 28-35.
9. Watkins, J.D., R. Lawrence, J.E. Taylor, S.D. Bull, G.W. Nelson, J.S. Foord, D. Wolverson, L. Rassaei, N.D.M. Evans, S.A. Gascon, and F. Marken, *Carbon Nanoparticle Surface Functionalisation: Converting Negatively Charged Sulfonate to Positively Charged Sulfonamide,* Phys. Chem. Chem. Phys., 2010, **12**, 4872-4878.
10. Szot, K., J.D. Watkins, S.D. Bull, F. Marken, and M. Opallo, *Three Dimensional Film Electrode Prepared from Oppositely Charged Carbon Nanoparticles as Efficient Enzyme Host*, Electrochem. Commun., 2010, **12**, 737-739.
11. Watkins, J.D., K. Lawrence, J.E. Taylor, T.D. James, S.D. Bull, and F. Marken, *Carbon Nanoparticle Surface Electrochemistry: High-Density Covalent Immobilisation and Pore-Reactivity of 9,10-Anthraquinone,* Electroanalysis, 2011, **23**, 1320-1324.
12. Bin Ibrahim, N., K. Lawrence, T.D. James, F. Xia, M. Pan, S. Mu, J.M. Mitchels, and F. Marken, *Surface-Dopylated Carbon Nanoparticles Sense Gas-Induced pH Changes*, Sens. Actuators, B, 2012, **161**, 184-190.
13. Morrison, L.E., J.E. Schellhorn, T.M. Cotton, C.L. Bering, and P.A. Loach, *Function of Quinones in Energy Conserving Systems*, B.L. Trumpower, 1982, Academic Press, New York.
14. Yamamoto, Y., *Coenzyme Q10 as a Front-Line Antioxidant Against Oxidative Stress,* J. Clin. Biochem. Nutr., 2005, **36**, 29-35.

15. Franke, A.A., C.M. Morrison, J.L. Bakke, L.J. Custer, X.N. Li, and R.V. Cooney, *Coenzyme Q10 in Human Blood: Native Levels and Determinants of Oxidation During Processing and Storage,* Free Radical Biol. Med., 2010, **48**, 1610-1617.
16. Bianchi, G.P., P.L. Fiorella, A.M. Bargossi, G. Grossi, and G. Marchesini, *Reduced Ubiquinone Plasma-Levels in Patients with Liver-Cirrhosis and in Chronic-Alcoholics,* Liver, 1994, **14**, 138-140.
17. Gironi, M., A. Russo, A. Bianchi, M. Alberoni, E. Farina, A. Angelini, M. Cursano, C. Kullmann, E. Mariani, L. Bonalumi, L. Ceresa, F. Martinelli-Boneschi, and R. Nemni, *Oxidative and Antioxidant Markers in Patients with Neurodegenerative Diseases: a Pilot Study to Estimate Risk and Protective Factors,* J. Neurol. Sci., 2009, **285**, S136-S136.
18. Hickey, M.A., C. Zhu, V. Medvedeva, N.R. Franich, M.S. Levine, and M.-F. Chesselet, *Evidence for Behavioral Benefits of Early Dietary Supplementation with CoEnzymeQ10 in a Slowly Progressing Mouse Model of Huntington's Disease,* Mol. Cell. Neurosci., 2012, **49**, 149-157.
19. Spindler, M., M.F. Beal, and C. Henchcliffe, *Coenzyme Q10 Effects in Neurodegenerative Disease,* Neuropsychiatr. Dis. Treat., 2009, **5**, 597-610.
20. Kaya, Y., A. Cebi, N. Soylemez, H. Demir, H.A.L.P. Hakan, and E. Bakan, *Correlations between Oxidative DNA Damage, Oxidative Stress and Coenzyme Q10 in Patients with Coronary Artery Disease,* Int. J. Med. Sci., 2012, **9**, 621-626.
21. Miles, M.V., P.S. Horn, P.H. Tang, J.A. Morrison, L. Miles, T. DeGrauw, and A.J. Pesce, *Age-Related Changes in Plasma Coenzyme Q10 Concentrations and Redox State in Apparently Healthy Children and Adults,* Clin. Chim. Acta, 2004, **347**, 139-144.
22. Takehara, K. and Y. Ide, *Electrochemical-Behavior of the Ubiquinone-Q10 Film Coated onto a Glassy-Carbon Electrode by the Spinner Method,* Bioelectrochem. Bioenerg., 1991, **26**, 297-305.
23. Laval, J.M. and M. Majda, *Electrochemical Investigations of the Structure and Electron-Transfer Properties of Phospholipid-Bilayers Incorporating Ubiquinone,* Thin Solid Films, 1994, **244**, 836-840.
24. Swenton, J., *Chemistry of Quinones*. 1988, Wiley, New York.
25. Moncelli, M.R., L. Becucci, A. Nelson, and R. Guidelli, *Electrochemical Modeling of Electron and Proton Transfer to Ubiquinone-10 in a Self-Assembled Phospholipid Monolayer,* Biophys. J., 1996, **70**, 2716-2726.
26. Gordillo, G.J. and D.J. Schiffrin, *Redox Properties of Ubiquinone (UQ10) Adsorbed on a Mercury-Electrode,* J. Chem. Soc.-Faraday Trans., 1994, **90**, 1913-1922.
27. Gordillo, G.J. and D.J. Schiffrin, *The Electrochemistry of Ubiquinone-10 in a Phospholipid Model Membrane,* Faraday Discuss., 2000, **116**, 89-107.
28. Barnes, G.T., G.A. Lawrie, B.J. Battersby, S.M. Sarge, H.K. Cammenga, and P.B. Schneider, *Dimyristoyl Phosphatidylcholine - Equilibrium Spreading Behavior,* Thin Solid Films, 1994, **242**, 201-207.
29. Ghosh, S., A. Adhikari, S. Sen Mojumdar, and K. Bhattacharyya, *A Fluorescence Correlation Spectroscopy Study of the Diffusion of an Organic Dye in the Gel Phase and Fluid Phase of a Single Lipid Vesicle,* J. Phys. Chem. B, 2010, **114**, 5736-5741.
30. Tien, H.T. and A.L. Ottova, *Supported Planar Lipid Bilayers (s-BLMs) as Electrochemical Biosensors,* Electrochim. Acta, 1998, **43**, 3587-3610.

31. Wagner, C.D., L.E. Davis, M.V. Zeller, J.A. Taylor, R.H. Raymond, and L.H. Gale, *Empirical Atomic Sensitivity Factors for Quantitative-Analysis by Electron-Spectroscopy for Chemical-Analysis,* Surf. Interface Anal., 1981, **3**, 211-225.
32. Wain, A.J., J.D. Wadhawan, and R.G. Compton, *Electrochemical Studies of Vitamin K-1 Microdroplets: Electrocatalytic Hydrogen Evolution,* ChemPhysChem, 2003, **4**, 974-982.
33. Bond, A.M., F. Marken, E. Hill, R.G. Compton, and H. Hugel, *The Electrochemical Reduction of Indigo Dissolved in Organic Solvents and as a Solid Mechanically Attached to a Basal Plane Pyrolytic Graphite Electrode Immersed in Aqueous Electrolyte Solution,* J. Chem. Soc.-Perkin Trans., 1997, **9**, 1735-1742.
34. Bogeski, I., R. Guaboski, R. Kappl, V. Mirceski, M. Stefova, J. Petreska, and M. Hoth, *Calcium Binding and Transport by Coenzyme Q,* J. Am. Chem. Soc., 2011, **133**, 9293-9303.

Chapter 6

Electrochemical Probing of Phase Transformations in Modified Composites: Carbon Nanoparticles-Lipid-Coenzyme Q_{10}

Contents

Thanks to Emma Daulton for help with BAM, Tom Forder and Matthew Jones for help with DSC measurements, and Masters Student Charlotte Baker who carried out her final year project as part of this study.

This work is to be submitted to Bioelectrochemistry for publication;

manuscript in preparation

6.1 Abstract

1,2-Dimyristoyl-*sn*-glycero-3-phosphocholine (DMPC) is a component in lipid cell membranes. Like other lipids, DMPC is known to undergo a gel-liquid phase transition. In this work the phase transition is investigated by using modified carbon nanoparticles (with approximately 9 to 18 nm diameters) as a hydrophobic support and a conduit for electrons. In the presence of coenzyme Q_{10} (CoQ_{10}), well-defined voltammetric responses are obtained with a strong irreversible change in the kinetic parameters at the gel-liquid transition point, which is observed between 25 and 30 ^{o}C. The transition is only observed during heating and is not visible in the cyclic voltammograms during cooling. The transformation is confirmed by differential scanning calorimmetry, which also suggests a further phase change upon cooling that occurs at 17 ^{o}C. The morphology of the lipid film is observed to be largely unchanged on heating; this was investigated by using Brewster angle microscopy. In future research, the dioctylamine-modified carbon nanoparticles could provide a hydrophobic tool for wide explorations into membrane properties.

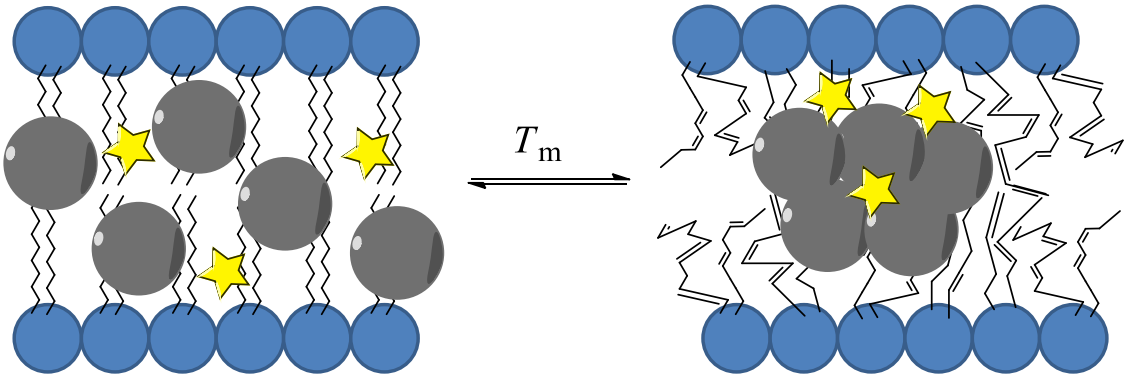

6.2 Introduction

Biological membrane processes are extremely complex and important functions that impact everyday life. The study of such processes is important for the understanding of biochemical pathways and being able to create new biomedicines and biosensors.[1, 2] One method for studying these processes is by using electrochemical analysis.[1, 3] Electrochemistry offers an inexpensive means to efficiently monitor redox-active moieties within cell membranes. Previous studies have focused on combining electroanalysis with membrane-type materials; the most prominent in recent literature is the use of lipids.[1, 4, 5] Biological membrane processes take place in lipophilic environments and it is therefore important to fabricate new materials that are lipophilic so that they can be utilized within cell membranes and biological environments. Supported phospholipid bilayers are commonly used because biologically active substrates can be directly attached and studied.[1] However, one limitation of studying lipid-based systems is that the chemistry within a lipid can change dramatically as a function of temperature.[6] This is caused by the intrinsic structure of lipids; the hydrocarbon chains are assembled in layers that manifest weak interactions between adjacent layers, and the headgroups combine through stronger polar interactions. When heated, this type of structure begins to melt, initially at the hydrocarbon chains, which become more fluid and disordered, when heated further, the head group interactions are also broken and the lipid adopts a liquid state. When the lipids begin to melt they still possess long range order; however, at the atomic scale they are very disordered, that is, fluid; this results in mesomeric phase transitions.[6, 7]

In cholesterol-based phospholipid systems, there is a "gel" phase that occurs.[7, 8] These gel phases contain adjacent layers of intact bilayer and liquid-crystalline layers. The transition between this stage and the liquid-like state occurs at a specific temperature for each individual lipid material; this is known as the gel-fluid transition point. 1,2-dimyristoyl-sn-glycero-3-phosphocholine (DMPC) is a commonly used phospholipid, and the gel-fluid transition point for which has been measured as 23.8 ^{o}C.[9, 10]

Electrochemical measurements in the presence of DMPC have previously been investigated;[5] however, the effect of temperature and the phase of the lipid on such analytical methods are not understood. Herein, DMPC is combined with a modified carbon nanoparticle support for the analysis of coenzyme Q_{10}. This is an important system as coenzyme Q_{10} is an important lipophilic redox-active compound that is ubiquitous in the body. It is an essential mediator in the mitochondrial transfer chain, it can also be found at elevated levels within the blood as it is also a common disease marker.[11, 12] Therefore, the accurate analysis of coenzyme Q_{10} is important. The carbon support used herein in the composite is significant because it has been demonstrated to greatly enhance the electrochemical signals of coenzyme Q_{10}, especially in the presence of DMPC, as this amplifies the Faradaic signals by suppressing the background capacitance.[13]

6.3 Experimental

6.3.1 Reagents

Emperor 2000 carbon nanoparticles used as the starting material were obtained from Cabot Corporation. DMPC and coenzyme Q_{10} were purchased from Sigma Aldrich. All other reagents were used without further purification: ortho-phosphoric acid (Fisher Scientific), sodium hydroxide (Aldrich, Sigma ultra, 98%), toluene (Sigma, ACS reagent, ≥99.5%). Demineralised and filtered water was taken from a Thermo Scientific water purification system (Barnstead Nanopure) of approximately 18.2 MOhm cm resistivity.

6.3.2 Instrumentation

For voltammetric studies a microAutolab III potentiostat system (EcoChemie, Netherlands) was employed with a Pt wire counter electrode and a KCl-saturated Calomel (SCE) reference electrode (Radiometer, Copenhagen). A 3 mm diameter glassy carbon electrode (BAS) served as working electrode. The temperature was 22 ± 2 ^{o}C.

The differential scanning calorimmetry (DSC) measurements were performed by using DSC Q20 V24.10 apparatus and the analysis was performed over a temperature range of 10 – 50 ^{o}C. The temperature was increased at a temperature ramp rate of 1 ^{o}C per minute to 50 ^{o}C, at which the temperature was kept constant for 5 min before the temperature was decreased at 1 ^{o}C per min. To prepare the films, DMPC (17 mg) was added to dioctylamine-modified CNPs (15 mg) and toluene (5 mL). This mixture was place in an ultrasonication bath for 30 min, after which a black suspension was obtained. This was then deposited onto the surface of a white tile (approximately 225 cm^2) together with CoQ_{10} (1 μL, 0.1 mg mL^{-1} in toluene) at a CNP-DMPC/CoQ_{10} ratio of 5:1, that is, the same ratio as the film produced on the surface of the electrodes in the voltammetric studies. The CNP-DMPC and CoQ_{10} solutions were mixed before evaporating at room temperature to form a composite film. After 24 h, the film was scraped off and used in the DSC measurements.

Brewster angle microscopy (BAM) measurements were performed on a BAM2Plus microscope (Nanofilm Technology, Goettingen, Germany). The temperature of the sample slide was controlled by using a heat stage. The microscope was equipped with a frequency doubled Nd:YaG laser (532 nm, 20 mW), polarizer, analyzer, and charge-coupled device (CCD) camera. Images were taken by using a 10 × objective with an actual magnification of 15 ×. This resulted in an *x*-axis on the image of 430 μm, and the geometry of the *y*-axis was calculated by using Equation 6.1:

$$y = \frac{x}{\alpha \cos\theta} \tag{6.1}$$

in which α is the aspect ratio, which is equal to 768/572, and θ is equal to the angle of incidence, which in this case was the Brewster angle of glass equal to 56°.[14]

To prepare the films, DMPC (17 mg) was added to dioctylamine-modified CNPs (15 mg) and toluene (5 mL). This was placed in an ultrasonication bath for 30 min to yield a black suspension. This was then deposited onto a microscope slide together with CoQ_{10} (1 μL, 0.1 mg mL^{-1} in toluene) to achieve a CNP-DMPC/CoQ_{10} ratio of 5:1. After

20 min, the toluene had evaporated and the microscope slide was placed inside the BAM chamber.

6.3.3 Electrode Preparation

The working electrodes were prepared as described in a previous study.[13] Typically, DMPC (17 mg) was added to dioctylamine-modified CNPs (15 mg) in addition to toluene (5 mL). This was mixed with the aid of an ultrasonication bath to yield a black solution. The CNP-DMPC solution (5 µL) was deposited onto a polished glassy carbon electrode. Coenzyme Q_{10} (1 µL, 0.1 mg mL^{-1} in toluene) was co-deposited with the nanoparticles before drying together at room temperature to produce a CNP-Q_{10}-DMPC composite on the electrode surface.

For all films, that is, for DSC, BAM, and electrochemical measurements, described as "half-CNP" and "no carbon" the same procedure was followed; however, 7.5 mg or 0 mg of dioctylamine-modified CNPs were used, respectively. All other components were used at the same volume, concentration, and amount.

6.4 Results and Discussion

6.4.1 Voltammetric Responses as a Function of Temperature

The CNP-Q_{10}-DMPC modified electrodes were used directly in a three-electrode electrochemical cell containing 0.1 M phosphate buffer solution (at pH 2, 7, or 12). The temperature of the electrolyte was controlled by using a thermostatic bath. At the starting temperature (10 ^{o}C), clear reduction and back oxidation peaks could be observed with a midpoint potential (E_{mid}) of approximately 150 mV at pH 2, which corresponded to the coenzyme Q_{10} redox couple. The peak-to-peak separation was approximately 490 mV. As the temperature of the system was increased, the peak-to-peak separation decreased, and at 55 ^{o}C, the peak-to-peak separation was 300 mV in pH 2 buffer solution. Interestingly, the position of the reduction peak was unchanged (-50 mV), whereas the oxidation response became progressively more favourable as the

temperature increased. This was demonstrated by the oxidation potential becoming lower (i.e., shifting from 420 mV at 10 ^{o}C to 250 mV at 55 ^{o}C), see Figure 6.1(a) to (c).

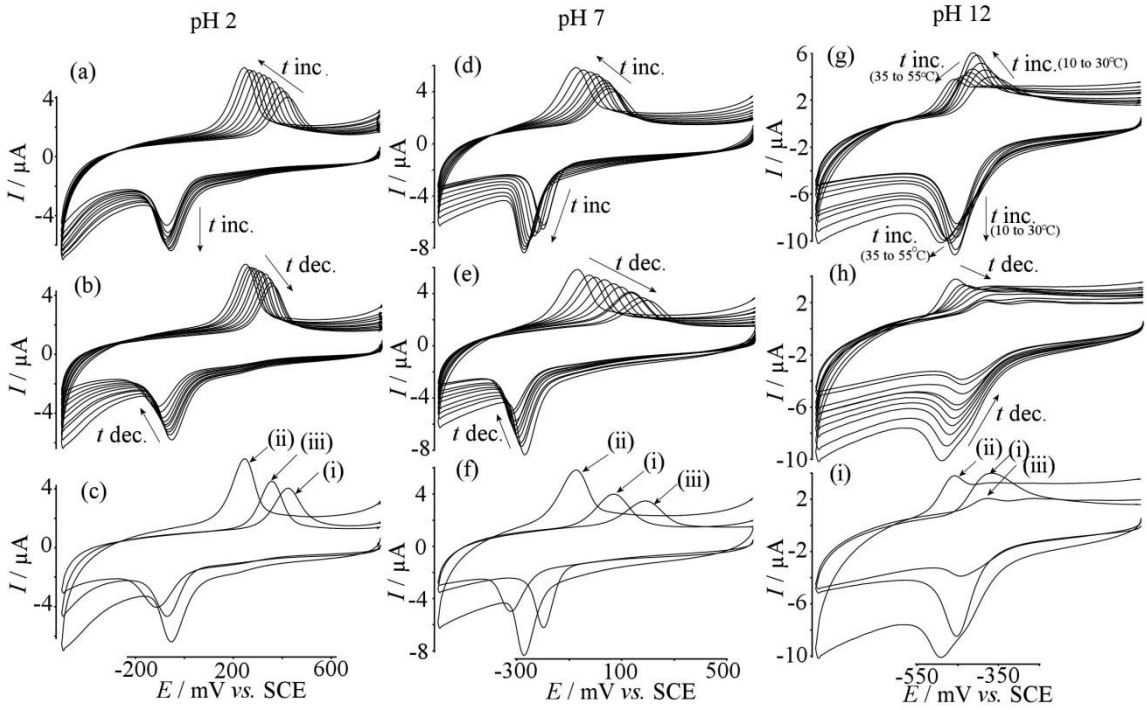

Figure 6.1. Cyclic voltammograms for CNP-Q_{10}-DMPC modified electrodes in 0.1 M phosphate buffer solution recorded with a scan rate of 100 mV s^{-1}. (a, d and g) Increasing temperature from 10^{o}C to 55^{o}C in 5^{o}C steps, (b, e and h) decreasing temperature from 55^{o}C to 10^{o}C, in 5^{o}C steps, (c, f and i) a summary of the data at (i) the starting temperature, 10^{o}C, (ii) the maximum temperature, 55^{o}C, and (iii) the final temperature, 10^{o}C. (a to c) were buffered at pH 2, (d to f) were buffered at pH 7 and (g to i) were buffered at pH 12.

As the cell was cooled in temperature from 55 ^{o}C back to 10 ^{o}C, the peak-to-peak separation increased to 450 mV. The oxidation potential also shifts; mirroring the effect seen during the heating process, the oxidation potential sequentially reaches more positive values as the temperature is lowered. However, when the temperature is returned to 10 ^{o}C, the oxidation potential is not the same as the starting electrode. After heating and cooling the oxidation peak is seen at 350 mV. It can be seen from Figure 6.1(c) that the peak-to-peak separations at 10 ^{o}C, both initially and after the temperature changes, are very similar. This is because during the cooling process the reduction peak potential is also affected, and it shifts from 50 mV to 110 mV, Figure 6.1(b).

In pH 7 electrolyte solution, the initial peak-to-peak separation at 10 ^{o}C was 260 mV, this reduced to 145 mV when the temperature reached 55 ^{o}C, and after cooling back to 10 ^{o}C there was a large increase in the peak-to-peak separation with it reaching 520 mV. This dramatic change was caused by both the oxidation and reduction signals being shifted, oppositely to that observed at pH 2. At a pH value of 7, both the oxidative and reductive responses shift to less positive values as the temperature is increased, see Figure 6.1(d). It is important to note that the oxidative signal was shifted to a greater extent than the reductive signal. When the temperature was decreased, the reductive signals continued to shift to more negative potentials; however, the oxidative responses were seen to shift consistently to greater potentials at each incremental change in the temperature, Fig 6.1(e).

In alkaline conditions (pH 12), there was a less significant change in the peak positions upon heating. As seen for both pH 2 and 7, the signal intensity increased consistently with the temperature increase. However, at pH 12 a maximum was achieved at 30 ^{o}C (in the other cases, the maximum peak potential was achieved at the maximum temperature, i.e., 55 ^{o}C), upon further heat treatment, there was a splitting of the oxidation and reduction signals (more significant in the oxidative signal). This could be attributed to a change in the electron transfer mechanism. It is likely that the high temperature and highly alkaline conditions instigated a structural change of the coenzyme Q_{10}, resulting in a change from a fast concerted $2H^{+}/2e^{-}$ mechanism to two $1e^{-}$ steps.

6.4.2 Voltammetric Detection of Phase Transitions

The maximum peak current was extracted from the CV data and plotted against temperature. Figure 6.2(a) shows the data in pH 2 phosphate buffer electrolyte. It can be clearly observed that as the temperature increased, there was an associated linear increase in the maximum peak current for both the oxidative and reductive responses. Between 20 and 25 ^{o}C there was a step in the maximum peak current before the linear increase is resumed. A similar pattern was observed for the reduction data. For both the oxidation and reduction processes, there was no clear step observed in the potential when the temperature was decreased and returned to 10 ^{o}C. The step in the maximum peak current can be attributed to a phase-change process. The temperature at which this

occurred was similar to the temperature reported in the literature for DMPC lipid gel-fluid transition. Therefore, by using this methodology it is possible to detect phase transitions through simple electrochemical analysis.

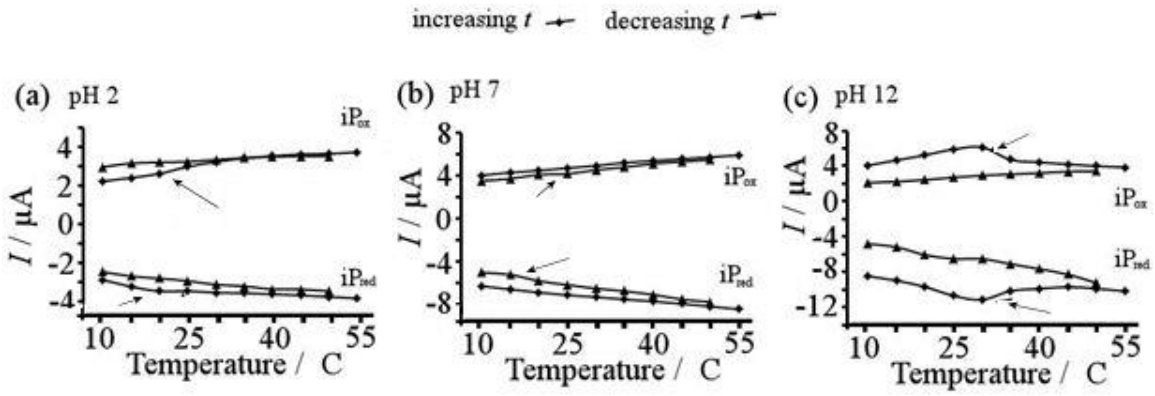

Figure 6.2 Maximum peak currents for oxidative (iP_{ox}) and reductive (iP_{red}) signals as a function of changing temperature.

At pH 7, the step was much more subtle and no clear change in the phase could be identified in the system from the plot of peak current versus temperature, Figure 6.2(b). However, in the case of pH 12, there was a very clear peak in the plots for both iP_{ox} and iP_{red} between 25 and 30 ^{o}C, Figure 6.2(c). This is consistent with the data in Figure 6.1 and suggests that the gel-fluid transition is also associated with a change in mechanism of the coenzyme Q_{10}.

6.4.3 Charge Response of Coenzyme Q_{10}

Integration of the cyclic voltammograms indicates that the maximum charge, that is, at 55 ^{o}C, is approximately 5 µC, whereas the theoretical maximum charge is 23 µC. This suggests that a lot of the coenzyme Q_{10} was confined within the DMPC-CNP composite and; therefore, was not available for electron transfer processes. At the initial temperature, 10 ^{o}C, it is likely that a greater proportion of the Q_{10} was unavailable for electron transfer processes that are taking place at the electrode. However, as the system

is heated, the structure of the lipid becomes more fluidic and allows for easier transport of the Q_{10} throughout the film allowing it better access to the electrode surface.

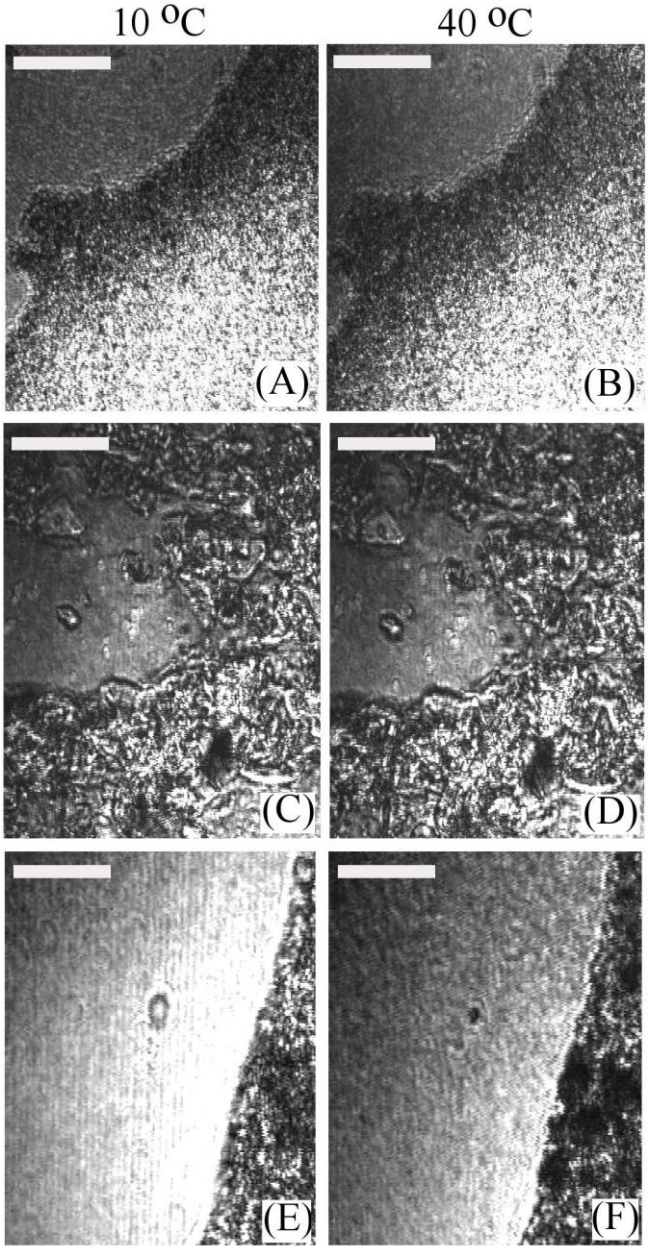

Figure 6.3 BAM images of DMPC lipid film at 10 °C (A) and 40 °C (B); DMPC film containing half-loading of CNPs at 10 °C (C) and 40 °C (D); DMPC with full loading of CNPs at 10 °C (E) and 40 °C (F). The scale bars represent 10 μm.

The effect of temperature on the film morphology was observed by using Brewster angle microscopy (BAM). Figure 6.3 shows the lipid and the lipid with carbon film edges at 10 and 40 °C. Figure 6.3(A) and (B) show an incomplete DMPC-only film on a

microscope slide at 10 and 40 ^{o}C, respectively. Figure 6.3(C) and (D) show a CNP-DMPC film, with "half-loading" of CNPs, at 10 and 40 ^{o}C, respectively. Figure 6.3(E) and (F) show as small portion (on the right-hand side) of a CNP-DMPC film on a microscope slide, with full carbon loading, at 10 and 40 ^{o}C, respectively. The samples were evaporated onto the microscope slides, and the images were obtained at the sample/air interface. From the images, there was no apparent change in the film morphology at the molecular scale. It is possible that when the film dried, especially for the sample with half-carbon-loading, the CNPs became trapped within the rough surface of the microscope slide, and when the lipid underwent the phase transition the film was unable to reorganise itself as it does when it is deposited onto a polished glassy carbon electrode that has been immersed into buffer solution. However, when looking at the film with full carbon loading [Figure 6.3(E) and (F)], the film became darker, which implies that the carbon nanoparticles were able to move through the fluidic film and settle into a thicker, more aggregated film of carbon nanoparticles instead of more dispersed particles throughout the film.

This theory also helps to explain the decrease in coulombic charge as the system was cooled back to the starting temperature because the DMPC returns to a more gel-like state, again hindering the movement of the redox moiety. However, even the maximum charge that is observed is still much below that what is expected. This is likely to be caused by some of the CoQ_{10} being incorporated into aggregates of the CNPs, which are not subjected to phase changes within the studied temperature range. This aggregative behaviour confining the compound has been seen in previous studies with Emperor 2000 carbon blacks.[13, 15, 16]

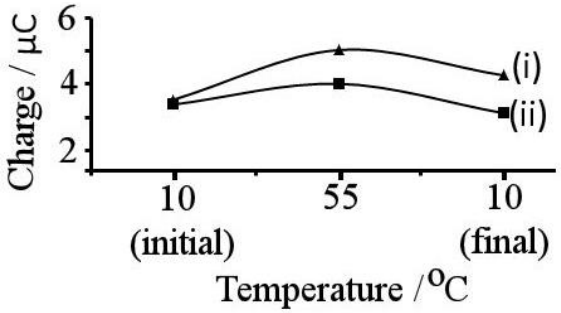

Figure 6.4 A plot of the charge under the voltammetric curves for the oxidative (i) and reductive (ii) responses in 0.1 M phosphate buffer at pH 2.

According to Figure 6.4, the oxidative and reductive charge is identical at the initial temperature, 10 ^{o}C, as expected. However, with increasing temperature the oxidative charge becomes increasingly greater than the reductive charge. Upon cooling the system, the difference of approximately 1 μC remains constant.

6.4.4 pH Dependence

The pH dependence was investigated at different temperatures. The initial CVs resemble those observed for the same system at room temperature (see Chapter 5, Figure 5.5). The characteristic shift in midpoint potential and a widening of the peak-to-peak separation in more acidic media were once again observed. Also, the E_{mid} value shifted by approximately 60 mV per pH unit, consistent with that expected for a two-electron two-proton reduction and is in agreement with the data obtained in Chapter 5.[17]

When the temperature of the system was increased from 10 ^{o}C to 55 ^{o}C, the oxidation peaks in pH 2 and 7 buffer shifted slightly towards more negative E_{mid} values. This indicated that the oxidation of the system became more facile at elevated temperature, see Figure 6.5. The reduction peak at pH 7 remained relatively unchanged, whereas the reduction signal at pH 2 shifted slightly towards a more positive E_{mid} value; therefore reducing the peak-to-peak separation. For the system in pH 12 phosphate buffer, the process was more complex, the oxidation peak decreased dramatically and split into two separate signals, likely due to two slower 1 e^- processes occurring rather than a concerted 2 e^- mechanism. The reduction signal at pH 12 also became less intense but broadened, indicating the emergence of a second signal. The capacitive response at 55 ^{o}C was also greater in this instance, which could be masking some of the faradaic response.

When the system is cooled back to 10 ^{o}C, the pH 2 buffered film signals return almost to the same positions as the initial temperature. The oxidation signal moves towards a more positive potential. It also is more intense compared to the original signal, which implies that there is less diffusion control and that the conducting carbon nanoparticles are more condensed and in closer proximity to the coenzyme Q_{10} after the heating and

cooling process. The reduction signal is almost unchanged; however, it appears slightly broader and suggests more coenzyme Q_{10} is available for reduction and that some may have been released from aggregates within the phase change processes. The pH 7 system behaves very differently; the oxidation peaks shifts to more positive potential and results in a higher oxidation potential than the original system. Conversely, the reductive signal moves even more towards a negative potential, the result of this is a much greater E_{mid}, than the initial and high temperature systems. This suggests that the electrochemical reversibility of coenzyme Q_{10} is reduced and is further evidence that system is converting to a 1 e^- process. At pH 12, there are two distinct faradaic oxidation signals; however, they are very weak and suggest that under such conditions the coenzyme Q_{10} is degraded.

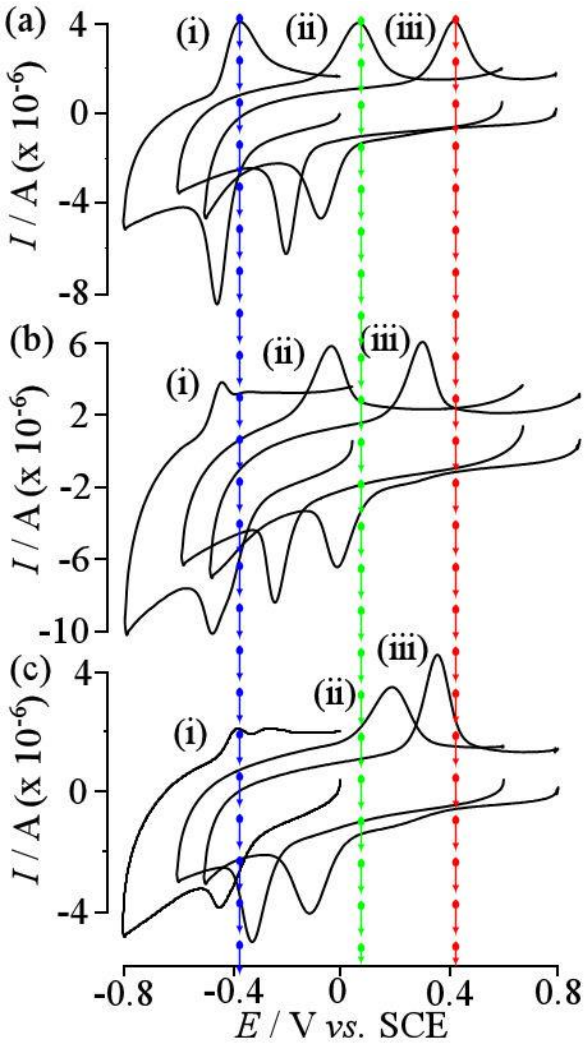

Figure 6.5 Cyclic voltammograms for CNP-Q_{10}-DMPC modified electrodes recorded with a scan rate of 100 mV s^{-1} at (a) the starting temperature, 10°C, (b) the maximum temperature, 55°C, and (c) the final temperature, 10°C after heating and re-cooling in 0.1 M phosphate buffer solution at a pH value of (i) 12, (ii) 7, and (iii) 2.

Overall, there is a clear dependence on the pH of the system; however, the temperature change at these different pH values causes complex electrochemical changes, which would need to be investigated in more detail for clear understanding of such processes.

6.4.5 The Effect of Different Amounts of CNPs in the Composite Film

The effect of carbon loading was studied by investigating films containing DMPC, coenzyme Q_{10}, and modified CNPs as well as films containing only half the proportion of CNPs (i.e., 7.5 mg instead of 15 mg; see the experimental section), also films containing only DMPC lipid and coenzyme Q_{10} were studied, that is, in the absence of CNPs. As expected, the signal intensity decreased with decreasing amounts of carbon in the composite films, which is associated with a lower accessible and active surface area.

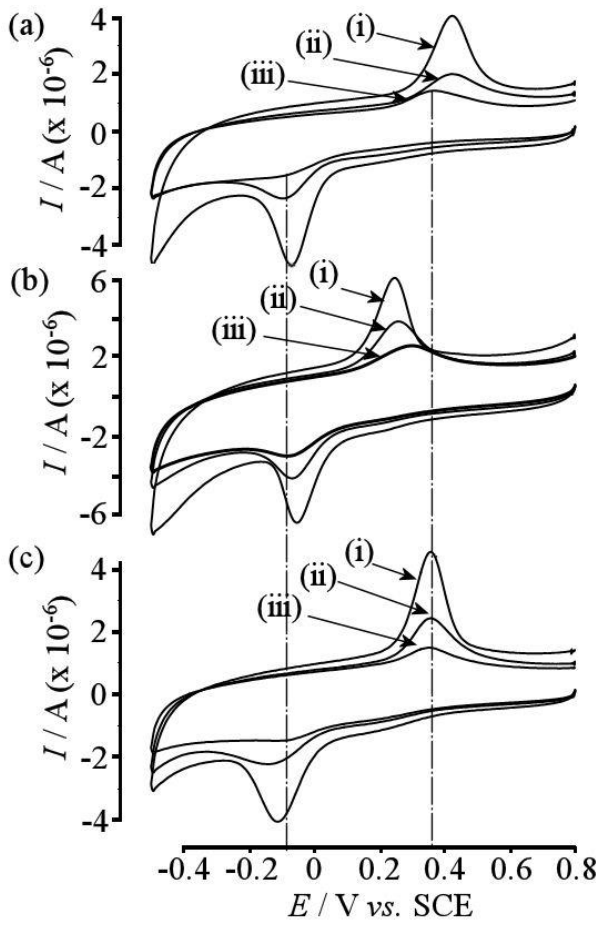

Figure 6.6 Cyclic voltammograms for CNP-Q_{10}-DMPC modified electrodes in pH 2 0.1 M phosphate buffer solution with a scan rate of 100 mV s^{-1} at (a) the starting temperature, 10°C, (b) the maximum temperature, 55°C, and (c) the final temperature, 10°C after heating and re-cooling with (i) full carbon loading, (ii) half CNPs, and (iii) no CNPs.

Without any carbon, the peak positions are unchanged. The positions of the peaks were relatively unchanged with the different carbon loading; however, it is interesting to note that the effect of temperature on the film containing no CNPs was much less significant than for films containing carbon. This indicates that the temperature is more influential on the composites containing carbon, which could be attributed to localised heating around the carbon particles leading to greater effects on the gel-fluid transition and thus affecting the redox mechanism to a greater extent.

6.4.6 Monitoring Phase Transitions in the Film by Using DSC

DSC experiments were performed on the composite material. Films of CNP-DMPC-Q_{10} were prepared on glass microscope slides and then removed by scraping to yield a solid composite sample for DSC measurements. The results, as shown in Figure 6.7, demonstrated a phase transition at 24.17 ^{o}C upon heating. This is consistent with the voltammetry-indicated phase change of the system in pH 7 buffer.

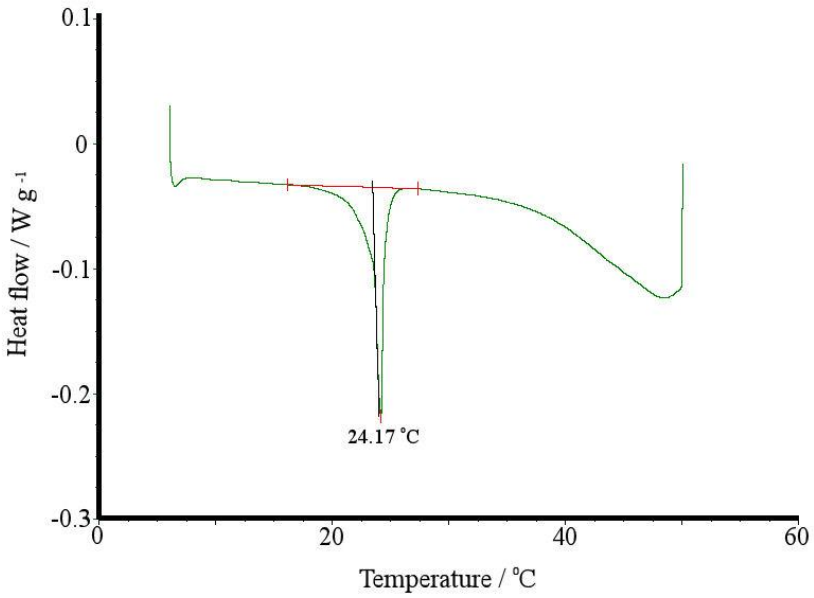

Figure 6.7. DSC trace for the CNP-DMPC-Q_{10} composite film when heating from 10 to 50 ^{o}C.

This demonstrates that the phase change detected in the CV measurements is genuine; however, the pH value is demonstrated to have a clear effect on the behaviour of the system. Therefore, further DSC experiments are required for further insight into the phase transformations of the lipid-based films, which should enable the clarification and understanding of the mechanisms occurring within the lipid films on the electrode.

6.5 Conclusions

This work has demonstrated that temperature plays an important role in the behaviours of lipid-based electrochemistry. By using a CNP-DMPC-Q_{10} composite, the effects of temperature and pH were studied. The temperature induces a phase change in the lipid structure at a gel-fluid transition point, this was observed electrochemically through a step change in the peak current. This was most prominent in the system at pH 7, in which the phase transformation occurred between 24 and 25 ^{o}C. This was confirmed by DSC, in which there was a very clear phase change at 24.17 ^{o}C. However, the effect of pH was not considered in the DSC analysis and further experiments are being performed to further understand these processes.

At different pH values, the temperature effects change; this is associated with a change in mechanism under the different conditions. It is theorised that this change in mechanism is influenced by the lipid structure, which is shown to be dependent upon the environment in which it is in.

6.6 References

1. Tien, H.T. and A.L. Ottova, *Supported Planar Lipid Bilayers (s-BLMs) as Electrochemical Biosensors,* Electrochim. Acta, 1998, **43**, 3587-3610.
2. Tantawi, K.H., R. Cerro, B. Berdiev, M.E.D. Martin, F.J. Montes, D. Patel, and J.D. Williams, *Investigation of Transmembrane Protein Fused in Lipid Bilayer Membranes Supported on Porous Silicon,* J. Med. Eng. Tech., 2013, **37**, 28-34.
3. Moncelli, M.R., L. Becucci, A. Nelson, and R. Guidelli, *Electrochemical Modeling of Electron and Proton Transfer to Ubiquinone-10 in a Self-Assembled Phospholipid Monolayer,* Biophys. J., 1996, **70**, 2716-2726.
4. Koerner, M.M., L.A. Palacio, J.W. Wright, K.S. Schweitzer, B.D. Ray, and H.I. Petrache, *Electrodynamics of Lipid Membrane Interactions in the Presence of Zwitterionic Buffers,* Biophys. J., 2011, **101**, 362-369.
5. Laval, J.M. and M. Majda, *Electrochemical Investigations of the Structure and Electron-Transfer Properties of Phospholipid-Bilayers Incorporating Ubiquinone,* Thin Solid Films, 1994, **244**, 836-840.
6. Larsson, K., P. Quinn, K. Sato, and F. Tiberg, *Lipids: Structure, Physical Properties amd Functionality,* 2006, The Oily Press, Bridgwater, UK.
7. Janiak, M.J., D.M. Small, and G.G. Shipley, *Nature of the Thermal Pretransition of Synthetic Phospholipids: Dimyristoyl- and Dipalmitolylecithin,* Biochemistry, 1976, **15**, 4575-4580.
8. Luzzati, V., *Biological Significance of Lipid Polymorphism: The Cubic Phases,* Curr. Opin. Struct. Biol., 1997, **7**, 661-668.
9. Ghosh, S., A. Adhikari, S. Sen Mojumdar, and K. Bhattacharyya, *A Fluorescence Correlation Spectroscopy Study of the Diffusion of an Organic Dye in the Gel Phase and Fluid Phase of a Single Lipid Vesicle,* J. Phys. Chem., B, 2010, **114**, 5736-5741.
10. Barnes, G.T., G.A. Lawrie, B.J. Battersby, S.M. Sarge, H.K. Cammenga, and P.B. Schneider, *Dimyristoyl Phosphatidylcholine - Equilibrium Spreading Behavior,* Thin Solid Films, 1994, **242**, 201-207.
11. Morrison, L.E., J.E. Schellhorn, T.M. Cotton, C.L. Bering, and P.A. Loach, *Function of Quinones in Energy Conserving Systems*, B.L. Trumpower, 1982, Academic Press, New York.
12. Franke, A.A., C.M. Morrison, J.L. Bakke, L.J. Custer, X.N. Li, and R.V. Cooney, *Coenzyme Q10 in Human blood: Native Levels and Determinants of Oxidation During Processing and Storage,* Free Radical Biol. Med., 2010, **48**, 1610-1617.
13. Lawrence, K., J.D. Watkins, T.D. James, J.E. Taylor, S.D. Bull, G.W. Nelson, J.S. Foord, Y.-T. Long, and F. Marken, *Dioctylamine-Sulfonamide-Modified Carbon Nanoparticles as High Surface Area Substrates for Coenzyme Q10-Lipid Electrochemistry,* Electroanalysis, 2012, **24**, 1003-1010.
14. Clifton, L.A., R.J. Green, A.V. Hughes, and R.A. Frazier, *Interfacial Structure of Wild-Type and Mutant Forms of Puroindoline-b Bound to DPPG Monolayers,* J. Phys. Chem., B, 2008, **112**, 15907-15913.
15. Watkins, J.D., K. Lawrence, J.E. Taylor, T.D. James, S.D. Bull, and F. Marken, *Carbon Nanoparticle Surface Electrochemistry: High-Density Covalent Immobilisation and Pore-Reactivity of 9,10-Anthraquinone,* Electroanalysis, 2011, **23**, 1320-1324.

16. Ibrahim, N.B., Lawrence, K., James, T.D., Xia, F., Pan, M., Mu, S., Mitchels, J.M., Marken, F., *Surface Dopylated Carbon Nanoparticles Sense Gas-Induced pH Changes*, Sens. Actuators, B, 2011 **161**, 184-190.
17. Gordillo, G.J. and D.J. Schiffrin, *The Electrochemistry of Ubiquinone-10 in a Phospholipid Model Membrane,* Faraday Discuss., 2000, **116**, 89-107.

Chapter 7

Hydrothermal Conversion of Poly-(4-Vinylpyridine) into Fluorescent Carbon Nanodots

Contents

Thanks to Dr. Stan Botchway at Rutherford Appleton Laboratory and Dr. Sofia Pascu and Haobo Ge for help with the *in vitro* cell imaging studies.

This work has been submitted for publication in JACS.

7.1 Abstract

A fluorescent N,O-heteroatom-rich carbon nanomaterial (C-dot) has been synthesized and characterized. These C-dots were produced by hydrothermal synthesis from poly-(4-vinylpyridine) [P4VP] and have a particle size between 10 and 100 nm in diameter. The particles exhibit strong fluorescent properties in different solvents and have also been investigated in cell culture medium. The P4VP C-dots retain their intrinsic fluorescence in a cellular environment and exhibit an excited state lifetime of 2.1 ± 0.9 ns in cell culture medium. The P4VP C-dots enter HeLa cells and do not cause significant damage to outer cell membranes, providing excellent scope for designing new nanomedicines as well as non-toxic fluorescent synthetic scaffolds for imaging applications such as scaffolds for drug delivery materials.

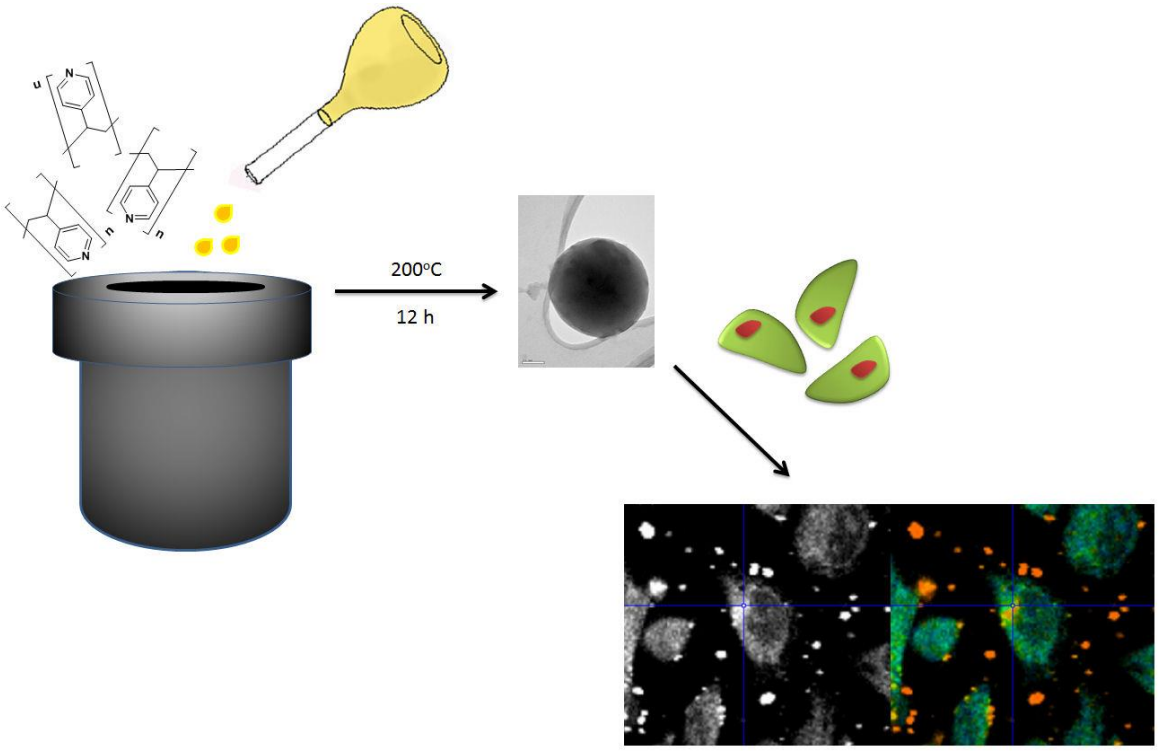

7.2 Introduction

Carbon nanomaterials including fullerenes, carbon nanotubes (CNTs), nanodiamonds, and graphene have attracted increasing interest over the past decade because of their unique properties such as large surface area, multiple adsorption sites, and large number of reactive surface sites.[1] Carbon nanodots (C-dots) are carbon-based nanomaterials that were first isolated in 2004 by Xu et al. serendipitously when purifying single wall CNTs (SWNTs) prepared by using arc-discharge methods.[2] C-dots are nanocarbons that comprise discrete nanoparticles with diameters of approximately 10 nm, which exhibit intrinsic fluorescent properties.[3, 4]

Following the first isolation of C-dots in 2004, a significant number of approaches for the synthesis of such materials have been developed and reported.[5, 6] These methods include top-down methods such as arc-discharge,[2] electrochemical synthesis,[7-10] and laser ablation.[11-13] Such top-down methods involve breaking down large carbonaceous materials into nano-sized carbon. Alternatively, bottom-up methods, which involve the formation of C-dots from molecular precursors, have also been reported. These techniques include the use of synthetic supports,[3, 14] microwave methods,[15] combustion,[16, 17] and hydrothermal techniques (such as those discussed in Chapter 1).[3, 4, 18]

One of the major characteristics of C-dots is that they possess intrinsic luminescent properties, this attribute enables C-dots to be potential alternatives to quantum dots (QDs).[19] QDs are metal-based fluorescent semiconductor nanomaterials, which are frequently used for bioimaging studies, *in-vivo* sensing as well as in photovoltaic applications; however, QDs are inherently toxic towards living cells.[10, 20] Because of the severe environmental and biological hazards that QDs threaten, C-dots are a promising alternative as they are considerably less hazardous to the environment and are comparatively low cost.[21] One of the major drawbacks to using C-dots as a replacement for QDs is that C-dots do not possess quantum yields of the same magnitude. However, C-dots have lower cytotoxicity and are far more biocompatible in comparison to QDs, making them a favourable alternative.

This chapter demonstrates a simple hydrothermal method for the synthesis of fluorescent P4VP C-dots from poly-(4-vinylpyridine). The amorphous P4VP C-dots show strong fluorescent properties that are superior to the fluorescence of the parent polymer; this is

likely to be due to the quantum size of the nanodots produced. The fluorescence is weakly pH and strongly solvent dependent. Herein, the potential of P4VP C-dots to be used in bioimaging applications is explored. The P4VP C-dots show apparent biocompatibility, as demonstrated by using confocal fluorescence imaging and fluorescence lifetime imaging (FLIM) techniques. The excited-state fluorescence lifetime of the C-dots is estimated in cellular media (EMEM, Eagle's Modified Essential Medium) and compared to the corresponding lifetime in organic solvent (DMSO). The images obtained indicate that the nanoparticles are not affected by the change in their chemical environment. Even without any further surface functionalization, the most highly dispersed P4VP C-dots show intrinsic fluorescence and are visualized by confocal fluorescence microscopy, the C-dots are shown to bind to the exterior of the cells without causing any significant damage to the outer cell membrane within the timescale of the cellular imaging experiments (1 h).

7.3 Experimental Section

7.3.1 Reagents

All reagents were used as supplied, without further purification: P4VP, typical Mw 60,000 (Aldrich), acetic acid (Aldrich, 99.7 %, ACS reagent), absolute EtOH (Sigma-Aldrich), DMSO (Sigma-Aldrich, >99.5 %), *ortho*-phosphoric acid (Fisher Scientific), NaOH (Aldrich, Sigma ultra, 98 %). Demineralized and filtered water was obtained from a Thermo Scientific water purification system (Barnstead Nanopure) with no less than 18.2 MΩ resistivity.

7.3.2 Instrumentation

X-ray photoelectron spectroscopy (XPS) was conducted using an Al Kα X-ray anode using an energy of 1486.6 eV. All peaks were calibrated to the adventitious C1s peak (i.e., to 285 eV). Zeta potential and particle size measurements were achieved by using a ZetaMaster S (Malvern Instruments Ltd, UK). Particle size measurements were validated with NIST traceable nanobeadsTM, a polystyrene polymer size standard (220 ± 6 nm, Polysciences Inc., Warrington, UK). To verify the zeta potential measurements, zeta

potential transfer standard (-50 mV ± 5, Malvern Instruments Ltd, UK) was used. Each measurement took approximately 30 s and this was repeated ten times for each sample, the average reading was quoted. The data were recorded using ZetaMaster S standard software PCS v1.41.

The zeta potential is a physical property that is exhibited by any particles in a suspension, and it is a measure of the magnitude of charge repulsion or attraction between particles (i.e., the magnitude of electrostatic interactions). This property influences the stability of particles in a colloidal suspension, and the measurement of the zeta potential gives insight into the causes of dispersion, aggregation, and flocculation. In aqueous media, the pH is generally one of the most important factors that affect the zeta potential. If a colloidal particle has a negative zeta potential and the pH of the solution is made more alkaline, then that particle tends to accumulate more negative charge; however, if the solution is made more acidic, that negative charge can be neutralised. If there is a further addition of acid to the solution, the particle can accumulate a positive charge; therefore, a plot of zeta potential versus pH can be obtained, see Figure 7.1. If the plot passes through zero, that is, the point of zero charge (PZC) or the isoelectric point, then this is the pH at which the colloidal system is least stable. Generally, it is assumed that a colloidal suspension is unstable with a zeta potential between -30 and 30 mV, at potentials either side of these values, the system is thought to be stable.

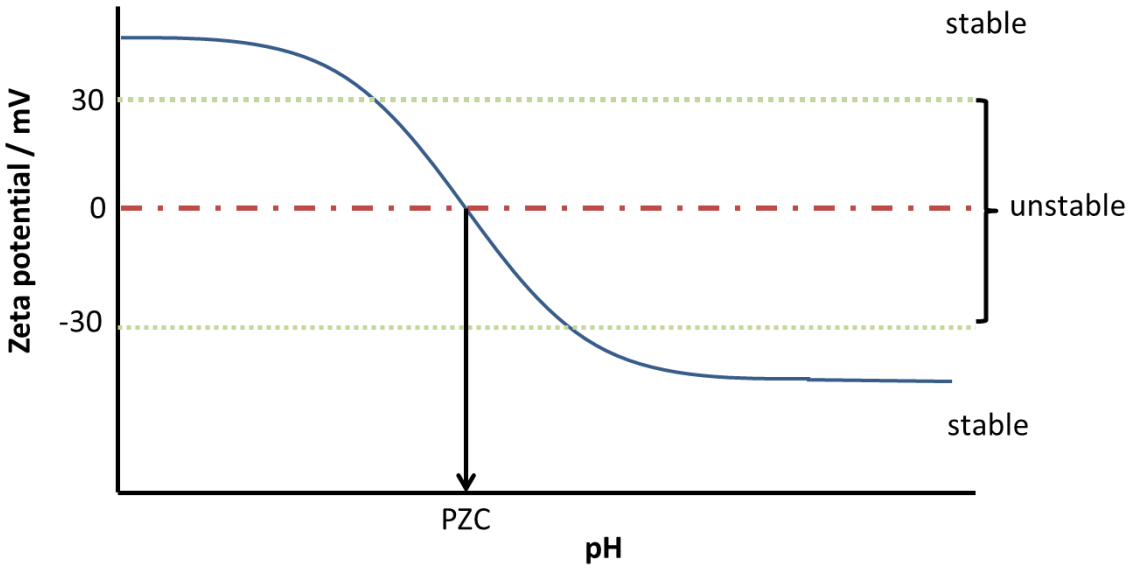

Figure 7.1. Illustration to show how the zeta potential can change as a function of pH

UV/Vis spectra were obtained on a Lambda 20 UV/Vis spectrometer (PerkinElmer, USA) with UV Winlab version 2.70.01 software. Fluorescence measurements were recorded by using either a fluoroSENS fluorimeter (Gilden Photonics, UK) with fluoroSENS system software version 1.88.7, or an LS50b luminescence spectrometer (Perkin Elmer, USA) with FL Winlab version 4.00.02 software. Fourier-transform infrared (FTIR) spectra were recorded on a Spectrum 100 FTIR-Spectrometer (PerkinElmer, USA) using Spectrum Express software. A JEM1200EXII (JEOL, Japan) transmission electron microscope (TEM) was used for imaging the P4VP starting material and P4VP C-dots.

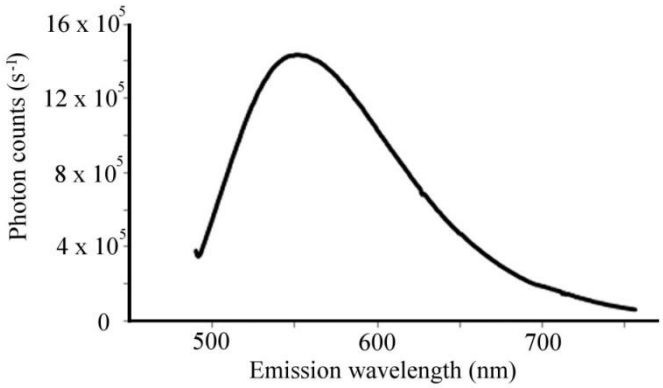

Figure 7.2. Single photon fluorescence spectrum with an excitation wavelength of 488 nm for 1 mg mL-1 P4VP C-dots in DMSO

For bioimaging studies, a multiphoton excitation technique was used. Laser light with a wavelength of 488 nm (see Figure 7.2 for the single photon fluorescence at λ_{ex} = 488 nm) was obtained from an optical parametric oscillator pumped by a pulsed mode-locked titanium sapphire laser (Mira F900, Coherent Inc. Lasers, US) that produced 180 femtosecond pulses at 75 MHz. This in turn was pumped by a solid-state continuous wave 532 nm laser (Verdi V8, Coherent Inc. Lasers, US). The oscillator's fundamental output of 910 ± 2 nm was also used for the multiphoton excitation. The laser beam was focused onto a diffraction-limited spot through a high numerical aperture (1.2) microscope objective, Nikon Corporation, Japan). Samples were illuminated at the stage of an inverted microscope (Nikon TE2000-U). An X-Y galvanometer (CGS Lumonics, US) was used to raster scan the focused laser spot for imaging. Fluorescence emission data were generated without de-scanning, therefore bypassing the scanning system and passing through a BG39 coloured glass optical filter, and the signals were detected with an external fast

microchannel plate photomultiplier tube (R3809-U, Hamamatsu, Japan). The components were linked through a Time-Correlated Single Photon Counting (TCSPC) module (SPC830, Becker & Hickl GmbH, Berlin).

Fluorescence lifetime measurements were recorded by using a TCSPC (Becker & Hickl GmbH, Berlin) following excitation at a wavelength of 910 ± 2 nm, with emissions at 360-580 nm when the P4VP C-dots were dispersed in 1: 99 DMSO: EMEM. Emission spectra data were obtained with an Acton Research Component 275 Spectrograph (Princeton Instruments, US) and an Andor iDus 420-BU CCD camera (Andor Technology, Belfast). Lifetime calculations were carried out using Becker & Hickl SPCImage Analysis software.

7.3.3 Procedure: Hydrothermal Synthesis

P4VP (400 mg) was dissolved by sonication in 1 mM acetic acid (20 mL) for 30 minutes. The solution was transferred into a 125 mL high pressure vessel (Parr Instrument Company) and heated at 200 ^{o}C for 12 h. The dark solid was removed by filtration and copiously washed with water. The solid was dissolved in EtOH and dried *in vacuo* to give a shiny brown solid (47 % yield, elemental analysis $C_7H_{7.25}NO_{0.5}$) that was collected and characterized by XPS, TEM, zeta potential measurements, IR, UV/Vis spectroscopy, and fluorescence experiments. The theorised reaction scheme is shown in Figure 7.3 and a photograph before and after carbonisation is shown in Figure 7.4.

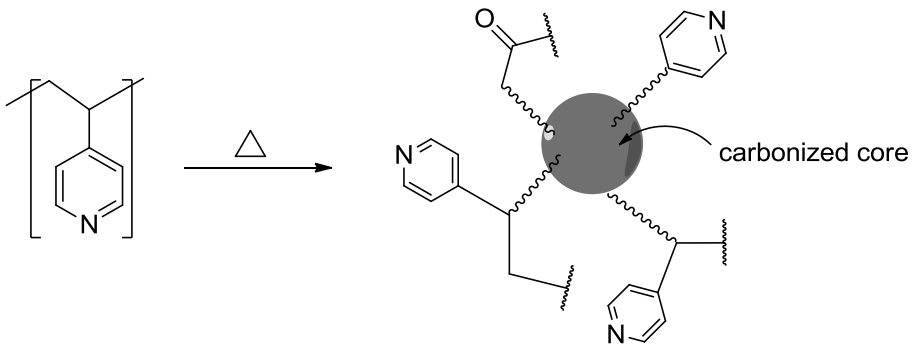

Figure 7.3. Reaction of P4VP showing a schematic of the C-dots with the expected surface functionality.

Figure 7.4. Photograph of the white P4VP starting material and the post-carbonisation P4VP C-dots product.

7.4 Results and Discussion

A TEM image of the P4VP C-dots after hydrothermal synthesis is shown in Figure 7.5(a); these can be considered more accurately as polymer aggregates containing carbonised C-dots. The P4VP polymeric starting material showed large globular structures; however, post-synthesis the P4VP has formed discrete nanoparticles within a globular matrix. The polymer aggregates containing C-dots (P4VP C-dots) have a reasonably broad size distribution of centred around 20 nm, with many larger discrete particles having a diameter of approximately 100 nm, see Figure 7.5(b).

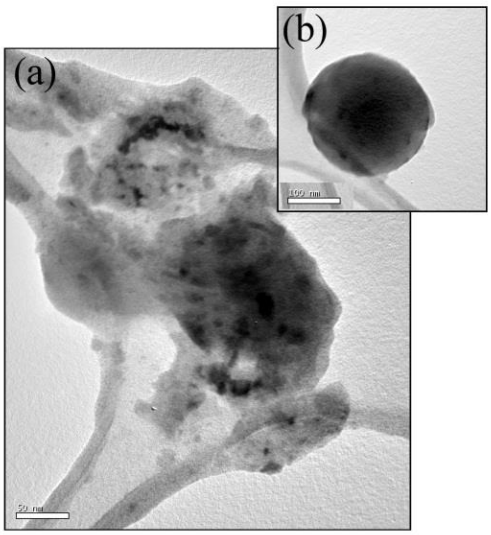

Figure 7.5. TEM images of (a) P4VP C-dots shown to be encased in uncarbonised P4VP polymer (scale bar 50 nm) and (b) individual P4VP C-dot (scale bar 100 nm) from a dispersion in water evaporated onto Lacey carbon TEM grids.

The starting P4VP polymer and the carbonized P4VP C-dots were examined using surface XPS, Figure 7.6. The P4VP starting material showed a single N1s peak with a binding energy of 398.8 eV, this is consistent with sp^2 hybridized nitrogen in the pyridine rings. The C1s signal was deconvoluted into two peaks associated with C-C/C-H-adventitious carbon (285.0 eV) and C-N from the pyridine functionality (286.0 eV). In addition to this, a C1s "shake-up" peak was observed at 292.0 eV. This signal is consistent with photoelectrons interacting with π-π* transitions associated with the aromatic pyridine ring systems.[22] There is also a signal of weak intensity corresponding to O1s at binding energy 231.8 eV and this is thought to be due to slow oxidation of the polymer surface due to ageing.

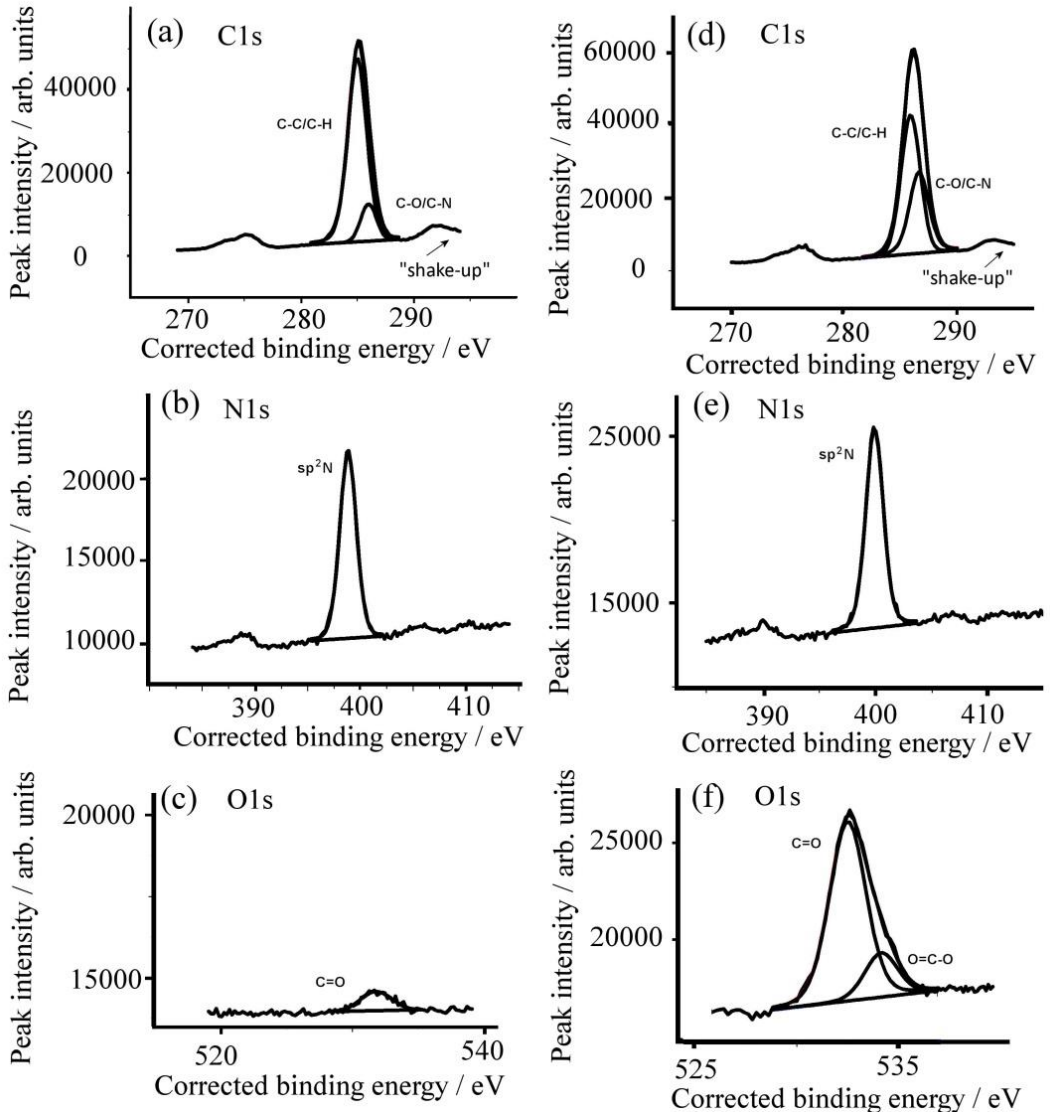

Figure 7.6. XPS data for P4VP starting material (a) C1s (b) N1s (c) O1s and P4VP C-dots (d) C1s (e) N1s (f) O1s

In comparison to the starting material XPS data, the carbonized P4VP C-dots show many similarities. The intensity of the N1s signal has a high N1s/C1s ratio (0.10) indicating that this sample has a photoelectron signal intensity close to that of the P4VP polymeric starting material. Also, the N1s peak at 398.2 eV and C1s and C1s "shake up" peaks are of similar binding energies to that observed for the P4VP starting material. The main difference between the two samples can be seen when examining the O1s signals. For the starting material, a weak single signal is seen at 531.8 eV, probably due to slow oxidation of the compound surface by ageing. Also, the carbonized P4VP C-dots showed a strong signal that could be resolved into two peaks of binding energies 531.6 and 533.3 eV, which are due to carbonyl and carboxyl oxygen, respectively.[23] This is thought to be due to oxidation/hydrolysis processes that occur during the hydrothermal carbonization of the material.

From the XPS analysis, it is clear that the synthesized material contained much of the starting material functionality as well as new oxygen functionalities, indicating the likelihood that carboxylic groups decorate the P4VP C-dot materials that have been synthesized. Thus, the P4VP C-dots still possessed important pyridine functionality after the hydrothermal treatment; this retention of functionality demonstrates that the original fluorescence properties should be maintained and the enhancement of such properties is likely attributed to the quantum size of the C-dots.

The FTIR spectrum of the synthesized P4VP C-dots is shown in Figure 7.7. A broad peak is seen at 3300 cm^{-1} ascribed (in comparison to the P4VP starting material) to an N-H stretch of the protonated pyridinium ring. The adsorption bands at 3030 and 2920 cm^{-1} are characteristic of the aromatic C-H stretching vibrations of the CH_2 groups in the pyridine ring and the asymmetric vibrations of the CH_2 groups, respectively. A peak was observed at 1650 cm^{-1} due to the N-H bending.

A small C=O peak was also observed at approximately 1700 cm^{-1} which was absent from the starting material. This is only a small peak as it is likely that only some of the outer surface had become oxidized using the hydrothermal conversion, the core material could still resemble the P4VP polymeric starting material, as confirmed by elemental analysis (P4VP C_7H_7N and C-dots $C_7H_{7.25}NO_{0.5}$). Most importantly, there was a very sharp, strong band observed at 1600 cm^{-1} that is characteristic of the stretching vibrations in the pyridine ring. This demonstrates that the pyridine functionality has been retained during the

carbonization process. Adsorption bands between 1220 and 880 cm^{-1} can be attributed to the amine C-N stretch and the peak at 820 cm^{-1} is indicative of pyridine ring out-of-plane bending. The FTIR confirms that the main functional groups of the starting material remain intact with addition carbonyl and oxygen functionalities being introduced upon carbonisation. Therefore, the fluorescence can be attributed to the P4VP starting material, which is enhanced upon carbonisation due to the formation of materials on the nanoscale.

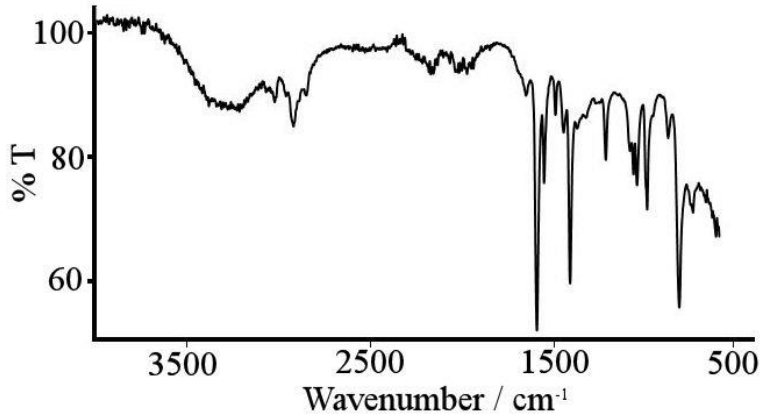

Figure 7.7. Solid state FTIR spectrum for P4VP C-dots

The zeta potential, Figure 7.8, was measured for the P4VP C-dots as a function of pH. A solution of P4VP C-dots was prepared in DMSO and then diluted to a concentration of 1 µg mL^{-1} with 0.1 M phosphate buffer at different pH values at a ratio of 50:50 DMSO: buffer. This ratio of buffer to DMSO was used to maintain solubility, but also to observe the trends as a function of pH; when more DMSO was used, there was no effect of buffer pH value observed. It is likely that there could be a more dramatic change with pH if less DMSO was used; however, this was not practically possible due to precipitation.

The zeta potential across a pH range from 2 to 12 was relatively constant at approximately -7 ± 2 mV. This value suggests a dominating effect of carboxylates on the zeta potential.[24] Zeta measurements indicated that the isoelectric point of the P4VP C-dots occurred at approximately pH 2. However, over the entire pH range, the P4VP C-dots in DMSO/buffer were relatively unstable and formed aggregates, presumably because of the low zeta potential.

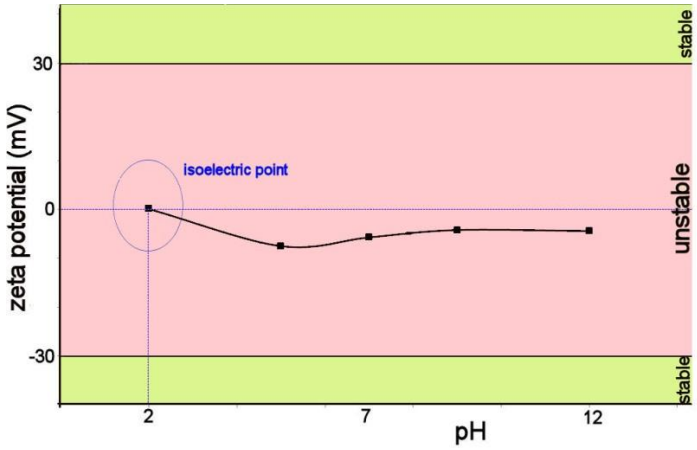

Figure 7.8. Zeta potential versus pH for P4VP C-dots in 50:50 DMSO: 0.1 M phosphate buffer

UV/Vis measurements of 1 mg mL^{-1} P4VP C-dots in DMSO showed a peak at 350 nm, Figure 7.9(b). This correlated well with a 3-dimensional map of excitation wavelength versus emission wavelength for the same sample, as shown in Figure 7.9(a). The 3-D contour map clearly shows that the greatest emission was observed at 410 nm with an excitation wavelength of 350 nm.

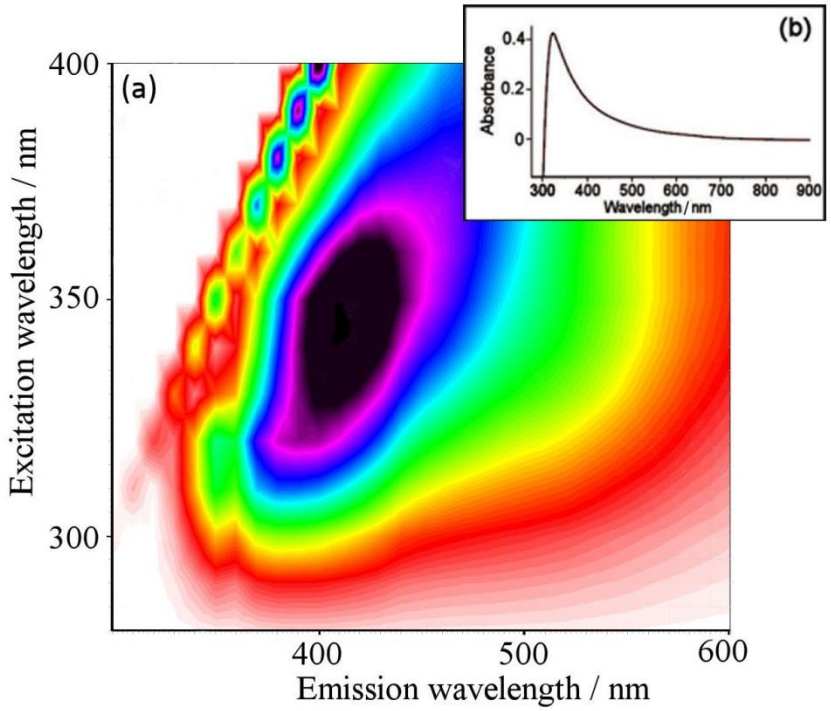

Figure 7.9. Fluorescence mapping (a) and UV/Vis spectrum (b) for P4VP C-dots in DMSO (1 mg mL-1) showing that the maximum emission (at 410 nm) is observed when the excitation wavelength is 350 nm in agreement with the maximum UV/Vis absorbance.

The relative quantum yield (QY) of the P4VP C-dots in DMSO was determined by comparison to a $[Ru(bipy)_3](PF_6)_2$ standard in water with a known quantum yield of 4.2% following Equation (7.1), where Φ is the relative quantum yield, *D* is the integrated area of fluorescence emission peak, *A* is the absorbance at the excitation wavelength, *I* is the flux at the excitation wavelength and η is refractive index (subscript R and S refer to the reference and the sample, respectively).

$$\Phi_{S=}\Phi_R.\left(\frac{D_S}{D_R}\right).\left(\frac{A_R}{A_S}\right).\left(\frac{I_R}{I_S}\right).\left(\frac{\eta_S}{\eta_R}\right)^2 \quad (7.1)$$

The P4VP C-dots in DMSO exhibited a QY of approximately 3 % at an excitation wavelength of 350 nm. The quantum yield of the most of C-dots is below 1 % and not to the magnitude of QDs; however, this simple and effective method which requires minimal work up, results in improved QY without the need for surface passivation.[8, 16, 25]

The effect that different solvents had on the fluorescence emission was investigated as shown in Figure 7.10. By comparing DMSO; a polar aprotic solvent, with EtOH and chloroform, polar protic and non-polar respectively; a clear shift in the maximum fluorescence intensity was observed. Once the fluorophore has been excited to the first excited state, the fluorophore begins to lose vibrational energy to the solvent molecules as relaxation from higher to lower energy levels occurs. The surrounding solvent molecules assist with the stabilization process and the more polar the solvent; the further the energy level of the excited state is lowered. This is because of solvent relaxation caused by the re-orientation of solvent molecules around the fluorophore for the re-alignment of the dipole moments. Thus, with more polar solvents further decreasing the energy level of the solvent-relaxed state, there is a smaller separation between the ground state and the excited state. A lower energy separation results in a shift to longer wavelengths of the fluorescence emission, known as the bathochromic shift.[26, 27] In the case of the P4VP C-dots, the bathochromic shift was due to the stabilization of the excited state fluorophore in more polar solvents, i.e., in DMSO. Therefore, a shift of 11 nm (0.084 eV) was observed when changing from chloroform to EtOH and a shift of 20 nm (0.15 eV) was observed when the solvent was changed from chloroform to DMSO.

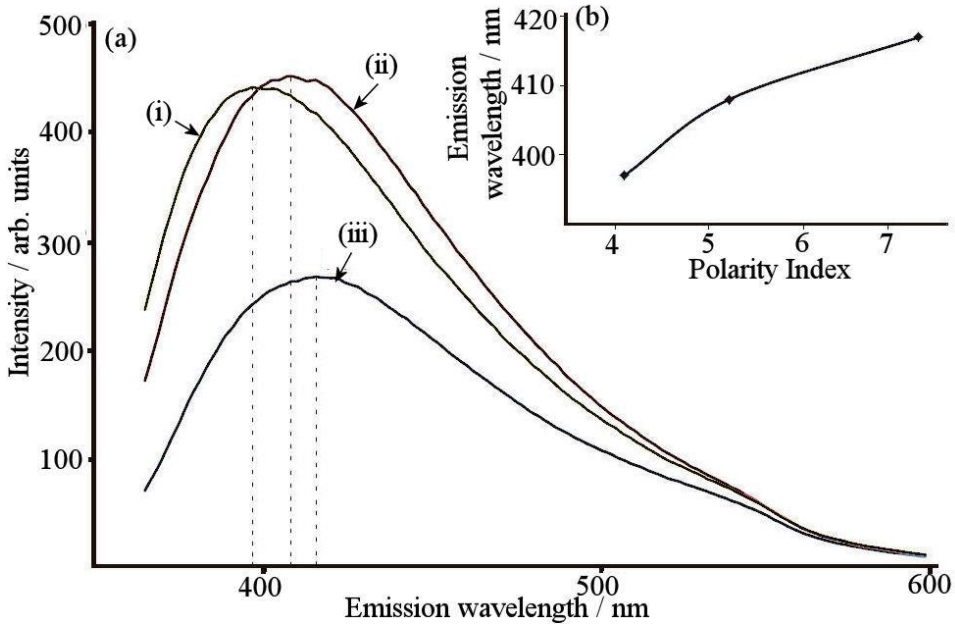

Figure 7.10. (a) Fluorescence emission spectra at an excitation wavelength of 350 nm for 1 mg mL-1 P4VP in (i) chloroform (ii) ethanol and (iii) DMSO (b) A plot of the emission wavelength for the maximum fluorescence intensity versus the polarity index of the solvent.[28]

The pH effect on the fluorescence was investigated and minor changes in the maximum wavelength were observed [see Figure 7.11(a)]. There was a slight decrease in intensity of the signal (more dramatic with less DMSO), which is likely to have been caused by the colloidal material becoming less stabilized in phosphate buffer at pH 12. It was observed that the maximum of the emission shifted by 5 nm between pH 2 and pH 7, and a further 5 nm when the pH was adjusted from 7 to pH 12, averaging 1 nm per pH unit. In summary, there appears only to be a small effect of pH (e.g. no pyridine/pyridinium equilibrium), possibly due to the chromophore being buried in the particle core.

Three-dimensional fluorescence mapping of the C-dots revealed further information at different pH. At pH 2 there was one significant correlation observed consistent with the previous data, that the maximum intensity was observed at an emission wavelength of 410 nm when excited at 350 nm, see Figure 7.11(b). When the pH was increased, additional excitation/emission signals were seen. At pH 7, there was one additional peak at an excitation wavelength of 320 nm with a corresponding emission at 380 nm [Figure 7.11(c)]. At pH 12 [Figure 7.11(d)], there were a large number of additional signals (λ_{ex} = 320, λ_{em} = 380; λ_{ex} = 350, λ_{em} = 410; λ_{ex} = 370, λ_{em} = 470; λ_{ex} = 380, λ_{em} = 480; λ_{ex} = 390, λ_{em} = 490; λ_{ex} = 400, λ_{em} = 510).

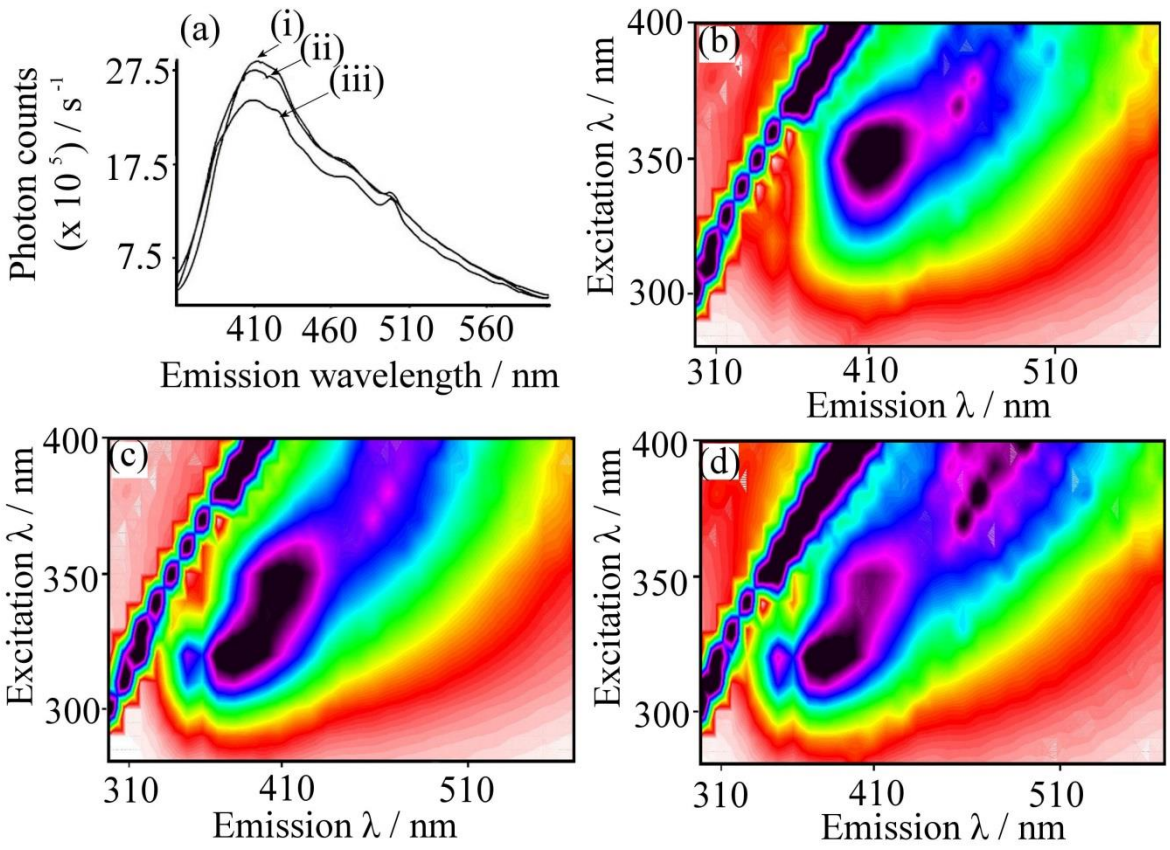

Figure 7.11. Single photon fluorescence spectra in 50:50 DMSO:0.1M phosphate buffer solution (a) at λ_{ex} = 350 nm (i) pH 2 (ii), pH 7, and (iii) pH 12; 3D fluorescence map pH 2 (b) pH 7 (c), and pH 12 (d)

The fluorescence map of the parent starting material is shown in Figure 7.12, this shows that the parent material displays a similar mechanism both before and after hydrothermal conversion. Much of this is probably due to the fact that the P4VP C-dots are contained within the polymer matrix, i.e., the some of the starting polymer remains in the product. The intensity of the emission signal at 410 nm in the post-carbonisation material indicates that there has been an enhancement due to the formation of particles with a quantum size. This also proves that the main fluorophore is most likely to be the pyridine units and this provides further evidence to support the presence of intact pyridine species post-hydrothermal treatment. The fluorescence mapping at different pH values reveals a complex behaviour of the P4VP and indicates that protonation of the pyridine functionality is likely to result in different fluorophore behaviour, also at pH 12, there is some indication that the quantum material is broken down as the 3D map begins to resemble to starting material spectrum.

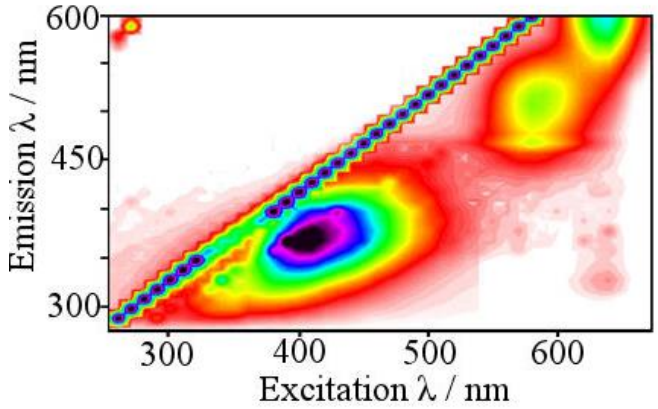

Figure 7.12. 3D fluorescence map of the P4VP polymeric starting material dissolved in EtOH at 1 mg mL^{-1}

The fluorescence was extended from single photon to two photon excitation. Two photon fluorescence data are given in Figure 7.13(b) [at λ_{ex} = 910 nm; the corresponding single photon spectrum, λ_{ex} = 455 nm, is shown in Figure 7.13(a)]. The observed short lived component of a two component lifetime may be due to aggregation of the sample (ps order lifetime). A good fit, with a $\chi 2$ value of 1.37, was obtained for two exponential component analysis of the decay data, see Figure 7.13(c). The two-component exponential fit gave a pre-exponential factor of 49 % with a lifetime of 1.24 ns and 51 % with a lifetime of 4.67 ns.

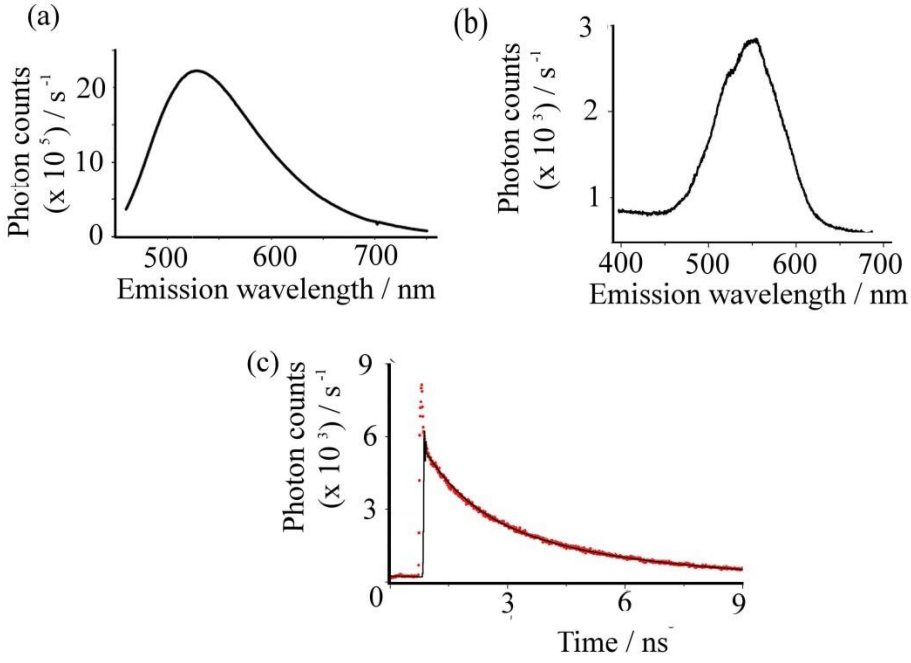

Figure 7.13. Single photon fluorescence emission spectra at excitation wavelength at excitation wavelength 455 nm (a), (c) two photon fluorescence spectrum at excitation wavelength 910 nm (b) and the corresponding fluorescence decay trace (c) for 1 mg mL^{-1} P4VP C-dots in DMSO.

Confocal fluorescence imaging, coupled with fluorescence lifetime imaging microscopy (FLIM) following multiphoton excitation with near infrared (NIR) femtosecond laser pulses are widely used in the study of small molecule fluorophores particularly for *in vitro* imaging studies.[29-32] To date, FLIM has been used primarily on common fluorescent dyes (e.g., green fluorescent protein (GFP)-tagged proteins, fluorescein-based derivatives as well as indole containing compounds).[33-35] Recent studies have explored lifetime imaging of fluorescent CNT complexes which permitted, for the first time, to probe functional carbon nanomaterials' integrity in a cellular environment.[36] The combination of two-photon excitation with FLIM allows the use of NIR light to provide deeper tissue penetration, reduced cellular cytotoxicity and scattering, and improved signal detection since the standard photomultiplier tube used as detectors are less sensitive above 850nm. By exploiting the sensitivity of lifetime measurements, which are independent of intensity, excited state lifetime measurements were used to provide a method for studying the integrity of newly synthesized P4VP C-dots in cellular media. This could open up new vistas for the design and spectroscopic investigation of such new carbon nanomaterials with light emitting properties as synthetic scaffolds for future drug delivery materials.

Control cell viability studies were performed by using 1:99 DMSO/EMEM to ensure that the cells could survive the presence of DMSO. Often, DMSO is used as an aid for penetrative drug delivery methods because DMSO can easily penetrate cell membranes.[37, 38] It has also been demonstrated that the presence of DMSO can enhance the cytotoxicity of some drugs, such as cisplatin, by breaking down the cell membrane and encouraging cell death.[39-41] However, at low concentrations, DMSO has also been shown to be biocompatible and can be used without destroying the integrity of the cell membrane.[41-43] Despite the adverse effects of DMSO, by performing cell viability studies for 15 and 60 minutes, it was proven that at 1:99 DMSO/EMEM, the cells were living and the cell membranes were intact.

High-resolution confocal imaging under single-photon (405, 488 and 543 nm) or two-photon excitation (910 nm), using a mode-locked Ti-sapphire laser, generated images of the dispersed P4VP C-dots in cellular media by the raster scanning of the laser spot in the *xy* plane (Figure 7.14). Two-photon fluorescence imaging and emission lifetime measurements were carried out using FLIM in the presence of HeLa cell lines for the P4VP C-dots. Single photon laser scanning confocal fluorescence imaging showed that the

nanoparticles retained their intrinsic fluorescence emission under single photon excitation (λ_{ex} 405, 488 and 543 nm) in the presence of cells.

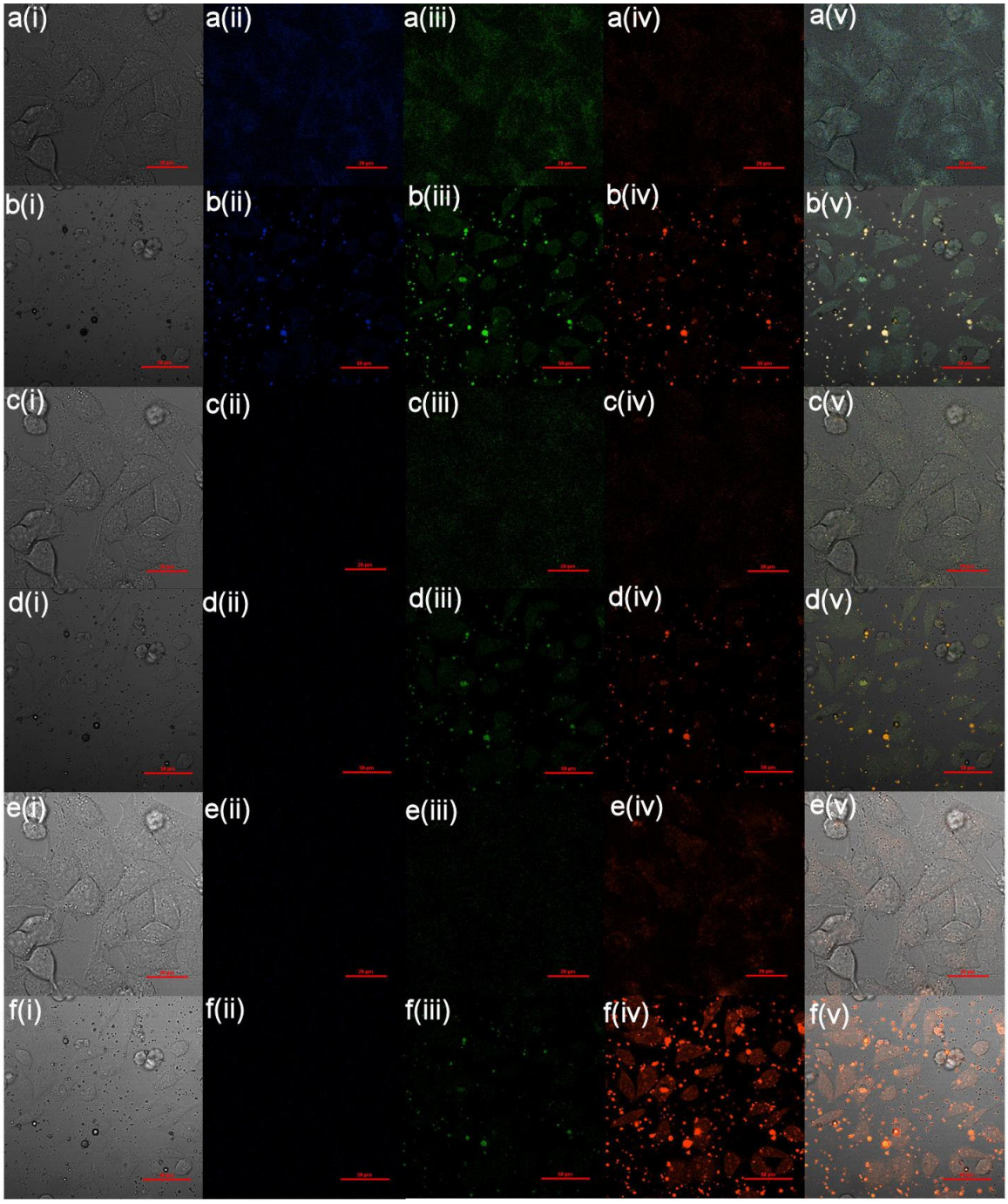

Figure 7.14. Single Photon laser scanning confocal imaging of HeLa cells incubated at 37^{o}C for 1 h in 1: 99 DMSO/EMEM for (a) control (scale bar 20 pm) and (b) P4VP C-dots, λ_{ex} = 405 nm (scale bar 50 pm), (c) control (scale bar 20 pm) and (d) P4VP C-dots, λ_{ex} = 488 nm (scale bar 50 pm), (e) control (scale bar 20 pm) and (f) P4VP C-dots, λ_{ex} = 543 nm (scale bar 50 pm) (i) brightfield microscopy image (ii) blue channel (450-435 nm) (iii) green channel (515-530 nm) (iv) red channel (605-675 nm) and (v) overlay of (i) – (iv) images. These are raw unprocessed images, visualized with NISlight (Nikon).

The control experiments showed weak fluorescence intensity assignable to the cells autofluorescence when excited at 405 nm. At this wavelength the fluorescence from the C-dot is just above the autofluorescence background. However, at the 543 nm excitation Figure 7.14(f) clearly shows higher signal intensity with respect to the background autofluorescence. The intensity of this emission in the presence of HeLa cells compares well with standard organic dyes such as Hoechst under similar imaging assays (Figure 7.15).

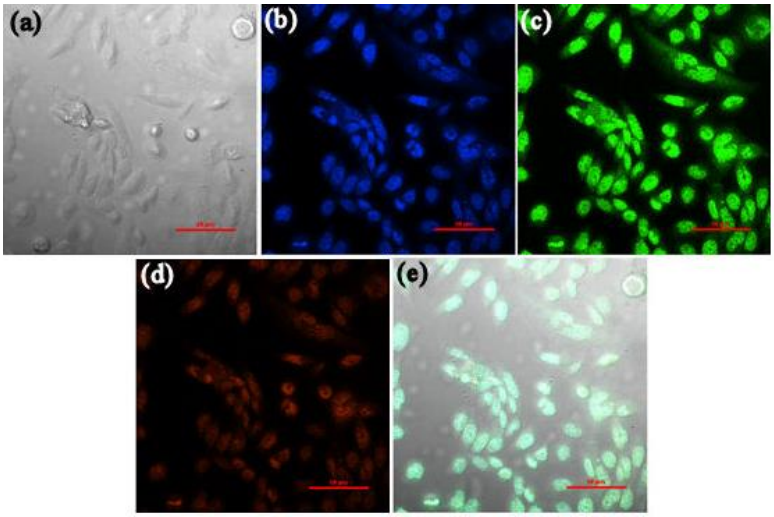

Figure 7.15. Single photon confocal images of HeLa cells incubated at 37^{o}C in 1: 99 DMSO: EMEM with Hoechst dye (a) brightfield microscopy image, (b) blue channel (450 – 435 nm), (c) green channel (515 – 530 nm), (d) red channel (605 – 675 nm) and (e) overlay of images (a) – (d).

To further probe the potential of P4VP C-dots as nanomedicines, or as a synthetic scaffold for future applications as traceable imaging probes inside living cells; two-photon emission decay lifetime spectroscopy was applied. Firstly, spectra were recorded following pulsed laser excitation (λ_{ex} = 910 nm in DMSO). DMSO was selected as the solvent of choice as the P4VP C-dots showed minimum scattering due to aggregation within the experimental timescale in this solvent and due to its low volatility. Secondly, excited state lifetimes were recorded by using time-correlated single photon counting with a less than 40 ps instrument-response function. Furthermore, to verify whether the new materials remain stable *in vitro* with respect to decomposition, fluorescence emission lifetime measurements were carried out using two-photon FLIM in the presence of HeLa cell lines (1 h incubation,

37°C, using 910 nm excitation wavelength from a mode locked Mira Ti-sapphire laser, 180 fs pulse, 75 MHz).

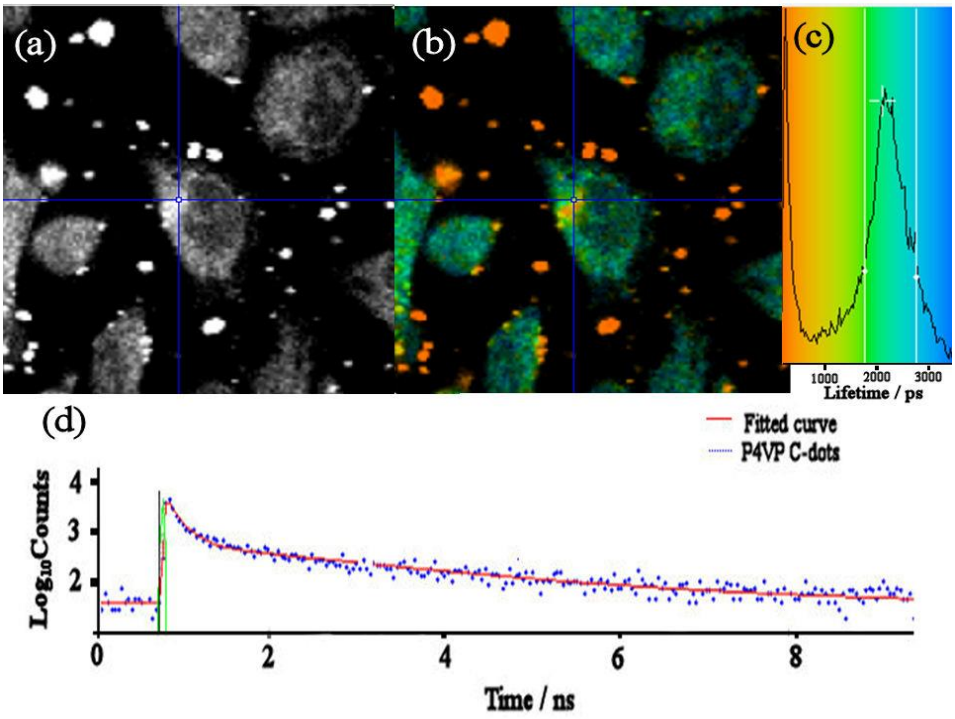

Figure 7.16. Two-photon confocal fluorescence (λex = 910 nm) intensity image (a), lifetime mapping (b), corresponding lifetime distribution curve (c) and fluorescence decay trace (d) for P4VP C-dots in DMSO/EMEM 1:99.

In both systems (solution experiments in DMSO versus *in vitro* imaging in the presence of HeLa cells) these nanoparticles exhibited strong fluorescence emission with more than one lifetime component: calculations (SPC Image analysis software) indicated a long component on the order of several nanoseconds (2.2 ns, 13 %) for highly dispersed particles and a much shorter component on the order of several hundred picoseconds (0.14 ps, 87 %) for aggregated P4VP C-dots. The P4VP C-dots of the greatest interest, those that are highly dispersed, have an average lifetime of 2.1 ± 0.9 ns at full width half height (FWHH), see Figure 7.16.

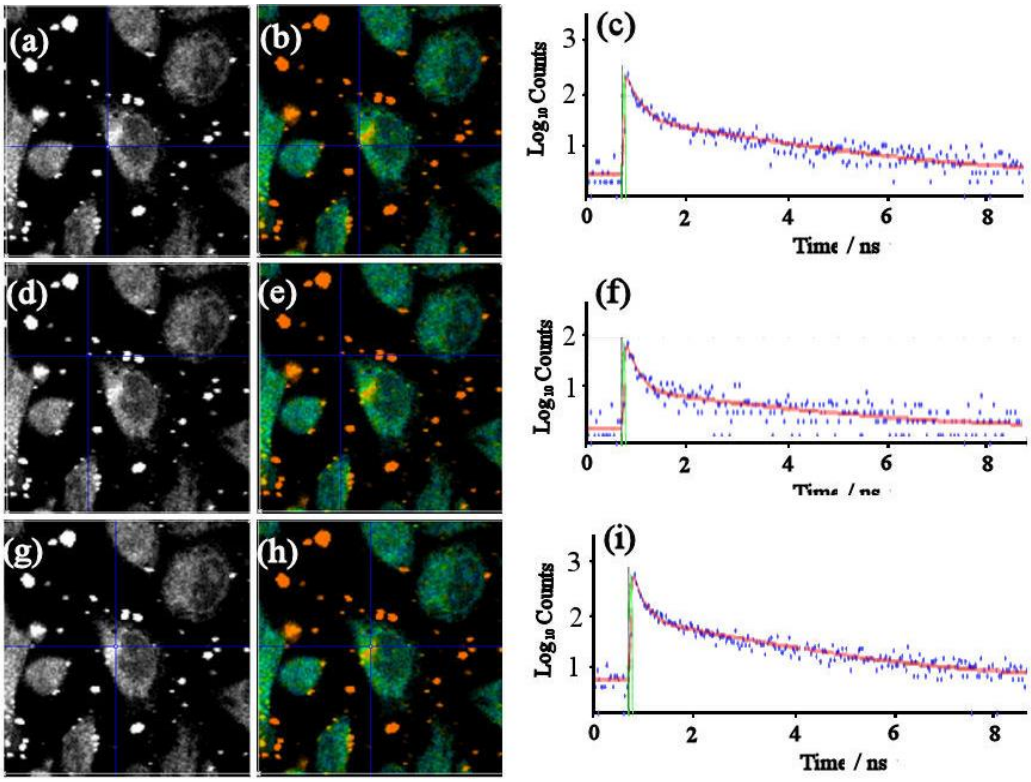

Figure 7.17. Two-photon confocal fluorescence (λ_{ex} = 910 nm) for P4VP C-dots in 1:99 DMSO: EMEM after incubation for 15 minutes; intensity image in cell membrane (a), in cell medium (d) and inside the cell (g); lifetime mapping in cell membrane (b), in cell medium (e), and inside the cell (h); fluorescence decay in cell membrane (c), in cell medium (f) ,and inside the cell (i)

To study the effect that the P4VP C-dots had on HeLa cells, the fluorescence data was obtained after both 15 minutes and 1 hour. After 15 minutes incubation, the P4VP CNPs were seen in the cell medium, in cell membranes, and inside the cells, see Figure 7.17. For each different environment the nanoparticles exhibited strong fluorescence emission with two lifetime components. Calculations (SPC Image analysis software) indicated a long component of several nanoseconds for highly disperesed CNPs and a very short component on the order of several picoseconds, see Table 7.1.

Table 7.1. Two photon lifetime decays: χ^2 values and lifetimes of P4VP CNPs in 1: 99 DMSO: EMEM after incubation for 15 minutes at 37°C

CNP location	X^2	Long lifetime component (ns)	Short lifetime component (ps)
Cell membrane	1.07	2.44 (14.3 %)	175 (85.7 %)
Cell medium	1.01	2.80 (10.3 %)	150 (89.7 %)
Inside cell	1.11	2.16 (12.7 %)	143 (87.3 %)

After 1 hour incubation at 37°C, the P4VP CNPs were once again seen in the cell medium, cell membranes, and inside the cells. Compared to the same images after 15 minutes (Figure 7.17), the aggregations were larger but also more nanoparticles were seen to have entered the cells and bound to the cell memberanes, see Figure 7.18.

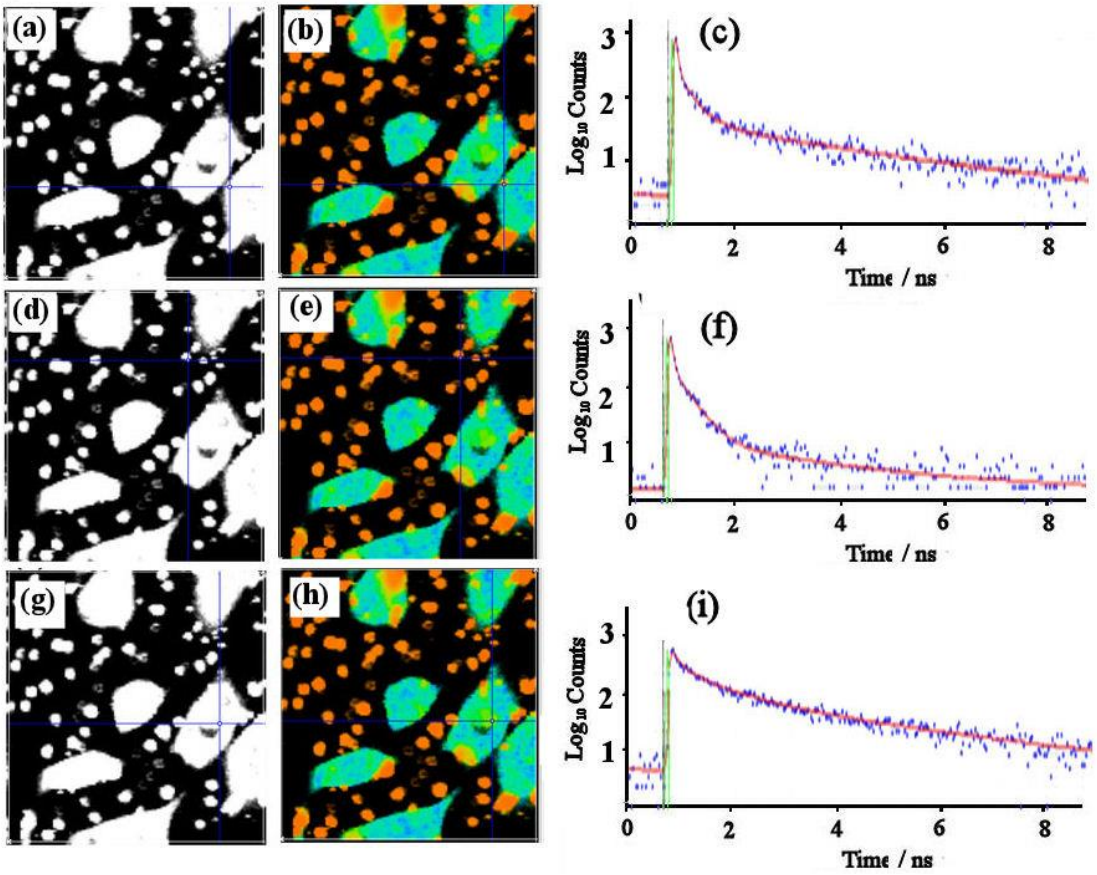

Figure 7.18. Two-photon confocal fluorescence (λ_{ex} = 910 nm) for P4VP C-dots in 1:99 DMSO: EMEM after incubation for 1 hour; intensity image in cell membrane (a), in cell medium (d) and inside the cell (g); lifetime mapping in cell membrane (b), in cell medium (e), and inside the cell (h); fluorescence decay in cell membrane (c), in cell medium (f), and inside the cell (i)

For each different environment the nanoparticles exhibited strong fluorescence emission with three lifetime components, the extra component is likely to be due to conformational changes and interactions that occur within cells. Calculations (SPC Image analysis software) indicated a long component of several nanoseconds for highly disperesed CNPs, a short component on the order of several hundreds of picoseconds and an extremely short component in the picosecond timescale, see Table 7.2.

Table 7.2. Two photon lifetime decays: χ^2 values and lifetimes of P4VP CNPs in 1: 99 DMSO: EMEM after incubation for 1 hour at 37°C

CNP location	X^2	Long lifetime component (ns)	Shorter lifetime component (ps)	Shortest lifetime component (ps)
Cell membrane	1.15	2.94 (2.3 %)	260 (14.9 %)	41 (82.7 %)
Cell medium	1.20	2.35 (0.6 %)	286 (15.4 %)	42 (84 %)
Inside cell	1.24	3.21 (12.9 %)	806 (30.5 %)	164 (56.6 %)

7.5 Conclusion

In summary, a simple hydrothermal synthesis for the formation of a novel fluorescent carbon nanomaterial has been developed. These new P4VP C-dots have been fully characterized using XPS, IR, zeta potential measurements, and TEM. The amorphous P4VP C-dots exhibit strong fluorescent properties that show only weak pH and solvent dependency in single photon fluorescence experiments. Finally, the potential for bio-imaging applications has been investigated. The P4VP C-dots retain their intrinsic fluorescence in cell medium and the most highly dispersed particles were seen to enter HeLa cells without causing significant damage to the outer cell membrane. This provides an excellent new and general pathway for developing non-toxic nanomedicines and novel synthetic scaffolds for future applications as traceable imaging probes inside living cells.

7.6 References

1. Rassaei, L., M.J. Bonne, M. Sillanpaa, and F. Marken, *Binding Site Control in a Layer-by-Layer Deposited Chitosan-Carbon Nanoparticle Film Electrode,* New J. Chem., 2008, **32**, 1253-1258.
2. Xu, X.Y., R. Ray, Y.L. Gu, H.J. Ploehn, L. Gearheart, K. Raker, and W.A. Scrivens, *Electrophoretic Analysis and Purification of Fluorescent Single-Walled Carbon Nanotube Fragments,* J. Am. Chem. Soc., 2004, **126**, 12736-12737.
3. Bourlinos, A.B., A. Stassinopoulos, D. Anglos, R. Zboril, V. Georgakilas, and E.P. Giannelis, *Photoluminescent Carbogenic Dots,* Chem. Mater., 2008, **20**, 4539-4541.
4. Lu, W., X. Qin, S. Liu, G. Chang, Y. Zhang, Y. Luo, A.M. Asiri, A.O. Al-Youbi, and X. Sun, *Economical, Green Synthesis of Fluorescent Carbon Nanoparticles and Their Use as Probes for Sensitive and Selective Detection of Mercury(II) Ions*, Anal. Chem., 2012, **84**, 5351-5357.
5. Baker, S.N. and G.A. Baker, *Luminescent Carbon Nanodots: Emergent Nanolights*, Angew. Chem. Int. Ed., 2010, **49**, 6726-6744.
6. Titirici, M.-M. and M. Antonietti, *Chemistry and Materials Options of Sustainable Carbon Materials Made by Hydrothermal Carbonization,* Chem. Soc. Rev., 2010, **39**, 103-116.
7. Zheng, L., Y. Chi, Y. Dong, J. Lin, and B. Wang, *Electrochemiluminescence of Water-Soluble Carbon Nanocrystals Released Electrochemically from Graphite*, J. Am. Chem. Soc., 2009, **131**, 4564-4565.
8. Zhao, Q.-L., Z.-L. Zhang, B.-H. Huang, J. Peng, M. Zhang, and D.-W. Pang, *Facile Preparation of Low Cytotoxicity Fluorescent Carbon Nanocrystals by Electrooxidation of Graphite,* Chem. Commun., 2008, **41**, 5116-5118.
9. Zhou, J., C. Booker, R. Li, X. Zhou, T.-K. Sham, X. Sun, and Z. Ding, *An Electrochemical Avenue to Blue Luminescent Nanocrystals from Multiwalled Carbon Nanotubes (MWCNTs),* J. Am. Chem. Soc., 2007, **129**, 744-745.
10. Ming, H., Z. Ma, Y. Liu, K. Pan, H. Yu, F. Wang, and Z. Kang, *Large Scale Electrochemical Synthesis of High Quality Carbon Nanodots and their Photocatalytic Property,* Dalton Trans., 2012, **41**, 9526-9531.
11. Cao, L., X. Wang, M.J. Meziani, F. Lu, H. Wang, P.G. Luo, Y. Lin, B.A. Harruff, L.M. Veca, D. Murray, S.-Y. Xie, and Y.-P. Sun, *Carbon Dots for Multiphoton Bioimaging,* J. Am. Chem. Soc., 2007, **129**, 11318-11319.
12. Hu, S.-L., K.-Y. Niu, J. Sun, J. Yang, N.-Q. Zhao, and X.-W. Du, *One-Step Synthesis of Fluorescent Carbon Nanoparticles by Laser Irradiation,* J. Mater. Chem., 2009, **19**, 484-488.
13. Sun, Y.P., B. Zhou, Y. Lin, W. Wang, K.A.S. Fernando, P. Pathak, M.J. Meziani, B.A. Harruff, X. Wang, H.F. Wang, P.J.G. Luo, H. Yang, M.E. Kose, B.L. Chen, L.M. Veca, and S.Y. Xie, *Quantum-Sized Carbon Dots for Bright and Colorful Photoluminescence,* J. Am. Chem. Soc., 2006, **128**, 7756-7757.
14. Liu, R., D. Wu, S. Liu, K. Koynov, W. Knoll, and Q. Li, *An Aqueous Route to Multicolor Photoluminescent Carbon Dots Using Silica Spheres as Carriers*, Angew. Chem. Int. Ed., 2009, **48**, 4598-4601.
15. Zhu, H., X. Wang, Y. Li, Z. Wang, F. Yang, and X. Yang, *Microwave Synthesis of Fluorescent Carbon Nanoparticles with Electrochemiluminescence Properties,* Chem. Commun., 2009, **34**, 5118-5120.

16. Ray, S.C., A. Saha, N.R. Jana, and R. Sarkar, *Fluorescent Carbon Nanoparticles: Synthesis, Characterization, and Bioimaging Application*, J. Phys. Chem. C, 2009, **113**, 18546-18551.
17. Tian, L., D. Ghosh, W. Chen, S. Pradhan, X. Chang, and S. Chen, *Nanosized Carbon Particles From Natural Gas Soot*, Chem. Mater., 2009, **21**, 2803-2809.
18. Hsu, P.-C. and H.-T. Chang, *Synthesis of High-quality Carbon Nanodots from Hydrophilic Compounds: Role of Functional Groups*, Chem. Commun., 2012, **48**, 3984-3986.
19. Yang, Y., J. Cui, M. Zheng, C. Hu, S. Tan, Y. Xiao, Q. Yang, and Y. Liu, *One-Step Synthesis of Amino-Functionalized Fluorescent Carbon Nanoparticles by Hydrothermal Carbonization of Chitosan*, Chem. Commun., 2012, **48**, 380-382.
20. Li, H., X. He, Z. Kang, H. Huang, Y. Liu, J. Liu, S. Lian, C.H.A. Tsang, X. Yang, and S.-T. Lee, *Water-Soluble Fluorescent Carbon Quantum Dots and Photocatalyst Design*, Angew. Chem. Int. Ed., 2010, **49**, 4430-4434.
21. Yang, S.-T., X. Wang, H. Wang, F. Lu, P.G. Luo, L. Cao, M.J. Meziani, J.-H. Liu, Y. Liu, M. Chen, Y. Huang, and Y.-P. Sun, *Carbon Dots as Nontoxic and High-Performance Fluorescence Imaging Agents*, J. Phys. Chem. C, 2009, **113**, 18110-18114.
22. Pels, J.R., F. Kapteijn, J.A. Moulijn, Q. Zhu, and K.M. Thomas, *Evolution of Nitrogen Functionalities in Carbonaceous Materials During Pyrolysis*, Carbon, 1995, **33**, 1641-1653.
23. Zhang, D., S.M. Dougal, and M.S. Yeganeh, *Effects of UV Irradiation and Plasma Treatment on a Polystyrene Surface Studied by IR-Visible Sum Frequency Generation Spectroscopy*, Langmuir, 2000, **16**, 4528-4532.
24. Song, S.-H., S.J. Lee, and S.-H. Rhee, *Synthesis of Biodegradable Poly(epsilon-caprolactone)-Organosiloxane Hybrid with Carboxylate Groups*, J. Biomed. Mater. Res., B, 2012, **100B**, 1289-1297.
25. Liu, H., T. Ye, and C. Mao, *Fluorescent Carbon Nanoparticles Derived from Candle Soot*, Angew. Chem. Int. Ed., 2007 **46**, 6473-6475.
26. Demeter, A., T. Berces, L. Biczok, V. Wintgens, P. Valat, and J. Kossanyi, *Comprehensive Model of the Photophysics of N-Phenylnaphthalimides: The Role of Solvent and Rotational Relaxation*, J. Phys. Chem., 1996, **100**, 2001-2011.
27. Fdez. Galvan, I., M. Elena Martin, A. Munoz-Losa, M. Luz Sanchez, and M.A. Aguilar, *Solvent Effects on the Structure and Spectroscopy of the Emitting States of 1-Phenylpyrrole*, J. Chem. Theory Comput., 2011, **7**, 1850-1857.
28. Fisher Scientific, *http://www.fisher.co.uk/index.php/en/chemical-technical-tools/194-chemical-data--information-tables/1079-summary-of-key-physical-data-for-solvents*. [24th September 2012].
29. König, K., *Multiphoton Microscopy in Life Sciences*, J. Microsc.-Oxford, 2000, **200**, 83-104.
30. Suhling, K., P.M.W. French, and D. Phillips, *Time-Resolved Fluorescence Microscopy*, Photochem. Photobiol. Sci., 2005, **4**, 13-22.
31. Stutzmann, G.E. and I. Parker, *Dynamic Multiphoton Imaging: A Live View from Cells to Systems*, Physiology, 2005, **20**, 15-21.
32. Oheim, M., D.J. Michael, M. Geisbauer, D. Madsen, and R.H. Chow, *Principles of Two-Photon Excitation Fluorescence Microscopy and Other Nonlinear Imaging Approaches*, Adv. Drug Delivery Rev., 2006, **58**, 788-808.
33. Botchway, S.W., A.W. Parker, R.H. Bisby, and A.G. Crisostomo, *Real-Time Cellular Uptake of Serotonin using Fluorescence Lifetime Imaging with Two-Photon Excitation*, Microsc. Res. Tech., 2008, **71**, 267-273.

34. Bisby, R.H., A.G. Crisostomo, S.W. Botchway, and A.W. Parker, *Nanoscale Hydroxyl Radical Generation from Multiphoton Ionization of Tryptophan.* Photochem. Photobiol., 2009. **85**, 353-357.
35. Treanor, B., P.M.P. Lanigan, K. Suhling, T. Schreiber, I. Munro, M.A.A. Neil, D. Phillips, D.M. Davis, and P.M.W. French, *Imaging Fluorescence Lifetime Heterogeneity Applied to GFP-Tagged MHC Protein at an Immunological Synapse,* J. Microsc.-Oxford, 2005. **217**, 36-43.
36. Hu, Z., G.D. Pantos, N. Kuganathan, R.L. Arrowsmith, R.M.J. Jacobs, G. Kociok-Koehn, J. O'Byrne, K. Jurkschat, P. Burgos, R.M. Tyrrell, S.W. Botchway, J.K.M. Sanders, and S.I. Pascu, *Interactions Between Amino Acid-Tagged Naphthalenediimide and Single Walled Carbon Nanotubes for the Design and Construction of New Bioimaging Probes,* Adv. Funct. Mater., 2012, **22**, 503-518.
37. Dearman, R.J., D.A. Basketter, and I. Kimber, *Selective Induction of Type 2 Cytokines Following Topical Exposure of Mice to Platinum Salt,*. Food Chem. Toxicol., 1998, **36**, 199-207.
38. Huang, R.S., E.O. Kistner, W.K. Bleibel, S.J. Shukla, and M.E. Dolan, *Effect of Population and Gender on Chemotherapeutic Agent-Induced Cytotoxicity,* Mol. Cancer Ther., 2007, **6**, 31-36.
39. Tanley, S.W.M., A.M.M. Schreurs, L.M.J. Kroon-Batenburg, J. Meredith, R. Prendergast, D. Walsh, P. Bryant, C. Levy, and J.R. Helliwell, *Structural Studies of the Effect that Dimethyl Sulfoxide (DMSO) has on Cisplatin and Carboplatin Binding to Histidine in a Protein,* Acta Crystallogr., D, 2012, **68**, 601-612.
40. Mickey, D.D., L. Carvalho, and K. Foulkes, *Conventional Chemotherapeutic-Agents Combined with DMSO or DFMO in Treatment of Rat Prostate Carcinoma,* Prostate, 1989, **15**, 221-232.
41. Pommier, R.F., E.A. Woltering, G. Milo, and W.S. Fletcher, *Cyto-Toxicity of Dimethyl-Sulfoxide and Antineoplastic Combinations Against Human-Tumors,* Am. J. Surg., 1988, **155**, 672-676.
42. Malinin, T.I. and V.P. Perry, *Toxicity of Dimethyl Sulfoxide on HeLa Cells,* Cryobiology, 1967, **4**, 90-96.
43. Pope, D.C. and W.T. Oliver, *Dimethyl Sulfoxide (DMSO),* Can. J. Comp. Med. Vet. S., 1966, **30**, 3-8.

Chapter 8

Hydrothermal Core-Shell Materials: Poly-(4-Vinylpyridine) Wrapped Carbon Nanoparticles

Contents

This work has been published in Journal of Materials Chemistry A;

DOI: 10.1039/C3TA10198C

K. Lawrence, G. W. Nelson, J. S. Foord, M. Felipe-Sotelo, N. D. M. Evans, J. M. Mitchels, T. D. James, F. Xia and F. Marken, J. Mater. Chem. A, ***2013**, 1,* 4559-4564.

8.1 Abstract

Negatively charged carbon nanoparticles (Emperor 2000, Cabot Corporation) are wrapped in a poly-(4-vinylpyridine) cationomer (P4VP) and hydrothermally converted into a pH-responsive core-shell nano-composite. The core-shell material synthesized with a thin shell (20-40 nm wrapped particle diameter) is water-insoluble but is readily dispersed into ethanol for straight forward deposition onto electrodes. Zeta-potential measurements suggest a point of zero charge (PZC) occurring at approximately pH 4.5 suggesting that negative functional groups are dominating in the more alkaline range and positive functional groups are dominating in acidic conditions. X-ray photoelectron spectroscopy (XPS) data suggest carboxylate and pyridinium functional groups, which is confirmed by using voltammetric measurements for adsorbed cations (methylene blue) and adsorbed anions (indigo carmine). The specific capacitance reaches a maximum of 13 Fg^{-1} at the PZC, this is thought to be explained by a "double layer compression" effect within the nanoparticle shell.

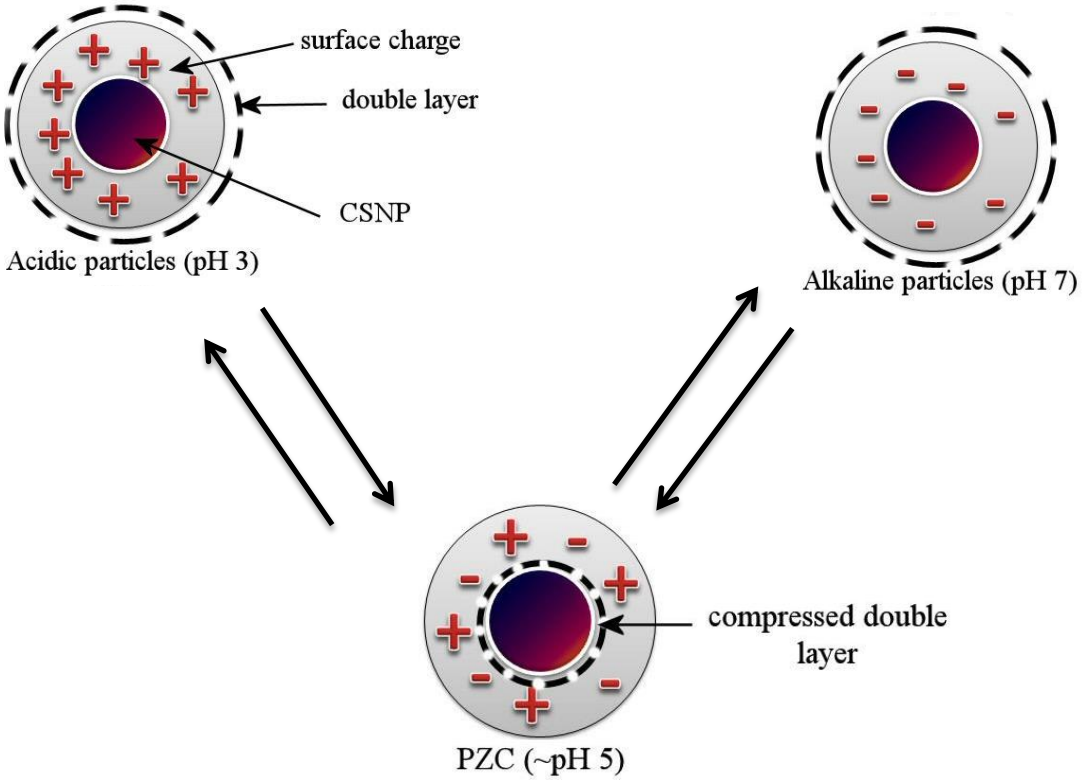

8.2 Introduction

There is a vast amount of research being performed on nanocarbons,[1-6] with a large emphasis on the functionalisation of such materials. Functionalised nanocarbon materials are readily obtained by covalent binding,[7, 8] physisorption,[9] and through the interaction of polymers with carbon surfaces.[10] Functionalised carbon blacks are used in industry [such as the phenylsulfonate-functionalised carbon nanoparticles (CNPs) known as Emperor 2000, which have been focused on throughout this thesis] and are attracting renewed attention for electrochemical systems.[11, 12] The beneficial aspects of these materials (large-scale accessibility, low cost, safety) outweigh the major disadvantage of poor chemical structure definition for electrochemical applications.[13] The Marken group have recently demonstrated the use of commercial carbon blacks to synthesise useful materials such as anthraquinone-functionalised CNPs[14] and $_{L}$-dopa modified CNPs for gas sensing.[15]

The hydrothermal transformation of carbon-rich precursor materials such as glucose,[16] starch,[17] cellulose,[18] or chitosan[19] is known to yield carbon products that demonstrate relatively poor electrochemical properties, which can be attributed to incomplete surface carbonisation because of the contact with the aqueous phase.[20] However, partially carbonised materials can be useful in the surface functionalisation of conducting substrates and the concept of simple hydrothermal wrapping was introduced, for example, for the synthesis of pH-responsive nanocarbon composites.[21] This method has also been used to modify carbon-palladium nano-composites for selective catalysis.[22]

Here, the cationic P4VP polymer is used to form a shell coating in a hydrothermal wrapping process. Negatively charged Emperor 2000 particles are initially wrapped with P4VP polycation in aqueous solution before being treated under hydrothermal conditions at 200 ^{o}C, which results in a novel core-shell polymer-wrapped nano-composite with interesting properties. The shell formed from P4VP introduces both anion and cation binding sites at pH values positive and negative to the PZC, respectively. The maximum specific capacitance of this core-shell material is observed at the PZC and the properties of the new core-shell material are discussed in terms of shell charging.

8.3 Experimental

8.3.1 Chemical Reagents

All reagents were used as supplied, without further purification: Emperor 2000 phenylsulfonate-functionalised carbon nanoparticles (9-18 nm average diameter, Cabot Corporation), poly-(4-vinylpyridine) with typical M_w 60,000 (Aldrich), acetic acid (Aldrich, 99.7 %, ACS reagent), absolute ethanol (Sigma-Aldrich), ortho-phosphoric acid (Fisher Scientific), sodium hydroxide (Aldrich, Sigma ultra, 98 %), indigo carmine, certified (Aldrich), methylene blue, certified (Aldrich). Demineralised and filtered water was obtained from a Thermo Scientific water purification system (Barnstead Nanopure) with approximately 18.2 MΩ cm resistivity. Argon (Pureshield, BOC) was used to de-aerate solutions prior to voltammetric studies.

8.3.2 Instrumentation

Zeta potential measurements were obtained with a ZetaMaster S (Malvern Instruments Ltd., UK) calibrated with zeta potential transfer standard (-50 ± 5 mV, Malvern Instruments Ltd., UK). The data were recorded and analysed using ZetaMaster S standard software PCS v1.41. X-ray photoelectron spectroscopy (XPS) was carried out with an Al Kα X-ray anode at 1486.6 eV. All peaks were calibrated to 285 eV, that is, the adventitious C1s peak. To obtain transmission electron microscopy (TEM) images, a JEM1200EXII (JEOL, Japan) was employed. Voltammetric studies were performed by using a microAutolab III potentiostat system (EcoChemie, Netherlands) with a Pt wire counter electrode and a KCl-saturated Calomel reference electrode (SCE, Radiometer, Copenhagen). A 3 mm diameter glassy carbon electrode (BAS Inc.) served as the basis for the working electrode. All experiments were performed at room temperature, that is, 22 ± 2 ^{o}C.

8.3.3 Hydrothermal Synthesis of "Thin" and "Thick" Shell P4VP-Wrapped Carbon

The P4VP-CNP nanocomposite materials were prepared based on a reported literature procedure.[21] In brief, P4VP (0.1 g) was added to 2% acetic acid (18 mL) and dissolved by ultrasonication. Emperor 2000 CNPs (0.24 g) were then added and after ultrasonication for 1 h, a stable suspension was formed. The black suspension was transferred into a Teflon-lined high pressure reaction vessel (125 mL; Parr Instrument Company, US) and sealed. The vessel was placed into the oven at room temperature before being heated to 200 ^{o}C, it was maintained at this temperature for 12 h before cooling back to room temperature. The solid black product was collected by using Büchner filtration, washed copiously with water and ethanol, before drying in an 80 ^{o}C oven for 1 h. This yielded a "thin" shell nanocomposite material. For the "thick" shell material, the procedure was repeated with half as much carbon, that is, 0.12 g Emperor 2000.

8.3.4 Electrode Preparation

A suspension of core-shell nanoparticles was prepared (3 mg CNPs per 1 mL ethanol, ultrasonicated). A carbon film was prepared by direct deposition of the ethanolic core-shell nanoparticle suspension (typically 15 µL) onto a glassy carbon electrode; following solvent evaporation in air, a carbonaceous film could be seen. For voltammetric investigations with adsorbed dyes, the modified electrode was immersed into a phosphate-buffered solution of either methylene blue or indigo carmine (0.1 M) for 5 min to allow adsorption. The electrodes were then rinsed in fresh phosphate buffer solution (PBS) and dried in air before being transferred directly into aqueous electrolyte solution for voltammetric measurements.

8.4 Results and Discussion

8.4.1 Characterisation of "Thin Shell" Core-Shell Nanoparticles

The initial electrochemical characterisation of these new polymer-coated core-shell materials suggested that only the particles with a thin shell were of interest. This is because the materials with a thick polymer shell were electrochemically inert. Therefore, only the thin shell material was fully characterised in this study. TEM imaging demonstrated that the core-shell nanoparticles had a tendency to form aggregates; however, there were also a number of more disperse particles that were observed (see Figure 8.1). According to the TEM images, the polymer-carbon nanocomposite particles had diameters of approximately 20 – 40 nm (compared to 9-18 nm for the Emperor 2000 starting material). The TEM images also showed that the particles had an irregular shape; the edges were not well defined, which could be attributed to the polymeric covering. After comparison with previous reports exhibiting Emperor 2000 TEM data,[21] the images obtained for the core-shell material demonstrated that after hydrothermal processing, the different types of carbon (core and shell) could not be distinguished by using TEM.

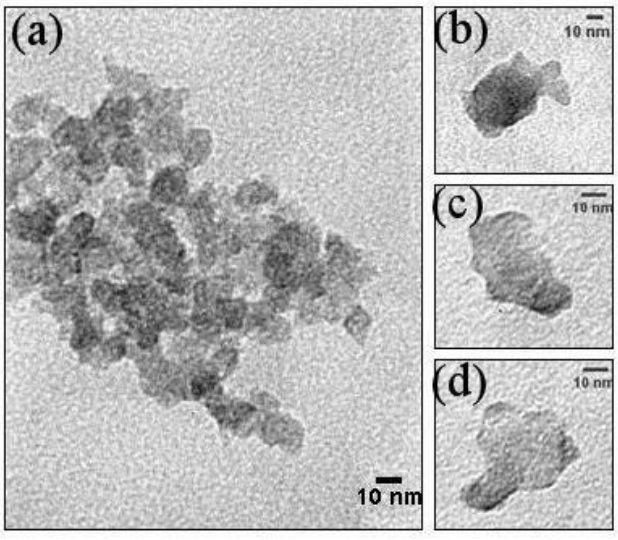

Figure 8.1. TEM images of hydrothermally P4VP-wrapped Emperor 2000 nanoparticle aggregates (a) and as dispersed particles (b)-(d); scale bar 10 nm.

Powder samples of P4VP-coated CNPs were analysed by XPS (see Figure 8.2) to characterise the surface composition of the core-shell material. Two samples of the nanocomposite were investigated; one sample was prewashed with 0.1 M NaOH and another was prewashed with 0.1 M HCl. This pre-treatment was performed to reveal surface functional groups by studying the material under difference pH conditions.

The acid washed nanocomposite displayed a C1s signal that was assigned to two peaks associated with C-C/C-H and C-N at 285.0 and 286.4 eV, respectively [Figure 8.2(a)]. The S2p signal at 168.8 eV was indicative of sulfonate functionality, which was attributed to core Emperor 2000 material [Figure 8.2(d)].[23] The low S2p/C1s ratio implied that the sulfur signal was attenuated by the polymer shell; this provided further indication that the sulfonate was present only in the core of the material and not in the shell. The N1s region was deconvoluted into two chemical environments; the peak with lower binding energy (399.3 eV) was assigned to sp^2 hybridized nitrogen of pyridine-like ring systems. The peak with slightly higher binding energy (401.1 eV) was explained by the presence of protonated nitrogen in pyridinium systems.[24] Interaction between pyridinium nitrogen (cation) and chloride (anion) was confirmed by the Cl2p spectrum [Figure 8.2(e)]. The Cl2p peak was associated with two forms of chloride, at 198.4 and 200.7 eV. These two peaks were not simply a doublet arising from spin-orbit coupling as the peak at lower binding energy would be of greater intensity.[25, 26]

For the alkali-washed sample, the C1s and O1s spectra [see Figure 8.2(f) and (h)] were each deconvoluted into three environments, in each case there was an additional signal at higher binding energy with respect to the acid-washed sample. The higher binding energies were indicative of additional carbon and oxygen species being present in more electronegative environments, and suggested a greater carboxylate presence in the NaOH treated material than in the HCl treated shell. The N1s region exhibited two signals, as observed in the acid-washed equivalent [Figure 8.2(g)]. This suggests that cation-bound nitrogen was still present. The Na1s spectrum confirms the presence of sodium, which in NaOH would be seen at 1072.5 eV, whereas two peaks were observed at -1.2 eV and + 1.1 eV, relative to the expected NaOH signal [Figure 8.2(j)]. Sodium cations that are not involved or are only weakly involved in an ionic interaction tend to manifest at lower binding energies and could explain the peak seen at 1071.3 eV, which was attributed to weak interactions with carboxylates. The peak at 1073.6 eV was indicative of Na^+ possibly interacting with nitrogen and producing quaternary nitrogen

species that were observed in the N1s spectrum.[27] Therefore, XPS demonstrated two sodium interactions neither of which was caused by residual NaOH. These interactions were likely occurring between carboxylate oxygen and pyridine nitrogen.

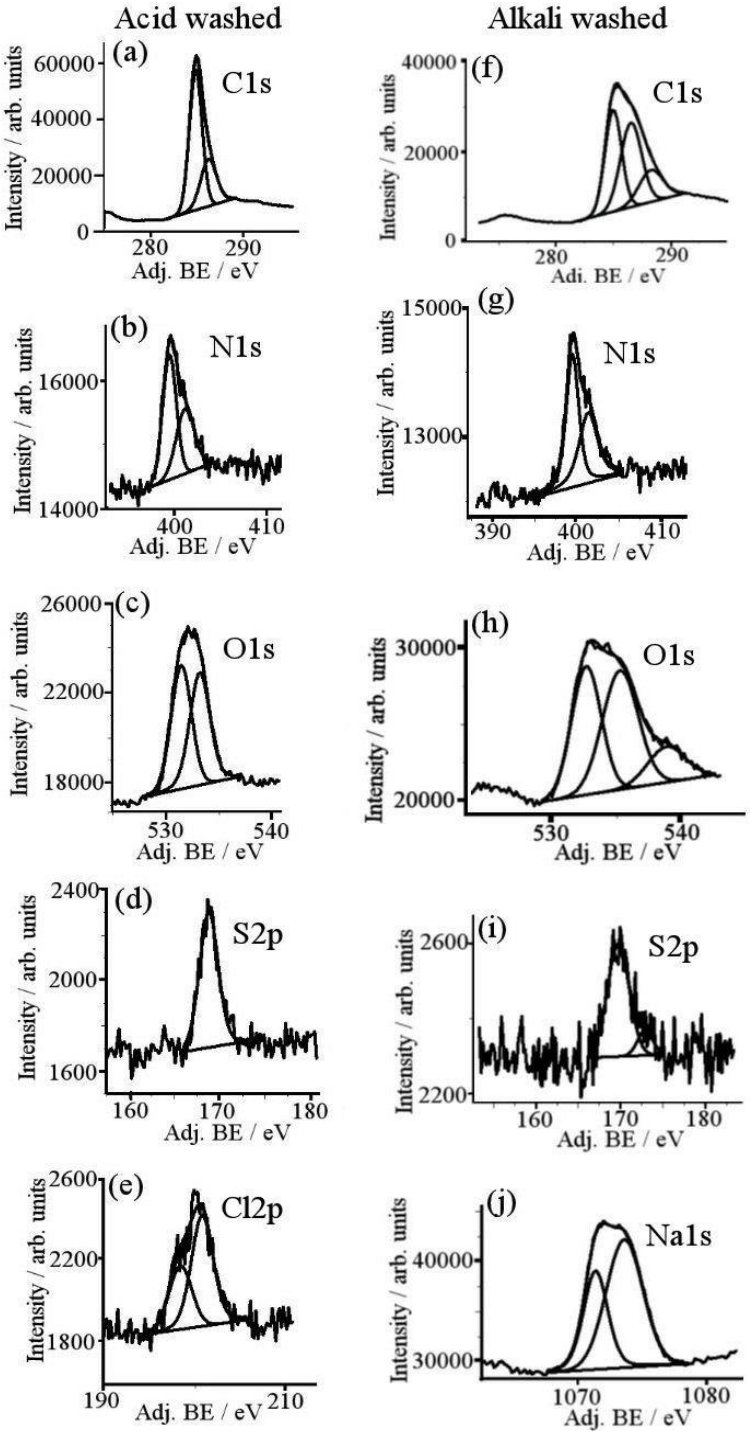

Figure 8.2. XPS data for core-shell nanoparticles: (a) C1s, (b) N1s, (c) O1s, (d) S2p, and (e) Cl2p prewashed with 0.1 M HCl; (f) C1s, (g) N1s, (h) O1s, (i) S2p, and (j) Na1s prewashed with 0.1 M NaOH. Binding energies adjusted to C1s = 285 eV.

XPS analysis confirmed the core-shell structure of the nanocomposite synthesised with an Emperor 2000 core coated with a film of carbonised P4VP. The core exhibited characteristic S2p peaks; however, these were low (as seen by the S2p/C1s ratio), this demonstrated that the sulfur signal was well-attenuated by the polymer shell. In each case, the pyridine functionality was retained and this was demonstrated by ionic interactions. The N1s/C1s ratio was much higher for the NaOH washed sample (0.076 compared to 0.028 for the HCl washed sample), which suggested a greater number of pyridine moieties were present at the surface in comparison to the acid-washed material. The film thickness could be estimated by using XPS when employing Equation 8.1, where I is the intensity of the photoelectron signal of interest, I_{infinite} is the intensity expected for an infinitely thick film, t is the film thickness, and λ is the photoelectron attenuation length.[28, 29]

$$\frac{I}{I_{\text{infinite}}} = \left(1 - e^{-\frac{t}{\lambda}}\right) \tag{8.1}$$

This calculation can be used in conjunction with XPS data by substituting the N1s/C1s ratio of the sample of interest in place of I, and I_{infinite} can be substituted with the N1s/C1s ratio of P4VP starting material. The photoelectron attenuation length was estimated by following Equation 8.2, where B is a material parameter equal to 0.087 for organic layers and E_{kin} is the energy of the photoelectron of interest.[30, 31]

$$\lambda = B\sqrt{E_{kin}} \tag{8.2}$$

The photoelectron attenuation length (λ) for an N1s photoelectron that has been excited with Al Kα radiation through an organic overlayer is approximately 2.8 nm. This approximate calculation estimated an average shell thickness of 0.8 and 3.2 nm for the acid and alkali washed core-shell carbon nanoparticles, respectively (with an error of approximately 15 %). The acid washed particles presented a decreased average shell

thickness, which could have been attributed to structural changes in the shell; however, the assumption of the validity of $I_{infinite}$ for both cases was uncertain. Generally, a shell thickness of approximately 2-4 nm for the thin shell material is consistent with observations for chitosan-wrapped nanoparticles.[20]

8.4.2 Electrochemical Characterisation I: Capacitive Responses

When the ethanolic suspension was drop-cast onto a glassy carbon electrode, a black water-insoluble film was produced. The modified electrode was then placed directly into an electrochemical cell with PBS and cyclic voltammetry (CV) experiments were performed. The initial deposition amount of core-shell nanoparticles was 60 µg, which resulted in an observed capacitance of approximately 1 mF [Figure 8.3(a)].

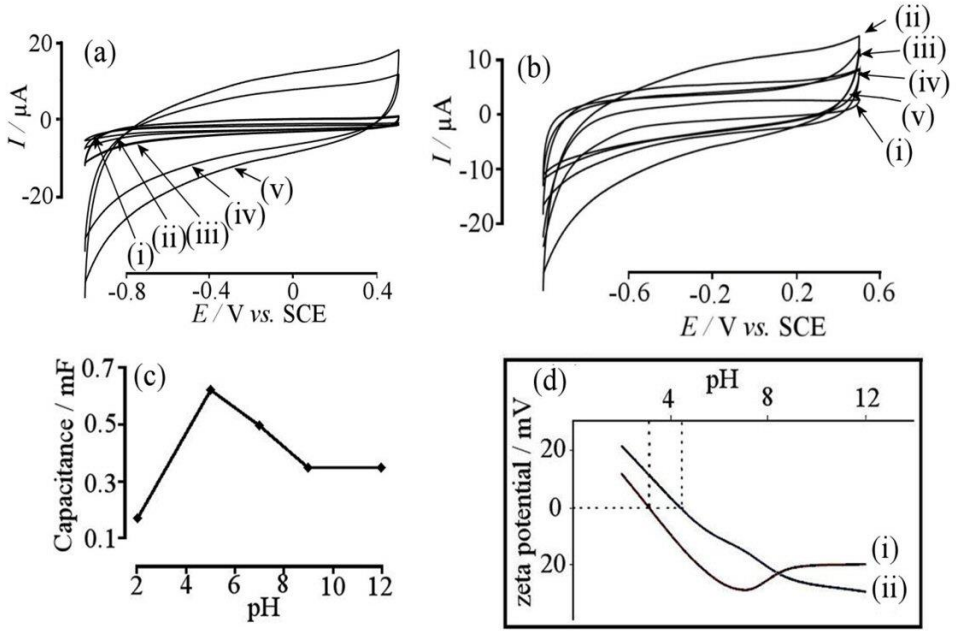

Figure 8.3. (a) CVs (scan rate 10 mV s^{-1}) in 0.1 M PBS at pH 5 for (i) 0 µg (ii) 6 µg (iii) 15 µg (iv) 45 µg (v) 60 µg. (b) CVs (scan rate 10 mV s^{-1}) with 45 µg deposit of core-shell nanoparticles in 0.1 M PBS at pH (i) 2 (ii) 5 (iii) 7 (iv) 9 (v) 12. (c) Plot of capacitance as a function of pH. (d) Zeta potential measurements in 0.1 M PBS for (i) Emperor 2000 CNPs and (ii) for P4VP-wrapped carbon nanoparticles.

The capacitance of the core-shell nanoparticle film was investigated as a function of buffer pH [see Figure 8.3(b) and (c)]. The lowest capacitance in the pH range 2 - 12 was observed when the pH of 0.1 M PBS was at pH 2 and at alkaline pH values. At approximately pH 5 there was a considerable increase in the capacitance to 0.65 F (the specific capacitance was calculated to be 13 Fg^{-1}). When the pH was increased above pH 5, the capacitance decreased again. The zeta potential of the particles was measured and showed that the PZC of the core-shell material occurred at approximately pH 4.5 [see Figure 8.3(d)]. The similarity between the point of maximum capacitance and the PZC suggested a link between the capacitance and the zeta potential associated with the presence of ionic charges in the shell (assuming no significant losses of the charged material into the solution).

8.4.3 Electrochemical Characterisation II: Faradaic Responses

To further investigate the surface charge of the core-shell material, the coated electrodes were immersed into either a cationic or anionic redox-active dye and investigated as a function of concentration. Methylene blue (0.1 M) was used as a positively charged adsorption probe (Figure 8.4), which showed a steady increase in current as the concentration of the dye solution was increased [pH 7, Figure 8.4(a)]. The charge under the curve was extracted, see Figure 8.4(b) and was shown to exhibit Langmuir-type behaviour with a maximum charge of approximately 9×10^{-4} C, which equates to 2.8×10^{15} methylene blue molecules adsorbed into the core-shell nanoparticle film (assuming a two-electron process).[32] Interestingly, at lower concentrations the oxidation, reduction, and mid-point potentials all increased with increasing concentration of dye before reaching a plateau, see Figure 8.4(c). The variation in mid-point potential could have been associated with a change in the relative binding energy, that is, at higher concentrations the reduced form becomes more stable.

Indigo carmine (0.1 M, pH 3) was used as a negatively charged adsorption probe (Figure 8.4), as the concentration of the dye increased, the charge under the curve increased in a way that was consistent with methylene blue at pH 7 [see Figure 8.4(d)]. The charge under the curve once indicated a Langmuir-type curve that plateaued at approximately 3.3×10^{-4} C, see Figure 8.4(e). This corresponded to a maximum number

of adsorption sites on the core-shell nanoparticulate film of approximately 4.1 x 10^{15} (assuming a two-electron process).[33] The oxidation and reduction peak-to-peak separation at low concentrations was approximately 75 mV, which increased with increasing concentration to 95 mV. After the concentration reached 0.5 mM, the oxidation and reduction peak potential remained constant. The mid-point potential remained approximately constant over the entire concentration range, see Figure 8.4(f).

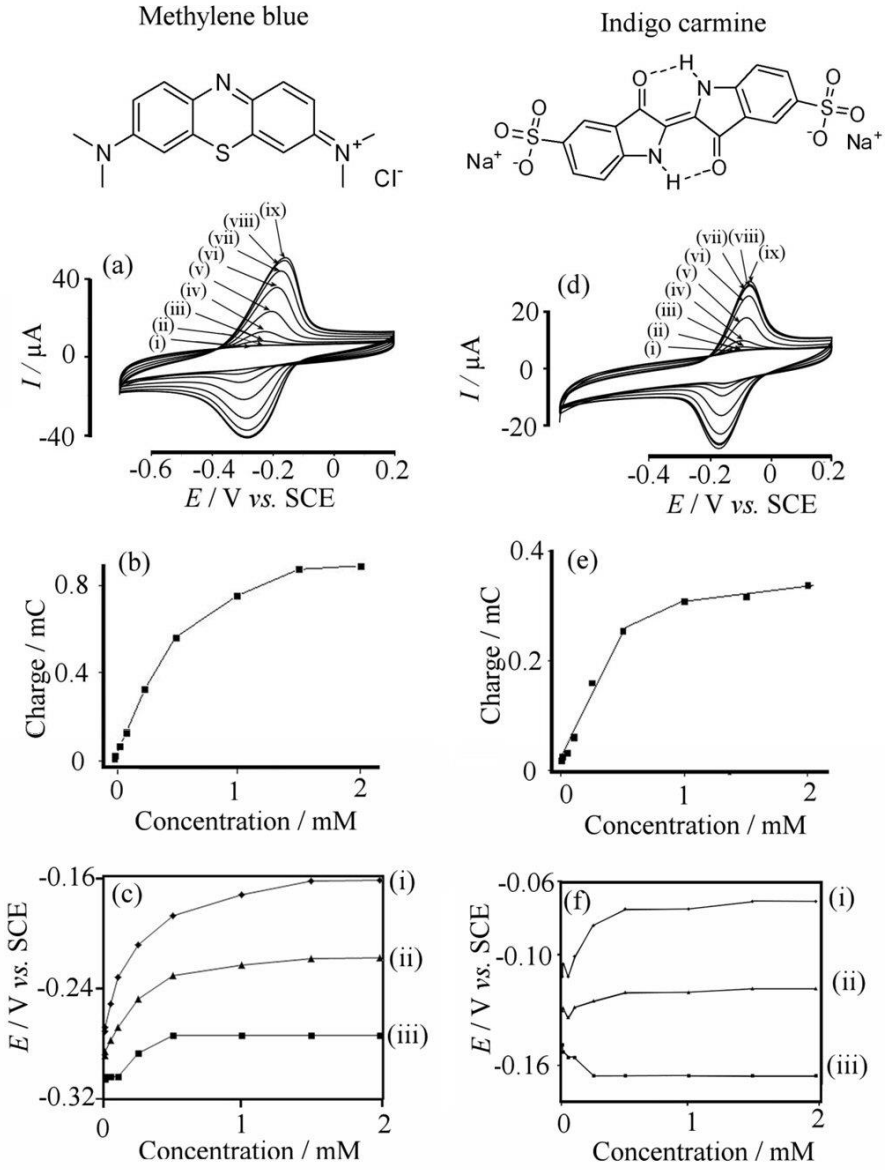

Figure 8.4. (a) and (d) CVs (scan rate 10 mV s^{-1}) for 45 µg nanoparticle deposit dipped in dye solution for 5 minutes at concentrations of (i) 5 µM, (ii) 10 µM, (iii) 50 µM, (iv) 100 µM, (v) 250 µM, (vi) 500 µM, (vii) 1 mM, (viii) 1.5 mM and (ix) 2 mM in 0.1 M PBS (pH 7 for methylene blue and pH 3 for indigo carmine). (b) and (e) Plot of charge *vs*. concentration of dye. (c) and (f) Plot of peak potential *vs*. concentration of dye for (i) oxidation potential, (ii) mid-point potential and (iii) reduction potential.

Zeta potential measurements showed that the PZC of the core-shell CNPs occurred at approximately pH 4.5. Therefore, the effect of dye adsorption at different pH values both above and below pH 4.5 was investigated. Methylene blue, a cationic dye, showed the greatest Faradaic response at pH 7 [see Figure 8.5(a)]. The Faradaic current progressively decreased in intensity as the pH became more acidic. This provided evidence that at higher pH values the surface/shell of the nanoparticles possessed more anionic character. Interestingly, when the experiment was repeated for indigo carmine, an anionic dye, the opposite trend was observed. In this case, the greatest current was obtained at pH 3 [see Figure 8.5(b)]. For both the anionic and cationic dye, the pH 5 signal showed a Faradaic current of a similar magnitude, which was consistent with equal amounts of positive and negative charges at the core-shell nanoparticle surface.

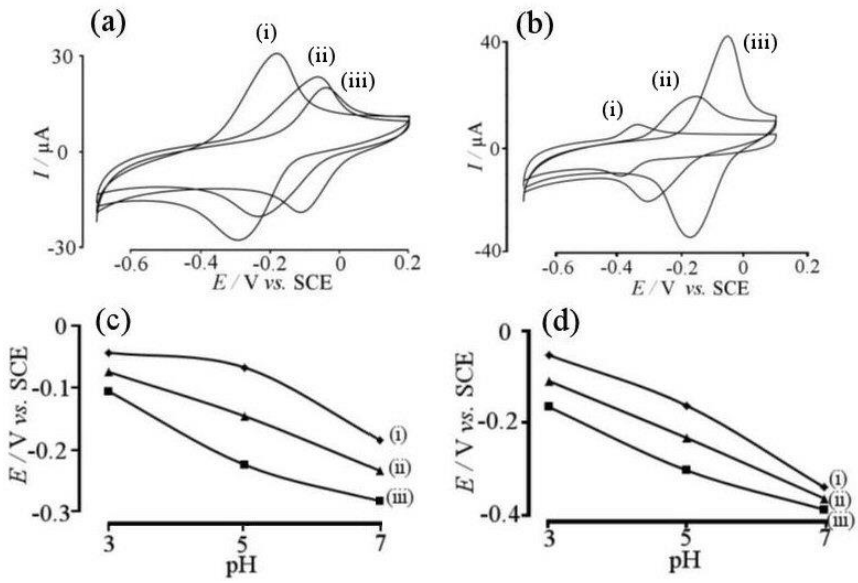

Figure 8.5. CVs (scan rate 10 mV s^{-1}) for (a) methylene blue and (b) indigo carmine in 0.1 M PBS at pH (i) 7 (ii) 5 (iii) 3. Also shown are plots of (i) oxidation peak, (ii) mid-point, and (iii) reduction peak potentials for (c) methylene blue and (d) indigo carmine.

When considering the oxidation peak, reduction peak, and mid-point potentials, a Nernstian shift of approximately 60 mV per pH unit can be observed. A decrease in peak-to-peak separation occurred at lower dye loading [see Figure 8.5(c) and (d)]. Most importantly, the presence of positive and negative binding sites in equal quantities at pH values close to the PZC has been implied for this type of core-shell nanoparticle material. In conjunction with the observation of the maximum capacitance at the PZC a

simplified model is proposed in Figure 8.6. Immobilised cationic (pyridinium-like) and anionic (carboxylate-like) functionalities existed in the shell as a function of the solution pH. In the absence of additional electrolyte ions (such as in the case of a dense shell) under acidic conditions, the resultant material included a shell that was positively charged. Under alkaline conditions the shell had more excess anionic charges. At the PZC approximately equal amounts of positive and negative charges were present that allowed the extent of the double layer to decrease with a resulting increase in capacitance, that is, the dielectric properties of the shell contribute to the observed capacitive current response.

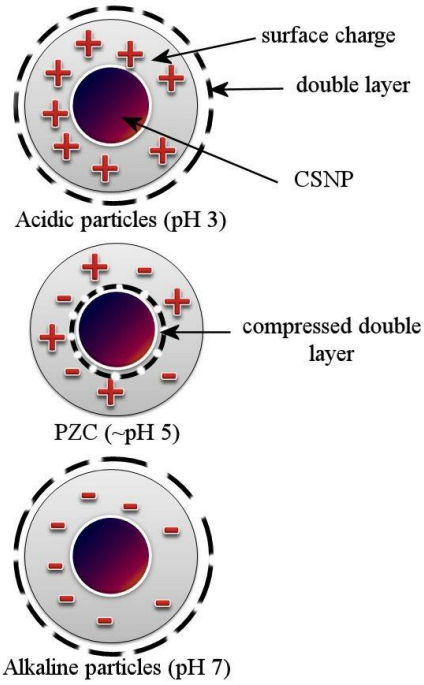

Figure 8.6. Schematic diagram of core-shell nanoparticles at different pH values to demonstrate the compression of the double layer at the PZC.

8.5 Conclusions

This investigation has demonstrated that hydrothermal wrapping of negatively charged carbon nanoparticles with a poly-(4-vinyl-pyridine) precursor polymer results in the formation of a functional shell with strongly pH-dependent properties. The chemical

structure of the carbonised material is not well-defined; however, pyridinium and carboxylate functionalities have been identified as positive and negative charge bearers, respectively. By adjusting the shell thickness, it was possible to prepare a material with a maximum capacitive current (approximately 13 Fg^{-1} for the specific capacitance) at the PZC, this allowed for a model of "double layer compression" within the shell to be proposed. This type of core-shell nanomaterial and similar functionalised materials could be useful for future sensing applications. The proton-sensitivity function could be developed into a series of more selective response mechanisms, for example to detect analytes such as heavy metals, pollutants, glucose, or trace bio-markers. Further possible synthetic methodologies to prepare highly functionalised materials could involve the post-hydrothermal synthetic modification of the shell or the impregnation of redox systems into the shell. The molecular weight distribution of the precursor polymer wrapping agent could also have a significant effect on the properties and uniformity of the resulting materials.

8.6 References

1. Poh, H.L. and M. Pumera, *Nanoporous Carbon Materials for Electrochemical Sensing,* Chem. Asian J., 2012, **7**, 412-416.
2. Wildgoose, G.G., C.E. Banks, and R.G. Compton, *Metal Nanopartictes and Related Materials Supported on Carbon Nanotubes: Methods and Applications,* Small, 2006, **2**, 182-193.
3. Gao, C., Z. Guo, J.H. Liu, and X.J. Huang, *The New Age of Carbon Nanotubes: An Updated Review of Functionalized Carbon Nanotubes in Electrochemical Sensors,* Nanoscale, 2012, **4**, 1948-1963.
4. Melechko, A.V., V.I. Merkulov, T.E. McKnight, M.A. Guillorn, K.L. Klein, D.H. Lowndes, and M.L. Simpson, *Vertically Aligned Carbon Nanofibers and Related Structures: Controlled Synthesis and Directed Assembly,* J. Appl. Phys., 2005, **97**, 041301/1-041301/39.
5. Hwang, K.C., *Recent Progress in the Preparation and Application of Carbon Nanocapsules,* J. Phys. D: Appl. Phys., 2010, **43**, 374001/1-374001/13.
6. Zhu, Z.G., L. Garcia-Gancedo, A.J. Flewitt, H.Q. Xie, F. Moussy, and W.I. Milne, *A Critical Review of Glucose Biosensors Based on Carbon Nanomaterials: Carbon Nanotubes and Graphene,* Sensors, 2012, **12**, 5996-6022.
7. Barriere, F. and A.J. Downard, *Covalent Modification of Graphitic Carbon Substrates by Non-Electrochemical Methods,* J. Solid State Electrochem., 2008, **12**, 1231-1244.
8. Downard, A.J., *Electrochemically Assisted Covalent Modification of Carbon Electrodes,* Electroanalysis, 2000, **12**, 1085-1096.
9. Fujigaya, T., Y. Tanaka, and N. Nakashima, *Soluble Carbon Nanotubes and Application to Electrochemistry,* Electrochemistry, 2010, **78**, 2-15.
10. Yogeswaran, U. and S.M. Chen, *Recent Trends in the Application of Carbon Nanotubes-Polymer Composite Modified Electrodes for Biosensors: A Review,* Anal. Lett., 2008, **41**, 210-243.
11. Vidal, L., A. Chisvert, A. Canals, E. Psillakis, A. Lapkin, F. Acosta, K.J. Edler, J.A. Holdaway, and F. Marken, *Chemically Surface-Modified Carbon Nanoparticle Carrier for Phenolic Pollutants: Extraction and Electrochemical Determination of Benzophenone-3 and Triclosan,* Anal. Chim. Acta, 2008, **616**, 28-35.
12. Lo, T.W.B., L. Aldous, and R.G. Compton, *The Use of Nano-Carbon as an Alternative to Multi-Walled Carbon Nanotubes in Modified Electrodes for Adsorptive Stripping Voltammetry,* Sens. Actuators, B, 2012, **162**, 361-368.
13. Sanders, I.J. and T.L. Peeten, *Carbon Black: Production, Properties & Uses,* 2011, London: Nova Science Publishers Inc.
14. Watkins, J.D., K. Lawrence, J.E. Taylor, T.D. James, S.D. Bull, and F. Marken, *Carbon Nanoparticle Surface Electrochemistry: High-Density Covalent Immobilisation and Pore-Reactivity of 9,10-Anthraquinone,* Electroanalysis, 2011, **23**, 1320-1324.
15. Bin Ibrahim, N., K. Lawrence, T.D. James, F. Xia, M. Pan, S. Mu, J.M. Mitchels, and F. Marken, *Surface-Dopylated Carbon Nanoparticles Sense Gas-Induced pH Changes,* Sens. Actuators, B, 2012, **161**, 184-190.

16. Li, T., J.F. Shen, N. Li, and M.X. Ye, *Facile and Novel Hydrothermal Preparation of Functionalised Carbon Microspheres from Glucose by Using Graphene Sheets as a Substrate,* Mater. Lett., 2012, **89**, 202-205.
17. Yu, L.H., C. Falco, J. Weber, R.J. White, J.Y. Howe, and M.M. Titirici, *Carbohydrate-Derived Hydrothermal Carbons: A Thorough Characterization Study,* Langmuir, 2012, **28**, 12373-12383.
18. Sevilla, M. and A.B. Fuertes, *The Production of Carbon Materials by Hydrothermal Carbonization of Cellulose,* Carbon, 2009, **47**, 2281-2289.
19. Yang, Y., J. Cui, M. Zheng, C. Hu, S. Tan, Y. Xiao, Q. Yang, and Y. Liu, *One-Step Synthesis of Amino-Functionalized Fluorescent Carbon Nanoparticles by Hydrothermal Carbonization of Chitosan,* Chem. Commun., 2012, **48**, 380-382.
20. Xia, F., M. Pan, S. Mu, M.D. Jones, D. Wolverson, and F. Marken, *Chitosan-Based Hydrothermal Nanocarbon: Core-Shell Characteristics and Composite Electrodes,* Electroanalysis, 2012, **24**, 1703-1708.
21. Xia, F., M. Pan, S. Mu, Y. Xiong, K.J. Edler, I. Idini, M.D. Jones, S.C. Tsang, and F. Marken, *Hydrothermal Core-Shell Carbon Nanoparticle Films: Thinning the Shell Leads to Dramatic pH Response,* Phys. Chem. Chem. Phys., 2012, **14**, 15860-15865.
22. Xia, F., M. Pan, S. Mu, M.D. Jones, G. Kociok-Köhn, S.C. Tsang, and F. Marken, *Imparting pH- and Small Molecule Selectivity to Nano-Pd Catalysts via Hydrothermal Wrapping with Chitosan,* Electrochim. Acta, DOI: 10.1016/j.electacta.2013.01.014.
23. Nelson, G.W., M. Perry, S.M. He, D.L. Zechel, and J.H. Horton, *Characterization of Covalently Bonded Proteins on Poly(methyl methacrylate) by X-ray Photoelectron Spectroscopy,* Colloids Surf., B, 2010. **78**, 61-68.
24. Hulicova, D., J. Yamashita, Y. Soneda, H. Hatori, and M. Kodama, *Supercapacitors Prepared from Melamine-Based Carbon,* Chem. Mater., 2005, **17**, 1241-1247.
25. Huang, X.D. and S.H. Goh, *Miscibility of C-60-End-Capped Poly(ethylene oxide) with Poly(vinyl chloride),* Polymer, 2002, **43**, 1417-1421.
26. Tan, K.L., B.T.G. Tan, E.T. Kang, and K.G. Neoh, *The Chemical Nature of the Nitrogens in Polypyrrole and Polyaniline - A Comparative-Study by X-Ray Photoelectron-Spectroscopy,* J. Chem. Phys., 1991, **94**, 5382-5388.
27. Kumar, S.N., G. Bouyssoux, and F. Gaillard, *Electronic and Structural Characterization of Electrochemically Synthesized Conducting Polyaniline from XPS Studies,* Surf. Interface Anal., 1990, **15**, 531-536.
28. Petrovykh, D.Y., H. Kimura-Suda, M.J. Tarlov, and L.J. Whitman, *Quantitative Characterization of DNA Films by X-ray Photoelectron Spectroscopy,* Langmuir, 2004, **20**, 429-440.
29. Flitsch, R. and S.I. Raider, *Electron Mean Escape Depths from X-Ray Photoelectron-Spectra of Thermally Oxidized Silicon Dioxide Films on Silicon,* J. Vac. Sci. Technol., 1975, **12**, 305-308.
30. Textor, M., L. Ruiz, R. Hofer, A. Rossi, K. Feldman, G. Hahner, and N.D. Spencer, *Structural Chemistry of Self-Assembled Monolayers of Octadecylphosphoric Acid on Tantalum Oxide Surfaces,* Langmuir, 2000, **16**, 3257-3271.
31. Seah, M.P. and W.A. Dench, *Quantitative Electron Spectroscopy of Surfaces: A Standard Data Base for Electron Inelastic Mean Free Paths in Solids.* Surf. Interface Anal., 1979. **1**, 2-11.

32. Halls, J.E., C.Y. Cummings, J. Ellis, L.L. Keenan, D.M. Jiang, A.D. Burrows, and F. Marken, *Redox Reactivity of Methylene Blue Bound in Pores of UMCM-1 Metal-Organic Frameworks,* Mol. Cryst. Liq. Cryst., 2012, **554**, 12-21.
33. Amiri, M., S. Shahrokhian, and F. Marken, *Ultrathin Carbon Nanoparticle Composite Film Electrodes: Distinguishing Dopamine and Ascorbate*, Electroanalysis, 2007, **19**, 1032-1038.

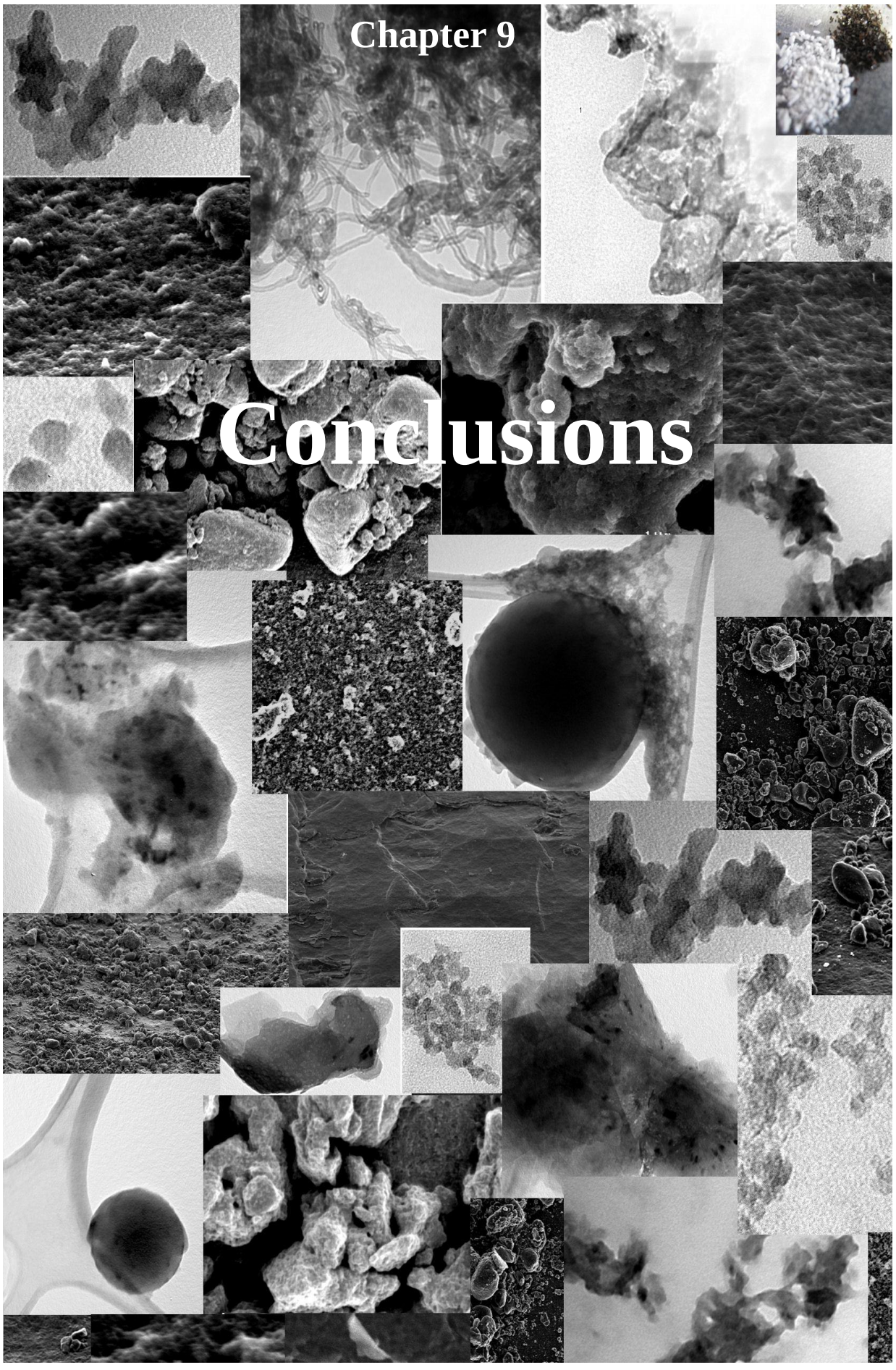

Chapter 9

Conclusions

9.1. Conclusions

This thesis demonstrates that carbon nanoparticles remain important classes of carbon-based nanomaterials. Carbon nanoparticles possess a number of properties that render them useful in a vast range of applications. Herein, it is documented that the functional groups on the surface of carbon nanoparticles can be tailored to prepare a number of useful carbon-based nanostructures. In this thesis, the synthesised and modified nanoparticles are demonstrated to have important fluorescent or electrochemical sensing applications. The preparation methods for novel carbon nanomaterials are presented and the potential uses are investigated.

Carbon blacks are the basis of much of the research that is presented. Namely, Emperor 2000, a commercial bulk-produced carbon black available from Cabot Corporation, is the starting material for many of the new carbon nanoparticles. The surface of Emperor 2000 is modified by using a number of chemical methods: the first modification presented herein utilises a physisorption mechanism through π-π stacking. The interactions between the delocalised π cloud of pyridine ring systems and the π electrons at the carbonaceous core of Emperor 2000 nanoparticles allow pyrene-based compounds to be attached to the surface of the carbon nanoparticles. This methodology results in nanoparticles with a carbon core and surface boronic acid functionality, which is effective in the electrochemical detection of catecholic caffeic acid. By using cyclic voltammetry, it is clear that, compared to caffeic acid adsorbed directly onto a graphitic surface, the carbon nanoparticle-based system enhances the electrochemical output and allows for further insight to be sought into the electrochemical mechanism, see Figure 9.1. The redox signals for the modified nanoparticle-based sensor allow the fluxionality to be considered and investigated. This discovery highlights the potential to detect other important molecules that contain the ortho-quinone functionality by using this new versatile sensing platform to obtain high sensitivity and probe the modes of attachment during the redox process.

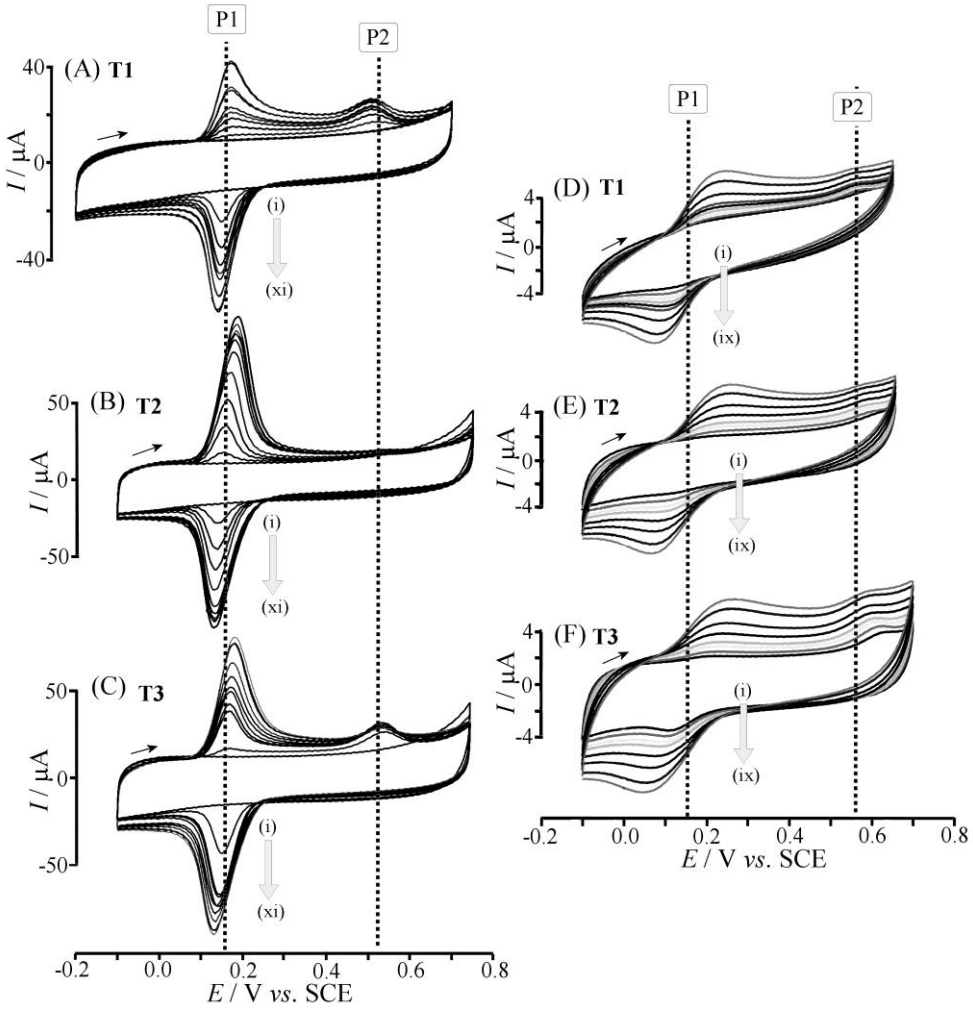

Figure 9.1. (A-C) Cyclic voltammograms (50 mV s^{-1}) with increasing caffeic acid concentration from (i) 0.0, (ii) 2.5, (iii) 5.0, (iv) 7.5 (v) 10.0, (vi)12.5, (vii) 15.0, (viii) 17.5, (ix) 20.0, (x) 22.5, to (xi) 25 µM with (A) T1-modified, (B) T2-modified, and (C) T3-modified CNPs (15 µg) deposited onto a graphite electrode. (D-F) Cyclic voltammograms (50 mV s^{-1}) with increasing caffeic acid concentration from (i) 0.5, (ii) 1.0, (iii) 1.5, (iv) 2.0 (v) 2.5, (vi) 3.0, (vii) 5.0, (viii) 8.0, to (ix) 10.0 µM with (D) T1-modified, (E) T2-modified, and (F) T3-modified graphite electrode immersed in 0.1 M phosphate buffer solution at pH 7.

In addition to physisorption methods, Emperor 2000 carbon nanoparticles are also subjected to synthetic methods to covalently functionalise the surface with desired groups. Emperor 2000 particles are commercially produced with phenylsulphonic acid functionality on the surface. Herein it is shown that modifying the surface with dioctylamine affords carbon nanoparticles with an extremely hydrophobic character. These modified nanoparticles are demonstrated to be important substrates for probing lipophilic redox systems and lipid character under different experimental conditions. Coenzyme Q_{10} is directly immobilised into a composite film of the modified nanoparticles and lipid; the voltammetric response was greatly enhanced. The high

surface area hydrophobic carbon nanoparticles provide a support for coenzyme Q_{10}, and because of their hydrophobic nature; the modified particles can be combined with lipids to mimic membrane processes. The presence of the lipid also enhances the electrochemical response, see Figure 9.2. The cyclic voltammograms in Figure 9.2A were obtained with 1 nmol coenzyme Q_{10} (over pH range 2 to 12) contained within a modified nanoparticle-coenzyme Q_{10} deposit, and those in Figure 9.2B were obtained over the same pH range in the presence of lipid and correspond to only 0.1 nmol coenzyme $Q_{10,}$ that is, an order of magnitude less redox-active material. The clear peaks and uniform shift observed for the lipid-containing composite simplify the response and allow for further insight to be obtained at much lower concentrations. It should also be noted that for the composite without lipid, 0.1 nmol was almost indistinguishable from the background capacitive current. In short, a new and versatile carbon nanomaterial is produced and in combination with a lipid is demonstrated as an effective and sensitive probe for hydrophobic redox systems and lipid-based processes.

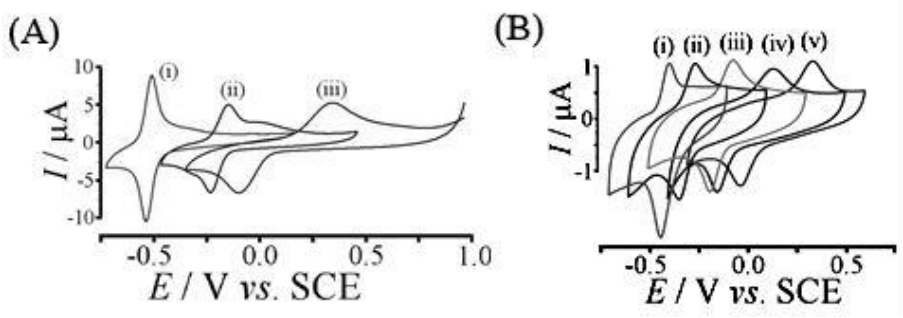

Figure 9.2. Cyclic voltammograms (scan rate 10 mVs^{-1}) for the reduction and back-oxidation of (A) 1 nmol Q_{10} in 15 μg CNP immobilised at a glassy carbon electrode and immersed in aqueous 0.5 M PBS at pH (i) 12, (ii) 7, and (iii) 2. (B) 0.1 nmol Q_{10} in 25 nmol DMPC and 15 μg CNP immobilised at a glassy carbon electrode and immersed in aqueous 0.5 M PBS at pH (i) 12, (ii) 10, (iii) 7, (iv) 5, and (v) 2.

The composite films of hydrophobic carbon nanoparticles, lipid, and coenzyme Q_{10} are also investigated under different reaction conditions, that is, at different temperatures and different pH environments. It is clear that the pH value of the system has an effect on the electrochemical behaviour of the coenzyme Q_{10} redox couple; however, perhaps more interestingly, the temperature exacerbates the pH effect. The reasons are unclear; however, a change in the phase of the lipid occurs at approximately 24 ^{o}C, which is detectable by electrochemical methods. This gel-fluid transition results in a change in

mechanism; which differs depending on the surrounding environment being acidic, neutral, or alkaline. This study demonstrates the versatility of the carbon-based composite, demonstrates the ability of electrochemical methods to detect phase changes, and highlights mechanistic challenges that are introduced with temperature and pH.

Fluorescent carbon nanodots are another important class of carbon nanoparticle. Herein, the facile hydrothermal synthesis of carbon nanodots is described. These nanodots, synthesised from poly(4-vinyl pyridine), contain surface pyridine and pyridinium species as determined by a range of characterization methods. This novel carbonaceous material exhibits two-photon fluorescence that is observed in solution and also in HeLa cells. The nanodots are demonstrated to have the potential to be developed into nanomedicines and biocompatible scaffolds for new drug delivery mechanisms as they retain their intrinsic fluorescence properties inside cells and they do not appear to cause any significant detrimental impact to HeLa cells, even after one hour of incubation (Figure 9.3). This proves to be an important development for biocompatible and traceable imaging probes.

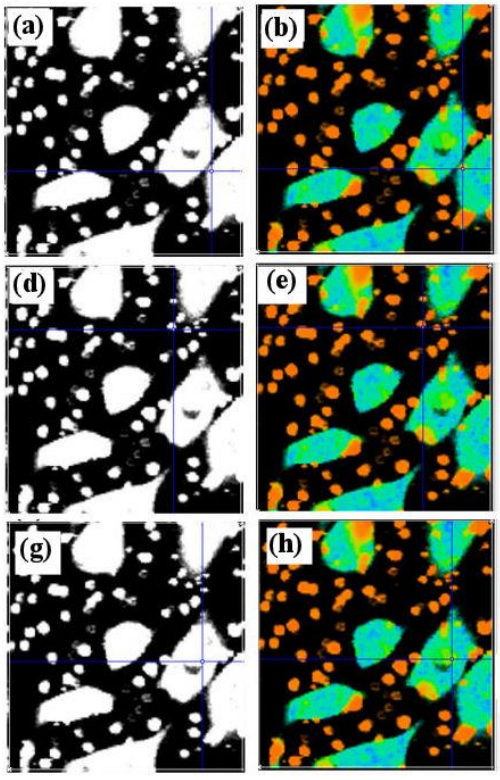

Figure 9.3. Two-photon confocal fluorescence (λ_{ex} = 910 nm) for P4VP C-dots in 1:99 DMSO: EMEM after incubation for 1 hour; intensity image in cell membrane (a), in cell medium (d) and inside the cell (g); lifetime mapping in cell membrane (b), in cell medium (e), and inside the cell (h); fluorescence decay in cell membrane (c), in cell medium (f), and inside the cell (i)

The final carbon-based nanomaterial that is documented in this thesis shows the combination of carbon black nanoparticles with the hydrothermal methodology that yielded the novel carbon dots. When the two materials, that is, Emperor 2000 and poly(4-vinyl pyridine), and subjected to hydrothermal carbonisation procedures, a novel core-shell carbon nanomaterial was produced. The shell exhibits strong pH-dependent properties. The chemical structure of the carbonised material is not well-defined; however, pyridinium and carboxylate functionalities are identified as positive and negative charge bearers, respectively. A core-shell carbon nanomaterial is prepared with a maximum capacitive current (approximately 13 Fg^{-1} for the specific capacitance) at the point of zero charge, see Figure 9.4. This is achieved by adjusting the thickness of the shell with respect to the core, which can be attributed to a shell charging effect. This type of core-shell nanomaterial and similar functionalised materials could be useful for future sensing applications.

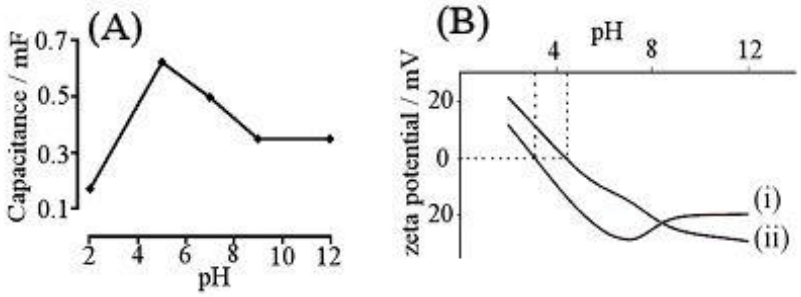

Figure 9.4. (A) Plot of capacitance as a function of pH. (B) Zeta potential measurements in 0.1 M PBS for (i) Emperor 2000 CNPs and (ii) for P4VP-wrapped carbon nanoparticles.

The straightforward synthesis, modification, and application methods developed in this thesis demonstrate the effectiveness and the versatility of carbon nanoparticles. This class of nanomaterial is generally outclassed by modern and more fashionable carbon nanotubes and graphene-based systems. However, carbon nanoparticles are more cost effective and readily available carbon-based nanomaterials that can be used for a wide range of applications, including some of those applications in which other nanocarbons are currently being utilized. This thesis demonstrates that carbon nanoparticles can be synthesised and modified to attain desirable properties and characteristic by using facile methodologies and accessible chemistry.